# The development of porous texture in steam gasified coal chars.

Causton, Peter David

*Award date:*
1985

*Awarding institution:*
University of Bath

THE DEVELOPMENT OF POROUS TEXTURE IN

STEAM GASIFIED COAL CHARS

submitted by

Peter David Causton

for the degree of Doctor of Philosophy

of the University of Bath

1985



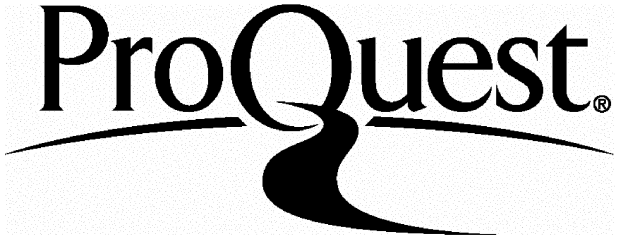

## ABSTRACT

The work reported in this thesis is a study of the changes in porous texture during steam gasification of a model char derived from a PVDC/PAN copolymer and a char derived from a highly volatile, bituminous coal (Markham Main). The techniques employed to analyse the complete pore structure of the chars were helium pycnometry, mercury porosimetry and gas adsorption. Adsorption measurements were made using Ar at 77 K, $CO_2$ at 195 K and $CO_2$ at 273 K in an attempt to analyse as much of the pore structure as possible. Total surface area (TSA) and micropore volume were shown to increase with burn-off for both chars, reaching a maximum value at about 70% burn-off. The proportion of non-microporous surface area, obtained using the Isotherm Subtraction method, increased with progressive gasification up to about 60% burn-off, confirming quantitatively what was expected from mercury porosimetry measurements. All results indicate that the model char is more microporous than the coal char.

A new dynamic method is described for measuring the active surface area (ASA) of carbons and chars, which involves oxygen chemisorption followed by a temperature-programmed desorption of $CO_2$ and CO; the method gives similar results to the standard volumetric technique. ASA, measured by this technique, increases with burn-off for both chars, reaching a maximum value at 70-80% burn-off.

Reactivities of the two chars were measured using a fixed-bed reactor and a thermogravimetric balance; results from the two

techniques are in good agreement. Gasification conditions were chosen such that the rate was chemically controlled. Maximum reactivity was observed at about 70% burn-off for both chars. When reactivity is expressed on a weight basis (gC/g sec) the model char is more reactive than the coal char. However, when the reactivity is expressed per unit ASA the coal char appears to be the most reactive of the two. It is concluded from this survey that ASA is a more reliable reactivity normalisation parameter than TSA.

ACKNOWLEDGEMENTS

I wish to express my sincere gratitude to the following people for their help during the course of this work:-

Dr. B. McEnaney for his help and advice as supervisor of the project; the Science and Engineering Research Council and the British Gas Corporation for financial support; Dr. N.D. Parkyns and Dr. C. Komodromos of British Gas, London Research Station, for their joint supervision and useful discussions; Mr. P. Wakeford (Chief Technician, School of Materials Science) and Mr. P. Dicken for their invaluable experimental assistance; Mr. B. Chapman and Mr. H. Perrot for help with *X*-ray diffraction and SEM work respectively; Prof. P.L. Walker Jr. of Pennsylvania State University, U.S.A. for gifts of coal char samples; Mrs. Paula Keilthy for her typing expertise and finally Miss Linda Osman, my fiancée, for her support, encouragement and assistance.

CONTENTS

CONTENTS (Cont.)

CONTENTS (Cont.)

CONTENTS (Cont.)

# CHAPTER ONE

## INTRODUCTION

The seventies was a decade in which the industrial world became aware that the supply of gaseous and liquid fossil fuels was limited and that the era of cheap energy had passed. After many years of scepticism and reluctance, corporate and government energy planners are now realising the importance of the problem and are turning their attention to the efficient utilisation of large world reserves of coal. Part of the reason for this reluctance lies in the complexity and lack of complete understanding of the fundamental phenomena involved in the emerging coal utilisation technologies, resulting in undesirably high scale-up risks.

For coal, as with oil, it is essential to use its energy content efficiently, not only to conserve reserves, but also to minimise process plant size, feedstock requirements and thus overall fuel production costs. Coal gasification offers not only routes at high thermal efficiencies for the production of gaseous and liquid fuels and chemicals, but also a means of reducing dependence upon increasingly costly and uncertain supplies of petroleum feedstocks.

The efficiency of coal combustion and gasification processes and the design parameters of combustors and gasifiers depend to a great extent on the kinetics of the heterogeneous reactions between the rapidly devolatilised coal char and the reactant gases. It has been found experimentally that char gasification reactivity (and hence gasifier performance) is a function of such variables as reaction atmosphere, properties of the parent coal (*e.g.*, rank and mineral matter content),

particle size, pyrolysis conditions and porous texture. For example, the reactivity of a char in a particular gas atmosphere can increase with decreasing rank of the parent coal, with decreasing pyrolysis temperature, with decreasing coal (char) particle size and with increasing total and active surface area.

At the present time the experimentally observed differences in the gasification reactivity of coal chars are not well understood. From a qualitative viewpoint it can be argued that one char is more reactive than another because it has a higher concentration of active sites, or because catalytic effects of mineral matter are more pronounced, or because it has a more highly accessible internal pore structure. However a complete quantitative assessment of these factors is difficult to make. It is a desirable objective to gain a better (and hopefully quantitative) understanding of these fundamental aspects of coal char reactivity in an attempt to improve gasifier performance and utilise existing coal supplies more efficiently. The work reported in this thesis is a contribution towards achieving this objective.

The research was undertaken as part of the Science and Engineering Research Council's CASE studentship scheme, in association with the British Gas Corporation (BGC). In recent years, as a result of the considerations already discussed, studies of coal gasification at BGC have become increasingly important [1]. Much attention has been given to optimising the performance of the fixed-bed Lurgi slagging gasifier for eventual production of gaseous fuels such as substitute natural gas. The performance of the gasifier depends critically upon the reactivity of the coal char in the gasification zone, which, in turn, is a function of changes in pore texture of the char with progressive gasification.

The purpose of the work is therefore to study the development of porous texture (*i.e.*, pore volume, pore size distribution, total and active surface area) in a coal char with progressive gasification by steam. In order to facilitate a comparison with a relatively pure char, the gasification characteristics of a model char derived from a polymeric precursor were also investigated.

In addition to supporting the work currently being carried out on steam gasification at BGC, in particular the development of the slagging gasifier, the research programme also has considerable merit and timeliness elsewhere. The proposed topic of study has been identified as one of the major areas requiring further research, if our understanding of the fundamental processes involved in coal gasification is to be improved [2].

## 1.1 Structure of the Review

It is apparent from the preceding introduction that the structure of the parent coal has a significant effect on the overall gasification process. Both the physical and chemical structure play an important role in determining conversion efficiency. It is therefore appropriate that a review of the literature should commence by assessing the important structural features of coals and chars which may affect their usefulness in the gasification process (Chapter Two).

It has become conventional to separate the overall gasification process into coal pyrolysis and char gasification. Chapter Three assesses the major physical and chemical changes that occur during the various stages of pyrolysis and carbonisation. A section is also included dealing with the pyrolysis of polymers. Chapter Four discusses

the relevant reactions occurring during steam gasification of coal chars, the kinetics of these reactions and the important coal characteristics which affect gasification.

# CHAPTER TWO

# STRUCTURE OF COAL

## 2.1 Formation and Classification of Coal

Coal is an aggregate of heterogeneous substances composed of organic and inorganic materials. The organic constituents are derived mainly from plant remains which have undergone various degrees of decomposition in peat swamps, and physical and chemical changes after burial. The bulk of all coal deposits was formed in a peat swamp environment where different types of vegetation flourished, reflecting primarily conditions of climate, water level and water chemistry.

The continuous evolution and degradation of the parent plant material towards a carbon or graphite structure is known as coalification [3]. The degree of coalification forms the basis of classification of coals by rank. Coal is ranked as peat, lignite, sub-bituminous coal, bituminous coal and anthracite. The rank increases progressively from lignite through low and high rank coals to anthracite. The carbon content increases with rank while the oxygen and hydrogen contents usually decrease, as does the reactivity of the coal. Classification by rank is based upon the maturity of the coal, as a whole, in the coalification process. Consequently, the percentage carbon content of a coal is a basic variable in coal classification by rank. Nevertheless, the ASTM rank classification [4] is based upon the percentage volatile content for high rank coals and the calorific value for low rank coals. Since the amount of volatile matter derived from a coal depends largely on the conditions of devolatilisation, the measurement conditions of percentage volatile have been standardised [5]. The standard technique involves heating a weighed sample at a rate of 100° C/min in a covered crucible to a temperature of 950° C with a

residence time of six minutes at that temperature.

Coals can also be classified by petrographic composition [6]. The parent material itself, originating from different parts of the plant, is rather heterogeneous. The heterogeneity is increased as a result of mixing with inorganic sediment during coalification. It is these physically distinctive, chemically different entities, derived from degradation of different parts of the parent material, which form the basis for petrographic classification of coals.

The constituents of coal were classified microscopically by Thiessen in 1920 [7] as anthraxylon, attritus and fusain. This classification was based on visual characteristics of the coal constituents in thin sections under transmitted light [8]. The use of thin sections for this purpose was later replaced by a technique involving the measurement of the reflectance on a polished surface [9].

The microconstituents of coal are usually defined as macerals [10] (derived from maceration of plant matter). These macerals are commonly grouped under the names vitrinite, exinite and inertinite [8], as shown in Table 2.1. Vitrinite is the principal constituent of coal (60-90% by weight); it originates from the woody tissue of the plant material and possesses a highly vitreous lustre. Exinite is the hydrogen-rich portion of the coal structure and arises mainly from plant spores, cuticles and resins. Inertinite is a dull granular form composed of fossil charcoal and highly decayed plant material. Inertinite is frequently divided into micrinite and fusinite. The properties of the macerals are found to be different, but these differences become smaller as rank increases [11,12]. Figure 2.1 shows an example of the convergence of density values at high rank [8].

Coal constituents were classified macroscopically by Stopes [10] into four lithotypes: vitrain, clarain, durain and fusain. The maceral groups of these lithotypes are given in Table 2.2. Vitrain and fusain contain vitrinite and fusinite, respectively. Vitrinite is the main constituent of clarain while durain contains predominantly micrinite.

The three maceral groups are, to a certain extent, characterised by their chemical composition, as shown in Figures 2.2 and 2.3. The data presented in these figures were obtained from extensive investigations on bituminous coal maceral groups [13-16]. As a reference, the percentage carbon and the H/C ratio (both on an atomic basis) of a number of aromatic molecules are also given in Figure 2.2. These figures lead to the determination of the atomic carbon content, the H/C atomic ratio and the volatile content of the three maceral groups, the results of which are summarised in Table 2.3. The results indicate that volatile content and H/C ratio increase in the order: inertinite, titrinite, exinite [13].

## 2.2 Classification Systems

Originally (up to the year 1800) coals were merely classified as bright coal, black coal and brown coal. In 1826 Karsten [17] introduced a classification of coal based on the composition of the residue left when coal is heated. This led to a distinction being made between sand coals and caking coals. The first system in which elementary composition was used for classification purposes was proposed by Regnault in 1837 [18]. He developed a system in which coals were classified according to their oxygen content. Many classifications have since been proposed based on such parameters as percentage residue [19], carbon/volatile matter ratio [20,21], calorific value [22,23] and caking and swelling character-

istics [24-26]. However, none of these classification systems has found universal application.

The most widely used method in Britain is that developed by Gray and King [27]. The coal is slowly heated and the resulting coke examined visually (Figure 2.4). If the coke appears to be strongly caking (> type G), it is determined how many parts of electrode carbon ($x$) must be mixed with ($20-x$) parts by weight of the sample to obtain a coke of type G. When four parts of electrode carbon are needed, the coke type is indicated by the code number $G_4$.

Since coals consist mainly of carbon, hydrogen and oxygen, it is logical that classification should be based on elementary analysis. Methods based on oxygen content are unreliable since direct determination of oxygen content is difficult. It is usually derived from the deficit in the elementary balance. Seyler (1900) [28] therefore designed a classification using the carbon and hydrogen contents as the relevant parameters. Seyler's original system is shown in Table 2.4. The coals are classified in four main groups or species according to carbon content and each of these species is sub-divided into varieties or genera according to hydrogen content. After the introduction of some modifications and improvements, Seyler's system has resulted in the renowned coal chart (Figure 2.5) in which technological properties of coal are correlated with the elementary composition. All coals tend to fall into a well defined band when classified in this manner. Unfortunately, Seyler's classification system has never been adopted in practice. The reason for this is that the elementary analysis procedure is too involved to be used in industrial laboratories. Commercial classification systems are usually based primarily on volatile matter content. However, some

countries employ a second classification parameter, such as calorific value or swelling index to obtain a more detailed differentiation between coals [8].

## 2.3 Molecular Structure of Coal

The chemical analysis of coal, although giving information on the carbon, hydrogen and oxygen contents, does not convey much about its chemical make-up or molecular structure. The complex molecular structure of coal can be categorised into three groups [11]: (a) condensed aromatic lamellae; (b) aliphatic and alicyclic interstitials and bridge groups; (c) heteroatomic interstitials and bridges (cross-links). It is generally accepted that a significant portion of the carbon in coal is combined in the condensed aromatic lamellae. As might be expected, the aromaticity, namely the aromatic carbon fraction, increases with rank ranging from about 0.72 for sub-bituminous coal up to almost 1.0 for anthracite [29,30].

The carbon atoms common to two or three aromatic rings are non-reactive. However, the peripheral carbons, common to only one ring, such as:

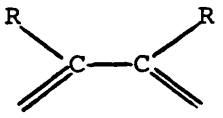


where R could be -H, -OH, $-CH_3$ *etc.*, form functional groups which can be subject to hydrogenation and ring breakage during heat treatment [31]. This ring breakage results in the production of lower weight molecules. Thus the percentage reactive carbon (peripheral carbon) is an important variable in the determination of the effect of aromatic structure on coal conversion. As the condensed aromatic lamellae increase in size, the percentage reactive carbon (and the H/C atomic ratio) decreases [11].

The number and size of the rings increases with carbon content, resulting in a decrease in overall reactivity as a pure graphitic structure is approached. A pure graphitic structure is never achieved due to the lack of mutual orientation between adjacent layers and a greater average spacing between layers compared with graphite. The aromatic units indigenous to coal are shown in Figure 2.6.

It has been observed [32,33] that the percentage of the aromatic and hydroaromatic units contained in the hydrocarbon portion of coals containing 80-90 wt % carbon, remains practically constant (92±2%). The balance (6-10%) comprises aliphatic and methyl groups.

The aliphatic and alicyclic functional groups are characterised by their high hydrogen content as well as their ease of dehydrogenation and devolatilisation. The type and number of these functional groups, which are bonded to the peripheral carbons of aromatic lamellae, dictate, to a large extent, the activity of coal in various reactions [34].

The heteroatoms present in coal are oxygen, nitrogen and sulphur [11]. Nitrogen appears to be evenly distributed and has no significant effect on coal reactivity, but oxygen functional groups play a very important role in coal conversion. Some of the heteroatom-containing units which have been identified [35] are shown in Figure 2.6. The major oxygen functional groups present are methoxyl, carboxyl, carbonyl, hydroxyl, etheric and heterocyclic oxygen. A typical distribution of oxygen functional groups for a sub-bituminous and a bituminous coal is shown in Table 2.5 [36]. The appearance of the aforementioned functional groups is dependent upon the rank of the coal as shown in Figure 2.7, which is a plot of percentage carbon of the samples against percentage oxygen. Although the presence of specific groups in various coals is widely researched and disputed, it

is generally accepted that the oxygen content of coal decreases with increasing rank. The oxygen functional groups have an important bearing on the coal characteristics relevant to different reactions. For example, the etheric oxygen which cross-links the aromatic lamellae plays an important role in determining the caking properties of coals. Specifically, the oxygen bridges are broken when heated and the aromatic lamellae become mobile, conferring a certain amount of plasticity to the coal.

Sulphur is interchangeable with oxygen in structures such as those involving heteroatomic rings and is also present in linking units. The presence of sulphur affects the reactivity of coal and total sulphur content has been correlated with the level of coal conversion [37]. Most importantly, sulphur is the primary pollutant in coal combustion and gasification and its removal is the most important criterion in coal cleaning [6].

The three main types of coal, namely low, medium and high rank, correspond approximately to three types of structure [38], shown in Figure 2.8. Low rank coal, Figure 2.8(a), is composed of small layers, more or less randomly orientated, connected by cross-links. This produces a highly porous, and consequently highly reactive, structure. Medium rank coal, Figure 2.8(b), exhibits a greater degree of orientation and hence a greater tendency towards parallel stacking. This structure contains fewer cross-links and pores than low rank coals. Anthracite, (Figure 2.8(c), shows a growth of individual layers, a marked increase in degree of orientation and the development of a new type of pore elongated parallel to the stacked layers.

## 2.4 Pore Structure of Coals and Chars

The internal pore structure of coal is very complex and has some characteristics similar to molecular sieves, that is certain molecules are permitted to penetrate the pore structure while larger molecules are excluded. In addition, diffusion of gases within this type of pore structure is an activated process, which means that temperature plays an important role. The pore structure of coal is generally characterised by internal surface area and pore size. The internal surface area and its accessibility to reactants have a significant effect on the combustion and gasification rate during the gasificcation process. Furthermore, the nature of the products from the reactions also depends upon the porosity or the internal surface area of the coal or coal char.

The pores present in coal can be classified by considering three broad size ranges [39-41]: (i) micropores, with a diameter of less than 20 Å; (ii) mesopores, with a diameter ranging from 20 to 500 Å; (iii) macropores, which are pores of greater than 500 Å in diameter. This classification suggests cylindrical pores; however, electron microscopy indicates conical pores and flat cavities, as well as cylindrical pores [42]. Small interstices combine these three basic shapes and *X*-ray work carried out by Hirsch [38,43] showed that, (i) coal micropores reflect weak cross-linking among condensed aromatic hydroaromatic clusters and (ii) average pore size decreases with increasing rank, since aromaticity and thus cluster size increases. Harris and Yust [42] found that certain macerals are characterised by their pore sizes. Vitrinite contains predominantly micropores, inertinite contains mostly mesopores and exinite exhibits a generally macroporous structure. Most of the internal surface area in coals (> 90%) lies in the micropore-mesopore range [8,44], with only a small contribution to the total surface area from large mesopores and

macropores.

Pore structure can be studied using a wide variety of techniques [8, 45,46], but the three major methods are (i) adsorption; (ii) porosimetry; (iii) pycnometry. The important practical aspects of these techniques will be discussed at a later stage.

Coal chars are generally porous materials with relatively high values of total surface area (TSA), typically greater than 100 $m^2/g$. The pore size distribution in the chars is a function of coal rank and pyrolysis conditions [47]. Gan *et al.* [48] have found that mesopores are particularly influential in middle rank coals; hence the molecular sieve effect is not evident and a minimum in porosity and internal surface area is observed in these coals (Figure 2.9). Macropores were found to dominate in low rank coals ('open' structure), while micropores were more abundant in high rank coals ('anthracite' structure), as shown in Figure 2.10 [8,48,49].

Traditionally, the surface area of both porous and non-porous materials is determined by gas adsorption in conjunction with a suitable isotherm equation. Analysis of coal chars usually employs the BET equation [50] and the D-R equation [51-53], despite controversy and confusion over the applicability of such equations in some circumstances [54]. The crucial issue is the mechanism of adsorption. Most research has indicated that pores with very small diameters (close to molecular dimensions) exhibit gas-solid interactions of unusually high magnitudes due to the close proximity of the pore walls [55,56]. As a result of the enhanced adsorption energy, the entire volume of the pores is filled with physisorbed molecules, even at low relative pressures. Consequently, as several workers have pointed out [57,58], the concept

of a surface area of a microporous material, as measured by gas adsorption, becomes meaningless.

Micropore volumes of carbonaceous materials, including coal chars, have been determined by Marsh *et al.* [59-62] and Walker *et al.* [63-66] using the D-R equation. They have attempted to convert this value to an effective surface area using the BET equation and assuming that the micropore volume is equivalent to the monolayer capacity. This assumption is, of course, strictly valid only for materials possessing a homogeneous microporous structure.

Many coal chars possess a wide pore size distribution [67] and both mechanisms of adsorption are expected to be operative: layer-by-layer adsorption in the wider pores (as envisaged by the BET theory) and volume filling in very narrow pores (as hypothesised by the D-R theory). Thus the applicability of either one of these two isotherms alone for calculating the TSA of coals and chars is subject to some uncertainty.

The BET approach has been modified by Brunauer *et al.* [68] in an attempt to include the analysis of micropores. These authors contend that it correctly measures the microporous surface area except when a significant fraction of the pore surface consists of ultramicropores ($d < 2$ Å). Dubinin [58] has pointed out that the D-R equation is strictly applicable only in the absence of significant mesoporosity and several methods have been postulated to correct for adsorption on the mesopore surface [69-74].

## 2.5 Mineral Content of Coals

The inorganic fraction of coal (5-20%) is primarily composed of minerals and to a lesser extent organometallic compounds and exchangeable cations (*e.g.*, $Na^+$, $K^+$, $Ca^{2+}$, $Fe^{2+}$ and $Fe^{3+}$) [75,76]. The aforementioned

constituents usually have a pronounced catalytic effect on gasification and consequently play an important role in coal utilisation. Mineral composition determines the mode of ash removal during combustion, either as dry ash or as liquid slag. In the latter case the mineral composition also determines the slag viscosity and this affects the ease of ash removal. Typically, mineral matter is randomly distributed in coal as approximately 2 μm inclusions. Four major mineral types have been identified and these are shown in Table 2.6 [2,77].

Pyrites in coal is an obvious source of $SO_2$ pollution in combustion and the presence of coal minerals may lead to problems in filtration, solid build-up and catalyst poisoning. However, certain minerals are knwon to have a beneficial effect in coal conversion processes, *e.g.*, carbonates. The mineral composition of a particular coal feed is therefore a signi-cant variable in process design and in characterising the behaviour of coals in these processes.

# CHAPTER THREE

# PYROLYSIS AND CARBONISATION

## 3.1 Introduction

Due to the complexity and lack of complete understanding of the various phenomena occurring during coal gasification, it has become conventional to separate the overall process, both experimentally and conceptually, into coal pyrolysis and subsequent char gasification. This chapter assesses the important aspects of the coal pyrolysis stage; coal char gasification will be dealt with in Chapter Four.

In many respects, the pyrolysis stage is the most important in the overall gasification process, since it is the conditions of pyrolysis which ultimately affect the reactivity of the coal char in the gasification zone of the gasifier. This chapter aims to assess the structural and chemical changes occurring during carbonisation, the kinetics of the reactions involved and the implications of these reactions with regard to the eventual complete conversion of the coal.

Since this investigation is concerned with the carbonisation and gasification of a model char (derived from a polymeric precursor) as well as a coal char, Section 3.7 deals with the pyrolysis and carbonisation of polymeric materials.

## 3.2 Physical and Chemical Changes occurring during Carbonisation

From a practical standpoint, the most important properties of coal are those associated with its behaviour when heated. When coal is heated in the absence of air, the sequence of changes which occurs forms the basis of the carbonisation process from which products such as metallurgical coke, domestic coke, coal tar, town gas and ammonia are

derived [3]. The volatile products consist essentially of gas, ammonia, tar and light oil; and coal chemicals are subsequently produced from the oil and tar [78]. A typical distribution of carbonisation products as a function of carbonising temperature is shown in Figure 3.1. The product yield [79-81] varies with coal rank and pyrolysis conditions such as heating rate, residence time and maximum temperature.

During pyrolysis, the aromatic and hydroaromatic structures in coal lose their functional groups and cross-links between them may break. The breakage of cross-links is important in the evolution of tar during pyrolysis [82]. However, this process is limited because the breakage of cross-links generates free valencies and these tend to recombine. Hydrogen release during pyrolysis converts hydroaromatic groups to aromatic groups and eventually to small trigonally-bonded carbon crystallites. This breakage of bonds to peripheral substituent groups results in the formation of gaseous products such as methane and hydrogen. Subsequently, due to the generation of free valencies, recombination occurs and the remaining solid becomes more cross-linked and involatile [78].

Coal carbonisation can be classified into low temperature carbonisation (coking temperature < 700° C) and high temperature carbonisation (coking temperature > 900° C) [6,78]. This temperature difference reflects the pronounced physical changes that coal undergoes at temperatures from 600 to 800° C. The ultrafine pore structure of the parent coal is usually retained to a large extent until a temperature of about 700° C is reached. Therefore low temperature chars are substantially as reactive as the parent coal, but become progressively less reactive through devolatilisation and loss of porosity as the carbonisation temperature is increased above 700° C.

Three major changes are seen to occur at the coal surface during heat treatment:

(i) Oxygen and hydrogen atoms are lost [8]. Above a temperature of about 700° C all chars have similar carbon, hydrogen and oxygen contents. Most of the oxygen is lost at low temperatures; heat treatment above 700° C is dominated by loss of hydrogen.

(ii) Conversion of mineral matter to metal oxides [75], for example:

$$Al_2Si_2O_5(OH)_4 = Al_2O_3 + 2SiO_2 + 2H_2O$$

$$CaCO_3 = CaO + CO_2$$

$$CaSO_4 = CaO + SO_3$$

(iii) Thermal annealing at temperatures from about 700 to 1100° C [8,83,84]. Microporosity and edge carbon atoms are lost due to cluster reorganisation. The char structure becomes more graphitic and unpaired surface electrons disappear, as verified by ESR work [85]. Structural defects also tend to disappear; however, impurities may promote permanent dislocations even at high heat treatment temperatures [45,86].

Franklin [83] has postulated the existence of two types of coal: (i) graphitising coals corresponding to Hirsch's 'ordered' structure and (ii) non-graphitising coals which correspond to Hirsch's 'open' structure [38,43]. In the first case [8] cluster mobility and weak cross-linking encourage realignment due to cluster growth and coalescence, lamellae packing and graphitisation at temperatures above about 1500° C. In the second case, heating promotes cross-linking which means that

microporosity persists up to temperatures of at least 2000° C. Franklin [83] showed that edge carbon atoms are more abundant in chars produced from non-graphitising coals than those derived from graphitising coals.

These considerations are a clear indication that heat treatment should reduce intrinsic char reactivity due to loss of active sites. There appears to be no direct evidence to support this, but there is, however, indirect evidence based on overall reactivity [87], which will be discussed in Section 3.5. Blake *et al.* [84] suggested a two site theory to explain reactivity losses during carbonisation. Highly active sites (*e.g.*, oxygen and mineral matter) are lost quickly, whereas less active sites (*e.g.*, edge carbon atoms) lose reactivity slowly. Intrinsic reactivity after extensive heat treatment probably results from mineral matter-induced dislocations.

## 3.3 Stages of Pyrolysis

Although usually associated with the 350-500° C temperature range in which devolatilisation proceeds rapidly, thermal decomposition actually begins at much lower temperatures and can, as illustrated by a typical cumulative weight loss curve (Figure 3.2), be divided into three stages [80, 88].

In the first stage, which commences well below 200° C, decomposition is fairly slow and manifests itself primarily in the release of small quantities of "chemically combined" water, oxides of carbon and hydrogen. However, above 200° C, some benzylic carbon begins to isomerise to form methyl-phenyl derivatives and traces of alkyl benzenes are evolved [88]. Little is known about these low temperature processes except that they alter the structure sufficiently to influence its subsequent thermal behaviour.

The second stage ranges from about 350-500° C and exhibits a formal decomposition temperature ($T_d$), conventionally set at a point at which the weight loss curve suddenly turns upward [80]. $T_d$ tends to increase with increasing rank of the coal, as shown in Figure 3.3. About 75% of all volatile matter ultimately released by the coal, including all tar and lighter condensable hydrocarbons, are evolved in this stage. However, product compositions are notably dependent on pyrolysis conditions such as pressure and heating rate. This is attributed to the fact that extensive fragmentation of the coal molecule is involved. If the coal possesses coking properties it will pass through a characteristic transient "plastic state" between 350 and 450° C, thereby forming a more or less porous coke. The plastic properties of coals are discussed further in Section 3.4.1.

The final stage of decomposition is characterised by gradual elimination of heteroatoms (principally oxygen and hydrogen) and ends, strictly speaking, only when the char is transformed into a graphitic solid. In practice, however, the composition and quantity of volatile matter released above 900° C is of little interest. The principal by-products of third stage decomposition are water, oxides of carbon, hydrogen, methane and traces of $C_2$ hydrocarbons. The most important feature is the progressive "aromatisation" of the char to develop increasingly large hexagonal carbon platelets and thus decrease the reactivity of the structure.

## 3.4 Coal Characteristics affecting Carbonisation

### 3.4.1 Plastic properties:

When bituminous coals are heated they undergo a series of phase changes [89]:- (i) the coal particles soften and become fluid-like at temperatures of about 400° C; (ii) swelling takes place as soon as the

particles are sufficiently fused together to offer appreciable resistance to the flow of volatile matter resulting from decomposition; (iii) swelling ceases at about 500° C when the coal has lost its plasticity and begins to resolidify into a coherent body with a porous structure, known as coke.

Decomposition initially depolymerises the coal and gives rise to fluid products, which plasticise the other components of the coal, and gases which form bubbles. Swelling results from the flow of gas bubbles through the macropores and fissures in the coal. The fluid products then decompose into volatile matter and an insoluble residue is formed,

In general [89], the plastic properties become evident when the volatile content exceeds 13-15% of dry, ash-free coal. These properties initially increase with increasing volatile content and reach a maximum value for coals with 25-30% volatile content. As the volatile content exceeds 35-40%, the plastic properties diminish markedly. Figure 3,4 shows the contraction/expansion behaviour, as determined by low temperature dilatometry, for coals of different rank.

3.4.2 Coal rank:

Pyrolysis product distributions vary considerably with coal rank [90]. This is illustrated in Figure 3.5, the volatiles from lignite pyrolysis [Figure 3.5(a)] are dominated by CO, $CO_2$ and $H_2O$, whereas the main volatiles from bituminous coal pyrolysis [Figure 3.5(b)] are tars and hydrocarbon liquids. Obviously the rank of the parent coal must be considered carefully when selecting coals for particular applications,

3.4.3 Petrographic composition:

The entities of coal can be divided into two classes, reactives and inerts, according to their thermal characteristics [78]. The reactives consist of vitrinoids (except those in anthracite), exinoids (exinites), resinoids (resinites) and reactive semi-fusinoids. The inerts consist of micrinoids (micrinites), fusinoids (fusinites), inert semi-fusinoids and coal minerals. During carbonisation the reactives soften, flow, fuse and resolidify to form coke, whereas the inerts remain relatively unchanged. As the reactives flow around, they envelop and bond the inerts together. Since small particles of the inerts are well assimilated in the plastic matrix, coke strength increases as a result [91]. Large particles of inerts are often sources of fissures and cracks.

## 3.5 Effect of Pyrolysis on Pore Structure

Pore structure undergoes little change until devolatilisation occurs at temperatures of 350-400° C. Upon pyrolysis we expect [8,83]:- (i) an increase in porosity; (ii) an increase in average macropore size; (iii) a decrease in average micropore size due to volatile repolymerisation. Hence no dramatic change in the pore size distribution is anticipated. Available evidence [92] supports these expectations for typical carbonisation conditions, *i.e.*, low temperature and low heating rate. At high heating rates, volatile escape is greater and more rapid, repolymerisation is less favoured and a higher porosity is therefore developed with significant amounts of microporosity and mesoporosity present [93].

Using adsorption and *X*-ray techniques Chiche *et al.* [92] investigated surface area variations for heat treatment temperatures between 500° C and 3000° C. The results, shown in Figure 3.6, indicate that coking

coals experience a much smaller increase in surface area than non-coking coals. Coking coals also exhibit a sharp decrease in surface area for heat treatment temperatures above 1000° C. This results from sealing of pores *via* coalescence, volatile repolymerisation and graphitisation. Toda [94] used pycnometric techniques to study pore size changes and found that micropore volume in coking coals is virtually eliminated above 1000° C, in agreement with Chiche *et al.* [92]. With non-coking coals the micropore and mesopore volume varies only slightly with carbonisation temperature. This indicates that development and plugging of these pores offset each other, implying a retention of molecular sieve properties.

Since high heat treatment temperatures cause loss of internal surface area and active sites, it is reasonable to expect that heat treatment reduces overall char reactivity. Indeed, increased heat treatment temperature [84,85,87,95,96] and soaking time [84] have been shown to decrease reactivity substantially. Low heating rates can also reduce reactivity due to the existence of favourable thermal annealing conditions and slow devolatilisation which causes increased tar deposition and lower porosity [93].

### 3.6 Kinetics of Coal Pyrolysis [8,97-100]

Coal pyrolysis involves a complex thermal decomposition of the basic aromatic and hydroaromatic structures in coal. Transportation of the resulting volatiles and secondary reactions must also be considered. While the yield depends on competition between mass transport and secondary reactions, the rate is determined by the total resistance derived

from decomposition plus heat and/or mass transfer. For fine particles (< 75 μm) the transport resistance is negligible and the reaction is controlled by chemical kinetics. In contrast, if the mass and/or heat transfer resistances make up nearly the total resistance, the reaction is diffusion controlled. In the case of chemical control, activation energies of 200-400 kJ/mol are common; diffusion control leads to activation energies of 20-50 kJ/mol.

Bearing in mind the complexity of the various decomposition reactions previously discussed, it is not surprising that the kinetics of coal pyrolysis are extremely difficult to treat mathematically. The simplest approach is to assume an overall first order process with respect to the amount of volatiles remaining in the coal [101,102]. This amounts to an empirical fitting of experimental results in which it is impossible to attribute physical meaning to the kinetic parameters obtained; however, it is useful as a comparative technique [103].

Other investigators have proposed models which focus on the rate of evolution of the individual gaseous products [104-107]. Solomon and Colket [106] found that the evolution of gases is directly related to the quantity of various functional groups in the coal. They obtained first order rate constants for these processes which were independent of coal rank. This is an indication that, although the quantity of evolved pyrolysis products is a strong function of coal rank, the rate of their evolution is relatively constant. The validity of this conclusion is still a matter of controversy [104], but this type of approach is useful in that it offers the possibility of predicting the product distribution as a function of pyrolysis conditions.

Although the data available on the effect of heating rate on volatile yield do not allow any firm conclusions to be drawn, the following argument is given to support an increased yield of volatiles at high heating rates [80,97-99,108]. Rapid heating (> $10^4$ K/sec) is achieved in experimental systems in which the coal particles are well dispersed in a stream of carrier gas (*e.g.*, entrained flow systems). In such systems, due to the short residence time and/or low concentration of primary volatile products in contact with the coal/char surface, the possibility of secondary char forming reactions, such as cracking, occurring is greatly reduced. Thus the overall yield of volatiles is increased compared with that obtained in slow pyrolysis (found in fixed-bed systems) where secondary reactions are more probable.

Many kinetic models of coal pyrolysis have been proposed [109-113], but a discussion of these models is not deemed to be relevant in this particular work.

In addition to these purely chemical kinetic considerations, it is also necessary to take into account the possible kinetic limitations imposed by heat and/or mass transfer, especially if intrinsic kinetic parameters are required [114,115]. The differences in observed kinetic parameters, in many cases, are probably partly due to the different heat and/or mass transfer conditions (and limitations) in the different experimental systems used. Similar problems arise when considering char gasification and these will be discussed in detail in Section 4.6.1. From the standpoint of kinetics of pyrolysis, however, it is important to emphasise that diffusion generally does not affect the rate of evolution of volatiles - it does, however, affect their total yield and distribution, depending upon conditions such as gas pressure, particle diameter and degree of dispersion in the gas phase [116,117].

## 3.7 Pyrolysis and Carbonisation of Polymers [118,119]

When polymers are heated in an inert atmosphere, reactions take place initially within the C-C chain. These intramolecular reactions result in one of the following three possibilities:-

(i) The chains degrade into small molecules and gaseous products are evolved leaving little or no carbon residue. Polyethylene is an example of a polymer which exhibits this type of behaviour.

(ii) The chains collapse to form aromatic lamellae. The structure is then in a plastic phase and aromatic lamellae stack above each other to form spherulitic liquid crystals - the so-called 'mesophase'. A crystalline anisotropic coke is produced which will soften to a graphitic material on heating to 2700° C. Polyvinyl chloride exhibits this type of behaviour.

(iii) The chains remain intact and coalesce with neighbours; the material does not pass through a plastic state. A 'hard', non-graphitisable char of this sort is formed by polyvinylidene chloride.

The mechanisms of pyrolysis and carbonisation of polymers are not well understood, because it is very difficult to determine the crystallographic and chemical structure of intermediates existing during the process. In general, when polymers of type (iii) are pyrolysed, the following stages of structural change are seen:

(a) The precarbonisation stage in which the polymer turns black at an early stage, which usually corresponds to the beginniing of the regime of rapid weight loss.

(b) The carbonisation regime during which rapid weight loss occurs, at temperatures between 200° C and 500° C. Oxygen, nitrogen, chlorine, *etc.*, are removed during this stage.

(c) Dehydrogenation occurs at the end of the carbonisation stage. The material still contains, typically, one hydrogen for every two carbon atoms; thus a third stage exists, between 500° C and 1200° C, in which hydrogen is gradually eliminated. The H/C ratio is characteristic of a given heat treatment temperature.

(d) Heat treatment above 1200° C removes defects and the component crystallites achieve greater perfection. This is known as the annealing stage.

The chemical nature of the precursor is the most important factor in determining the nature of carbonisation. The thermal reactivity of an organic molecule depends on factors such as its size, ease of free radical formation and the presence of substituents in aromatic rings. The initial chemical reactions [118] that are the most important are:- (i) bond cleavage at the most reactive molecular site to produce a free radical intermediate; (ii) formation of more stable intermediates by radical rearrangement; (iii) polymerisation of radical units; (iv) eliminarion of hydrogen from polymerised structures. In many cases these reactions do not proceed independently in distinct steps, but occur simultaneously. The structure and properties of the resulting carbons are influenced considerably by the carbonisation conditions.

Many long chain polymers break down completely into gaseous products during heat treatment [119], *e.g.*, polyethylene. However, when polyvinylidene chloride (PVDC), which is of interest in this work, is heated, it starts decomposing at fairly low temperatures (150-200° C) with evolution of hydrogen chloride (HCl) and nearly all the original carbon is left behind. Polyacrylonitrile (PAN), also of importance in this investigation, leaves a char consisting of most of the original carbon with elimination of only hydrogen and nitrogen. The structures of these two polymeric systems, which leave chars on carbonisation, are shown in Figure 3.7. Since this investigation is concerned with the synthesis of a model char from a vinylidene chloride/20% acrylonitrile copolymer, a more detailed discussion of the thermal degradation of these two polymers is appropriate and will be given in Chapter Eleven.

# CHAPTER FOUR

# GASIFICATION OF COAL

## 4.1 Introduction

Coal gasification generally refers to the reaction of coal with air, oxygen, steam, carbon dioxide or a mixture of these gases to yield a gaseous product for use as a fuel or as a feed in the synthesis of chemicals, liquid fuel and other gases. Gasification of coal in a hydrogen atmosphere is known as hydrogasification [113].

When the raw coal has passed through the drying and pyrolysis stage in the gasifier (see Section 4.2.1), the so-called coal char and the volatile matter can react with oxygen, steam and hydrogen to form CO, $H_2$ and $CH_4$. Thus gasification differs from carbonisation in that the volatiles and char are further converted to gaseous products. Gasification, in essence, is incomplete combustion; CO and $H_2$ are produced during gasification as opposed to $CO_2$ and $H_2O$ in complete combustion. However, the basic chemical reactions involved in the two processes are similar.

This chapter briefly discusses the fundamental phenomena involved in coal gasification, the kinetics of the reactions involved and the principles of the main gasification processes. A complete review of all aspects of the subject would be impossible in this thesis, so only the points relevant to this work are discussed. Attention is drawn, however, to comprehensive reviews of the subject [2,86].

## 4.2 Classification of Gasification Processes

Classification is usually based on the method of contacting reactants and the condition of the residue removed. Using the method of contacting reactants, the processes can be divided into three groups [120]:- (i) fixed-bed gasification; (ii) fluidised-bed gasification; (iii) entrained-bed gasification. If the processes are distinguished by the condition of the residue removed, they are usually said to operate either in the slagging or non-slagging mode. These processes will now be discussed in more detail, paying particular attention to the fixed-bed process currently being used by the British Gas Corporation [121, 122].

### 4.2.1 Fixed-bed gasifier [123-126]

Fixed-bed, in gasification terms, usually refers to a moving bed with fixed extremities. Fixed beds possess numerous inherent characteristics that are advantageous to gasification: (i) flow of fuel and ash counter-current to the gasification medium and product gas leads to maximum heat economy; (ii) relatively long residence time of the fuel in the reaction vessel permits high carbon conversion; (iii) the product gas is free of solids and the plug-flow of solids minimises loss of fuel in the ash.

The fuel bed in fixed-bed gasification is characterised by zones of different temperature [1], as shown in Figure 4.1. Zone 1 is the preheat zone where incoming fuel, charged to the top of the fuel bed, is dried and heated by the hot gas flowing upward. Drying and pyrolysis of the coal in zone 1 produces, what should ideally be, a reactive coal char which is subsequently gasified. The volatile matter content of the coal is partially devolatilised in the preheat zone and appears as

methane, higher hydrocarbons and tar. Zone 2 is the reduction (or gasification) zone where steam is decomposed and $CO_2$ reacts with carbon to form CO and $H_2$. The complex reactions in this zone are dominated by the endothermic C-$H_2O$ and C-$CO_2$ gasification reactions. Zone 3 is the oxidation zone which occurs at the bottom of the bed and is the hottest region due to the strongly exothermic C-$O_2$ combustion reaction. Zone 4 at the bottom of the gasifier (known as the ash zone) is where the mineral matter content of the coal is collected as ash. The temperature profile through the bed is therefore determined by a balance between exothermic combustion and endothermic gasification of the coal char.

The most important characteristics of the coal affecting its use in fixed-bed gasification systems are: particle size and particle size distribution, agglomerating tendency, reactivity and ash fusion temperature [120]. A particle size of 12-50 mm is usually preferred and the sizes should be uniformly distributed within the range and free of fines. Coking coals cannot be used without pretreatment to render them non-agglomerating. Problems with agglomeration and fines can be removed to a certain extent using a stirrer in the gasifier.

While the reactivity of the coal determines the minimum practical temperature in the gasification zone, the ash fusion temperature dictates selection between slagging and non-slagging operation. In non-slagging operation, ash is removed as a dry ash and therefore an ash fusion temperature of greater than 1200° C is desirable. The maximum temperatures of the reaction zone in non-slagging operation (1200-1300 °C) are considerably lower than those in slagging operation (1500-1800 °C).

Operation of a gasifier under slagging conditions eliminates the limitation imposed by the fusibility of the ash; however, operating conditions must be such that the slag has the necessary fluidity for free flow [127]. With slagging gasifiers, the oxygen concentration for obtaining maximum gasification efficiency is considerably higher than that for a non-slagging gasifier, 40-48% compared with 22-30%. As a result, steam decomposition increases and steam requirement decreases [128, 129].

The most widely used commercial fixed-bed gasification system is the Lurgi gasifier [126], which was first introduced in 1936. Many commercial units have since been installed around the world and the current standard 12 ft diameter units can gasify up to 600 tons of coal per day. The Lurgi gasifier consists of a vertical water-cooled pressure shell into which coal is intermittently charged from above through a lock hopper (Figure 4.2). Steam and oxygen are injected through a rotary bottom grate, through which crushed clinker is also continuously withdrawn into a lock hopper under the reactor. In slagging operation, the system incorporates a slag quench chamber and a slag lock hopper at the bottom of the gasifier. The steam and oxygen is injected into the gasifier using tuyeres and a region of low density solids entrained in high velocity turbulent gases called the raceway is produced in front of the tuyeres where the temperature is in the region of 2000 °C.

In the dry ash Lurgi gasifier, gasification of the fuel bed is normally carried out at pressures of 350-450 psi (3-5 MPa) at temperatures between 925-1035 °C. Since these conditions favour carbon hydrogenation, the cleaned $CO_2$ free gas produced generally contains

50% $H_2$, 35% CO and 15% $CH_4$.

Since the output of a gasifier is ultimately limited [129] by the rate at which gases can be passed through the bed without excessive dust carry over; the lack of undecomposed steam and higher temperatures in the slagging gasifier means that a greater output can be achieved compared with a dry ash gasifier of the same size. The lack of excess steam and the higher temperature means that the CO shift reaction (see Section 4.4) is not significant and higher yields of CO and less of $CO_2$, are obtained from the slagging gasifier compared with the dry ash Lurgi gasifier [129, 130].

There are many uses for the product gas (mainly CO and $H_2$) from a fixed-bed gasifier and these are outlined below [129]:

(a) After removal of hydrogen sulphide and tar, it is an excellent fuel for industrial use,

(b) It can be converted to substitute natural gas (SNG) by catalytic methanation and distributed to domestic users [131].

(c) Electricity generation [123] by coal gasification, together with combined cycle of a gas turbine followed by a steam turbine has benefits in efficiency as well as environmentally, due to the lower pollution levels compared with conventional combustion methods,

(d) It is an excellent feedstock for the production of chemicals (*e.g.*, ammonia synthesis and Fischer-Tropsch synthesis).

4.2.2 Fluidised-bed gasifier [6, 132]

Fluidisation techniques were first applied to gasification on a commercial basis in the Winkler Process in the 1920's. There are several advantages attached to using a fluidised-bed system. They allow very rapid internal heat transfer and a uniform temperature distribution can be achieved throughout the bed. Systems of this type are also capable of handling fines, which is almost impossible in fixed-bed systems, and a high specific gasification rate can be achieved. However, some disadvantages do exist and must be taken into account when selecting gasification systems for particular applications. The sensible heat of the exit gases, which are in thermal equilibrium with the uniformly mixed solid at the gasification temperature, has to be recovered separately. Also, as a result of high length/diameter ratio of the coal bed, narrow particle size distribution and agglomeration of the feed coal, slagging (coarse particles) and channelling (fine particles) can occur. In some cases some ungasified coal may be lost as entrained dust, which can obviously have a deleterious effect on process efficiency.

4.2.3 Entrained flow gasifier [133]

The most important inherent characteristic of fully-entrained suspension or dilute phase fluid-bed gasification processes is the ability to utilise any grade of coal. Size consistency and swelling or coking characteristics of coal have no significant effect on the operability of the process. Fully entrained systems produce a gas containing no tar and very little methane because the volatile matter of the coal is almost completely oxidised in the early stages of gasification. However, these processes have low inventory of fuel in the reaction zone

because of the low concentration of fuel in suspension. Furthermore, since the temperature and the concentration of reactants decreases from inlet to outlet (as a result of concurrent flow), the rates of gasification are lowest at the outlet. Therefore it is not economically feasible to gasify more than 85-90% of the carbon in a single pass. The concurrent flow of fully entrained processes also necessitates heat exchange to improve thermal efficiency; and the heat recovery is complicated by the presence of solids, particularly molten ash particles. The most important commercial entrained-flow gasification system is the Koppers-Tozek process, commercialised in 1938.

## 4.3 Coal Characteristics affecting Gasification

There are several important coal characteristics which affect the efficiency and eventual selection of gasification processes. Coking or agglomeration tends to cause slagging of fluid-bed and excessive clinkering in fixed-bed gasification [129]. Therefore coking coals which have not been pretreated to remove coking properties are not suitable for use in these gasifiers [134]. However, with the provision of a stirrer the Lurgi gasifier can handle weakly coking coals. In contrast, coking properties have no effect on fully entrained gasification.

An important coal characteristic which determines the mode of gasification is the ash fusion temperature. In non-slagging operation the ash is removed as dry ash and high ash fusion temperatures of greater than 1200 °C are desirable. Slagging gasifiers remove the ash as molten slag and operating temperatures are therefore higher than those used in non-slagging gasifiers.

Lignites and sub-bituminous coals contain significant amounts of carboxylic acid groups, in which a fraction of the $H^+$ ions have been exchanged by different cations such as $Na^+$, $K^+$, $Ca^{2+}$, $Fe^{2+}$ and $Fe^{3+}$, as a result of extended contact with salts containing ground water. The high reactivity of low rank coals is thought to be, at least in part, due to the presence of exchangeable metal cations on the surface of the coal. The catalytic effects of these metal cations on the char reacrivity vary with gasification atmosphere [135]. In an oxidising atmosphere (air or $CO_2$) sodium, potassium and calcium improve the char reactivity, while iron and magnesium impair it (Figure 4.3). In a reducing atmosphere such as hydrogen, sodium is the most effective catalyst below 45% carbon burn-off, whereas iron is more effective at high burn-offs. Potassium and calcium have adverse effects on char reactivity to hydrogen, but the reverse is true in a steam atmosphere. Iron is the most efficient catalyst in a hydrogen/steam atmosphere.

Various studies [136-139] on gasification of coal chars have shown that the reactivity of the char increases as the rank of its precursor coal decreases. For example, the char produced from a Montana lignite is gasified at a rate 200 times that of a char produced from a low volatile bituminous coal [139]. The increased reactivity of chars obtained from low rank coals can be attributed to a high active site concentration, high porosity and a significant calcium content.

As the coal rank increases, the size of the aromatic lamellae increases and the crystallite size of the char increases as a result. Since the active sites exist at the edges of the crystallites, it follows that there will be fewer active sites in chars derived from

high rank coals than those derived from low rank coals. This leads to high reactivity in low rank coals. In addition, as the coal rank increases, the volatile content of the coal decreases. The resulting char is less proous and its accessibility to the reacting gas is reduced accordingly. High rank coals also contain less calcium than low rank coals, thereby reducing any catalytic effects imposed by the element.

## 4.4 Chemical Reactions in Coal Gasification

The principal gases produced during coal gasification by oxygen, steam and/or hydrogen are CO, $H_2$, $CO_2$, small amounts of $CH_4$, undecomposed steam and traces of sulphur bearing gases. These products are formed by a combination of the following reactions [120]:

(1) Sequential oxidation of carbon

$$2C + O_2 = 2CO$$

$$2CO + O_2 = 2CO_2$$

(2) Oxidation of the hydrogen in the volatile matter

$$H_2 + \tfrac{1}{2}O_2 = H_2O$$

(3) Gasification of carbon with steam and $CO_2$

$$C + H_2O = CO + H_2$$

$$C + CO_2 = 2CO$$

(4) Water-gas shift reaction

$$CO + H_2O = CO_2 + H_2$$

(5) Decomposition of volatile matter

$$C_nH_m = \frac{m}{4} CH_4 + \frac{4n-m}{4} C$$

(6) Methanation

$$CO + 3H_2 = CH_4 + H_2O$$

(7) Hydrogenation of volatile matter and 'active' carbon to methane and higher hydrocarbons

$$C_nH_m + \frac{2n-m}{2}H_2 = nCH_4$$

$$C + 2H_2 = CH_4$$

The oxygen consuming reactions, (1) and (2), proceed rapidly to completion under normal gasification conditions [86, 128]. However, the carbon gasification reactions (3) never reach equilibrium because the equilibrium requires practically 100% steam decomposition and negligible $CO_2$ content at temperatures above 1090 °C and pressures of up to 20 atm. The C-$CO_2$ reaction is generally slower than the C-$H_2O$ reaction.

The water-gas shift reaction (4) is primarily a heterogeneous reaction taking place on the solid surface rather than in the gas phase [2]. At a sufficiently high level of steam decomposition, and with a moderate amount of $CO_2$ present, the reaction tends to operate in the reverse direction. At temperatures above 1090 °C thermodynamic equilibrium can be assumed.

Methane forming reactions, (5), (6) and (7), are of particular importance in gasification at temperatures below 1090 °C, at and above atmospheric pressure. The presence of hydrogen and/or steam and rapid heating are favourable for methane formation and methane yield increases with hydrogen partial pressure [140]. Rapid heating of coal ($2\text{-}5 \times 10^4$ K/sec) in the presence of hydrogen produces, in addition to gaseous pyrolysis products, an active, but transient, species, which reacts rapidly with hydrogen to form additional methane. Accordingly, complete

conversion of the carbon in coal to methane is possible under favourable conditions (500 atm and 950 °C) [140]. Methane yield is substantially higher in continuous feed fluid-bed processes than in fixed-bed gasification systems [141]. This may be due to continuous mixing in the fluid-bed which brings the steam activated particles from regions of high steam partial pressure in the lower portion of the bed to regions of high hydrogen partial pressure in the upper portion.

## 4.5 Mechanism of the Carbon-Steam Reaction [142-147]

Kinetic models of the various gas-carbon reactions are developed primarily based on the mechanistic assumption that active carbon free sites ($C_f$) exist and are distributed throughout the carbon structure as a result of lattice imperfections or discontinuities. These sites provide unpaired electrons required for effecting chemisorption of reactant gas constituents to form surface complexes. The presence of unpaired electrons in various carbon types has been confirmed through paramagnetic resonance adsorption [148, 149]. The bonds between the carbon atoms and the reacting gas in the surface complexes must be stronger than the carbon-carbon bonds in the lattice, so that a reaction product can be released. The rate and order of reaction depends on the rate of formation of these surface complexes; it also depends on the number and extent of coverage of the active carbon free sites. Thus the reactivity of carbons may, by definition, be assumed to vary with the number density of active carbon free sites,

The complexity of the carbon-steam reaction arises because of the presence of hydrogen. The primary products are generally believed to be CO and $H_2$. $CO_2$ is a secondary product arising from the water-gas

shift reaction. The elementary reactions involved are as follows:

(1) Reversible oxygen exchange between active sites and steam

$$C_f + H_2O \rightleftharpoons C(O) + H_2$$

(2) Decomposition of surface oxides

$$C(O) \rightleftharpoons CO + nC_f$$

(3) Reversible oxygen exchange between surface oxides and CO

$$C(O) + CO \rightleftharpoons CO_2 + C_f$$

(4) Annealing

$$C_f \longrightarrow C_{inactive}$$

Combination of steps (1) and (3) results in the water-gas shift reaction. Experimental data [141] on steam gasification of carbons are in general agreement with a Langmuir type equation over a range of 100-200 °C at temperature levels of 700-1100 °C.

## 4.6 Kinetics of Char Gasficiation [2, 86, 150, 151]

On the basis of extensive experimental studies Walker [152] has shown that high reactivities of coal chars, and indeed carbons in general, are due to : (i) high concentration of carbon active sites, *i.e.*, carbon atoms located at the edge of the crystallites within the char; (ii) high accessibility of reactant gases to the active sites; (iii) high catalytic activity and/or dispersion of the inorganic impurities present in the char.

Quantitative understanding of factors (i) and (iii) does not exist. However, factor (ii) has been studied extensively and the effects of mass transport are well documented. These three factors will now be discussed.

4.6.1 Diffusion/mass transport effects

The overall char gasification process consists essentially of diffusional and chemical steps which govern the intrinsic chemical rate. There are three major steps involved in a reaction of this type [86, 153]:

(1) Transport of gas molecules to the external geometric surface of the solid from the bulk gas.

(2) Transport of gas molecules from the external surface to reactive sites on the internal surface of the pores.

(3) Reaction at these sites.

Gas transport is normally by molecular diffusion; in step (1) across an external boundary layer, and in step (2), through the pores. If the gasification temperature is increased, the rate controlling step changes from (3) to (2) and finally (1).

It has been shown [154, 155] that the temperature dependence of the rate can be idealised in the form of an Arrhenius type plot (Figure 4.4). At the lowest temperature, zone I, the overall rate is controlled by the surface reaction, step (3). In this case, gas diffusivities are greater than reaction rates and the concentrations of reactants and products are substantially uniform in the pore structure, and are equal to the values in the bulk gas. The effect is shown schematically in Figure 4.5.

As the temperature is increased, the rate of reaction increases faster than the gas diffusivities, so that the former approaches the latter. This causes a depletion of reactant molecules along the length of the pores and a corresponding increase in the concentration of the product. Eventually a situation will arise where the concentration of reactant falls to zero at some point inside the specimen

(Figure 4.5). Under these conditions, zone II, all gas molecules entering the pores will react. There will also be a concentration gradient within the pores, but if there is a rapid flow of gas along the surface, this will be of secondary importance and the rate controlling step will be in-pore diffusion. Under these conditions the observed activation energy for zone II is approximately half that for zone I [86].

With further increasing temperature, the depth to which molecules can penetrate before reacting becomes smaller and the reaction becomes confined to a thinner layer adjacent to the external surface (Figure 4.5). At the same time, the concentration gradient external to the surface becomes more important until eventually this controls the rate (zone III). The rate controlling step is then transport of gas molecules from the bulk of the gas to the surface of the specimen. The activation energy for this process is very small.

Thus the diffusional step in this process depends on concentration gradient and molecular velocity of gases near the external surface and in the pores; the chemical step depends on the external and pore surface interactions with the gases. These surface interactions, in turn, vary with the number of discontinuities and impurity atoms in the crystalline lattice, namely the active sites. The relative importance of diffusional resistance with respect to chemical resistance increases with the reactivity of the carbon surface, particle size and pore size [16]. Therefore, coal characteristics which may affect the reactivity of the coal-derived char are:

(1) Chemical composition, particularly the amount of hydrogen and sulphur which affect the imperfections in the lattice;

(2) coal ash content which may provide catalytic effects; and

(3) rank of the parent coal which determines the pore structure, the extent of graphitisation, the size of crystallites and the degree of annealing which determines the extent to which active sites are deactivated.

A satisfactory level of understanding of the mass transport effect in porous solid catalysts has been achieved *via* the work of several pioneers in the field [156-158]. However, with porous carbons such as coal chars, a more complicated situation arises due to the dynamic structure of the porous solid. During gasification the char is being consumed, pores are created and existing pores are enlarged until they finally coalesce. It is therefore apparent that the total and active surface area of the char and the effective diffusivity of the reactant gas in the pores of the char are not constant parameters during gasification. Consequently, realistic modelling of the pore structure needs to take into account the development of porosity and surface area and the change in effective diffusivity during the reaction. In recent years many such models have been proposed [159-171].

In recognition of the dynamic nature of the porous structure of coal chars, Simons and co-workers [162-165] have developed a semi-empirical 'tree (or river) system' model of pore branching and combination. When applied to char reactivity this model predicts a change in reactivity of up to one order of magnitude with progressive conversion.

Gavalas [166, 167] has proposed a random capillary model and he concludes that char reactivity (calculated also taking into account the changing pore structure) is over 100 times smaller than the reactivity

calculated by the traditional reaction-diffusion theory. However, this difference in reactivity results from the choice of an unrealistically low value of initial porosity (∿2%). A more realistic value for coal chars is about 10% and using this value the effect predicted by this model is much smaller. The models proposed by both Simons and Gavalas seem insufficient to explain the reactivity differences observed by other workers [172].

These findings indicate that quantification of the effects of carbon active sites and catalysis is essential if one is to understand the reactivity behaviour of coal chars. Sophisticated reaction-diffusion models, taking into account the changing surface area and effective diffusivity during reaction, do not seem to provide a basis for explaining the differences in observed char reactivities.

4.6.2 The role of carbon active sites in gasification

The number of active sites and thus the intrinsic reactivity of a char sample is primarily determined by: (i) the concentration of edge carbon atoms and defects; (ii) the oxygen and hydrogen content; (iii) the mineral matter and trace element concentration. These three chemical parameters, plus char porosity, account for variations in overall reactivity. Generally low rank coals possess higher porosity, concentration of edge carbon atoms, mineral matter and oxygen content than high rank coals. Thus it is not surprising that char reactivity increases substantially with decreasing rank of the parent coal [95, 96, 173].

Oxygen and hydrogen content vary widely for different chars. Increased content of these two elements should promote carbon reactivity, since chemisorption on non-aromatic sites is usually favoured compared

with aromatic sites [8]. Many correlations have therefore been formulated between char reactivity and oxygen and hydrogen content [85, 87, 95, 174, 175]. Oxygen sites are thought to influence reactivity by electron exchange [8, 85], while hydrogen sites increase reactivity by preferential oxidation [8], with subsequent production of highly active nascent carbon sites [95].

The concept of active sites at the edges of carbon crystallites is now generally accepted. Early microscopic work [176] on graphite showed attack at the edges of the basal planes or at discontinuities in the basal plane when the graphite was reacted with oxygen. Later Hennig [177] made oxygen chemisorption measurements on graphite single crystals to study the formation of surface oxides. Hennig found that the amount of oxygen complex decomposed upon heating to 1173 K was essentially the same, even after the crystal had been cleaved five times. This suggests that although the basal plane area increased by a factor of six, the concentration of edge carbon sites and the amount of oxygen complex adsorbed, remained constant.

Graham [178] studied the adsorption of nitrogen upon Graphon, a highly graphitised carbon black, at 77 K. At very low equilibrium pressures he found that there was a strong adsorption of nitrogen. Extrapolation of the linear portion of the adsorption isotherm to zero pressure enabled Graham to determine the amount of nitrogen adsorbed by the strong active sites. The active surface area (ASA) was found to be about 1.25% of the total BET surface area of the graphite.

Healey *et al.* [179] determined the areas covered by surface complexes on Graphon samples, which had been activated to several levels of burn-off at 803 K in oxygen, by measuring the BET surface areas from water adsorption isotherms. They reasoned that oxygen complexes

formed on the surface (which was initially hydrophobic) would be hydrophilic in nature. Therefore the measure of BET water surface area was taken to be equivalent to the area covered by oxygen complexes. Healey *et al.* observed that the amount of water adsorbed increased with progressive oxidation of the Graphon and they concluded that water adsorption was occurring around grouped sites, possibly at the edges of graphitic planes. Later work by Walker and Janov [180] reported that the extent of water adsorption is quantitatively proportional to the fraction of the Graphon surface covered by chemisorbed oxygen.

For heterogeneous microcrystalline materials, such as coal chars, it is possible that the majority of surface sites might be active sites. Watt and Frnklin [181] investigated a variety of "disordered" carbons in their reaction with "ozonised" oxygen. They used *X*-ray diffraction to study the structure of the carbons before and after oxidation. The authors found that it was the fraction of carbon in the form of single, unstacked, graphite-like layers which was most susceptible to oxidation, rather than the carbon involved in either multilayer stacking of layers or "amorphous" carbon.

The most important quantitative work on the role of active sites during carbon gasification was conducted by Laine *et al.* [182]. They studied the reaction of Graphon with low pressure oxygen (5.2 Pa) at 848, 898 and 948 K. The Graphon samples used were pre-oxidised to seven levels of burn-off up to 35% weight loss. The total active surface area (TASA) of the samples was determined by exposing clean Graphon surfaces to an oxygen pressure of 65 Pa at 573 K for 24 hours and subsequently measuring the CO and $CO_2$ desorbed after three hours at 1223 K. After removal of the complex, the Graphon samples were reacted with additional oxygen. The depletion of oxygen and the

build-up of CO and $CO_2$ were followed with a mass spectrometer. The amount of stable oxygen complex formed on the active carbon surface during the reaction could be followed by an oxygen material balance during the run. From the difference between the TASA and the active surface areas occupied during the reaction (OASA), unoccupied active surface areas (UASA) were obtained.

Hart and co-workers [183] studied the kinetics of the low temperature (298-673 K) chemisorption of oxygen on clean Graphon surfaces. They found the adsorption to be dissociative and non-reversible. Using $O_{18}$ as a tracer Hart *et al.* [183] found that the stable surface oxide does not act as an intermediate in the formation of gaseous products. They concluded, in agreement with Laine *et al.*, [182] that the stable surface oxide inhibits the reaction by covering the active sites on the surface, thus preventing any further reaction.

Further discussion of active surface area, in relation to gasification of coal chars, is included in Chapter Thirteen.

4.6.3 Catalytic effects during gasification

In the case of coal chars catalysis by inorganic impurities inherently present in the coal can play a major role in determining their reactivity behaviour. Several workers [95, 184-186] have found that the observed catalytic rate during gasification falls between or above the correlations of the models [165, 172] discussed in Section 4.6.1. This illustrates the fact that at least part of the differences in observed reactivities of carbons and chars can be attributed to the different levels of catalytic activity of the impurities present.

Most metals, metal oxides and salts exhibit some catalytic activity [45, 187, 188]. Iron, calcium and magnesium compounds are of prime interest and many investigators have found that a good correlation exists between char reactivity and metal oxide content [95, 96]. It has also been found that secondary reactions, such as the water-gas shift reaction, are also affected by surface impurities. An increase in reactivity of two orders of magnitude is not uncommon, even with as little as 100 ppm Fe in the char [182, 187].

The effect of mineral matter on carbon gasification is usually explained *via* one of two unconfirmed theories [45]. The geometric or transfer theory suggests that an oxidative intermediate, formed by reactant dissociation at a nearby catalytic site, migrates to react with carbon. The electronic theory suggests that chemisorption and desorption is favoured at covalent or ionic carbon-metal bonds generated by electron transfer.

The catalytic activity of a particular species depends on the chemical form of the species, the amount present and the inclusion size [173, 188]. Reactivity often increases with decreasing particle size due to the larger mineral matter content of smaller particles [189, 190]. However, it is usually the distribution of the catalyst, and not the total amount present, which is the most important factor. De-ashing of low rank (porous) chars normally results in a decrease in reactivity compared to the original sample [95, 96]. However, the removal of mineral matter from chars derived from high coals increases the overall reactivity due to development of porosity and increased accessibility to internal surface area.

Apart from the catalytic effects of materials inherently present in coals much work has been carried out to assess the affect of deliberate

catalyst additions in the gasification process [191-204]. A number of materials have been shown to exhibit catalytic activity, the most active being transition metals, alkali metals and alkaline earth metals. Catalytic coal gasification can have the effect of increasing the specific coal throughput in a gasifier without increasing oxygen and coal consumption, provided the temperature allows chemical or pore diffusion control. If this is the case, the specific investment costs for the gas generator can be decreased. The use of catalysts also permits a one step process for the conversion of coal to methane [205]. The application of catalysts can, however, involve problems [203] such as additional costs for catalysts, the necessity for the recovery of catalysts (especially if expensive materials are used), possible side effects such as corrosion of materials in the gasifier, and possible environmental impacts concerning ash disposal. It is therefore apparent that many factors must be considered when assessing catalysts for use in coal gasification and a fine balance must exist between economic and practical aspects.

## 4.7 Aims and Structure of the Research Programme

The preceding review chapters emphasise that there are many physical and chemical factors which may govern the reactivity of coal chars during gasification, with the obvious conclusion that generalisation of the heterogneous reactions involved is impossible. A review of this sort, in conjunction with the requirements of the British Gas Corporation, has led to an appropriate research programme being formulated. The work can be divided into four principal areas:

(1) Synthesis and characterisation of a model char derived from a suitable polymeric precursor. This was to be used as a 'pure' catalytically inactive material for comparison

with a coal char of interest to BGC.

(2) Investigation of the kinetics of steam gasification at atmospheric pressure of the model char and the coal char.

(3) Parallel studies to assess the effect of steam gasification on textural parameters such as surface area and pore volume.

(4) Development of a technique for measuring the active surface area of the chars as a function of progressive gasification.

Chapters Five to Nine describe, in detail, the important features of the experimental systems and procedures used during this work. Chapters Ten to Fourteen present a thorough analysis of the results obtained for both chars. Chapter Fifteen is a general discussion which attempts to establish a correlation between surface area and reactivity data to ascertain which factors influence the reactivity behaviour of the chars. The conclusions which can be derived from the present study are given in Chapter Sixteen.

# CHAPTER FIVE

# EXPERIMENTAL

## 5.1 Materials

Initial experiments were concerned with synthesising a reproducible, catalytically inactive, model char. This was achieved by carbonising a high molecular weight vinylidene chloride/20% acrylonitrile copolymer (British Drug Houses Ltd.) in nitrogen at 1050 °C (termed PVDC char). Small scale pilot studies were carried out to ascertain the optimum treatment conditions to produce a good model char. The heat treatment circuit is shown in Figure 5.1. The apparatus consists of a horizontal furnace with copper cooling tubes at each end. The sample is sealed inside the furnace using a pair of aluminium flanges. Product gases (mainly hydrogen chloride) are bubbled through several neutralising solutions. NUtrogen flow rates were measured and controlled using a Fisher Products flow meter/regulator and the temperature of the furnace was controlled by a Eurotherm linear temperature programmer. Use of several thermocouples led to determination of the temperature profile in the furnace and the sample was placed in the constant, maximum temperature zone of the furnace which was approximately 15 cm in length.

A 2 g sample of the powdered PVDC based precursor was pelleted and subjected to a linear temperature programme at various heating rates. The effect of varying rhe nitrogen flowrate and the treatment time was also investigated. The results of this work are shown in Table 5.1. This indicates that nitrogen flowrate has no apparent effect on the carbon yield and that treatment times of more than a few minutes

also give rise to a constant carbon yield. The effect of heating rate on carbonisation characteristics was further investigated using dilatometry and thermogravimetry and the results are presented and discussed in Chapter Eleven. Larger scale carbonisation experiments were subsequently carried out to obtain considerable amounts of the model char for gasification purposes.

The coal char used in this work was obtained from Markham Main coal, which is a highly volatile, weakly caking coal (NCB Rank No.702). Carbonisation conditions were the same as those for the model char.

## 5.2 X-Ray Analyses of the Chars

The two chars were studied using a scanning electron microscope (JEOL JSM 35C) fitted with energy dispersive X-ray analysis (EDAX). This enabled semi-quantitative studies to be carried out to analyse the chemical elements present in the chars. Particles of the two chars were mounted in resin, polished and analysed using the "Semi-Quant" programme available on the EDAX instrument. The programme reports results for each chemical element as wt% of the detected elements; the elements surveyed were Na, Mg, Al, Si, K, Ca, Ti and Fe. Appropriate corrections were made to correct for atomic number, absorption and fluorescence effects [206]. To minimise any possible effects of micro-segregation of the mineral matter within the samples, mean results for each sample were obtained on five polished particles.

X-Ray powder diffraction analysis of the ash derived from the coal char was carried out using a Philips PW 1050 diffraction goniometer, using NI-filtered Cu-K$\alpha$ radiation. The results of the X-ray analyses are given in Chapter Ten.

# CHAPTER SIX

# ANALYSIS OF THE THERMAL DEGRADATION BEHAVIOUR OF PVDC

## 6.1 Thermogravimetric Analysis of PVDC Degradation

The pyrolysis behaviour of the PVDC based precursor was investgated using a Stanton Redcroft TG 750 thermobalance. Details of the apparatus and procedure are given in Chapter Nine on steam gasification measurements. The only differences between the two procedures were that an atmosphere of dry nitrogen (instead of steam) was maintained in the reaction zone during pyrolysis of the PVDC and a complete range of heating rates were used. The results of this enalysis are shown in Chapter Eleven.

## 6.2 Dilatometric Analysis of PVDC Degradation

### 6.2.1 Apparatus

Dilatometry experiments were performed on the PVDC based precursor to determine the variation in swelling with heating rate. This was accomplished using a Dupont 990 Thermal Analyser in conjunction with a Dupont 943 Thermomechanical Analyser. The system is shown in block digram form in Figure 6.1.

The analyser uses a movable core linear variable differential transducer (LVDT) which provides a DC output proportional to the linear displacement of its core. This voltage is supplied to the Y-axis of the recorder. The sensitivity of the instrument can be altered to detect a wide range of percentage dilatations. A thermocouple in close

proximity to the sample provides a direct measure of the temperature of the sample. The thermocouple output, compensated with a suitable reference junction, is applied to the X-axis of the recorder. The sample and probe are surrounded by a temperature-controlled cylindrical heater, which is also encapsulated in a Dewar vessel to aid good temperature control. A weight is situated on top of the probe to minimise vibration and noise.

6.2.2 Method

The PVDC sample, contained in a standard sample holder, was subjected to a linear temperature programme in a stream of dry nitrogen, at a flowrate of 25 $cm^3$/min. These conditions were selected to simulate the PVDC carbonisation conditions (Chapter Five). The transducer was zeroed on the surface of the sample and vertical dilatation was measured as a function of temperature and time. The net result was a trace of probe displacement against temperature or time. This procedure was carried out using a range of linear heating rates (0.5, 1, 2, 5 and 10 °C/min); the results are given in Chapter Eleven.

# CHAPTER SEVEN

# CHARACTERISATION OF PORE TEXTURE

## 7.1 Helium Pycnometry

Helium density measurements were carried out using a Micromeritics Autopycnometer 1320. Char samples were prepared for analysis by drying at 100 °C for 15 hours, followed by degassing for at least 2 hours under vacuum. This dry weight was used in all calculations. The Autopycnometer determines the volume of both empty and sample filled container and the density is automatically calculated by helium displacement. A direct reading of the helium density ($g/cm^3$) is given by the instrument. Appropriate corrections were made to take into account the shift in ambient temperature during the experiment.

## 7.2 Mercury Porosimetry

The volume distribution of pores, cumulative pore volume and the mercury (apparent) densities of the chars were measured using a Micromeritics Autopore 9200 mercury porosimeter. The instrument measures the amount of mercury forced into the pores of the char samples as a function of applied pressure. Corrections for mercury compressibility were made automatically by the porosimeter. This technique is capable of examining the $30\text{-}10^6$ Å pore size range.

Both helium and mercury experiments were carried out on activated series of the PVDC char and the Markham Main coal char (prepared by gasification in $H_2/H_2O$ at 960 °C and 1 atm.) and the results are presented in Chapter Twelve.

## 7.3 Adsorption

### 7.3.1 Adsorptives

The adsorptives used in this work to obtain adsorption isotherms were argon at 77 K and carbon dioxide at 195 K and 273 K.

The advantages of using argon [207] are (i) it is chemically inert which means there is no possibility of interaction with any polar groups in the system, *e.g.*, water, and (ii) at the operating temperature (77 K) the vapour pressure of the supercooled liquid is 217 Torr, which permits a whole isotherm (up to $P/P_0 = 1$) to be measured directly. One disadvantage, however, is the possibility of activated diffusion in fine micropores. This problem can be overcome by increasing equilibrium times to allow complete adsorption at low relative pressures. The alternative is to use a different adsorptive at a higher temperature.

$CO_2$ at 195 K has been used successfully with microporous carbons and coals by several workers [208, 209], but some disadvantages have been identified. $CO_2$ possesses a high quadrupole moment which may produce variations in isotherms due to the presence of polar groups in the solid surface [210]. Another problem which occurs when using $CO_2$ arises as a result of its very high vapour pressure (1413.6 Torr for the supercooled liquid at 195 K) which means that whole isotherms cannot be measured with conventional adsorption apparatus. The only apparent advantage of using $CO_2$ at 195 K is that activated diffusion effects are usually removed.

Some investigators [211] have found that $CO_2$ at 195 K fails to reach all the micropores in some pore systems. Consequently the use of $CO_2$ at 273 K has been suggested to assist the complete characterisation of

activated carbons and coals [211-213]. The aforementioned problem of using $CO_2$ at 195 K is amplified somewhat at 273 K since the saturation pressure at this temperature is 26142 Torr. This means that a maximum relative pressure of only 0.03 can be achieved using conventional gravimetric apparatus. However, activated diffusion effects are non-existent at 273 K [214].

The limitations of the three systems discussed previously leads to the conclusion that use of any single adsorptive (at a given temperature) to characterise the pore systems of the chars used would probably be unsatisfactory. Consequently adsorption isotherms were measured on activated series of the two chars, using three different systems: Ar at 77 K, $CO_2$ at 195 K and $CO_2$ at 273 K.

### 7.3.2 Adsorption balances

Adsorption isotherms were measured gravimetrically using two types of adsorption balance. A spring balance for adsorbents with large surface areas and a vacuum microbalance for adsorbents with surface areas of less than 100 $m^2/g$.

7.3.2.1 Spring balance.-The balance used was a McBain spring type [215] built by Masters [216], shown in Figure 7.1. The outer case was constructed from pyrex glass and attached by clamps to a framework, which was secured to a solid wall. Outgassing problems due to adsorption of organic vapours by vacuum grease were avoided by using PTFE 'O' ring sealed taps. The tubes, J, are attached by cup and socket 'O' ring joints (T), thus allowing considerable movement of the tubes, so as to avoid contact between the helical springs and the tube walls. The use of four pyrex hangdown tubes allows four samples of carbon to be analysed simultaneously.

Adsorption pressures of $10^{-4}$ to 100 Torr were measured by a capacitance pressure gauge (MKS Baratron Model No.270) which is capable of high accuracy (0.12% of reading) over a wide range of pressures. Higher pressures from 100 Torr to atmospheric (760 Torr) were measured by a mercury manometer (N). The manometer is isolated from the system by a tap, M, so as to reduce the possibility of contamination of the samples by mercury vapour. During gas adsorption the manometer was isolated under vacuum until it was required. A Pirani gauge (LKB Autovac Mddel No.3294B) was also used at low pressures as a further check of adsorptive pressure since it does not suffer from temperature induced fluctuations in pressure. Both the Pirani and Baratron heads were glass blown into the system to prevent leaks. The Baratron gauge was calibrated by the supplier (Chell Instruments Ltd., North Walsham, U.K.) against a MKS Baratron transfer standard. Accordingly the Pirani gauge and the mercury manometer were calibrated against the Baratron for air, argon and $CO_2$ (Figure 7.2). The results show that the Pirani gauge corresponds closely with the Baratron gauge over the pressure range $10^{-3}$ to 10 Torr for air, but only over the range $10^{-3}$ to $10^{-1}$ Torr for argon and $CO_2$. This result is in accordance with known experimental curves for Pirani gauges at high pressures (Figure 7.3) [217]. Therefore pressure measurements from $10^{-4}$ to 100 Torr were made using the Baratron gauge and the Pirani was used at low pressures as a check, especially if temperature variations were a problem. Apart from pressure measurements during adsorption the gauges were indispensable in checking for completion of outgassing and leaks in the system.

A one litre bulb, G, was incorporated in the system to allow very small amounts of adsorptive to be introduced into the system. The pumping system consisted of a rotary pump, A (Edwards Vacuum Products Ltd.) backing a water-cooled diffusion pump, B. The rotary pump possessed a power failure protection unit, which isolated the vacuum system and allowed the rotary pump back to atmospheric pressure in the event of a power failure. A liquid nitrogen trap, D, and a water-cooled baffle valve, E, were employed to reduce oil vapour back-streaming. A by-pass line, C, protected the diffusion pump whilst large quantities of gas were pumped out of the system.

The helical springs used were constructed from Pyrex in 0.3 m unextended lengths. Their advantages over silica equivalents are their considerably lower cost, reduced brittleness and ease of handling and repair. The only disadvantage of Pyrex springs is their low dimensional stability, *i.e.*, they creep under stress. Masters [216] solved this problem by following the practice of Chipalkatti and Giles [218] and annealing the springs under a 0.5 g load at 470 K for 8 hours. After such treatment no significant creep could be detected over a period of two weeks. Spring sensitivities were measured using standard weights and recording spring extensions with a cathetometer. Calculated sensitivities were not dissimilar for each spring and they remained constant for the duration of the adsorption work. The cathetometer was capable of detecting a minimum spring movement of about ± 30 μm; thus the minimum detectable weight change was ± 50 μg. A fiducial reference fibre was suspended within each spring to indicate any movement of the cathetometer in relation to the sample.

7.3.2.2 Vacuum microbalance.-Although the spring balance previously described provides a good measure of surface area in solids, its use is limited to materials possessing quite large surface areas, and cannot be used for materials with a total surface area of less than about 100 $m^2/g$. An appropriate device for the measurement of low surface areas is a vacuum microbalance with a sensitivity in the microgram range [219]. The microbalance used in this work was a CI Electronics Ltd. Mark 2 Model B. The case, P, was then modified by glass blowing one end to make a suitable attachment to the spring balance. The microbalance could be isolated from the system by a PTFE 'O' ring sealed tap, which permitted operation of either balance, jointly or separately. This arrangement enabled a maximum of five samples to be analysed simultaneously. The balance movement is controlled by a light sensitive servo mechanism and consequently requires constant light intensity to operate accurately. This was achieved by wrapping the microbalance assembly in aluminium foil.

Although the microbalance has a maximum sensitivity range of 0-25 μg full scale deflection (FSD), building vibrations made it impossible to use this range. Measurements were therefore made in the ranges 0-250 μg FSD, 0-2.5 mg FSD, 0-10 mg FSD and 0-100 mg FSD. The minimum detectable deflection was ±2.5 μg, producing a sensitivity twenty times better than that of the spring balance.

7.3.3 Experimental procedure

The sample of coal char (0.2 g) was suspended, using a fine glass fibre, in an aluminium foil bucket, L, from the helical springs in the spring balance and from the balance beam in the microbalance. The samples were then outgassed down to a pressure of less than $10^{-4}$ Torr

for a period of 12 hours at a temperature of 523 K. This was achieved by wrapping heating tape around the sample area of the hangdown tube. The temperature of this arrangement was controlled using a Variac controller. Completion of outgassing was indicated by cessation of spring extension and this was checked by closing off the system for 15 minutes and monitoring any rise in pressure. A pressure rise in excess of 0.01 Torr in this period was unacceptable and in this event a mass spectrometer was used as a leak detector to identify the position of the leak. Distinction can be made between a real leak and a virtual leak by examination of the pressure *versus* time plot. An example is shown in Figure 7.4, where curve A is a virtual leak resulting from slow outgassing of the system and curve B is a real leak.

When outgassing was complete and the system was leak free, the heating tape was removed and the hangdown tubes were immersed in a bath maintained at the required temperature (*i.e.*, liquid nitrogen for Ar at 77 K; solid $CO_2$ for $CO_2$ at 195 K; ice for $CO_2$ at 273 K). The bath level was maintained at a maximum by continual additions of cooling agent, ensuring that the sample was at least 10 cm below the surface of the coolant. Only when the samples were at temperature and being pumped were zero pressure extensions measured. High purity argon (99.999% Ar) and $CO_2$ (99.999% $CO_2$) supplied by Air Products Ltd. was dried by passing through two columns of 3 Å molecular seive before being admitted into the system for adsorption purposes.

Spring extension was then measured as a function of adsorptive pressure in the system using a cathetometer. Equilibrium times were indicated by cessation of spring extension at a constant pressure. The equilibration time varied considerably between chars, with times of up

to 12 hours for chars with a large proportion of fine micropores. Unfortunately the bath temperature could not be maintained overnight and the sample degassed. To overcome this problem the samples were outgassed overnight at 523 K and then returned to the required pressure the following day to continue adsorption measurements. The technique worked very well and isotherms were found to be smooth.

Errors in weight [220] and pressure [221] measurements may arise due to thermal transpiration, resulting from the temperature gradients in the hangdown tubes. The error in weight determination is mainly due to the mass changes caused by temperature gradients along the sample and the hangdown glass fibre. Thermal transpiration effects in this case were limited to the hangdown fibre since the sample was kept at least 10 cm beneath the coolant surface. This effect was only of the order of a few micrograms and was therefore neglected. However, corrections to pressure measurements were necessary over certain pressure ranges and these have been calculated using Liang's empirical equation as described by Bennett and Tompkins [221]. Using the dimensions of the hangdown tubes in the spring balance and microbalance, the errors in pressure readings were calculated and are shown in Table 7.1. It is clear from these results that correction of pressure readings is necessary in the range 0.001 to 0.01 Torr, for both balances.

Discrepancies may also arise due to a buoyancy effect during adsorption. This effect was found to be negligible for the spring balance (less than 1% correction of the weight increase at all pressures). However, corrections were necessary when using the microbalance and indeed in some cases the magnitude of the buoyancy effect made adsorption measurements difficult. This effect was most evident for unactivated

chars and argon adsorption due to the inaccessibility of part of the pore structure at 77 K. The effects of corrections for buoyancy and thermal transpiration were assessed by observing the adsorption characteristics of a reference adsorbent, in this case Vulcan 3-G (see Chapter Twelve).

# CHAPTER EIGHT

## DETERMINATION OF ACTIVE SURFACE AREA USING A TEMPERATURE-PROGRAMMED DESORPTION TECHNIQUE

As a result of the obvious importance of active surface area (ASA) in characterising the reactivity behaviour of coal chars, it was decided that the measurement of ASA should be an important part of the project. The most widely used techniques [182, 222-224] for studying active site concentrations involve continuous monitoring of reactant and product partial pressures in a closed, constant volume system. A known amount of oxygen is chemisorbed on the surface of the sample at a given pressure and temperature. A temperature-programmed desorption (TPD) [225] removes the carbon oxides from the surface, leading to an estimate of the amount of oxygen chemisorbed and thence to the ASA.

This chapter describes the development and validation of an alternative dynamic technique for assessing the ASA of coal chars using an oxygen chemisorption-temperature-programmed desorption method.

### 8.1 Apparatus

A block diagram of the system used is shown in Figure 8.1. The sample is situated in a right-angled quartz tube which is placed in a vertical tubular furnace of appropriate dimensions. The temperature of this arrangement is accurately controlled (±0.5% of the setpoint) by a Eurotherm 812 temperature programmer/controller. The capillary tube leading from the reaction vessel goes directly to the quadrupole mass spectrometer analyser head (Spectramass 100, Spectrum Scientific Ltd.) and the vacuum pumping system, consisting of a water cooled diffusion pump backed by a

rotary pump (Edwards Vacuum Products Ltd.). Isolation of the sample is achieved by incorporating two needle valves (Edwards Vacuum Products) into the system. Valve A enables predried oxygen to be introduced into the system for chemisorption purposes and valve B controls the pumping capacity in the reaction zone. A Stanton Redcroft BD-9 two channel recorder is used to record the temperature in the reactor and the partial pressures of desorbed gases.

## 8.2 Procedure

A 50 mg sample of char was placed in the reaction vessel which was outgassed to $10^{-7}$ Torr at 1223 K for 15 hours. The temperature was then reduced to the chemisorption temperature of 423 K and predried oxygen at atmospheric pressure was admitted into the system for a periof of 12 hours to saturate the surface with oxygen. Subsequently the pressure was reduced again to $10^{-7}$ Torr, removing all gaseous oxygen from the system. The char was then subjected to a temperature-programmed desorption at a linear heating rate of 5 K/min, under a total dynamic pressure range of $10^{-5}$ to $10^{-7}$ Torr, to desorb surface oxides as CO and $CO_2$. Desorption partial pressures were measured using the mass spectrometer.

## 8.3 Analysis of TPD Curves

A general analysis of the TPD technique may be developed by considering a schematic desorption curve of partial pressure of gas A, $P_A(t)$ as a function of time, t (Figure 8.2a), measured at the mass spectrometer sampling port at temperature, T(K) (Figure 8.2b). The pumping rate for gas A, $Q_A(m^3/s)$, from the sampling port is assumed constant (see below).

Assuming ideal gas behaviour:

$$P_A(t)Q_A = n_A(t)RT \qquad (1)$$

where $n_A(t)$ is the molar flux of gas A (mol/s) out of the sampling port at time t, and R is the gas constant.

Accordingly,

$$Q_A \int_{t_1}^{t_2} P_A(t)dt = RT \int_{t_1}^{t_2} n_A(t)dt \qquad (2)$$

where $t_1$ and $t_2$ are the starting and finishing times of the desorption curve, Figure 8.2a. The integral of the left-hand side of equation (2) is the area under the TPD curvd, I(A), while the integral on the right-hand side is $N_A$, the total number of moles of gas A desorbed in the time interval $t_2-t_1$. Thus equation (2) becomes:

$$N_A = \frac{Q_A}{RT} I(A) \qquad (3)$$

and the amount of A desorbed can be determined directly from integration of the TPD curve, provided that the pumping speed $Q_A$ can be determined (see below).

The assumption that $Q_A$ is constant over the time interval $t_1$ to $t_2$ is valid if the pumping rate is controlled by Knudsen diffusion [226], as is the case in the present work. The range of total pressures over which desorption curves were measured was from $10^{-5}$ to $10^{-7}$ Torr which is within the range of pressures ($10^{-2}$ to $10^{-8}$ Torr) where the pumping speed of the vacuum system is independent of total pressure [227]. The assumption that $Q_A$ is constant may also be acceptable at higher pressures where the flowrate is controlled by the Poiseuille equation, provided that $P_A$ is a small fraction of the total pressure. Thus the method may be adapted to gas chromatographic analysis of TPD curves.

## 8.4 Calibration and Application to Desorption of CO and $CO_2$

The TPD technique may be calibrated by determination of $N_A$ and I(A) in equation (3) using a desorption process or reaction which gives rise to a known amount of gas A. For calibration of the desorption of CO and $CO_2$ from carbons a suitable reaction is the decomposition of calcium oxalate:

Stage I $CaC_2O_4.H_2O = CaC_2O_4 + H_2O$

Stage II $CaC_2O_4 = CaCO_3 + CO$

SBage III $CaCO_3 = CaO + CO_2$

The TPD system was therefore calibrated by integrating the TPD peaks for CO and $CO_2$ during stage II and stage III of the decomposition reaction, using different amounts of calcium oxalate. The results are plotted in Figure 8.3, which shows linear relations between N and I for CO and $CO_2$, as expected from equation (3).

Assuming molecular flow, it is expected that [228]:

$$\left(\frac{Q_{CO}}{Q_{CO_2}}\right) = \left(\frac{M_{CO_2}}{M_{CO}}\right)^{0.5} = 1.25 \qquad (4)$$

where $M_{CO_2}$ and $M_{CO}$ are the molecular weights of $CO_2$ and CO respectively. The ratio of the slopes, K, of Figure 8.3 $K_{CO}/K_{CO_2}$ = 1.25, in excellent agreement with theory.

Estimates of the effective pumping speed at the mass spectrometer sampling port are about 10% of the maximum pumping speed of the diffusion pump. The low effective pumping speed may be attributed to constrictions in the pumping system, for example, the liquid nitrogen trap and the needle valves.

## 8.5 Calculation of ASA

The active surface area, $S_A$ ($m^2/g$) of a carbon may be calculated from the TPD curves using the equation:

$$S_A = \frac{N_0 \sigma_0 N_{AVO}}{x} \qquad (5)$$

where $N_0$ and $\sigma_0$ are the number of moles of oxygen desorbed and the cross-sectional area of the oxygen atom, respectively. $N_{AVO}$ is Avogadro's number and $x$ is the weight of carbon in grams. A value of 0.083 $nm^3$ was used for $\sigma_0$ [182]. $N_0$ is calculated from the relation:

$$N_0 = N_{CO} + 2N_{CO_2};$$

$N_{CO}$ and $N_{CO_2}$ are obtained from the calibration curves in Figure 8.3.

# CHAPTER NINE

# STEAM GASIFICATION OF CHARS

It was necessary during this project to have a system whereby the chars used could be gasified with steam at atmospheric pressure. Therefore a gasification rig was designed and built so that the required gas composition and flowrate could be generated downstream from the reactor. The reactant gas mixture used in this work was $Ar/H_2/H_2O$. This was used in preference to an $Ar/H_2O$ gas stream for the following reason [229]. In fixed-bed reactors and microbalance reactors (as used in this investigation) with a feed stream of excess water and no hydrogen, the partial pressure of hydrogen increases through the carbon bed as a result of its production in the $C-H_2O$ and water-gas shift reactions. The measured rate is therefore not a differential rate, but rather a surface-time yield. If the feed stream consists of both excess water and hydrogen (in the absence of mass transfer limitations) the water and hydrogen partial pressures are constant throughout the carbon bed. Thus the measured rate, as determined by gas analysis of CO, is also constant throughout the bed and is a differential rate. Therefore, if a hydrogen inhibitor is used in the feed stream true kinetic values can be obtained [230-233]. As a result of these considerations, a stream of $Ar/H_2$ was established in the reactor prior to gasification with $H_2O$ to give a constant $H_2$ partial pressure as measured by mass spectrometry.

## 9.1 Apparatus

The system used for steam gasification of the coal char and model char is shown in block diagram form in Figure 9.1. The two main gas streams of argon and argon/hydrogen are passed through drying and deoxygenation stages

to remove the possibility of gasification before the required gasification temperature is reached. The flow of argon is separated and takes two different paths to the reactor. One flows directly to the reactor as an inert atmosphere, whilst the second is bubbled through a saturator to provide the appropriate vapour pressure of water in the argon carrier gas. Temperature and flow conditions are discussed in Section 9.2. Condensation problems were alleviated by lagging of the system upstream from the saturator. This was achieved by wrapping heating tape around the stainless steel gas lines. There is also a stream of argon/hydrogen (for reasons previously discussed) which can be mixed with the argon/steam gas flow to produce the required $Ar/H_2/H_2O$ mixture. The separate gas streams pass through a mixing volume which thoroughly mixes the two streams prior to being transported to the reaction zone. The required gas composition is then bled into the reactor system for gasification purposes. The two systems used for gasification were a thermogravimetric balance and a fixed-bed reactor which was specially designed and built for the purposes of this project. The fixed-bed reactor was used in conjunction with a mass spectrometer as a gas analyser. The aforementioned apparatus is described in Sections 9.3, 9.4 and 9.5.

The whole gas supply system was constructed from 7 mm stainless steel tubing with Swagelok connections. All gas streams were regulated using Fisher flow meters/regulators (maximum flowrate - 100 $cm^3/min$). These are shown in Figure 9.1 as A, B and C. Needle valves (Edwards Vacuum Products Ltd.) were incorporated into the system to allow accurate control of gas streams. The pressure in each gas line was monitored by oil filled manometers.

## 9.2 Design of the Reactant Gas Supply System

Prior to construction of the gas supply system it was necessary to undertake preliminary design calculations to ascertain suitable gas flow conditions. These calculations were carried out as follows:-

50 $cm^3$/min was selected as a standardised flowrate since it corresponds to mid-scale on the thermobalance flow meter. It should be noted that $cm^3$/min implies standard $cm^3$/min, *i.e.*, measured at 0 °C and 1 atm. The linear flowrate over the specimen ($cm^3$/min) is given by:

$$U = \frac{50}{\pi r^2} \frac{T_r}{273} \qquad (1)$$

where r is the furnace radius (cm) and $T_r$ is the reaction temperature, (K). The flowrate of water vapour ($cm^3$/min) is given by:

$$F_{H_2O} = \frac{bP}{P_0} \qquad (2)$$

where b ($cm^3$/min) is the flow of argon to the saturator, P (mmHg) is the vapour pressure of the water at the saturator temperature and $P_0$ is atmospheric pressure. The total flow of $Ar/H_2O$ ($cm^3$/min) is therefore given by

$$F_{Ar/H_2O} = b + \frac{bP}{P_0} \qquad (3)$$

Assuming there is no $Ar/H_2$ flow, the flow into the reactor (equivalent to 50 $cm^3$/min) is $b(1-P/P_0)$. This leads to a value of b, at a given pressure and, using equation (2), to the determination of the flow of $H_2O$.

Calculations were performed using a wide range of $Ar/H_2$ mixtures and this led to an Ar/1% $H_2$ mixture being chosen in the standard procedure. Calculations for this composition are shown below.

Assuming an $Ar/H_2O$/5% $H_2$ mixture is required and a flow of Ar/1% $H_2$ is supplied then the flow of argon, $F_{Ar}$ ($cm^3$/min) is given by:

$$F_{Ar} = b + 0.99c \qquad (4)$$

where c ($cm^3$/min) is the Ar/1% $H_2$ flowrate. The flow of $H_2$ is 0.01 c and the flow of $H_2O$ is $bP/P_0$. Therefore the total flow $F_T$ ($cm^3$/min) is given by:

$$F_T = b + 0.99\ c + 0.01\ c + \frac{bP}{P_0} \qquad (5)$$

$F_T$ must equal 50 $cm^3$/min as previously stated.

5% $H_2$ is required in the reactant gas, therefore:

$$0.05 = \frac{0.01\ c.P_0}{bP} \qquad (6)$$

Accordingly,

$$c = \frac{5bP}{P_0}$$

Substituting for c in equation (5) gives:

$$b = \frac{3.8 \times 10^4}{6P\,P_0}$$

Hence values for b and c can be calculated for a given P. The results of this design procedure are shown in Table 9.1, indicating that a saturator temperature of 60 °C should be used to produce the required partial pressure of steam in the reactant gas mixtures (*i.e.*, Ar/20%/$H_2O$/5% $H_2$). Values of 22.9 and 22.5 $cm^3$/min for b and c respectively are required in the standard procedure.

## 9.3 Kinetic Studies using a Fixed-bed Reactor

Kinetic measurements of gasification were carried out using a specially designed fixed-bed reactor, similar to that used by Huttinger [234]. The vessel is shown in Figure 9.2. It consists of gas inlet and outlet

ports, a protective sheath for the thermocouple and quartz inner and outer vessels connected by a frit of appropriate mesh size (6 μm), upon which the char sample is laid. A vertical tubular furnace (Severn Science Ltd.) was used in conjunction with a Eurotherm linear temperature programmer to supply the necessary heat for gasification up to temperatures of about 1050 °C. The input is connected to the reactant gas supply system and the outlet goes directly to the gas analyser. The advantages of using a system of this sort are that back mixing of gases is totally excluded and a relatively large sample size of up to 5 g can be used.

A brief investigation was carried out to assess the maximum bed height that could be used without the gasification rate suffering from any diffusional influences. The results of this study are shown in Figure 9.3, which shows the variation of gasification rate with bed height, at a gasification temperature of 960 °C. This plot shows that the gasification rate increases linearly up to a bed height of 40 mm. This is an indication that the rate is chemically controlled for bed heights of 5 to 40 mm under the chosen gasification condtions and that mass transport resistance to diffusion of reactant gas molecules down through the bed is negligible.

## 9.4 Thermogravimetric Analysis

The reactivity of the chars to steam was measured using a Stanton Redcroft TG 750 thermobalance. The components of this system are shown in block diagram form in Figure 9.4. A maximum of 25 mg of the char sample is suspended in a shallow crucible from the microbalance. The crucible is positioned in the centre of a vertical tubular furnace, the temperature of which is controlled to ±2 °C and recorded by a specially designed Pt/Pt-13% Rh platform thermocouple situated 0.5 mm below the crucible in the microfurnace assembly. The sensitivity range of the microbalance was set at 0-25 mg FSD.

The $Ar/H_2/H_2O$ mixture was introduced into the system at a constant flowrate of 50 $cm^3/min$ (as specified in design calculations). In the normal operating mode the electrobalance system would become contaminated with water vapour. Consequently a special hangdown tube was constructed to allow the reactant gas to be introduced into the main flow of argon upstream from the electrobalance assembly. The rest of the system was purged with argon.

The char sample was heated linearly (5 K/min) to the required gasification temperature (900-1020 °C) in an argon/hydrogen atmosphere. The required $H_2/H_2O$ mixture was introduced into the reaction zone when the gasification temperature was attained. The weight and temperature of the sample were continuously monitored on the balance control unit and plotted using a Stanton Redcroft BD-9 two channel recorder. The slope of the essentially linear weight loss curve leads to determination of the gasification rate.

## 9.5 Mass Spectrometric Gas Analysis

The gas analyser used in conjunction with the thermobalance and the fixed-bed reactor was a Spectrum Scientific Ltd. Spectramass 100 quadrupole mass spectrometer. This unit and its associated vacuum system is shown in block diagram form in Figure 9.5. As in all mass spectrometers there are three principal components:

(1) The ion source for production of ions that are representative of the gases in the environment and the focussing and injection of these ions into the mass analyser.

(2) The mass analyser itself which separates ions of different mass to charge ratio and presents these selected ions to the detector. This analyser is of the quadrupole type.

(3) The detector which collects the separated ions on a Faraday collector.

A water cooled diffusion pump backed by a rotary pump (Edwards Vacuum Products Ltd.) is employed to produce a vacuum of better than $10^{-8}$ Torr in the system. Pirani and Penning gauges are used to monitor the pressure down to $10^{-5}$ Torr at which point the total pressure comes within the range of the mass spectrometer. The instrument is capable of measuring both the total pressure in the system and the partial pressures of specific gases. A facility for scanning a range of masses is also available and a spectrum of partial pressure peaks can be plotted on a recorder linked to the pressure output signal of the mass spectrometer. A typical spectrum is shown in Figure 9.6.

Calibration of the mass spectrometer was carried out using a mixed gas stream with accurately known proportions of four gases. The results of this calibration are shown in Table 9.2, indicating that the instrument was accurate to within 2% of the peak partial pressures.

The sensitivity of instruments of this type is usually quoted for dry nitrogen. Other gases ionise more or less readily than nitrogen, which means that equal pressures of different gases will give rise to different ion currents. For meaningful partial pressures to be determined the relative sensitivities of the gases in the system must be considered [235]. The relative sensitivities of the gases likely to be detected during this work are shown in Table 9.3. Therefore, to obtain the true partial pressure of any gas the following equation must be used:

$$\text{True partial pressure} = \frac{\text{Apparent partial pressure}}{\text{Relative sensitivity}}$$

Electron bombardment in the analyser produces simple, singly ionised molecules; however, other factors such as multiple ionisation, fragmentation and isotropic contributions may lead to relatively complex spectral patterns known as cracking patterns [235]. Cracking patterns exist for most gases and as a further test of the accuracy of the instrument several pure gases were bled into the system to obtain the appropriate principal peaks. The results of this test are shown in Table 9.4, compared with expected values from the literature. The measured cracking characteristics of the gases indicate that the instrument is capable of detecting and differentiating between different gases, even when they are present in small concentrations.

# CHAPTER TEN

# RESULTS AND DISCUSSION

## 10.1 Chemical Analyses of the Chars

Ultimate and proximate analyses for the two chars, carried out at BGC using a Leco CHN 600 analyser and a Leco MAC 400 analyser respectively, are shown in Table 10.1. The significant nitrogen content in the PVDC char results from the presence of acrylonitrile in the polymeric precursor. As expected, the ash content of the coal char is considerably higher than that for the model char.

The principal compound identified by *X*-ray powder diffraction analysis of the Markham Main coal char was haematite ($Fe_2O_3$) with some evidence for quartz ($SiO_2$) and alumina ($Al_2O_3$). It is probable that there are other materials present in the ash in small quantities which cannot be detected by *X*-ray powder diffraction.

Semi-quantitative analyses of metallic elements present in the model char and the coal char, as determined by EDAX, are shown in Table 10.2. Figure 10.1 shows typical examples of EDAX spectra for the two chars. It is apparent from these results that aluminium and silicon are the most abundant metallic species in the coal char. However, it is likely that any catalytic activity which may be evident in the coal char will be due to the presence of considerably smaller amounts of potassium, iron and calcium [86, 187, 236-242]. Qualitative EDAX analysis also indicated the presence of sulphur in both chars and a small amount of residual chlorine, left from the carbonisation process, in the PVDC char.

The preceding analyses of the chars indicates that the PVDC char was relatively pure. Those impurities which were present were thought to have been introduced after the char was formed, since the organic precursor for the model char was extremely pure. That is, the impurities were probably introduced as a result of the handling, grinding or sieving of the char. The impurities introduced by any of these operations would probably be well dispersed throughout the material, reducing any likelihood of strong catalytic effects. The coal char contains relatively large amounts of potentially active elements such as potassium and iron and catalytic effects would be more likely.

# CHAPTER ELEVEN

# ANALYSIS OF THE THERMAL DEGRADATION OF PVDC AND PAN

## 11.1 Thermogravimetric Analysis

The Stanton Redcroft TG 750 thermobalance was used to analyse the thermal degradation of the vinylidene chloride/acrylonitrile copolymer at different heating rates ranging from 1 to 10 °C/min. The heating rates used were comparable to those used in dilatometry experiments so that a direct comparison could be made. The thermograms obtained are shown in Figure 11,1. After the initial loss of moisture at very low temperatures (<120 °C), the weight of the copolymer remained constant up to temperatures of 160-190 °C, depending upon the heating rate, At this point the copolymer exhibits a rapid weight loss and a region of maximum constant reaction rate is observed. This region is relatively small in terms of temperature and spans only about 50 °C. Although it is difficult to demarcate between the regions of weight loss, this stage is roughly equivalent to quantitative elimination of one HCl molecule from the structure. Above about 250 °C a period of reduced reaction rate occurs until, at higher temperatures (approximately 800 °C), there is no further detectable weight loss. There is a possibility that further degradation may occur at higher temperatures than 900 °C, but this is of little interest in this work.

Figure 11.1 shows that the thermal degradation of the copolymer produces thermograms of similar shape, irrespective of heating rate, exhibiting four distinct zones, as shown in Figure 11.2. Zone 1 is an induction period during which no significant weight loss is observed; zone 2 is the region of maximum constant reaction rate (this is the

region in which the effect of heating rate is most apparent); zone 3 where a considerably reduced reaction rate is observed which decreases with temperature before entering zone 4 where carbonisation is apparently complete and no further weight loss is observed up to 900 °C.

As expected, the results indicate that an increased heating rate produces a higher reaction rate [243], which is measured as the rate of weight loss in zone 2. Indeed, when the reaction rate is plotted as a function of heating rate (Figure 11.3) an approximately linear relationship is found for the range of heating rates used.

TGA results therefore show the existence of two distinct weight loss regimes during the thermal degradation of the copolymer. A similar result is found for pure PVDC and the overall degradation reaction can be described as a two-step process [118, 244, 245]:

$$(-CH_2-CCl_2-)_n \xrightarrow{\text{fast}} (-CH=CCl-)_n + nHCl \qquad (1)$$

$$(-CH=CCl-)_n \xrightarrow{\text{slow}} 2nC + nHCl \qquad (2)$$

The first step is a rapid reaction and corresponds to the formation of a conjugated polyene chain and the loss of one hydrogen chloride molecule per pair of carbon atoms. This is a first order reaction which usually proceeds with a relatively high activation energy of the order of 200 kJ/mol [118]. This reaction involves a change in configuration of the polymeric chains because of the changed valency angles, so that reaction cannot occur without diffusion of the chains in the solid state [119]. The PVDC structure is effectively destroyed and the polymer becomes infusible. The first dehydrochlorination usually

occurs in the temperature range 150-200 °C, as was the case with the copolymer used in the present work.

The second step in the overall reaction occurs at a considerably reduced rate and corresponds to carbonisation of the structure and removal of the remaining hydrogen and chlorine. The loss of the second chlorine atom from the PVDC structure takes place over a wide range of temperatures, 250-800 °C in the case of the copolymer used here. During this stage the residue is undergoing considerable cyclisation and aromatisation, so that successive chlorine atoms are lost from changing molecular environments. Coalescence of neighbouring chains must occur before further HCl can be eliminated since an intramolecular mechanism is not favoured. An intramolecular mechanism implies loss of HCl by formation of linear polyethylene chains and the internal reorganisation into straight chains is highly improbable. Step 2 in the overall reaction is a second order reaction with a small activation energy [118].

The behaviour of PVDC during the carbonisation stage differs from that of PVC in that there is no evolution of tar or other volatile matter usually associated with carbonisation [243, 245]. Since HCl is the only volatile product, the extent of reaction can be measured in terms of HCl loss. Maximum reaction rate was observed in the range 25-35% reaction. Above this range the reaction slows down markedly until carbonisation is complete and 100% HCl loss is achieved. In the present work this appears to occur at about 800 °C. At considerably higher temperatures than those used in this investigation, graphitisation of the carbonaceous residue takes place.

The ratio of the weight of the carbon residue to the initial weight is known as the carbon yield, This ratio is commonly used to identify polymeric residues. Although the material studied behaved differently at different heating rates, the carbon yield in each case was the same. The yield was 33-34%, compared with a literature value of 26% for pure PVDC [118]. This difference arises because the material studied was a copolymer containing 20% acrylonitrile (see below).

Thermal degradation of polyacrylonitrile (PAN) occurs in three stages [244]. In the first two stages volatiles (mainly ammonia) and then tars are eliminated. A large percentage of nitrogen, however, is retained in the residue. From 600 °C upwards a third stage exists during which weight is lost slowly. Despite this the carbon yield is high (44%). It has been established [246, 247] that only very small amounts of hydrogen cyanide are removed thermally from the polymer. There is, however, evidence from infra-red spectra that the triple bond of the cyanide group can open with resultant formation of cross-links inter-molecularly and of 6-membered heterocyclic rings intra-molecularly [247]. Nitrogen retained in this form has very high thermal stability. Although the copolymer used in this work was heat treated to 1000 °C, 3.5% nitrogen remained in the structure. This heterocyclic nitrogen can be removed by heating up to temperatures of about 1500 °C. It is evident, therefore, that strictly speaking, carbonisation is incomplete at 1000 °C, but for the purposes of this investigation the reactions occurring above 1000 °C are not important.

The acrylonitrile content has a marked effect on the carbon yield of the copolymer, giving a value of 33-34%, instead of the expected 26% for PVDC [118]. Using a simple rule of mixtures a carbon yield

of 30% would be expected for a 80% PVDC/20% PAN copolymer. Thus there appears to be some synergistic effect operating in this case. Despite this, the thermograms obtained for the copolymer are similar to those obtained for PVDC by other workers [243-245]. This means that although the copolymer exhibits PVDC and PAN degradation characteristics, the acrylonitrile content is not sufficient to change the form of the thermogram.

## 11.2 Dilatometric Analysis

There is a very limited amount of information available in the vast literature on the properties of polymers concerning dilatometric analyses of the thermal degradation of PVDC. It was therefore thought that an investigation of this sort would provide useful information on the change in structure of the PVDC/PAN copolymer during pyrolysis.

Dilatometry experiments were performed to assess the effect of heating rate on the swelling behaviour of the copolymer precursor. Plots of percentage expansion against temperature are shown in Figure 11.4. Initially there is a slight increase in volume of the sample; this occurs below 100 °C and can be attributed to expansion as a result of moisture loss. In the temperature range 100 to 190 °C, there is a small decrease in volume (negative dilatation) as the copolymer begins to soften and the probe sinks into the specimen. This behaviour corresponds to zone 1 on the characteristic TGA curve (Figure 11.2). This is followed by rapid expansion at a temperature of about 190 °C which causes a 47% increase in volume. This expansion occurs over a small temperature range (approximately 15 °C) and is independent of heating rate. The rapid expansion corresponds to the region of maximum rate of weight loss (zone 2) on the characteristic TGA curve (Figure 11.2).

The heating rate does, however, affect the subsequent behaviour of the copolymer. A heating rate of 10 °C/min caused the sample to undergo no further change in volume after the initial 47% increase and the volume remained constant up to the final temperature of 900 °C. Lower heating rates (5 and 2 °C/min) caused the copolymer to pass through a shrinkage stage prior to reaching the final constant volume. This shrinkage effect was even more pronounced at the lowest heating rates used (1 and 0.5 °C/min).

Shrinkage of the structure at low heating rates is due to the slower passage of the copolymer through its region of maximum plasticity, causing a collapse of the structure under the probe. Some of the shrinkage may indeed be due to the transfer of weight from the probe, but this was considered to be negligible. The rapid "blow-out" of the structure, which corrresponds to elimination of one HCl molecule, and subsequent shrinkage at low heating rates was followed by a period of relatively slow expansion. This must correspond to the slower removal of the second HCl molecule in the structure. The slow removal of nitrogen and volatiles from the acrylonitrile must make a contribution to the expansion, but this is overshadowed by the considerably higher HCl content in the copolymer, The region of slow expansion persists up to temperatures of 500-600 °C.

High heating rates (10 °C/min) do not allow time for structural collapse since the sample passes through the softening range too quickly. Resolidification of the structure occurs and there is no apparent shrinkage. Removal of the second HCl molecule in this case occurs through the large pores created by the rapid expansion and no further dilatation is observed.

Dilatometer curves obtained for the copolymer exhibit notable differences from those obtained for coking coals (Figure 3.4). The coals tend to exhibit a rapid swelling range at higher temperatures than the copolymer (350-500 °C compared with 200 °C). The magnitude of the dilatation in the coals is also considerably higher than that observed for the copolymer. This is presumably linked to the higher volatile matter content of the coals compared with the copolymer.

Brief examination of the samples using low power microscopy indicated that high heating rates resulted in the formation of large macropores. This was confirmed using mercury porosimetry (Chapter Twelve) for the model char prepared using a heating rate of 5 °C/min. Subsequent analysis of the model char using gas adsorption showed that, apart from the well developed macroporosity, the strong swelling and volatile removal gives rise to a highly porous structure with the majority of the surface area in the micropore range.

# CHAPTER TWELVE

# CHARACTERISATION OF PORE TEXTURE

## 12.1 Helium Pycnometry and Mercury Porosimetry

### 12.1.1 Helium density measurements

The densities of the PVDC char and the Markham Main char at various conversion levels were determined by helium displacement. Since helium can penetrate almost all pores ($d > 4$ Å), these values can be taken to be essentially the true densities. It is usually assumed that helium is not adsorbed to any appreciable extent at room temperature; this assumption, however, has been shown to be incorrect [248]. For certain carbons physical adsorption of helium does occur at room temperature, yielding erroneously high densities. Determination of helium densities at 300 °C can eliminate this effect, but it has been reported that in some cases, porosity which is inaccessible to helium at room temperature may become accessible at 300 °C [249]. Again, this would result in higher observed density values. Facilities were only available for density determination at room temperature, so the values obtained may suffer from the aforementioned problem. However, the technique should provide an indication of the variation in density with progressive gasification and allow a comparison between the two chars to be made.

The experimental data are summarised in Table 12.1. The fact that some of the density values are in excess of that reported for pure graphite is a good indication that significant helium adsorption is occurring. Other workers [250] have attributed the increase in helium density with conversion to the gasification of relatively light

matter such as carbon and volatile matter, with relatively heavy ash gradually becoming the major component of the system as gasification proceeds. However, in this case ash effects are unlikely to be dominant since the density of the model char is higher than that of the coal char at high burn-off. The considerable increase in microporosity with burn-off, as shown by adsorption measurements in Section 12.2, is also likely to cause an increase in helium density. This is thought to be a contributory factor here, since the more highly microporous model char exhibits higher densities than the less microporous coal char.

12.1.2 Mercury density measurements

The mercury densities of the char samples at various conversion levels were determined by mercury porosimetry. In determining the mercury density the following conditions must be met: (1) the interparticle voids must be completely filled with mercury during the measurement and (2) all the intraparticle voids must be free from mercury penetration. It is not clear whether these conditions were met during the experiment so the data are somewhat uncertain.

The minimum pressure at which the interparticle voids are completely filled was determined experimentally by Gan *et al.* [251], using glass powders. Considerable amounts of mercury were forced into interparticle voids below a pressure of one atmosphere, followed by very little mercury penetration beyond one atmosphere. It was therefore concluded that at one atmosphere, the interparticle voids of char samples would be filled and any further mercury penetration at higher pressures would be due to the presence of pores [2]. Of course, this conclusion is based on the assumption that all pores whose entrances

are open to the exterior surface of the particle are smaller than the size which mercury can penetrate at one atmosphere, *i.e.*, $d < 10^6$ Å. The values obtained must, therefore, be treated as apparent densities and accuracy must be questioned, since there is no guarantee that the above assumption is correct. The mercury density values for the two chars as a function of burn-off, determined by mercury porosimetry, are shown in Table 12.1.

12.1.3 Void volume and porosity

Using the helium and mercury densities as the true ($\rho_t$) and apparent ($\rho_A$) densities, one can calculate the total internal void volume, v, and the porosity, $\varepsilon$:

$$v = 1/\rho_A - 1/\rho_t$$

$$\varepsilon = 1 - \rho_A/\rho_t$$

This relation assumes that there is no swelling or shrinkage of the residual solid structure. Void volumes and porosities for the two chars at various conversion levels were calculated and are reported in Table 12.1. Values of both parameters increase with progressive gasification as the pore structure is developed. In general, the void volume and porosity of the model char is higher than that of the coal char, reflecting the highly microporous nature of the model char.

The porosity data are not further analysed here, due to the experimental uncertainties outlined in Sections 12.1.1 and 12.1.2. Hence the values reported should not be regarded as true porosities, but as a relative indication of the porosity during gasification,

12.1.4 Cumulative pore volumes and pore size distribution

Mercury porosimetry also allows determination of cumulative pore volume and pore size distribution. Mercury is forced into the pores at high pressures and by varying the pressure (up to 60,000 psi) the 30-$10^6$ Å pore size range can be examined. The high pressures required make it difficult to reach the micropore range (d < 20 Å), which means that accurate surface area data are impossible to obtain using this technique. It is hard to demarcate between interparticle and intra-particle void volumes. Distortion of results may also occur if the pore structure is affected by mercury at high pressures; for instance, if fracturing of pore walls occurs. Results at very high pressures should therefore be disregarded and only pore diameters of greater than 100 Å can be realistically examined.

Cumulative pore volumes [$cm^3/g$ (daf)] for the two chars at various conversion levels are shown in Figure 12.1. These results show that the porosity accessible to mercury in the PVDC char is higher than in the Markham Main char. There is a substantial increase in macropore volume with activation for both chars, suggesting that macropores are constantly being formed during gasification.

Pore size distributions (differential curves) for the activated series of both chars are shown in Figures 12.2 and 12.3. The PVDC char in the unactivated state has a pore size distribution which is uni-model with a peak pore entrance diameter of 15 μm (Figure 12.2a). This value increawes with burn-off reaching a maximum of about 50 μm at high burn-off. There is also some evidence for mesoporosity at high burn-offs (Figures 12.2c to 12.2e). The pore size distribution

in the unactivated Markham Main char is bi-modal with a peak pore entrance diameter of 30 μm increasing to 50 μm at high burn-offs (Figure 12.3). Figures 12.3a to 12.3e indicate that there is some mesoporosity present even in the unactivated char. The amount of mesoporosity increases with burn-off reaching a maximum at about 60% burn-off.

Most of the accessible macropore volume, in both chars, is in the range 10-50 μm, with more evidence for mesoporosity in the coal char than in the model char. The relatively large macropore size is presumably a result of the severe pyrolysis conditions and the pore structure observed is probably characteristic of the particular conditions used (*i.e.*, heating rate of 5 °C/min and a carbonisation temperature of 1000 °C). Indeed, low power microscopy reveals a significant increase in macropore size with heating rate. It is probable that the development of porosity is also affected by activation temperature, as well as extent of burn-off [252].

The macropores, shown by this technique, will act as admission pores in the adsorption process while the mesopores will act as diffusion pores towards the micropores where most of the adsorption and reaction of gases takes place. Mercury porosimetry results, combined with adsorption results (Section 12.2), indicate the existence of a tri-modal pore size distribution. This tri-modal distribution is more clearly observed at high levels of activation, The Markham Main char has quite a uniformly opened mesoporosity, whereas the PVDC char has a more developed macroporosity with less evidence for mesoporosity. Although the mesoporosity and macroporosity in both chars has been shown to be significant, adsorption studies will show that these pores make a small contribution to the overall surface areas of the chars.

## 12.2 Adsorption Studies

Many theories and developments of theories of adsorption have been proposed in the past. A brief review of the theories and equations used in this investigation is appropriate at this point.

### 12.2.1 Adsorption theories and equations

The relationship between the amount of gas adsorbed on the surface of a solid at a fixed temperature and the pressure of the gas is known as the adsorption isotherm. Adsorption isotherms are usually grouped, according to the BDDT classification [253], into five types, Figure 12.4. Measurement of adsorption isotherms can give useful information on the pore structure of most porous materials. Many theories have been proposed to account for different types of adsorption. There now follows a brief summary of the theories and equations which are relevant to this work.

12.2.1.1 The BET theory.-The earliest theory of adsorption was postulated by Langmuir in 1918 [254, 255]. He used a kinetic argument to derive an equation which fits the Type I isotherm in the BDDT classification. The Langmuir equation, in linear form, may be written:

$$\frac{P}{x} = \frac{1}{bx_m} + \frac{P}{x_m} \qquad (1)$$

where $x$ is the amount of gas adsorbed in grams per gram of adsorbent at pressure P (Torr); $x_m$ is the monolyaer capacity per gram of adsorbent, *i.e.*, the amount of adsorptive required to cover the surface with a molecular monolayer, and b is a coefficient specific to each adsorbate-adsorbent system. Thus, if the equation is applicable, a plot of $P/x$ against P should yield a straight line of slope $1/x_m$.

Langmuir made three basic assumptions: (1) that adsorption takes place on localised sites; (2) that all sites are of equal energy, and (3) that adsorption is limited to a monolayer. These assumptions are not generally correct when applied to physical adsorption, since it involves formation of multiple molecular layers, Langmuir's approach was later modified in order to account for multilayer adsorption by Brunauer, Emmett and Teller (BET) [50]. The BET approach assumes that the first layer is similar to the Langmuir monolayer and that the formation of the second and subsequent layers is similar to the condensation of the bulk gas.

The resultant BET equation allows monolayer capacities and surface areas of a large range of adsorbents to be found, assuming the size of the adsorbate molecule is known. If an infinite number of layers is assumed for adsorption on a non-porous surface, the BET equation is:

$$\frac{P}{x(P_0-P)} = \frac{1}{x_m C} + \frac{(C-1)P}{x_m C P_0} \qquad (2)$$

where $P_0$ is the saturated vapour pressure of the adsorptive and C is the BET constant which is approximately equal to $\exp[(q-L_v)/RT]$ where q is the heat of adsorption of the first layer and $L_v$ is the heat of adsorption of the second and subsequent layers and is equal to the latent heat of vaporisation of the adsorptive. A plot of $P/x(P_0-P)$ against $P/P_0$ should yield a straight line with a slope, s, equal to $C-1/x_m C$ and an intercept, i, of $1/x_m C$. Solving simultaneous equations gives:

$$x_m = \frac{1}{s+i} \quad \text{and} \quad C = \frac{s}{i} + 1$$

Therefore, values of $x_m$ and C can be calculated directly from the BET plot. The BET equation in the form shown in equation (2) is capable of describing Type II and Type III isotherms in the BDDT classification.

The specific surface area of an adsorbent, $S_A$ ($m^2/g$), can be determined using the calculated values for $x_m$ with the following equation:

$$S_A = \frac{x_m}{M} a_m N_A \times 10^{-18} \qquad (3)$$

where $a_m$ is the cross-sectional area of the adsorptive molecule ($nm^2$), M is the molecular weight of the adsorbate and $N_A$ is Avogadro's number.

Despite its wide use, a number of criticisms have been levelled at the BET model [256, 257], especially concerning its application to microporous adsorbents. These are now briefly outlined:

(1) The model assumes that the surface is energetically uniform, whereas it is usually heterogeneous.

(2) The model neglects the forces between an adsorbate molecule and its neighbour in the same layer.

(3) The model gives unrealistically high surface areas when applied to microporous adsorbents. This is due to filling of micropores at low relative pressures, caused by enhanced adsorption potential resulting from overlapping of adsorption energies of the pore walls. This casts some doubt upon the use of the term 'surface area' when referring to microporous materials. As a result, the term 'monolayer equivalent area' is often used [258]. Although the term 'surface area' is often used in this thesis, it should strictly be regarded as a 'monolayer equivalent area', since

the materials used are predominantly microporous.

Although the BET approach suffers severe limitations, the equation and developments of the method, *e.g.*, the t-plot [259, 260], have proved useful for identifying porosity in a wide range of adsorbents. In view of the obvious shortcomings of the BET approach, especially concerning microporous adsorbents, much attention has been given to the potential theory of Polanyi [261, 262] and developments of this theory [51, 263], by Dubinin for example, based on volume filling of micropores. A brief description of the relevant points of this theory will now be given.

12.2.1.2 The potential theory.-Polanyi [261, 262] proposed that the forces of attraction between a surface and adsorbed molecules decreased with increasing distance from the surface. The field of attraction is characterised by an adsorption potential, $\varepsilon$, which is defined as the isothermal work done, by the adsorption forces, on transforming a molecule from the gaseous phase to a particular point above the surface. Details of the theory are published elsewhere [261, 262]. Several workers have confirmed the success of the potential theory in predicting the temperature dependence of physical adsorption by using a number of adsorbate-adsorbent systems to derive isotherms at different temperatures from a single isotherm using the characteristic curve.

12.2.1.3 The Dubinin-Radushkevich (DR) approach.-The potential theory was later developed by Dubinin and co-workers so that more useful structural information could be extracted. Dubinin and Radushkevich [51, 263] extended Polanyi's potential theory by attempting to predict adsorption isotherms for any adsorptive, given a single isotherm for a

standard adsorptive on the same adsorbent. Details of the derivation of the DR equation are available elsewhere [51, 263, 264]. The linearised form, used in this investigation, is as follows:

$$\log V = \log V_0 - D \log^2 (P_0/P) \qquad (4)$$

where V is the volume of adsorbate adsorbed at relative pressure $P/P_0$, $V_0$ is the micropore volume and D is the DR isotherm constant. Equation (4) represents isotherms for microporous adsorbents and a plot of log V against $\log^2 (P_0/P)$ should yield a straight line whose intercept on the ordinate gives a value for $V_0$. The parameter D is a measure of the microporous structure of the adsorbent. A decrease in the magnitude of D indicates a steeper rise in the isotherms at low relative pressures and a decrease in pore size.

For many systems, equation (4) gives a linear relationship over a wide range of relative pressures. Unfortunately, deviations from linearity are often found, causing micropore volumes obtained by extrapolation to the ordinate, to be somewhat uncertain. Deviations from linearity of DR plots are often characteristic of a particular adsorbent structure and can therefore offer a useful tool for structural investigations. Marsh and Rand [265, 266] identified three types of deviation from the DR equation (Figure 12.5), which were attributed to particular distributions of potential.

12.2.1.4 Deviations from the DR equation.-Type A

This type possesses two linear sections with a downward deviation at low relative pressure (Figure 12.5). Such plots are commonly found for coals, for activated carbons with low degrees of burn-off (< 30%) [266]

and generally for homogeneous carbons. It is generally accepted that this type of deviation is due to activated diffusion [267, 268].

Type B

This type of DR plot is curved over the whole pressure range (Figure 12.5). Marsh and Rand [265] suggested that this was the result of a log-normal type distribution of adsorption volume with free energy. This type of deviation is found in highly activated carbons with burn-off levels greater than 30% [266].

Type C

Marsh and Rand [265, 266] concluded that this type of deviation was due to a bi-modal distribution of potential. These plots exhibit a linear section at low relative pressure with an upward deviation at high relative pressure (Figure 12.5). It is reasonable to assume that this upturn is due to capillary condensation in mesopores, since it occurs at high relative pressures.

12.2.1.5 Separation of microporous and non-microporous adsorption.- Evaluation of microporosity is often difficult because, in many adsorbents, other forms of porosity (mesopores and macropores) are present. Thus adsorption occurs in both micropores and non-micropores over a wide range of relative pressures. Determination of micropore volume and non-microporous surface area is usually unsuccessful if the BET approach is used, since it is assumed by this method that adsorption in micropores is completed at $P/P_0 = 0$. To be successful, the method must take into account the progressive filling of micropores with increasing relative pressure. There are several methods available for separating microporous and non-microporous adsorption,

including the t/F - V/F method of Kadlec [269, 270] and the nonane pre-adsorption method [271]. In the former case the choice of a non-porous reference material can cause problems and in the latter method problems with non-retention of nonane in wider micropores can arise in highly activated species. The method considered to be the most practical in this work is a single isotherm technique known as the Isotherm Subtraction (IS) method. The principle of this method is outlined in the following section.

12.2.1.5.1 The principle of the IS method.-The IS method is applied to adsorbate-adsorbent systems exhibiting Type C deviations in the Marsh-Rand classification, which means that both mesopores and micropores are present. The method is based on the following assumptions. At low relative pressure adsorption in micropores is dominant because of their high potential energy, and adsorption on the non-microporous surface can be neglected. Thus the linear low pressure region of the DR plot (bc in Figure 12.6) is attributed to micropore filling and extrapolation (bd in Figure 12.6) will give the microporous contribution to adsorption at high relative pressure. This is then subtracted from the total isotherm at high relative pressure (ab in Figure 12.6) to leave the residual, non-microporous isotherm. This isotherm can then be analysed using the BET method to evaluate the non-microporous surface area, S' ($m^2/g$) and the residual BET constant, C', appropriate to the non-microporous surface. This method has proved successful in analysing carbons and chars containing micropores and mesopores and it compares favourably with other methods for separating adsorption in different pores [272, 273].

12.2.2 Calibration using NPL reference material

Calibration of the apparatus and technique was carried out using Vulcan 3-G, a non-porous graphitised carbon black. It was also used to check the molecular cross-sectional areas of the adsorptives. Vulcan 3-G is an ideal choice, since it is a NPL standard reference material which means that it is well characterised.

Adsorption isotherms obtained for Vulcan 3-G using argon at 77 K and carbon dioxide at 195 K are shown in Figure 12.7. The argon adsorption isotherm is of Type II in the BDDT classification, while the $CO_2$ isotherm is of Type III.

Application of the BET equation using a value of 0.15 $nm^2$ for the argon molecular cross-sectional area ($a_m$) gave a surface area from argon adsorption of 71.5 $m^2/g$, which is well within the NPL standard of 71.3 ± 2.7 $m^2/g$. A similar value of $a_m$ for argon has been reported by Smith and Ford [274], although values proposed in the literature range from 0.13 to 0.18 $nm^2$ [274-277]. This variation in the $a_m$ value for argon has been attributed, by some workers, to the ill-defined monolayer, *i.e.*, a low BET C value, and to the chemical nature of the adsorbent surface [278]. In the present work the BET C value for argon adsorption on Vulcan 3-G was 1550.

When the BET equation was applied to the $CO_2$ adsorption isotherm, measured at 195 K, for Vulcan 3-G using an $a_m$ value of 0.208 $nm^2$, it gave a surface area of 74 $m^2/g$ which is also within one standard deviation of the NPL mean value of the surface area of Vulcan 3-G. This is a good indication that the chosen value of $a_m$ for $CO_2$ is acceptable. A low BET C value of about 8 was found for $CO_2$ adsorption on Vulcan 3-G at 195 K.

Harris and Sing [279] have found that the variation in $a_m$ values and also the choice of effective saturation pressure, $P_0$, of the adsorptive is dependent upon the porosity of the adsorbent. When dealing with porous adsorbents, as is the case in the present work, they proposed that the value of $P_0$ corresponding to the supercooled liquid should be used. Hence the following values for $P_0$ were used: 217 Torr for Ar at 77 K, 1413.6 Torr for $CO_2$ at 195 K and 26142 Torr for $CO_2$ at 273 K. Adsorption isotherms obtained using these three adsorptive systems are presented and discussed in the following three sections.

12.2.3 Argon adsorption at 77 K

Argon adsorption isotherms on the model char and the coal char were measured at 77 K. At this temperature the effective saturation vapour pressure of argon in the supercooled liquid state is 217 Torr [280]. The density of liquid argon calculated from extrapolation to 77 K is 1.4567 g/ml [281].

Adsorption isotherms of argon on activated series of the model char and the coal char (prepared by gasification in $H_2O/H_2$ at 960 °C and 1 atmosphere) are shown in Figures 12.8 and 12.9 respectively. Due to the well-known effects of activated diffusion of argon at 77 K in coals and chars [268, 272, 273, 282-284], a standard pseudo-equilibration time of 2 hours per point was used to determine each isotherm. All argon isotherms are of Type II in the BDDT classification, suggesting that both chars are not purely microporous in nature but possess a significant amount of mesoporosity and macroporosity. It is apparent from Figures 12.8 and 12.9 that the adsorption capacity of both chars increases with progressive gasification and reaches a maximum value at 70-80% burn-off.

BET plots are linear over the relative pressure range from 0.005 to 0.15. The BET surface areas (strictly monolayer equivalent areas, see Section 12.2.1) and values of the BET constant at different conversion levels for both chars are given in Tables 12.2 and 12.3. The surface areas given are expressed in $m^2/g$ (daf) and are not corrected for the surface area of ash present in the chars. Both chars exhibit an increase in surface area with progressive gasification. This is presumably due to the breakdown of the molecular sieve structure of the chars, *i.e.*, opening up of existing microcapillaries and development of new pore interconnections. Confirmation of this concept has been provided by Walker *et al.* [285] and Berger *et al.* [286].

Typical DR plots for the two chars at different burn-off levels are shown in Figures 12.10 and 12.11. At low burn-off, for both chars, there is a downward deviation from linearity at low relative pressures [high $\log^2 (P_0/P)$]. This is type A deviation in the Marsh-Rand classification [265, 266] of non-linear DR plots (Section 12.2.1.4) and indicates the presence of activated diffusion effects in these samples [267, 268]. The deviations from linearity become less severe with increasing burn-off, indicating that activated diffusion effects are diminishing as gasification proceeds. Above a burn-off level of about 20% in both chars there is no apparent deviation from linearity. At a burn-off level of greater than 20% the pore structure has been sufficiently opened so that activated diffusion effects are no longer a problem.

At high relative pressure [low $\log^2 (P_0/P)$] there is an upward deviation from linearity of the DR plot close to the ordinate (Type C in the Marsh-Rand classification). This effect is apparent for both chars at all burn-off levels, but appears to be more significant in the

coal char. This suggests that both chars are not wholly microporous, but possess a certain amount of mesoporosity. The magnitude of the upward deviation tends to suggest that the coal char contains more mesoporosity than the model char and, indeed, this is confirmed by application of the Isotherm Subtraction method (see Section 12.2.4). Thus the shapes of the DR isotherms indicate qualitatively the presence of a wide range of pore sizes.

The micropore volume, $V_0$, determined by extrapolation of the upper part of the DR plot to $\log^2 (P_0/P) = 0$, and the DR constant D (the slope of the linear portion) are shown in Taboes 12.2 and 12.3 for the two chars over a range of burn-off levels. Micropore volume increases with burn-off reaching a maximum value between 70 and 80% burn-off. Thus micropore volume varies in a similar manner to the surface area. D values increase with $V_0$ reaching a maximum at about 80% burn-off. This type of correlation is often found for activated series. A low D value is associated with a steeper rise of the isotherm at low relative pressures, which indicates smaller pore sizes [51] and an increase in the range of pore sizes. The increasing values of D with burn-off are therefore associated with the removal of fine micropores and the development of a more mesoporous structure. The increase in D corresponds to a decrease in the characteristic free energy ($E_0$) of the system which implies an increase in pore size [287].

12.2.4 Application of the isotherm subtraction method to argon isotherms

The above results indicate that both the model char and the coal char contain significant amounts of micropores and mesopores. In an attempt to separate adsorption in micropores and non-micropores, the

Isotherm Subtraction method was employed. The principle of this method has been previously outlined in Section 12,2.1.5.1.

The IS method was applied to the argon adsorption results for activated series of both chars. Typical examples of the resultant non-microporous (residual) isotherms are shown in Figure 12,12, compared with the whole adsorption isotherm for each char sample. In Figure 12.12 curve A represents argon adsorption on the total surface and curve B is the non-microporous isotherm ersulting from the application of the IS method. In all cases, both isotherms were parallel at high relative pressure, which indicates complete removal of the microporous adsorption contribution. Parameters obtained using the IS method are shown in Tables 12.2 and 12.3. The linear range of the BET equation for the residual isotherms was from $P/P_0$ = 0.23 to 0.4 because of the distorting effects of the subtraction procedure at $P/P_0 \lesssim 0.2$; similar results were reported by Kraehenbuehl. The BET constant C', for the non-microporous surface, was always lower than that for the total isotherm, C, due to the removal of the high energy contributions to C from adsorption in micropores.

It is assumed, for the total isotherm, that micropore filling is complete at some arbitrary, high relative pressure. Micropore volumes may then be estimated from the vertical separation of the total and residual isotherms at that relative pressure. In this investigation micropore volumes were estimated by subtracting curve B from curve A in the parallel region at about $P/P_0$ = 0.7. Micropore volumes obtained using the IS method are compared with the DR values in Table 12.4. These values are in good agreement (±0.01 ml/g), which is to be expected, since the DR isotherm extrapolates towards the micropore volume at high relative pressures.

The proportion of non-microporous surface area present in the two chars (S'/S) at different burn-off levels is given in Tables 12.2 and 12.3. This proportion increases with burn-off reaching a maximum value at 50-60% burn-off for both chars. It is also apparent from these results that the coal char contains more non-microporous surface area than the model char. These effects were observed qualitatively using mercury porosimetry (Section 12.1.4).

12.2.5 Carbon dioxide adsorption at 195 K

$CO_2$ adsorptkon isotherms on the PVDC char and the Markham Main coal char were measured at 195 K in an attempt to eliminate activated diffusion effects which were particularly evident when using argon at 77 K. The density of the supercooled liquid at 195 K is 1,23 g/ml [286], and the saturated vapour pressure, $P_0$, is 1413.6 Torr [289].

The $CO_2$ adsorption isotherms at 195 K for activated series of both chars are shown in Figures 12,13 and 12.14. It is difficult to classify the type of these isotherms according to the BDDT classification because the experimental data of these isotherms does not extend to $P/P_0 = 1$. BET plots are linear in the relative pressure range from 0.001 to 0.10 and parameters obtained by applying the BET equation to $CO_2$ isotherms for the two chars are given in Tables 12,5 and 12.6. Surface area increases with burn-off for both chars and, as with argon adsorption, reaches a maximum value at high burn-off (approximately 80%). The surface area values obtained from $CO_2$ adsorption at 195 K are higher than those obtained from argon adsorption at 77 K over the complete burn-off range. The difference is most marked at low burn-off (< 20%) due to the inability of argon to penetrate fine micropores which are present in this range, The BET C values obtained from $CO_2$ adsorption are lower than those obtained from argon adsorption.

Typical DR plots for both chars at different levels of activation are shown in Figures 12.15 and 12.16. It is apparent from these plots that there is little or no downward deviation at low relative pressures for all burn-off levels. This indicates that, in contrast to argon adsorption, activated diffusion effects are not prevalent, even at low burn-off. All DR isotherms, however, exhibit an upward deviation at high relative pressure (Type C deviation in the Marsh-Rand classification), suggesting the presence of mesoporosity. Values of micropore volume, $V_0$, and DR constant, D, are given in Tables 12.5 and 12.6. These results show that both $V_0$ and D vary with burn-off in a similar fashion to the surface area. Micropore volumes measured by $CO_2$ adsorption, as with the surface area, are higher than those measured by argon adsorption for all levels of activation in both chars. It can be concluded from this that argon at 77 K is excluded from a significant portion of the microporous structure, *i.e.*, fine micropores, whereas $CO_2$ at a higher temperature is not. This means that both chars must contain narrow micropores at low burn-offs, which are not penetrated by argon at 77 K, while $CO_2$ at 195 K has sufficient kinetic energy to penetrate all pores.

### 12.2.6 Carbon dioxide adsorption at 273 K

It has been concluded by several workers [211, 283, 290, 291] that $CO_2$ at 195 K does not reach some of the surface area in coals. On the basis of unsteady state diffusion measurements they concluded that a substantial fraction of the pore volume in coals and chars should be available to $CO_2$ at 195 K, allowing an equilibration time of 30 minutew [292]. However, their results did suggest thst some of the surface area will not be reached under these conditions. Recognising the

importance of working at as high an adsorption temperature as possible, some workers have studied adsorption of $CO_2$, and other adsorptives, at 273 K [211-214, 293]. These considerations prompted an investigation using $CO_2$ adsorption at 273 K, in an attempt to analyse the complete micropore systems of the two chars used. The saturation vapour pressure, $P_0$, of $CO_2$ at 273 K is 26142 Torr and the $CO_2$ liquid density at 273 K is 1.023 g/ml.

$CO_2$ adsorption isotherms at 273 K for activated series of both chars are shown in Figures 12.17 and 12.18. As with $CO_2$ adsorption at 195 K, it is impossible to classify these isotherms according to the BDDT classification, since the experimental data at 273 K only extends to $P/P_0 = 0.03$. The only way to overcome this problem is to use a high pressure adsorption rig which would extend the relative pressure range considerably. As expected from previous results, the adsorption capacity increases up to burn-off levels of about 80%.

To use the BET equation to calculate surface areas accurately from adsorption isotherms, it is necessary to measure adsorption up to a relative pressure of about 0.2. This condition was impossible to obtain using the gravimetric adsorption balance, since it operates at a maximum pressure of one atmosphere. Therefore, application of the BET equation to $CO_2$ isotherms measured at 273 K was not considered to be meaningful. The Langmuir equation may provide a better alternative for calculation of surface area, but a direct comparison between these results and the BET results in previous sections could not be made.

The preceding discussion indicates that a more realistic comparison between Ar at 77 K, $CO_2$ at 195 K and $CO_2$ at 273 K could be made using the DR approach, *i.e.*, comparing micropore volumes instead of surface areas. Typical DR plots derived from $CO_2$ adsorption at 273 K for the

two chars at different levels of activation are shown in Figures 12.19 and 12.20. As with $CO_2$ at 195 K, there is no downward deviation at low relative pressure because activated diffusion is not encountered at 273 K. At high relative pressure there is no significant upward deviation from linearity. This situation arises as a result of the restricted relative pressure range using $CO_2$ at 273 K, which means that adsorption on the mesopore surface is not significant. Under these conditions microporous adsorption dominates. $V_0$ and D values obtained from $CO_2$ adsorption results at 273 K are shown in Tables 12.7 and 12.8 for the two chars. The trends are similar to those observed for previous adsorptives, but micropore volumes are higher than those previously obtained, indicating that higher adsorption temperatures allow penetration of more of the microporous surface,

12.2.7 General comments

The adsorption results presented in previous sections all indicate that the PVDC char has a more highly developed microporous structure than the Markham Main coal char. High values of surface area, micropore volume and BET constant all imply a well developed micropore structure and this is characteristic of model chars and carbons of the sort used in this study. The way in which the pore structure affects the reactivity of the chars is discussed in Chapter Fifteen.

This chapter has shown that steam gasification of both chars induces a dramatic development of the pore structure. Detailed surface area changes during gas-char reactions were first studied by Walker *et al.* [285]. They suggested that the increase in total surface area (TSA) of chars with burn-off is a result of the breakdown

of the molecular sieve structure. They found that, despite the extensive feeder pore systems in the chars used, the results clearly demonstrated the degeneration of the molecular sieve effect during gasification. Similar results have also been obtained by Johnson [294] and Tomkow *et al.* [295]. These workers noted that complete accessibility to the highly developed micropore surface was achieved at about 70% burn-off. Above this level surface area decreases due to pore wall destruction and merging. The rate of surface area decrease depends, of course, on the competition between area formation and destruction. Surface area trends in this investigation are in reasonable agreement with those found by other workers [286].

Adsorption and porosimetry indicate that both chars contain significant amounts of microporosity and macroporosity; the coal char possesses a more highly developed mesopore structure. The chars therefore contain good feeder pore systems for diffusion of reactant gases during gasification. It must be noted, though, that most of the surface area in the chars, and therefore most of the reactive sites, are contained in the micropores.

# CHAPTER THIRTEEN

# DETERMINATION OF ACTIVE SURFACE AREA USING A TEMPERATURE-PROGRAMMED DESORPTION TECHNIQUE

## 13.1 Validation of the Dynamic Technique

### 13.1.1 Comparison with the volumetric technique

Although the dynamic TPD technique described in Chapter Eight appears satisfactory from a theoretical viewpoint, it was decided that an experimental validation was also required. This was carried out using two samples of coal chars obtained from a North Dakota lignite (PSOC-246) which were studied by Radovic *et al.* [296] using the standard volumetric technique of Laine *et al.* [182]. These chars had been devolatilised in nitrogen by slow pyrolysis (10 K/min) with residence times of one hour at the final temperatures of 975 K and 1475 K.

Table 13.1 compares ASA values for the two lignite coal chars obtained using the dynamic TPD technique described in Chapter Eight with values obtained by Radovic *et al.* [296] using the volumetric technique; agreement between the two methods is excellent. The TPD curves for the two lignite chars, from which the ASA values were derived, are shown in Figure 13.1.

### 13.1.2 Influence of chemisorption conditions

In an attempt to optimise process conditions and hence to improve the accuracy and reliability of ASA data, the effects of varying a number of the experimental parameters of the TPD technique were briefly investigated. Variation of the oxyten pressure in the range 10 to

760 Torr at 423 K did not affect the value of ASA for unactivated Markham Main coal char (Table 13.2). This suggests that the surface of the carbon is saturated with oxygen in this pressure range in the time allowed (12 hours).

The influence of temperature of chemisorption, in the range 300-530 K, upon the ASA of the unactivated Markham Main coal char was investigated; the results are shown in Figure 13.2. The value of ASA is constant in the range 373 to 523 K and decreases at low temperatures. At temperatures above 523 K oxygen chemisorption was accompanied by evolution of CO and $CO_2$, indicating that gasification was occurring. The decrease in ASA at low temperatures indicates that an equilibrium uptake of oxygen was not achieved in the time allowed (12 hours). At these lower temperatures (< 373 K) an increase in the residence time of the oxygen on the surface should result in an increase in ASA value up to that obtained at higher temperatures. As a result of this study, a chemisorption temperature of 423 K was chosen in the standard procedure.

### 13.1.3 Secondary reactions

A brief investigation was carried out to assess the effect of chemisorption-desorption cycling on the ASA of the unactivated Markham Main coal char. It was found that the ASA of the coal char increased slightly upon repeated oxygen chemsorption-TPD cycles (Table 13.3). The slight increase in ASA may be associated with the small extent of gasification (equivalent to 1-2% burn-off) which occurs upon desorption of surface oxides. The development of ASA on repeated cycling agrees well with the increase in ASA as a function of burn-off on gasification

with $H_2O/H_2$ (Section 13.2). This study shows that although a small amount of activation of the sample occurs during the cycle, it cannot be regarded as significant enough to affect ASA values to any great extent. Thus it is assumed that no weight loss occurs during the reaction.

It is usually assumed in determining ASA by desorption of CO and $CO_2$ that both gases are primary products of desorption and that secondary reactions make a negligible contribution [247]. This is a reasonable assumption in the present case, since product gases are removed immediately from the carbon surface, allowing little chance for secondary reactions to occur. It should be noted that if the reaction

$$CO_2 + C = 2CO$$

occurs, it will not affect the value of ASA, since the effect of the reaction is to redistribute the desorbed oxygen between CO and $CO_2$. The only difference which could be observed as a result of the reaction is a shift in the $CO/CO_2$ ratio for the complete temperature programmed desorption.

There is no evidence from the mass spectrometer for production of $H_2$, $H_2O$ or $CH_4$ during desorption, which indicates that the secondary reactions

$$CO + H_2O = CO_2 + H_2$$

and

$$C + 2H_2 = CH_4$$

are not significant.

There is evidence for production of oxygen in the very early stages of desorption ($T < 523$ K), but at higher temperatures the oxygen partial pressure falls to background levels. The presence of oxygen at low

temperatures may possibly be associated with decomposition of oxygen-rich surface complexes (*e.g.*, peroxides). At T > 523 K the secondary reactions

$$2CO + O_2 = 2CO_2$$

$$C + O_2 = CO_2$$

and

$$2C + O_2 = 2CO$$

are presumed to be insignificant.

13.2 Application to Activated Series of Chars

TPD curves for Markham Main and PVDC chars in the unactivated state, obtained using the standard procedure described in Chapter Eight, are shown in Figure 13.3. The surface oxygen complexes initially decomposed to carbon dioxide, with a peak occurring at about 570 K. Subsequently, desorption of $CO_2$ becomes less significant and CO is released in large quantities up to the final outgassing temperature of 1223 K. The desorption of CO was completed isothermally.

Previous studies of coal based carbons [298] and coal chars [296] have indicated similar desorption characteristics to those found here, *i.e.*, CO is rather more abundant than $CO_2$ during decomposition of surface oxides with CO release being favoured at high temperatures. The geometry of the TPD curves has previously been explained by assuming that CO is formed at carbon edges while $CO_2$ is formed at inorganic sites [2]. Low temperatures favour $CO_2$ desorption due to catalytic activity and higher temperatures promote utilisation of carbon edges. Thus the desorption behaviour is linked to the nature of the various active sites on the char surface, but it is difficult to explain the exact nature of these sites.

The ratio of the total amount of CO to the total amount of $CO_2$ ($[CO]/[CO_2]$) desorbed seems to support the previous explanation, since the ratio for the unactivated coal char is lower than that for the unactivated model char (Table 13.4). This means that the coal char has a relative abundance of inorganic sites, which is to be expected. However, the $[CO]/[CO_2]$ ratio at higher burn-off levels appears to be higher for the model char than the coal char. This may be linked to a gradually diminishing number of inorganic sites and carbon edge sites dominating at high burn-off. The ratio also appears to be constant over most of the burn-off range. The reason for this is unknown; it can only be concluded that, although the amount of CO and $CO_2$ desorbed increases with progressive activation, gasification affects CO and $CO_2$ production equally. The absence of any variation in the ratio may indicate that the previous reasoning does not offer a satisfactory explanation of the behaviour. One cannot rule out the possibility that some of the carbon oxides evolved could result from a char-ash interaction rather than direct decomposition of surface complexes. The implications of this are discussed in Chapter Fifteen.

Coal chars are known to include sites as diverse as those bonded to heteroatoms (principally H), nascent sites (*i.e.*, sites created during pyrolysis and gasification), dangling carbon atoms (singly bonded), edge carbon atoms (doubly bonded), trigonally bonded basal carbon atoms and mineral matter [296]. Therefore it is not surprising that relatively high values of ASA are often found in coal chars (see below).

Much of the pioneering work [182, 297] on ASA was carried out using highly ordered crystalline materials such as Graphon, but the same principles can be applied to more heterogeneous materials such as coal chars. Active sites have been shown to be located at the edge of large graphite-like crystallites, through the interaction of carbon with gases. Unfortunately, it is practically impossible to

study carbon active sites directly and the electronic configurations of active sites are not well understood. Coulson [301] proposed three different electronic configurations for atoms located at the edtes of graphite planes, namely: (i) valence orbital occupied by one electron; (ii) partial triple bond by deformation of the structure and pairing of the electrons; (iii) σ electron pairs (reversion from $sp^3$ to $sp^2$ hybridisation).

The application of electron-spin resonance spectroscopy to study the nature of the so-called "broken bonds" in carbons, which result in unpaired free-radical electron spin centres, has been examined [302-304]. However, no well defined relationships between the reactivity of carbons and the number of unpaired electron sites, as determined by ESR work, have been found to exist. The problem of examining active sites in coal chars is even more difficult to overcome and it is almost impossible to identify the specific nature of the active sites. These problems are a direct result of the heterogeneous nature of coal chars with the possibility of several different types of active site existing.

Using the chemisorption of oxygen on Graphon at different temperatures several investigators [183, 305-309] have postulated the existence of different stages of adsorption. They concluded that there are several discrete types of active site available on the surface, indicated by discontinuities in the desorption curve. Although some discontinuities were observed during desorption from the chars in this work, these were irregular and irreproducible (these discontinuities are not shown on the desorption curves, Figure 13,3). This effect may be attributed to the greater heterogeneity and impurity content of coal chars compared with Graphon.

The ASA values for the Markham Main and PVDC chars as a function of burn-off are shown in Figure 13,4. TPD curves for activated samples were of the same form as those shown in Figure 13,3 for the unactivated chars and are therefore not shown here. The only obvious difference is the total amount of CO and $CO_2$ desorbed which increased with burn-off. Consequently the ASA of both chars increases with burn-off, reaching a maximum value at 70-80% conversion. It can be assumed, therefore, that maximum accessibility to the ASA is achieved at these levels of activation. Above these levels, a decrease in ASA is expected, since the complex pore structure of the char is gradually destroyed and the amount of accessible ASA, located mainly in micropores, decreases. The values of ASA for PVDC char are greater than for Markham Main coal char over the whole burn-off range. This probably reflects the greater degree of accessible microporosity in the PVDC char (see Section 12.2). ASA and TSA are compared in Chapter Fifteen and these parameters are discussed in terms of the reactivity of the coal chars to steam.

# CHAPTER FOURTEEN

# REACTIVITY STUDIES

## 14.1 Calculation of Gasification Rate

Calculation of the gasification rate from the fixed-bed reactor system was carried out as follows. The true partial pressures of CO (x Torr) and Ar (y Torr) were determined from the mass spectrum, taking into account factors such as relative sensitivity, which were previously discussed in Section 9.5. From design calculations (Section 9.2), the flow of Ar/1% $H_2$ (a ml/min) is 22.5 and the flow of Ar/20% $H_2O$ (b ml/min) is 22.9. Thus the total flow of Ar (c ml/min) into the reactor is given by:

$$c = 0.99a + 0.8b$$

The flow rate of CO in the product gas stream is therefore c.x/y (ml/min) and the gasification rate, R, in gC/gsec is given by:

$$R = \frac{cxM}{ywt}$$

where M is the molecular weight of carbon and w is the weight of the sample used in grams. The factor t combines the conversion factors required to convert the flow rate of CO in ml/min to a rate in gC/gsec, *i.e.*, 60 secs and 22.413 litres/mol.

A similar approach can be adopted to calculate R using hydrogen partial pressures. However, a brief preliminary study indicated that significant errors can be introduced if this is done. As a result of the small amount of hydrogen produced in the reaction and complications arising from the hydrogen partial pressure contribution in the

reactant gas, errors in R of up to 40% were observed. Errors of this sort were not produced using CO partial pressures; gasification rates were therefore calculated using CO partial pressures.

Values of R calculated in this manner were compared with those obtained gravimetrically (*i.e.*, by weighing the gasified residue) and good agreement (± 3%) was found between the two methods. This, however, was not the case when small particle sizes were used. The gravimetric determination was affected by particle blow out from the reactor, causing an increase in weight loss.

Calculation of the gasification rate for the TGA technique was carried out using a standard technique. The rate of gasification, R gC/gsec, was obtained using $R = (dw/dt)/w_0$ where dw/dt is the linear maximum rate of weight loss (gC/sec) and $w_0$ is the original weight of the coal char (g daf). The following section compares the results obtained using the two techniques discussed.

## 14.2 Conversion Characteristics

Figure 14.1 shows plots of percentage conversion against time for a range of gasification temperatures (900-1020 °C) obtained using the fixed-bed reactor system for (a) the PVDC char and (b) the Markham Main char. A $pH_2/pH_2O$ ratio of 0.25 and a particle size range of 500-600 μm were used in this investigation.

The rate of burn-off for each char increases with gasification temperature and is higher, at a given temperature, for the PVDC char. The shape of the curve is similar for all gasification temperatures ranging from 900 to 1020 °C. An approximately linear relationship exists between burn-off and time up to about 60% burn-off. Above this conversion level the measured rate decreases due to consumption

of the char. Thus these curves are not of the sigmoid shape normally associated with microporous carbons and chars [310, 311]. The absence of a slowly increasing burn-off rate at short times and low bunr-off can be attributed to the small amount of material lost during treatment prior to gasification with $H_2O/H_2$, *i.e.*, preheating in $Ar/H_2$. That is, the char structure has probably been opened to a small extent equivalent to a few percent burn-off. This is due to desorption of oxygen complexes present in the as-received samples. Thus the zero percent burn-off starting point is equivalent to a small degree of burn-off (2-3%) which effectively removes the initial part of the sigmoidal plot. Walker *et al.* have shown that the slopes of conversion-time plots for pure carbons are similar to those for coal chars, as is found in this work.

The corresponding curves of weight loss against time for the two chars obtained from the TGA system are shown in Figure 14.2. These plots are of a similar form to those obtained using the fixed-bed reactor (Figure 14.1). The fact that the results are comparable is perhaps not surprising in the case of the PVDC char, since it is relatively homogeneous and catalytic effects are not important. The good agreement between the two techniques for the coal char is more surprising, since TGA measurements are often severely affected by localised catalytic effects leading to anomalously high reaction rates. This effect results from the small sample size used in the TGA apparatus (*i.e.*, 25 mg maximum). The absence of this sampling effect is presumably due to careful preparation of the samples and a good dispersion of catalytically active species throughout the structure.

14.3 Activation Energies

Since an Arrhenius type temperature dependence is assumed, the activation energy, $E_A$ (kJ/mol), can be obtained using an Arrhenius rate equation of the form:

$$R_g = A_0 \exp(-E_A/RT)$$

where $R_g$ is the maximum reaction rate obtained from the burn-off *versus* time plots in Figures 14.1 and 14.2. $A_0$ is the pre-exponential factor, R is the gas constant and T is the absolute temperature. Plotting log $R_g$ against 1/T enables determination of $E_A$ to be made. Arrhenius plots for the two chars derived from the FBR and TGA measurements are shown in Figure 14.3. The straight lines were obtained by a least-squares fit of the logarithm of $R_g$ with the inverse absolute temperature as the independent variable. $E_A$ and $A_0$ values obtained from Figure 14.3 are compared in Table 14.1. As expected from the similar forms of the burn-off *versus* time plots, activation energies calculated using data from the two different gasification systems are in good agreement.

The average $E_A$ value of 233 kJ/mol obtained for the PVDC char is comparable to literature values for the char-steam reaction [2, 86]. A much lower average $E_A$ value of 129 kJ/mol is found for the Markham Main coal char. This value is lower than values reported for the 'un-catalysed' carbon-steam reaction [86]. This can be attributed to the catalytic effect on the rate of mineral matter constituents of the char [187, 312]. It has been shown in the past that demineralisation of a char of this sort leads to an increase in activation energy [313, 314]. A similar variation in pre-exponential factor, $A_0$ is also found (Table 14.1). Although a difference exists between the calculated

activation energies for the two chars, the values still lie in the range previously reported for the char-steam reaction (69-310 kJ/mol) [315]. Obviously this range of $E_A$ values is strongly dependent on factors such as reactivity of the fuel, postulated reaction order and diffusional limitations.

Based on the rectilinearity of the Arrhenius plots in Figure 14.3 and the large values of the apparent activation energies, it can be safely concluded that the reaction rate is controlled only by the chemical reactions at the char surface and that diffusional limitations are absent up to a reaction temperature of about 1000 °C. Theere is a deviation from linearity of all Arrhenius plots at temperatures above 1000 °C, incidating that the reactivity in steam of the chars is becoming at least partially diffusion controlled. The absence of diffusional limitations under the standard conditions (*i.e.*, temperature of 960 °C, $pH_2/pH_2O$ ratio of 0.25 and particle size (range of 500-600 μm) is confirmed in Section 14.5, which shows that the reaction rate does not vary for a wide range of particle sizes.

## 14.4 Reactivity Plots

Using the maximum slopes taken from the burn-off *versus* time plots (Figure 14.1) the specific reaction rates, in grams of carbon reacting per second-per gram of carbon remaining in the bed, were determined at each burn-off level studied. The results for the two chars are plotted in Figure 14.4. These reactivity plots were measured at a gasification temperature of 960 °C. This temperature was chosen because the reaction rate was of a sufficient magnitude to be measured accurately and no diffusional influences exist.

The results show that, when the reactivity is expressed on a weight basis (gc/gsec) the PVDC char is substantially more reactive than the Markham Main char. This can be attributed to the highly accessible microporous structure of the PVDC char which has been elucidated previously by means of porosimetry and adsorption experiments. Further discussion of this point will be made in Chapter Fifteen. Both chars exhibit a maximum in reactivity between 70 and 80% burn-off. The variation in reactivity shown here is similar to the variation in ASA and TSA with burn-off. Possible correlations between these parameters are considered in Chapter Fifteen.

## 14.5 Effect of Particle Size on Reactivity

A brief investigation was conducted using the fixed-bed reactor to assess the effect of varying the char particle size on the gasification rate. The particle sizes examined ranged from 35 to 800 μm and the gasification temperature was 960 °C. The results, shown in Table 14.2 for the two chars, indicate that the reactivity is independent of particle size in the range studied. There does, however, appear to be a slight decrease in gasification rate for small particle sizes (< 100 μm) for both chars. Weighing of the gasified residue showed that this decrease in apparent gasification rate was due to removal of some of the fine particles in the gas stream. There is also a slight decrease in rate for the largest particle size range (700-800 μm), suggesting the presence of diffusional effects for large particle sizes, but this is difficult to predict unless larger particle sizes are analysed (> 800 μm). The particle size range used in all reactivity measurements (500-600 μm) does not suffer from any limitations of this sort and chemical rate control is assumed. The absence of diffusional

limitations is a good indication that the chars have an abundant supply of macropores acting as admittance pores and mesopores acting as feeder pores through which diffusion to the reacting micropores is relatively rapid. In the absence of mass transport limitations, other workers [315-319] have also found no dependency on particle size of the rate.

## 14.6 Effect of $pH_2/pH_2O$ ratio on Reactivity

The effect of varying the ratio of hydrogen partial pressure to steam partial pressure ($pH_2/pH_2O$) on the char-steam reaction was studied using the fixed-bed reactor described in Chapter Nine. A particle size range of 500-600 μm and a range of gasification temperatures from 900 to 1020 °C were used. Carbon monoxide and hydrogen were the only product gases observed over most of the $pH_2/pH_2O$ range; however, at high $pH_2/pH_2O$ ratios there was evidence for a small amount of methane.

Figure 14.5 shows the variation in gasification rate for the two chars with $pH_2/pH_2O$ ratio, over a range of gasification temperatures from 900 to 1020 °C. It is apparent from these plots that at all the gasification temperatures, an increase in hydrogen partial pressure results in a considerable decrease in gasification rate. This inhibiting effect of hydrogen is evident for both chars. It has been shown by a number of workers [2, 86, 229-233, 316, 320, 321] that hydrogen is a strong inhibitor of the uncatalysed char-steam reaction. It is generally agreed that this inhibition is caused by the strong dissociative chemisorption of hydrogen onto active carbon sites, thus blocking them for the oxygen transfer reaction with steam. The inhibition of the 'uncatalysed' carbon-steam reaction by hydrogen is also consistent with the finding that the rate of carbon gasification in hydrogen is about three orders of magnitude slower than the rate

of gasification by steam [86].

In contrast, McKee [322] has shown that hydrogen can be an accelerator for the 'catalysed' carbon-steam reaction. Whether hydrogen acts as an accelerator or an inhibitor in the presence of potential catalytic impurities depends upon the chemical state(s) in which the particular impurities are active catalysts. For example, iron, cobalt and nickel are active catalysts for the carbon-steam reaction when in the reduced state [187, 322]. On the other hand, impurities like vanadium, potassium and sodium are active catalysts in an oxidised state [187]. It can be concluded from the results obtained in this study that any potentially catalytically-active species in the chars, which are otherwise inactive, are not rendered active by increasing the hydrogen partial pressure. Thus the main role of hydrogen during steam gasification of both chars is expected to be that of blocking a fraction of the active carbon sites. The variation of activation energy and pre-exponential factor with $pH_2/pH_2O$ ratio, shown in Table 14.3 for both chars also emphasises the strong inhibiting effect of hydrogen on steam gasification of the chars. This effect has been observed by previous workers [316].

## 14.7 Normalisation of Reactivity Data

It has been noticed in the past that the shapes of burn-off *versus* time plots for various chars reacted in different gases are quite similar. Reactivity has been shown [2] to vary considerably with rank of the parent coal and gasification atmosphere and pressure, but it appears to be constant over a certain burn-off range. Indeed, the complete burn-off *versus* time plots for different coals and chars have been shown to be similar. This was shown to be the case by Walker *et al.* [311], who found it was possible to normalise all reactivity

plots using an adjustable time parameter, which can conveniently be used as a measure of differences in reactivity for a wide spectrum of chars.

Following the method of Walker *et al.* [311] all the reactivity plots in Figure 14.1 for both chars can be well normalised using a dimensionless time scale such that $t/t_{0.5}$ equals one at a fractional burn-off of 0.5. Values of $t_{0.5}$, or the times to reach a fractional burn-off of 0.5, decrease with temperature in the range studied for both chars. Specific values are given in Table 14.4. The normalised plot (Figure 14.6) is more or less typical of the shape of the burn-off *versus* time plots found for both chars at all gasification temperatures. That is, there is a maximum in slope of the plot at short times, which persists up to about 60% burn-off. This is followed by a region of decreasing slope as the fractional burn-off approaches one. The fact that the reactivity data for the two chars can be normalised on one plot is a good indication that the development of the active and total surface area is similar for both chars. The factors which determine reactivity are discussed further in Chapter Fifteen.

# CHAPTER FIFTEEN

## GENERAL DISCUSSION

Gasification rates are controlled by three prime factors, namely (i) the concentration of active sites; (ii) diffusional limitations or the extent to which ASA located in micropores is accessible to reactant molecules; and (iii) the amount, chemical form, particle size and degree of dispersion of catalytic inorganic impurities [86, 187]. These three factors governing gasification rates undergo complex, dynamic changes during gasification and it is these changes which ultimately affect the shape of burn-off plots [323].

Due to the complexity of the nature of char gasification reactions it is difficult to offer a quantitative explanation for the 'characteristic' shape of the reactivity plots. However, a qualitative explanation, based on what is known about the development of porosity and surface area in the chars during gasification, is possible. With the onset of gasification two important phenomena occur: (1) enlarging of pores that were open in the unreacted char and (2) opening up of closed pores. Since the total number of pores is increased as well as their average radius, specific pore volume and specific surface area increase with carbon burn-off. Activated chars possess a tridisperse pore structure with a well developed feeder pore network and the accessibility to reactant gases of the internal micropore volume (which is where most of the reactive surface is located) is high. This is confirmed through porosimetry and adsorption measurements. At some point, (70-80% burn-off for the chars used here), walls between existing pores are gasified away and the total number of open pores available for reaction begins to decrease. This leads to the total surface area and, indeed, the active

surface area ultimately going through a maximum as burn-off proceeds. On this basis it is expected that similar trends should exist for reactivity, TSA and ASA, as is the case in the present work (see below).

The TSA, as measured by adsorption of argon and $CO_2$, and the ASA, as measured by oxygen chemisorption experiments, are compared in Figure 15.1 for the two chars as a function of burn-off. Both TSA and ASA increase progressively with burn-off, reaching a maximum at 70-80% burn-off. It would seem from these results that the accessible ASA is linked with the TSA available during gasification. Examination of the ASA/TSA ratios for the two chars as a function of burn-off (Figure 15.2) confirms this. If the TSA is measured by argon adsorption the ASA/TSA ratio decreases sharply in the early stages of burn-off (< 20%) and then remains constant for a wide range of burn-off. Other workers [324] have also found an initial decrease in the ASA/TSA ratio for graphitised carbon blacks, but this was, in some cases, followed by an increase. ASA/TSA ratios measured for Graphon (0.03-0.04) are much lower than those obtained in the present work, although some workers found that the ASA/TSA ratio for Graphon increased to about 0.15 at high burn-off [182, 325]. The higher values for coal chars reflect the much greater heterogeneity and degree of structural disorder compared with graphitised carbon blacks.

The initial decrease in ASA/TSA ratio for the two chars (Figure 15.2), using argon adsorption to measure TSA, is the result of activated diffusion in narrow micropores, resulting in anomalously low TSA values.

This is confirmed by examination of the isotherms for the two chars at low levels of activation (< 20% burn-off) plotted in D-R co-ordinates (Figures 12.10 and 12.11). The low burn-off samples exhibit a marked downward deviation at low relative pressures, the magnitude of which decreases with progressive gasification, until no deviation is observed above 20% burn-off. This indicates the presence of activated diffusion effects at low degrees of activation. Values of ASA/TSA ratio obtained using $CO_2$ adsorption at 195 K to determine TSA (Figure 15.2) are almost constant over the whole burn-off range. This supports the theory that $CO_2$ adsorption at 195 K does not suffer from activated diffusion effects. In this instance ASA appears to be quite a good function of TSA and the two parameters seem to correlate well. This then reinforces the conclusion that the development of an accessible porous structure is closely related to the availability of ASA, and hence the reactivity, during the gasification process.

Although the values of TSA reported in this thesis appear to give a good indication of the reactivity behaviour of the chars, it must be noted that the surface area of microporous adsorbents is difficult, if not impossible to measure accurately. In this context, it may be advantageous to use micropore volume (determined using the DR equation) when attempting to predict the gasification behaviour of chars using textural measurements.

Variations in reactivity of chars have previously been ascribed to the fact that different samples have, initially, different amounts of ASA, which change to different extents with burn-off [296, 326]. It is therefore reasonable to suggest that the large spread in reported experimental values of reactivities of different carbons and chars,

under presumably identical reaction conditions, is due, at least in part, to the different amounts of ASA in carbons having the same TSA. Table 15.1 compares the reactivities of the two chars used in this work, expressed per square metre of TSA (measured by Ar and $CO_2$ adsorption) with those expressed per square metre of ASA. It is apparent from the values obtained that ASA is a good reactivity normalisation parameter. TSA measured by argon adsorption suffers from activated diffusion effects and the resultant values of reactivity per square metre of TSA are therefore significantly affected at low burn-off. TSA measured by $CO_2$ adsorption provides a better measure of the reactivity, since it explores more of the reactive micropore structure than argon adsorption, for reasons previously discussed.

The fact that ASA is a good index of reactivity has been found previously by other workers [85, 182, 297]; however, some workers have concluded that TSA cannot be used in this manner [196]. It was emphasised by Laine *et al.* [182] that a fundamental rate constant for the carbon-oxygen reaction (and, indeed, for char reactions in general) cannot be obtained on the basis of the TSA of the carbon. A fundamental rate constant should, of course, depend only on reaction temperature and not on the extent of reaction or the type of carbon used. Laine *et al.* [182] showed that, for a graphitised carbon black, the rate "constant" based on the TSA increased continuously with conversion. However, when the rate constant was expressed per unit ASA, taking into account the formation of a stable carbon-oxygen complex, it was essentially constant over the range studied. Radovic *et al.* [196] have also found that TSA is incapable of predicting reactivity behaviour. They observed an increase in reactivity with decreasing TSA, but were able to correlate reactivity behaviour with ASA values.

The current investigation has shown, in agreement with previous workers, that ASA can be used in this way. However, the results obtained here suggest that if the TSA can be determined reasonably accurately, the parameter can provide a good prediction of reactivity behaviour. Reactivity has been found to be proportional to TSA by some workers [328]. Otto and Shelef [329] explored the relative effect of TSA by gasifying various heat treated chars in steam at 800-900 °C. The authors showed that differences in TSA accounted for most of the variation in reactivity. Thus one cannot rule out either ASA or TSA when predicting gasification phenomena, since the former is undoubtedly linked to the latter. As previously stated, this may not be the case for relatively pure carbons; problems can arise because they possess a low concentration of active sites and most of the TSA is unreactive. The comparatively heterogeneous nature of coal chars suggests this would not be the case.

An important point to note from Table 15.1 is that when the reactivity is expressed on an ASA basis, the Markham Main coal char appears to be more reactive than the PVDC char over the whole burn-off range. This is in complete contrast to the results expressed on a weight basis (gC/g sec) which showed that the PVDC char was the more reactive of the two. This behaviour is presumably linked to the enhanced activity of specific sites by inorganic impurities acting as catalytic species. This is obviously a result of the relatively high ash content of the coal char. These results suggest that, although TSA measured by $CO_2$ adsorption appears to be a good index of gasification reactivity, it is not capable of detecting possible catalytic effects on the gasification rate. Thus, as previously expected, gasification reactivity can be

said to be more a function of ASA than TSA.

It must be stressed that it is the sites that are both active and available which are important when assessing gasification reactivity. Very active sites may be unavailable for reaction because of the formation of a stable carbon-oxygen complex. Sites of lower activity have difficulty in forming the carbon-oxygen reaction intermediate. It is therefore a possibility that ASA measured by oxygen chemisorption may not be an absolute measure of the number of active sites in the char. The method does, however, give a good indication of the relative concentration of carbon active sites in chars and carbons, and certainly provides a good index of gasification reactivity. Although this is the case, the question must be asked that if the ASA is affected by catalytic impurities, why does the reactivity remain constant over the whole burn-off range? A further course of work is required before this can be answered (see Chapter Sixteen).

# CHAPTER SIXTEEN

## SUMMARY, CONCLUSIONS AND SUGGESTIONS FOR FURTHER WORK

A detailed study of the changes in porous texture during steam gasification of a char derived from a highly volatile bituminous coal (Markham Main) and a model char derived from a PVDC/PAN copolymer was undertaken. The PVDC based char was used as a reproducible, catalytically inactive model for studying "uncatalysed" char gasification, in comparison with the probable "catalysed" reaction of the coal char. Chemical analyses revealed that the coal char contained ten times more ash than the model char and would therefore be expected to exhibit more catalytic activity. The value of 0.6% ash for the model char was thought to be rather high. The ash was thought to be in the form of well dispersed particles in both chars.

Since the carbonisation conditions ultimately affect char properties, a brief investigation was conducted to assess the thermal degradation characteristics of the PVDC/PAN copolymer. Thermogravimetric analysis reveals that the copolymer decomposes in two main stages: one rapid weight loss stage corresponding to loss of one HCl molecule and a relatively slow weight loss stage corresponding to loss of the second HCl molecule in the structure. The presence of 20% polyacrylonitrile, although it affected the carbon yield, did not affect the form of the weight loss curve, expected from the literature, for pure PVDC. The rate of decomposition of the copolymer was shown to increase with heating rate, but the final carbon yield was unaffected.

Dilatometric analysis of the thermal degradation of the copolymer revealed behaviour not dissimlar to that observed for coals, except that the magnitude of the dilatation and the temperature required are markedly

lower for the copolymer. A rapid swelling range was observed which corresponds with the rapid evolution of the first HCl molecule, seen previously in TGA experiments. The expansion/contraction behaviour of the copolymer was significantly affected by heating rate. Slow heating rates (< 2 °C/min) caused the polymer to pass through its range of maximum fluidity relatively slowly and, after the initial rapid expansion, the structure collapsed. This was not the case at high heating rates (> 5 °C/min) where the structure resolidified rapidly such that no shrinkage was observed. One can conclude from this study that rapid expansion and subsequent resolidification causes an increase in dilatation with heating rate and a resultant well developed macropore system. To simulate the pyrolysis conditions of the coal char (prepared at BGC) the copolymer was pyrolysed using a heating rate of 5 °C/min and a carbonisation temperature of 1000 °C.

In an attempt to assess the effect of steam gasification on the porous texture of the chars, helium pycnometry, mercury porosimetry and gas adsorption measurements were carried out on activated series of the two chars. The porosity of a particle is calculated by knowing the true (helium) and apparent (mercury) densities of the particle. Unfortunately, a meaningful interpretation of the results is impossible, due to the difficulty in measuring accurately the aforementioned densities. Cumulative pore volume and pore size distribution (in the mesopore-macropore range) were determined ny mercury porosimetry. Results indicate that macropore volume increases with burn-off for both chars as a result of the general opening up of the pore structure during gasification. Macropore volume in the model char was higher than that in the coal char, presumably because the 'severe' pyrolysis conditions

affected the polymer to a greater extent, causing a relatively large amount of swelling and highly developed macroporosity. The coal char exhibited a bi-model pore size distribution (as determined by mercury porosimetry) with a fairly uniformly developed mesoporous structure. From a qualitative standpoint, mesoporosity appears to reach a maximum at about 60% burn-off. Similar behaviour was observed for the model char, except that there was no evidence for a separate mesopore range in the unactivated char (*i.e.*, uni-model). However, a small amount of mesoporosity developed with increasing burn-off. One can conclude from this investigation that both chars have well developed feeder pore systems for transportation of reactant gases to micropores during gasification.

Mesopores and macropores analysed by mercury porosimetry make a relatively small contribution to the total surface areas of the chars. Gas adsorption was used to assess the development of the micropore-mesopore range during gasification, which is where most of the surface area is situated. In an attempt to analyse as much of the pore structure as possible, three different adsorptive systems were used: Ar at 77 K; $CO_2$ at 195 K and $CO_2$ at 273 K. Application of the BET equation and the D-R equation to the isotherms obtained led to the determination of total surface areas and micropore volumes of the chars as a function of burn-off. BET surface areas (from $CO_2$ adsorption at 273 K) were not considered valid, due to the restricted relative pressure range. Adsorption results indicate that micropore volume and TSA increase with burn-off attaining a maximum value at 70-80% burn-off. The similarity in trends of the two parameters is a good indication that most of the surface area is contained in the micropore region. The increase in TSA with burn-off results from the breakdown of the molecular sieve structure

of the chars such that maximum accessibility to reactive sites in the micropores is achieved at 70-80& burn-off.

Results plotted in DR co-ordinates reveal that argon isotherms exhibit a downward deviation at low relative pressure (Type A deviation in the Marsh-Rand classification) indicating the presence of acrivated diffusion in fine micropores. This effect is, however, only apparent for chars with low degrees of activation (< 20% burn-off). At higher activation levels, isotherms are linear over a wide range of relative pressure and activated diffusion effects are not a problem. DR isotherms derived from $CO_2$ adsorption results are linear over the same relative pressure range suggesting that adsorption at higher temperaturew (195 K and 273 K) does not suffer from activated diffusion effects. Micropore volumes calculated from $CO_2$ isotherms measured at 195 K were higher than those calculated from argon adsorption, implying that argon perhaps does not reach the whole micropore system. Indeed, in agreement with previous studies on coal chars, $CO_2$ at 273 K gives higher micropore volumes than $CO_2$ at 195 K, indicating that all micropores are not penetrated at the lower temperature. All results (TSA, $V_0$ and C) show that the PVDC char has a more highly developed microporous structure than the Markham Main coal char over the whole burn-off range.

All DR isotherms which extended into the high relative pressure range exhibited distinct upward deviations (Type C deviation in the Marsh-Rand classification). This is an indication of the presence of mesoporosity in the structure. Application of the Isotherm Subtraction method to DR isotherms revealed that mesoporosity develops with progressive gasification, reaching a maximum at 50-60% burn-off for both chars, The mesoporous contribution to the TSA was higher in the coal char than in

the model char. These results confirm quantitatively what might have been expected qualitatively from mercury porosimetry.

Conclusions can be drawn from an investigation of this sort concerning the suitability of different adsorptives for characteristion of the pore structure of coal chars. Argon as an adsorptive has several advantages, such as the absence of polar interactions with the surface, it is possible to measure isotherms over the complete relative pressure range, and it allows easy separation of microporous and non-microporous adsorption. The only obvious disadvantage is that of activated diffusion. This problem can be alleviated if equilibration times are extended; however, the practical feasibility of this procedure is questionable. The advantage of using $CO_2$ as an adsorptive is that activated diffusion is less likely to happen. However, disadvantages such as possible polar interactions, limited relative pressure range of isotherms and difficult separation of microporous and non-microporous adsorption means that results cannot be considered as an accurate representation of the true pore structure.

The preceding discussion is a good indication that it is advisable to use different adsorptive systems to characterise char pore structure with any degree of certainty. It is obvious that various adsorptives explore different parts of the pore structure and the use of a single adsorptive system for characterisation purposes could produce a misleading picture of the pore structure.

Reactivities of the coal char and the model char were measured using a fixed-bed reactor and a thermogravimetric balance. Kinetic results are comparable to those obtained gravimetrically, indicating that sampling effects were not prominent. Conditions of reaction

were chosen so as to eliminate interparticle and intraparticle diffusional limitations. Gasification rates were shown to increase with gasification temperature for both chars. Activation energies of 233 kJ/mol and 129 kJ/mol for the model char and the coal char respectively were obtained. These values are within the range of values reported for the char-steam reaction; however, the lower activation energy for the coal char reflects possible catalytic influences on the rate of the relatively high ash content. Activation energy values combined with the linearity of Arrhenius plots are a good indication that the measured reactivities were intrinsic, chemically controlled rates. The PVDC was found to be more reactive than the Markham Main coal char when reactivity was expressed on a weight basis (gC/g sec). This is presumably linked to the highly developed, accessible microporosity in the PVDC char.

A brief parametric survey indicated the following:

(1) Gasification rate does not vary with particle size in the range 100-800 μm.

(2) Gasification rate increases linearly with bed height up to 40 mm in the fixed-bed reactor.

(3) Addition of hydrogen to the reactant $H_2O/H_2$ mixture has an inhibiting effect on the rate.

(4) All the reactivity data for the two chars can be normalised on a single plot using a dimensionless time scale.

The first two factors are a further indication that diffusional limitations are not evident under the chosen conditions,

The results and discussion presented in this study have shown that a fundamental understanding of char reactivity requires the application of the concept of active sites. Thus a dynamic oxygen chemisorption-temperature programmed desorption method for determining active surface area (ASA) of carbons has been developed, which utilises mass spectrometry as the analytical method. The decomposition of calcium oxalate is shown to be a useful reaction for calibrating the experimental system for quantitative determination of the desorption of surface complexes such as $CO_2$ and CO. However, any compound or compounds which decompose to give $CO_2$ and CO in known amounts can be used. The technique is validated by showing that ASA values for lignite chars, determined using the new method, are in good agreement with values determined independently using the standard volumetric technique. It is also shown that (i) under the experimental conditions chosen for chemisorption, the carbon surface is saturated with oxygen and gasification reactions do not occur; (ii) during desorption there is no evidence for a number of possible secondary reactions. Values of ASA as a function of burn-off during gasification with $H_2O/H_2$ gas are reported for the coal char and the model char. It is shown that ASA increases with burn-off for both chars, reaching a maximum at 70-80% burn-off. As might be expected from TSA and reactivity results, the model char has a higher ASA than the coal char over the whole burn-off range. It is also noticeable that the trends exhibited by ASA are similar to those observed for TSA and reactivity.

The ASA/TSA ratio (with TSA measured by argon adsorption) decreases rapidly in the initial stages of gasification and then remains constant over a wide range of burn-off. The high initial ASA/TSA ratio is attributed to anomalously low TSA values caused by activated diffusion of argon into narrow micropores. As expected from adsorption results, ASA/TSA ratios

remain relatively constant over the whole burn-off range if the TSA is measured by $CO_2$ adsorption at 195 K. It is therefore apparent that, if the TSA is measured in the absence of diffusion effects, the ASA appears to be a function of the TSA.

ASA is found to be a good index of the reactivity of the chars in steam. TSA (measured by $CO_2$ adsorption) also appears to be quite a good reactivity normalisation parameter. At first glance, this would appear to be a reasonable conclusion; However, if the reactivity is expressed per square metre of ASA, the fact that the reactivity of the coal char is higher due, perhaps, to some sort of catalytic effect, is emphasised, *i.e.*, the coal char is more reactive than the model char when reactivity is expressed per unit ASA. This phenomenon cannot be detected if TSA is employed as the normalisation parameter. It can therefore be concluded that the amount of accessible ASA is the most important factor to consider when assessing reactivity changes in coal chars. Predictions of gasification behaviour on the basis of development of porosity and TSA are less likely to be successful.

All the techniques used in this investigation were considered to be satisfactory with perhaps the exception of the pycnometric and porosimetric methods, which both suffer from severe limitations and inaccuracies (outlined in Chapter Twelve). An interesting and useful alternative to mercury porosimetry is automatic image analysis; however, further development of the technique is required to obtain reliable information on macropore size, distribution and shape for heterogeneous structures such as coal chars. A combination of results from the two techniques could provide a useful aid in characterising the macropore structure of carbons and chars.

The dynamic oxygen chemisorption-TPD technique developed during this project seems to give a good indication of the active surface areas of coal chars. The only obvious limitation of the method is the sample size used. Although sampling problems were not evident in this work, materials with a non-uniform distribution of impurities may suffer from sampling effects. This problem could be alleviated to a certain extent by modifying the system to accommodate larger sample sizes. Obviously, this would necessitate a recalibration of the system with calcium oxalate, but once this was complete, results should be more reliable.

Using the ASA technique, it could be possible to obtain active site distributions for carbons and chars and thus aid complete characterisation of these materials. This could be done by following variations in activity after the addition of known amounts of site blocking stable complex, thus providing a means for the construction of a site distribution curve. One may also be able to extract an activation energy for oxide desorption by measuring rhe rate of desorption as a function of heating rate (linear TPD) or by using a stepped-isothermal desorption method and monitoring desorption characteristics over a range of ascending isothermal steps. Work of this sort has been carried out previously on structurally well defined carbons [330-336]. It would be interesting to ascertain if a similar procedure could be applied to more heterogeneous materials.

There has been considerable interest recently in hydrogasification as a direct source of methane for SNG production. Thus it would be advantageous to conduct an investigation studying the correlation of the kinetics of hydrogasification with the development of pore structure and active surface area. A certain amount of caution should be exercised, however, concerning the applicability of oxygen chemisorption studies to hydrogasification.

A further useful extension to this project would be to assess the effect of deliberate catalyst additions on the active surface area and the reactivity of the two chars used. The behaviour of the coal char could be particularly interesting because of the possibility of catalyst-ash interactions. A study of various cheap and readily available catalysts (or mixtures of catalysts, *e.g.*, potassium sulphate/calcium hydroxide) [337] would be advantageous from an economic point of view in commercial systems.

It would be of interest to conduct a detailed parametric survey on the gasification behaviour of chars and carbons, including (i) the effect of heating rate during pyrolysis on the internal pore structure, active surface area, swelling behaviour and reactivity; (ii) the effect of demineralisation on the active surface area, pore structure and reactivity of the Markham Main char; (iii) the effect of coal rank on active surface area, *etc*.... One would expect very different behaviour on demineralisation of coals of different rank. A programme of work similar to that outlined above would provide a useful assessment, along with work on structurally well defined carbons, of the accuracy and reliability of the ASA technique when applied to a wide range of physically and chemically different materials.

The work described in this thesis serves to show that the heterogeneous nature of coal chars means that it is impossible to generalise reactivity phenomena. A good understanding of the complex physical and chemical structure of coals and chars is required before reactivity behaviour can be predicted with any degree of certainty.

REFERENCES

1. Tart, K.R. and Rampling, T.W.A., Proc. Coal-Chem. 2000 Conf. Inst. Chem. Eng., (1980), British Gas Report No. MRS E 376, (1980).
2. Laurendau, N.M., *Proc. Energy Combust. Sci.*, 4, 221-270, (1978).
3. Gibson, J., in "Coal and Modern Coal Processing - An Introduction", (Eds) Pitt, G.J. and Millward. G.R.), Academic Press, London, (1979).
4. A.S.T.M. Standard D 388-77.
5. A.S.T.M. Standard 3-3175-77.
6. Tsai, S.C., "Fundamentals of Coal Beneficiation and Utilisation", Elsevier, New York, (1982).
7. Thiessen, R., U.S. *Bureau of Mines Bulletin*, 117, (1920).
8. Van Krevelen, D.W., "Coal", Elsevier, New York, (1961).
9. McCartney, J.T., O'Donnell, H.J. and Ergun, S., *Fuel*, 50, 226, (1971).
10. Stopes, M.C., *Proc. Roy. Soc. (London)*, 908, 470, (1919).
11. Davidson, R.M., "Molecular Structure of Coal", I.E.A. Coal Research (London) Report No. ICTIS/TR 08, (1980).
12. Neavel, R.C., in "Coal Structure", *Adv. in Chem. Series*, 192, (Eds) Gørbaty, M.L. and Ouchi, K.), p.1, (1979).
13. Kessler, M.F., *Fuel*, 52, 191, (1973).
14. Tschamler, H. and De Rulter, E., *Adv. in Chem*, No.55, "Coal Science", pp.332-341, (1966).
15. Van Krevelen, D.W. and Schuyer, J., "Coal Science", Elsevier, Amsterdam, (1957).
16. Given, P.H., Peover, M.E. and Wyss, W.F., *Fuel*, 39, 323, (1960).
17. Karsten, G.J.A., *Arch. Berghau*, 12, 3, (1826).
18. Regnault, V., *Ann. mines*, 12, (3), 161, (1837).

19. Gruner, L., *Ann. Mines*, 4, (7), 169, (1874).

20. Fraser, P., *Trans. Am. Inst. Mining Met. Engnrs*, 6, 430, (1877).

21. Rogers, H.D., "A Description of the Coal Fields of North America and Great Britain", published in London and Philadelphia (1858).

22. Parr, S.W., *Bull. Univ. Illinois* No.180, 116, (1928).

23. Campbell, M.R., *Trans. Am. Inst. Mining Met. Engnrs*, 36, 324, (1906).

24. A.S.T.M. Standard D 720-57, British Standards No.1016.

25. Audibert, E., *Rev. Ind. minerale*, 6, 115, (1926).

26. Campredon, L., *Compt. rend.*, 121, 820, (1895).

27. Fuel Research Survey Paper No.44, (1940); No.58, (1946).

28. Seyler, C.A., *Proc. S. Wales Inst. Engnrs*, 21, 483, (1899); 22, 112, (1900); 47, 547, (1931); 53, 254, (1938).

29. Wender, I., Heredy, L.A., Neuworth, M.B. and Dryden, I.G.C., in "Chemistry of Coal Utilisation", 2nd Suppl. Vol., (Ed.) Elliott, M.A., Wiley, New York, Ch.8, (1981).

30. Whitehurst, D.D., in "Organic Chemistry of Coal", (Ed.) Larson, J.W., *A.C.S. Symp. Ser.*, 71, 115, (1979).

31. Tingey, G.L. and Morrey, S.R., "Coal Structure and Reactivity", Battelle Energy Program Report, (1973).

32. Mazundar, B.K., Granguly, S., Sangal, P.K. and Lahari, A., *Adv. in Chem. Ser.*, 55, 475, (1966).

33. Gaines, A.F., *Fuel*, 41, 112, (1962).

34. Yohe, G.R. and Harris, J.M., *Fuel*, 40, 289, (1961).

35. Hayatsu, R., Scott, R.G., Moore, L.P. and Studier, M.H., *Nature (London)*, 257, 378, (1975).

36. Roberto, R.G. and Cronauer, D.C., *A.C.S, Symp. Ser.*, 71, (Ed.) Larson, J.W., 210, (1979).

37. Abdel-Baset, M.B., Yarzab, R.F. and Given, P.H., *Fuel*, 57, 89, (1978).

38. Hirsch, P.B., *Proc. Roy. Soc.*, A226, 143, (1954).

39. Dubinin, M.M., *Zhur. Phys. Chem.*, 34, 959, (1960).

40. I.U.P.A.C., "Definitions, Terminology and Symbols in Colloid and Surface Chemistry", Part I of Appendix II, (Ed.) Everett, D.H., *Pure Appl. Chem.*, 31, 579, (1972).

41. I.U.P.A.C, "Terminology in Heterogeneous Catalysis", Part II of Appendix II, (Ed.) Burwell, R.L., Jr., *Pure Appl. Chem.*, 45, 71, (1976).

42. Harris, L.R. and Yust, C.S., *Fuel*, 55, 233, (1976).

43. Hirsch, P.B., *Trans. Roy. Soc.*, A232, 68, (1960).

44. Tomkow, K., Siemieniewska, T., Czechowski, F. and Jankowska, A., *Fuel*, 56, 121, (1977).

45. Thomas, J.M. and Thomas, W.J., "Introduction to the Principles of Heterogeneous Catalysis", Academic Press, London, (1967).

46. Gregg, S.J. and Sing, K.S.W., "Adsorption, Surface Area and Porosity", 1st Edition, Academic Press, New York, (1967).

47. Mahajan, O.P. and Walker, P.L., Jr., in "Analytical Methods for Coals and Coal Products", (Ed.) Karr, C., Vol.1, Academic Press, New York, p.125, (1967).

48. Gan, H., Nandi, S.P. and Walker, P.L., Jr., *Fuel*, 51, 272, (1972).

49. Franklin, R.E., *Trans. Faraday Soc.*, 45, 274, (1949).

50. Brunauer, S., Emmett, P.H. and Teller, E., *J. Amer. Chem, Soc.*, 60, 309, (1938).

51. Dubinin, M.M., in "Industrial Carbon and Grahite", *Soc. of Chem. Ind., London*, p.219, (1958).

52. Dubinin, M.M., Zaverina, E.D. and Radushkevich, L.V., *Zhur Fiz. Khim.*, 21, 1351, (1947).

53. Dubinin, M.M., *Chem. Rev.*, 60, 235, (1960).

54. Brunauer, S., in "Surface Area Determination", *Proc. of Int. Symp., Bristol*, (1969), Butterworths, London, p.63, (1970).

55. Dubinin, M.M., *Quart. Rev.*, 9, 101, (1955).

56. Nicholson, D. and Sing, K.S.W., in "Colloid Science", Vol.3, (Ed.) Everett, D.H., The Chemical Society, London, p.1, (1979).

57. Dubinin, M.M., in "Chemistry and Physics of Carbon", Vol.2, (Ed.) Walker, P.L., Jr., Marcell Dekker, New York, p.51, (1966).

58. Dubinin, M.M., in "Progress in Surface and Membrane Science", Vol.9, (Eds) Cadenhead, D.A., Danielli, J.F. and Rosenberg, M.D., Academic Press, New York, p.1, (1975).

59. Lamond, T.G. and Marsh, H., *Carbon*, 1, 281, (1964).

60. Lamond, T.G. and Marsh, H., *Carbon*, 1, 293, (1964).

61. Marsh, H. and Siemieniewska, T., *Fuel*, 44, 355, (1965).

62. Marsh, H. and Rand, B., *J. Colloid Interface Sci.*, 33, 101, (1970).

63. Walker, P.L., Jr., and Patel, R.L., *Fuel*, 49, 91, (1970).

64. Gan, H., Nandi, S.P. and Walker, P.L., Jr., *Fuel*, 51, 272, (1972).

65. Kamishita, M., Mahajan, O.P. and Walker, P.L., Jr., *Fuel*, 56, 444, (1977).

66. Mahajan, O.P., Komatsu, M. and Walker, P.L., Jr., *Fuel*, 59, 3, (1980).

67. Nsakala, N.Y., Essenhigh, R.H. and Walker, P.L., Jr., *Fuel*, 57, 605, (1978

68. Mikhail, R.S., Brunauer, S. and Bodor, R.E., *J. Colloid Interface Sci.*, 26, 45, (1968).

69. Dubinin, M.M. and Kadlec, O., *Carbon*, 13, 263, (1975).

70. Dubinin, M.M. and Stoeckli, H.F., *J. Colloid Interface Sci.*, 75, 34, (1980).

71. Dubinin, M.M., *Carbon*, 18, 355, (1980).

72. Dubinin, M.M., *Carbon* 19, 321, (1981).

73. Kadlec, O., *Coll. Czech. Chem. Comm.*, 30, 2415, (1971).

74. Gregg, S.J. and Langford, J.F., *Trans. Faraday Soc.*, 65, 1394, (1969).

75. Gluskoter, H.J., "Trace Elements in Fuel", *Adv. in Chem. Ser.*, 141, p.1, American Chemical Society, Washington, (1975).

76. O'Gorman, J.V. and Walker, P.L., Jr., "Mineral matter and trace elements in U.S. coals", Office of Coal Research Report No.61-2, (1972).

77. Renton, J.J., in "Coal Structure", (Ed.) Meyers, R.A., Academic Press, New York, (1982).

78. Speight, J.G., "The Chemistry and Technology of Coat", Marcel Dekker, New York, (1983).

79. Dulhunty, J.A. and Harrison, B.L., *Fuel*, 32, 441, (1953).

80. Ahland, E., Nashau, G., Peters, W. and Weskamp, W., in "Chemical Feedstock from Coal", (Ed.) Falbe, J., Wiley, New York, p.12, (1982).

81. Che, S.C., Durai-Swamy, K., Blecker, K., Knell, E.W. and Zahradnik, R., A.C.S. Preprint, *Div. Fuel Chem.*, 24, 111, (1979).

82. Solomon, P.R., in "New Approaches in Coal Chemistry", *A.C.S. Symp. Ser.*, 169, (Eds) Blaustein, B.D., Bockrath, B.C. and Friedman, S., p.86, (1980).

83. Franklin, R., *Trans. Faraday Soc.*, 45, 668, (1949).

84. Blake, J.H., Bopp, G.R., Jones, J.F., Miller, M.G. and Tambo, W., *Fuel*, 46, 115, (1967).

85. Blackwood, J.D., Cullis, B.D. and McCarthey, D.J., *Aust. J. Chem.*, 20, 1561, (1967).

86. Walker, P.L., Jr., Rusinko, F. and Austin, L.G., in "Advances in Catalysis", Vol.XI, (Eds) Eley, D.D., Selwood, P.W. and Weisz, P.B., Academic Press, New York, p.133, (1959).

87. Blackwood, J.D. and McTaggart, F.K., *Aust. J. Chem.*, 12, 533, (1959).

88. Berkowitz, N., "An Introduction to Coal Technology", Academic Press, New York, p.131, (1979).

89. Habermehl, D., Orywal, F. and Berger, H.D., in "Chemistry of Coal Utilisation", 2nd Suppl. Vol., (Ed.) Elliott, M.A., Wiley, New York, p.338, (1981).

90. Souberg, E.M., Peters, W.A. and Howard, J.B., *Ind. Eng. Chem. Proc. Des. Dev.*, 17, 37, (1978).

91. Schapiro, N. and Gray, R.J., *J. Inst. Fuel*, 43, 234-242, (1964).

92. Chiche, P., Durie, S. and Pregermain, S., *Fuel*, 44, 5, (1965).

93. Orenbakh, M.S., "Reaction Surface During Heterogeneous Combustion", Novosibirsk, p.232 (1973).

94. Toda, Y., *Fuel*, 52, 36, 99, (1973).

95. Jenkins, R.G., Nandi, S.P. and Walker, P.L., Jr., *Fuel*, 52, 288, (1973).

96. Hippo, E. and Walker, P.L., Jr., *Fuel*, 54, 245, (1975).

97. Howard, J.B., in "Chemistry of Coal Utilisation", 2nd Suppl. Vol., (Ed.) Elliott, M.A., Wiley, New York, p.665, (1981).

98. Anthony, D.B. and Howard, J.B., *A.I.Ch.E. J.*, 22, 625, (1976).

99. Juntgen, H. and Van Hekk, K.H., *Fuel Processing Technol.*, 2, 261, (1979).

100. Gavalas, J.R., "Coal Pyrolysis", Elsevier, Amsterdam, (1982).

101. Walker, P.L., Jr., "Pyrolysis of Coal", presented at seminar on 'Modern Developments in Combustion Technology, Pennsylvania State University, July, (1979).

102. Scaroni, A.W., Walker, P.L., Jr., and Essenhigh, R.H., *Fuel*, 60, 71, (1981).

103. Kobayashi, H., Howard, J.B. and Sarofim, A.F., 16th Symp. (Int.) on Combustion, The Combustion Institute, Pittsburgh, p.411, (1977).

104. Souberg, E.M., Peters, W.A. and Howard, J,B., 17th Symp. (Int.) on Combustion, The Combustion Institute, Pittsburgh, p.117, (1979).

105. Souberg, E.M., Peters, W.A. and Howard, J.B., in "Thermal Hydrocarbon Chemistry", *Adv. in Chem. Ser.*, 183, (Eds) Oblad, A.G., Davis, H.G. and Eddinger, R.T., Washington, p.239, (1979).

106. Solomon, P.R. and Colket, M.B., 17th Symp. (Int,) on Combustion, The Combustion Institute, Pittsburgh, p.131, (1979).

107. Solomon, P.R., in "New Approaches in Coal Chemistry", *A.C.S. Symp. Ser.* No.169, (Eds) Blaustein, B.D., Bockrath, B.C. and Friedman, S., Washington, p.61, (1981).

108. Anthony, D.B., Howard, J.B., Hottel, H.C. and Meissner, H.P., 15th Symp. (Int.) on Combustion, The Combustion Institute, Pittsburgh, p.1303, (1975).

109. Essenhigh, R.H. and Howard, J.B., "Combustion Phenomena in Coal Dusts and the Two Component Hypothesis of Coal Constitution", Pensylvania State University Study No.31, (1971).

110. Essenhigh, R.H., in "Coal Conversion Technology", (Eds) Wen, C.Y. and Lee, E.S., Addison-Wesley, Reading, p.171, (1979).

111. Nsakala, N.T., Essenhigh, R.H. and Walker, P.L., Jr., *Combust. Sci. Technol.*, 16, 153, (1977).

112. Ubhayaker, S.K., Stickler, D.B., Von Rosenberg, C.W. and Cannon, R.E., 16th Symp. (Int.) on Combustion, The Combustion Institute, Pittsburgh, p.427, (1977).

113. Anthony, D.B. and Howard, J.B., *A.I.Ch.E. J.*, 22, No.4, 625, (1976).

114. Gavalas, G.R. and Wilks, K.A., *A.I.Ch.E. J.*, 26, 201, (1980).

115. Russel, W.B., Saville, D.A. and Greene, M.J., *A.I.Ch.E.J.*, 25, 69, (1979).

116. Howard, J.B., in "Chemistry of Coal Utilisation", 2nd Suppl. Vol., (Ed.) Elliott, M.A., Wiley, New York, p.665, (1981).

117. Anthony, D.B., Howard, J.B., Hottel, H.C. and Meissner, B.P., 15th Symp. (Int.) on Combustion, The Combustion Institute, Pittsburgh, p.1303, (1975).

118. Jenkins, G.M. and Kawamura, K., "Polymeric Carbons: Carbon Fibre, Glass and Char", Cambridge University Press, London, (1976).

119. "Encyclopedia of Polymer Science", Vol.14, (Eds) Mark, H.F., Gaylord, N.G. and Bikales, N.M., Wiley, New York, p.540, (1971).

120. Hebden, D. and Stroud, H.J.F., in "Chemistry of Coal Utilisation", 2nd Suppl. Vol., (Ed.) Elliott, M.A., Wiley, New York, p.1599, (1981).

121. Hebden, D. and Edge, R.F., *J.I.G.E.*, 108, 492, (1958), Gas Council Research Communication, GC 50.

122. Hebden, D., Lacey, J.A. and Horsler, A.G., *J.I.G.E.*, 5, 367, (1965), Gas Council Research Communication, GC 112.

123. Sharman, R., Lacey, J.A. and Scott, J.E., "The British Gas/Lurgi Slagging Gasifier: a springboard to synthetic fuels", paper presented at 8th Int. Conf. on Coal Gasification, Liquefaction and Conversion to Electricity, August, 1981.

124. Grainger, L. and Gibson, J., "Coal Utilisation Technology, Economics and Policy", Graham and Trotman, London, p.37, (1981).

125. Sparham, G. and Dryden, I.G.C., B.C.U.R.A. *Monthly Bull.*, 18, 1, (1963).

126. Rudolph, P.F.H., Coal Chem.-2000, *Inst. of Chem. Engrs Symp. Ser.*, No.62, paper C1, (1980).

127. Cohen, P. and Ried, W.T., U.S. Bureau of Mines Tech., Paper No.663, (1944).

128. Von Fredersdorff, C.G. and Elliott, M.A., in "Chemistry of Coal Utilisation", Suppl. Vol., Ch.20, (Ed.) Lowry, H.H., Wiley, New York, (1963).

129. Hebden, D. and Brooks, C.T., "Westfield - The Development of Processes for the Production of SNG from Coal", Inst. of Gas Engineers Communication 988, (1976).

130. Brooks, C.T., *Proc. 3rd BOC Priestly Conf., Spec. Publ. No.48*, The Royal Society of Chemistry, London, p.78, (1983).

131. Anderson, L.L. and Tillman, D.A., "Synthetic Fuels from Coal", Wiley, New York, (1979).

132. Dainton, A.D., in "Coal and Modern Coal Processing - An Introduction", (Eds) Pitt, G.J. and Millward, G.R., Academic Press, London, p.133, (1979).

133. Zahradnik, R.L. and Grace, R.J., in "Coal Gasification", *Adv. Chem. Ser., No.131*, 126, (1974).

134. Habermehl, D., Orywal, F. and Beyer, R.D., in "Chemistry of Coal Utilisation", 2nd Suppl. Vol., (Ed.) Elliott, M.A., Wiley, New York, p.317, (1981).

135. Walker, P.L., Jr., Mahajan, O.P. and Komatsu, M., *A.C.S. Div. Fuel Chem.*, 24, 10, (1979).

136. Jenkins, R.G., Nandi, S.P. and Walker, P.L., Jr., *Fuel*, 52, 288, (1973).

137. Hippo, E. and Walker, P.L., Jr., *Fuel*, 54, 245, (1975).

138. Soledade, L.E.B., Mahajan, O.P. and Walker, P.L., Jr., *Fuel*, 57, 56, (1978).

139. Beesting, M., Hartwell, R.R. and Wilkinson, H.C., *Fuel*, 56, 319, (1977).

140. Zahradnik, R.L. and Glenn, R.A., *Fuel*, 50, 77, (1971).

141. Parent, J.D. and Katz, S., *Inst. Gas Technol. Research Bull. No.2*, (1948).

142. Gadsby, J., Hinshelwood, C.N. and Sykes, K.W., *Proc. Roy. Soc.*, A187, 129, (1946).

143. Long, F.J. and Sykes, K.W., *Proc. Roy. Soc.*, A193, 377, (1948).

144. Strickland-Constable, R.F., *J. Chim. Phys.*, 47, 356, (1950).

145. Johnstone, J.F., Chen, C.Y. and Scott, D.S., *Ind. Engng Chem.*, 44, 1564, (1952).

146. Wicke, E. and Rossberg, M., *Z. Elektrochem.*, 57, 641, (1953).

147. Binford, J.S. and Eyring, H., *J. Phys. Chem.*, 60, 486, (1956).

148. Hennig, G.R. and Smaller, B., Proc. 3rd Conf. on Carbon, University of Buffalo, Buffalo, New York, p.11, (1956).

149. Anderson, R.B. and Emmett, P.H., *J. Phys. Chem.*, 56, 753, (1952).

150. Johnson, J.L., in "Chemistry of Coal Utilisation", 2nd Suppl. Vol., (Ed.) Elliott, M.A., Wiley, New York, p.1491, (1981).

151. Essenhigh, R.H., in "Chemistry of Coal Utilisation", 2nd Suppl. Vol., (Ed.) Elliott, M.A., Wiley, New York, p.1153, (1981).

152. Walker, P.L., Jr., *Fuel*, 60, 801, (1981).

153. Marsh, H., First BOC Priestly Conf., Spec. Publ. No.32, The Chemical Society, London, p.133, (1977).

154. Wicke, E., Proc. 5th Symp. on Combustion, Reinhold, p.245, (1955).

155. Rossberg, M. and Wicke, E., *Chem. Ingr. Tech.*, 28, 181, (1956).

156. Thiele, E.W., *Ind. Eng. Chem.*, 31, 916, (1939).

157. Wheeler, A., in "Advances in Catalysis", Vol.3, (Eds) Frankenburg, W.C., Kosarowsky, V.I. and Rideal, E.K., Academic Press, New York, p.249, (1951).

158. Satterfield, C.N., "Mass Transfer in Heterogeneous Catalysis", MIT Press, Cambridge, (1970).

159. Petersen, E.E., *A.I.Ch.E.J.*, 3, 443, (1957).

160. Hashimoto, K. and Silveston, P.L., *A.I.Ch.E.J.*, 19, 259, (1973).

161. Hashimoto, K. and Silveston, P.L., *A.I.Ch.E.J.*, 19, 268, (1973).

162. Simons, G.A. and Finson, M.L., *Combust. Sci. Technol.*, 19, 217, (1979).

163. Simons, G.A., *Combust. Sci. Technol.*, 19, 227, (1979).

164. Simons, G.A., *Combust. Sci. Technol.*, 20, 107, (1979).

165. Lewis, P.F. and Simons, G.A., *Combust. Sci. Technol.*, 20, 117, (1979).

166. Gavalas, G.R., *A.I.Ch.E.J.*, 26, 577, (1980).

167. Gavalas, G.R., *Combust. Sci. Technol.*, 24, 197, (1981).

168. Bhatia, S.K. and Perlmutter, D.D., *A.I.Ch.E.J.*, 26, 379, (1980).

169. Srinivas, B. and Amundson, N.R., *A.I.Ch.E.J.*, 26, 487, (1980).

170. Zygourakis, K., Arri, L. and Amundson, N.R., *Ind. Eng. Chem. Fundam.*, 21, 1, (1982).

171. Simons, G.A., *Combust. Sci. Technol.*, 24, 211, (1981).

172. Smith, I.W., *Fuel*, 57, 409, (1978).

173. Walker, P.L., Jr. and Hippo, E.J., *Am. Chem. Soc., Div. Fuel Chem. Prepr.*, 20(3), 45, (1975).

174. Dutta, S., Wen, C.Y. and Belt, R.J., *Ind. Engng Chem. Proc. Des. Div.*, 16(1), 20, (1977).

175. Dutta, S. and Wen, C.Y., *Ind. Engng Chem. Proc, Des. Dev.*, 16(1), 31, (1977).

176. Meyer, L., *Trans. Faraday Soc.*, 34, 1056, (1938).

177. Hennig, G.R., Proc. 5th Conf. on Carbon, Pergamon Press, New York, p.143, (1962).

178. Graham, D., *J. Phys. Chem.*, 61, 1310, (1957).

179. Healey, F.H., Yung-Fang, Yu. and Chessick, J.J., *J. Phys. Chem.*, 59, 399, (1959).

180. Walker, P.L., Jr. and Janov, J., *J. Colloid Interface Sci.*, 28, 449, (1968).

181. Watt, J.D. and Franklin, R.E., Conf. on Industrial Carbon and Graphite, Soc. of Chem. Ind., London, p.321, (1957).

182. Laine, N.R., Vastola, F.J. and Walker, P.L., Jr., *J. Phys. Chem.*, 67, 2030, (1963).

183. Hart, P.J., Vastola, F.J. and Walker, P.L., Jr., *Carbon*, 5, 363, (1967).

184. Walker, P.L., Jr., Mahajan, O.P. and Komatsu, M., *A.C.S. Div. Fuel Chem. Prepr.*, 24(3), 10, (1979).

185. Huttinger, K.J. and Krauss, W., *Fuel*, 61, 291, (1982).

186. Otto, K. and Shelef, M., Ext. Abstr. Prog. - Bienn. Conf. on Carbon, Vol.13, p.50, (1977).

187. Walker, P.L., Jr., Shelef, M. and Anderson, R.A., in "Chemistry and Physics of Carbon", Vol.4, (Ed.) Walker, P.L., Jr., Marcel Dekker, New York, p.287, (1968).

188. Tomita, A., Mahajan, O.P. and Walker, P.L., Jr., *A.C.S. Div. Fuel Chem. Prepr.*, 22(1), 4, (1977).

189. Field, M.A., Gill, D.W., Morgan, B.B. and Hawksley, P.G.W., "Combustion of Pulverised Coal", BCURA, Leatherhead, England, (1967).

190. Ergun, S., *J. Phys. Chem.*, 60, 480, (1956).

191. Kroger, C. and Melhorn, G., *Brennst. Chem.*, 19, 257, (1938).

192. Kroger, C. and Fingas, E., *Z. Angew. Allgem. Chem.*, 197, 321, (1931).

193. Thomas, J.M., in "Chemistry and Physics of Carbon", Vol.1, (Ed.) Walker, P.L., Jr., Marcel Dekker, New York, p.121, (1965).

194. Haynes, W.P., Gasior, S.J. and Forney, A.J., *Adv. Chem. Ser.*, 131, 179, (1974).

195. Willson, W.K., Sealock, L.J., Hoodmaker, F.C., Hoffman, R.W., and Stinson, D.L., *Adv. Chem. Ser.*, 131, 203, (1974).

196. Pabst, J.K. and Lang, R.J., European Patent No.035887, (1981).

197. Marsh, H., Taylor, D. and Lander, J.R., *Carbon*, 19, 375, (1981).

198. Marsh, H. and Rand, B., *Carbon*, 9, 63, (1971).

199. Marsh, H. and Adair, R.R., *Carbon*, 13, 327, (1975).

200. Mims, C.A. and Pabst, J.K., *A.C.S. Div. Fuel Chem.*, 25, 258, (1980).

201. Mims, C.A. and Pabst, J.K., *A.C.S. Div. Fuel Chem.*, 25, 263, (1980).

202. McKee, D.W., Proc. Int. Symp., FUNCAT COGAS, Amsterdam, p.37, (1982).

203. Juntgen, H., Proc. Int. Symp., FUNCAT COGAS, Amsterdam, p.53, (1982).

204. McKee, D.W., in "Chemistry and Physics of Carbon", Vol.16, (Eds) Walker, P.L., Jr. and Thrower, P.A., Marcel Dekker, New York, p.1, (1980).

205. Tomita, A., Ohtsuka, Y. and Tamai, Y., Proc. Int. Symp., FUNCAT COGAS, Amsterdam, p.71, (1982).

206. Love, G., in "Quantitative Electron Probe Microanalysis", (Eds) Scott, V.D. and Love, G., Ellis Horwood Ltd., Chichester, England, pp.218-263.

207. Gregg, S.J. and Sing, K.S.W., "Adsorption, Surface Area and Porosity", 2nd Edition, Academic Press, London and New York, (1982).

208. Walker, P.L., Jr. and Kini, K.A., *Fuel*, 44, 453, (1963).

209. Walker, P.L., Jr. and Patel, P.L., *Fuel*, 49, 91, (1968).

210. Lemcoff, N.O. and Sing, K.S.W., *J. Colloid Interface Sci.*, 61, 227, (1977).

211. Kini, K.A., *Fuel*, 43, 173, (1964).

212. Marsh, H. and Wynne-Jones, W.F.K., *Carbon*, 1, 269, (1964).

213. Walker, P.L., Jr. and Shelef, M., *Carbon*, 5, 7, (1967).

214. Lamond, T.G. and Marsh, H., *Carbon*, 1, 281, (1964).

215. McBain, J.W. and Bakr, A.M., *J. Amer. Chem. Soc.*, 48, 690, (1926).

216. Masters, K., "The Structure of Microporous Carbons", PhD Thesis, University of Bath, (1979).

217. Harris, N.S., "Vacuum Technology", Edwards High Vacuum, London Caledonian Press, (1981).

218. Chipalkatti, V. and Giles, C.H., *Nature*, 165, 735, (1950).

219. Gregg, S.J. and Sing, K.S.W., "Adsorption, Surface Area dnd Proosity", 1st Edition, Academic Press, London and New York, (1967).

220. Thomas, J.M. and Poulis, J.A., in "Vacuum Microbalance Techniques", Vol.3, (Ed.) Behrndt, K.M., Plenum Press, New York, p.15, (1963).

221. Bennett, J.M. and Tompkins, F.C., *Trans. Faraday Soc.*, 53, 185, (1957).

222. Radovic, L.R., Walker, P.L., Jr. and Jenkins, R.G., *Fuel*, 62, 849, (1983).

223. Tong, S.B., Pareja, P. and Back, M.H., *Carbon*, 20, 191, (1982).

224. Mentser, M. and Ergun, S., U.S. *Bureau of Mines Bull. No.664*, (1973.

225. Cvetanovic, R.J. and Amenomiya, Y., in "Advances in Catalysis", Vol.17, (Eds) Eley, D.D., Selwood, P.W. and Weisz, P.B., Academic Press, New York, p.114, (1967).

226. "Vacuum Technology - its Foundations, Formulae and Tables", HV 152, Section H-B, Leybold-Heraeus GMBH, pp.39-40, (1971).

227. Edwards Vacuum Products - Specifications, p.62, (1981).

228. Lewin, G., "Fundamentals of Vacuum Science and Technology", McGraw-Hill Company, New York, pp.11-16, (1965).

229. Holstein, W.L., "The Design of Laboratory REactors for the Measurement of Catalytic Carbon and Coal Gasification Kinetics", "Fuel Preprint".

230. Holstein, W.L. and Boudart, M., *J. Catal.*, 75, 337, (1982).

231. Mims, C.A. and Pbast, J.K., *A.C.S. Div. Fuel Chem. Prepr.*, 25, 258, (1980)

232. Otto, K. and Shelef, M., *Carbon*, 15, 317, (1977).

233. Rewick, R.T., Wentrock, P.R. and Wise, H., *Fuel*, 53, 274, (1974).

234. Huttinger, K.J. and Krauss, W., *Fuel*, 60, 93, (1981).

235. Spectrum Scientific Ltd. - Spectramass 100 Manual, (1983).

236. Huttinger, K.J. and Krauss, W., *Fuel*, 61, 291, (1982).

237. Otto, K. and Shelef, M., Ext. Abstr. Prog. - Bienn. Conf. on Carbon, Vol.13, p.50. (1977).

238. Fisher, P.M. and Szirmae, A., Proc. 14th Bienn. Conf. on Carbon, 151, (1979).

239. Otto, K., Bartosiewicz, L. and Shelef, M., *Fuel*, 58, 85, (1979).

240. McKee, D.W., Spiro, C.L., Kosky, P.G. and Lamby, E.J., Proc. Int. Symp., FUNCAT COGAS, Amsterdam, p.219, (1982).

241. Leonhardt, P., Sulimma, A., Van Heek, K.H. and Juntgen, H., Proc. Int. Symp., FUNCAT COGAS, Amsterdam, p.175, (1982).

242. Huhn, F., Klein, J. and Juntgen, H., Proc. Int. Symp., FUNCAT COGAS, Amsterdam, p.165, (1982).

243. Kipling, J.J. and McEnaney, B., *Fuel*, 53, 367, (1964).

244. Gilbert, J.B., Kipling, J.J., McEnaney, B. and Sherwood, J.N., "Polymer - The Chemistry, Physics and Technology of High Polymers", Vol.3, pp.1-10, (1962).

245. Dacey, J.R. and Thomas, D.G., *Trans. Faraday Soc.*, 50, 740, (1954).

246. Grassie, N., "Chemistry of High Polymer Degradation Processes", Butterworths, London, (1956).

247. Burlant, W.J. and Parsons, J.L., *J. Polymer Sci.*, 22, 249, (1956).

248. Maggs, F.A.P., Schwabe, P.H. and Williams, J.H., *Nature*, 186, 956, (1960).

249. Kipling, J.J., Sherwood, J.N., Shuster, P.V., Thompson, N.R. and Young, R.N., *Carbon*, 4, 5, (1966).

250. Lee, S., "Coal Char Gasification Studies", PhD Thesis, Case Western Reserve University, (1970).

251. Gan, H., Nandi, S.P. and Walker, P.L., Jr., *Fuel*, 51, 272, (1972).

252. Rodriquez-Reinoso, F., Almela-Alarcon, M., Linares-Solano, A., Salinas-Martinez de Lecea, C. and Supulveda-Escribano, A., Ext. Abstr. Prog., 17th Bienn. Conf. on Carbon, Kentucky, U.S.A., p.237, (1985).

253. Brunauer, S., Deming, L.S., Deming, W.E. and Teller, E., *J. Amer. Chem. Soc.*, 62, 1723, (1940).

254. Langmuir, I., *J. Amer. Chem. Soc.*, 38, 2221, (1916).

255. Langmuir, I., *J. Amer. Chem. Soc.*, 40, 1361, (1918).

256. Cook, M.A., *J. Amer. Chem. Soc.*, 70, 2925, (1948).

257. Singleton, J.H. and Habey, G.D., *Canad. J. Chem.*, 33, 184, (1955).

258. Barrer, R.M., in "Structure and Properties of Porous Materials", (Eds) Everett, D.H. and Stone, P.S., Butterworths, London, p.50, (1958).

259. Schull, C.G., Elkin, P.B. and Roess, L.C., *J. Amer. Chem. Soc.*, 70, 1405, (1948).

260. Barret, E.P., Joyner, L.G. and Halenda, P.P., *J. Amer. Chem. Soc.*, 73, 373, (1951).

261. Polanyi, M., *Verh. Deutsch. Phys. Ges.*, 16, 1012, (1914).

262. Polanyi, M., *Trans. Faraday Soc.*, 28, 316, (1932).

263. Dubinin, M.M., Zaverina, E.D. and Radushkevich, L.V., *Zhur. Fiz. Khim.*, 21, 1351, (1947).

264. Radushkevich, L.V., *Zhur. Fiz. Khim.*, 23, 1410, (1949).

265. Marsh, H. and Rand, B., *J. Colloid Interface Sci.*, 33, 101, (1970).

266. Marsh, H. and Rand, B., in "Proc, 3rd Conf. on Industrial Carbon and Graphite", London, Soc. of Chem. Ind., p.172, (1970).

267. Toda, Y., Hatami, M., Toyoda, S., Yashida, Y. and Honda, H., *Carbon*, 8, 565, (1970).

268. Masters, K. and McEnaney, B., *J. Colloid Interface Sci.*, 95, 340, (1983).

269. Kadlec, O., *Coll. Czech. Chem. Comm.*, 30, 2415, (1971).

270. Kadlec, O. and Dubinin, M.M., *Carbon*, 13, 263, (1975).

271. Gregg, S.J. and Langford, J.F., *Trans. Faraday Soc.*, 65, 1394, (1969).

272. Ali, S., "A Study of Microporous and Non-microporous Adsorption in Activated Carbons", MSc Thesis, University of Bath, (1984).

273. Ali, S. and McEnaney, B., *J. Colloid Interface Sci.*, in press.

274. Smith, W.R. and Ford, D.G., *J. Phys. Chem.*, 69, 3587, (1965).

275. Livingstone, H.K., *J. Colloid Interface Sic.*, 4, 447, (1949).

276. Rhodin, T.N., *J. Amer. Chem. Soc.*, 72, 4343, (1950).

277. Rhodin, T.N., *J. Phys. Chem.*, 57, 143, (1953).

278. Gregg, S.J. and Sing, K.S.W., "Adsorption, Surface Area and Porosity", 2nd Edition, Academic Press, London and New York, (1982).

279. Harris, M.R. and Sing, K.S.W., *Chem. Ind.*, 18, 757, (1967).

280. Michels, A., Wassenaar, T. and Zwietering, T.H., *Physica*, 17, 882, (1951).

281. Goldman, K. and Scrase, N.G., *Physica*, 45, 1, (1969).

282. Maggs, F.A.P., *Research*, 6, 135, (1953).

283. Walker, P.L., Jr. and Geller, I., *Nature*, 178, 1001, (1956).

284. Anderson, R.B., Hall, W.K., Leckey, J.A. and Stein, K.C., *J. Phys. Chem.*, 60, 1458, (1956).

285. Walker, P.L., Jr., Foresti, R.J. and Wright, C.C., *Ind. Engr Chem.*, 45, 1703, (1953).

286. Berger, J., Siemieniewska, T. and Tomkow, K., *Fuel*, 55, 9, (1976).

287. Stoeckli, H.F., Houriet, J.Ph., Perret, A. and Huber, U., in "Characterisation of Porous Solids", (Eds) Gregg, S.J., Sing, K.S.W. and Stoeckli, H.F., Soc. of Chem. Ind., London, p.31, (1979).

288. Dubinin, M.M., Bering, B.P., Serpinskii, V.V. and Vasiliev, B.N., in "Surface Phenomena in Chemistry and Biology", Pergamon Press, New York, p.172, (1958).

289. Bridgeman, O.C., *J. Amer. Chem. Soc.*, 49, 1174, (1927).

290. Kini, K.A., Reports of the 27th International Congress on Industrial Chemistry, Brussels, Vol.20, p.110, (1954).

291. Anderson, R.B., Hofer, L.J.E. and Bayer, J., *Fuel*, 41, 559, (1962).

292. Nandi, S.P. and Walker, P.L., Jr., *Fuel*, 43, 385, (1964).

293. Walker, P.L., Jr. and Kini, K.A., *Fuel*, 44, 453, (1965).

294. Johnson, J.L., *A.C.S. Div. Fuel Chem. Prepr.*, 20(4), 85, (1975).

295. Tomkow, K., Siemieniewska, T., Czechowski, F. and Jankowska, A., *Fuel*, 56, 121, (1977).

296. Radovic, L.R., Walker, P.L., Jr. and Jenkins, R.G., *Fuel*, 62, 849, (1983).

297. Laine, N.R., Vastola, F.J. and Walker, P.L., Jr., Proc. 5th Carbon Conf., Vol.2, Pergamon Press, New York, p.211, (1963).

298. Billinge, B.H.M., Docherty, J.B. and Bevan, M.J., *Carbon*, 22, 83, (1984).

299. Mulcahy, M.F.R. and Smith, I.W., *Rev. Pure Appl. Chem.*, 19, 81, (1969).

300. Phillips, R., Vastola, F.J. and Walker, P.L., Jr., *Carbon*, 8, 205, (1970).

301. Coulson, C.A., Proc. 4th Conf. on Carbon, Pergamon Press, New York, p.215, (1960).

302. Mattson, J.S. and Mark, H.B., Jr., "Activated Carbon", Marcel Dekker, New York, p.112, (1971).

303. Harker, H., Gallagher, J.T. and Parkin, A., *Carbon*, 4, 401, (1966).

304. Mrozowski, S. and Wobschall, D.J., *J. Chim. Phys.*, 58, 915, (1961).

305. Lussow, R.O., Vastola, F.J. and Walker, P.L., Jr., *Carbon*, 5, 591, (1967).

306. Bansal, R.C., Vastola, F.J. and Walker, P.L., Jr., *Carbon*, 8, 443, (1970).

307. Bansal, R.C., Vastola, F.J. and Walker, P.L., Jr., *J. Colloid Interface Sci.*, 32(2), 187, (1970).

308. Phillips, R., Vastola, F.J. and Walker, P.L., Jr., *Carbon*, 8, 197, (1970).

309. Walker, P.L., Jr., Bansal, R.C. and Vastola, F.J., "The Structure and Chemistry of Solid Surfaces", Wiley, New York, pp.81-1 to 81-16, (1969).

310. Taylor, R.L., PhD. Thesis, Pennsylvania State University, (1982).

311. Mahajan, O.P., Yarzab, R. and Walker, P.L., Jr., *Fuel*, 57, 643, (1978).

312. Hippo, E.J., PhD. Thesis, Pennsylvania State University, (1977).

313. Long, F.J. and Sykes, K.W., *J. Chem. Phys.*, 47, 361, (1950).

314. Long, F.J. and Sykes, K.W., *Proc. Roy. Soc.*, A193, 377, (1948).

315. Kayembe, N. and Pulsifer, A.H., *Fuel*, 55, 211, (1976).

316. Linares-Solano, A., Mahajan, O.P. and Walker, P.L., Jr., *Fuel*, 58, 327, (1979).

317. Ergun, S. and Mentser, M., in "Chemistry and Physics of Carbon", Vol.1, (Ed.) Walker, P.L., Jr., Marcel Dekker, New York, p.204, (1965).

318. Feldkirchner, H.L. and Linden, H.R., *Ind. Eng. Chem. Proc. Des. Dev.*, 2, 153, (1963).

319. Feldkirchner, H.L. and Huebler, J., *Ind. Eng. Chem. Proc. Des. Dev.*, 4, 134, (1965).

320. Gadsby, J., Hinshelwood, F.R.S. and Sykes, K.W., *Proc. Roy. Soc.*, A187, 129, (1946).

321. Walker, P.L., Jr., "Mater. Probl. Res. Oppor. Coal Convers. Workshop", Vol.2, Coal Science Paper, 109, (1974).

322. McKee, D.W., *Carbon*, 12, 453, (1974).

323. Tomita, A., Mahajan, O.P. and Walker, P.L., Jr., *Fuel*, 56, 137, (1977).

324. Rodriquez-Reinoso, F., Thrower, P.A. and Walker, P.L., Jr., *Carbon*, 12, 63, (1974).

325. Mentser, M. and Ergun, S., *U.S. Bureau of Mines Bull. No.664*, pp.1-42, (1973).

326. Essenhigh, R.H., in "Chemistry of Coal Utilisation", 2nd Suppl. Vol., (Ed.) Elliott, M.A., Wiley, New York, p.1153. (1981).

327. Tong, S.B.. Pareja, P. and Back, M.H., *Carbon*, 20, 191, (1982).

328. Tyler, R.J. and Smith, J.W., *Fuel*, 54, 99, (1975).

329. Otto, K. and Shelef, M., 6th Int. Cong. on Catalysis, London, Paper B47, (1976).

330. Tremblay, G., Vastola, F.J. and Walker, P.L., Jr., *Carbon*, 16, 35, (1978).

331. Freeman, E.S. and Carroll, B., *J. Phys. Chem.*, 62, 394, (1958).

332. Komers, R., Amenomiya, Y. and Cvetanovic, R.J., *J. Catal.*, 15, 293, (1969).

333. Czanderna, A.W., Biegen, J.R. and Kollen, W., *J. Colloid Interface Sci.*, 34, 406, (1970).

334. Redhead, P.A., *Vacuum*, 12, 203, (1963).

335. Carter, G., *Vacuum*, 12, 245, (1963).

336. Ehrlich, G., in "Advances in Catalysis", Vol.14, (Eds) Eley, D.D., Selwood, P.W. and Weisz, P.B., Academic Press, New York, pp.255-427, (1963).

337. Pabst, J.K. and Lang, R.J., European Patent No.035887, (1981).

TABLE 2.1 COAL MACERALS AND MACERAL GROUPS

| Maceral Group | Maceral |
|---|---|
| Vitrinite | Collinite |
| | Tellinite |
| Exinite | Sporinite |
| | Cutinite |
| | Alginite |
| | Resinite |
| | Waxes |
| Inertinite | Micrinite |
| | Sclerotinite |
| | Semi-fusinite |
| | Fusinite |

TABLE 2.2 STOPES' CLASSIFICATION OF LITHOTYPES

| Macroscopic Lithotypes | Microscopic Maceral Groups |
|---|---|
| Vitrain | Vitrinite |
| Clarain | Vitrinite dominant<br>Exinite and inertinite less dominant |
| Durain | Micrinite dominant<br>Vitrinite less dominant |

TABLE 2.3 CHEMICAL COMPOSITION OF MACERAL GROUPS

| Maceral Groups | Atomic Carbon Content | H/C Atomic Ratio | Volatile Content |
|---|---|---|---|
| Exinite | 43 - 62% | 1.18 - 0.59 | 79 - 18% |
| Vitrinite | 51 - 62% | 0.80 - 0.60 | 40 - 18% |
| Inertinite | 59 - 67% | 0.64 - 0.47 | 31 - 11% |

TABLE 2.4 SEYLER'S CLASSIFICATION OF COALS

| *Carbon* | *Anthracite* | *Carbonaceous* | *Bituminous* | | | *Lignitous* | |
|---|---|---|---|---|---|---|---|
| | | | *Meta-* | *Ortho-* | *Para-* | *Meta-* | *Ortho-* |
| | *Carbon over* 93.3 *per cent* | 93.3—91.2 | 91.2—89.0 | 89.0—87.0 | 87.0—84.0 | 84—80 | 80—75 |
| *Per-bituminous genus Hydrogen over* 5.8 *per cent* | | | Per-bituminous (Per-meta-bituminous) | Per-bituminous (Per-ortho-bituminous) | Per-bituminous (Per-para-bituminous) | Per-Lignitous | |
| *Bituminous genus Hydrogen* 5.0—5.8 *per cent* | | (Pseudo-bituminous species) | META-BITUMINOUS | ORTHO-BITUMINOUS | PARA-BITUMINOUS | LIGNITOUS (Meta-) | (Ortho-) |
| *Semi-bituminous genus Hydrogen* 4.5— 5.8 *per cent* | | SEMI-BITUMINOUS species (Ortho-semi-bituminous) | Sub-bituminous (Sub-meta-bituminous) | Sub-bituminous (Sub-ortho-bituminous) | Sub-bituminous (Sub-para-bituminous) | Sub-Lignitous (Meta-) | (Ortho-) |
| Carbonaceous *genus Hydrogen* 4.0—4.5 *per cent* | Semi-anthracitic species | CARBONACEOUS species (Ortho-carbonaceous) | Pseudo-carbonaceous (Sub-meta-bituminous) | Pseudo-carbonaceous (Sub-ortho-bituminous) | Pseudo-carbonaceous (Sub-para-bituminous) | | |
| *Anthracitic genus Hydrogen under* 4 *per cent* | ORTHO-ANTHRACITE True anthracite | Pseudo-anthracite (Sub-carbonaceous) | Pseudo-anthracite (Sub-meta-bituminous) | Pseudo-anthracite (Sub-ortho-bituminous) | Pseudo-anthracite (Sub-para-bituminous) | | |

TABLE 2.5 ANALYSES OF OXYGEN FUNCTIONALITY IN COALS

(wt % maf coal basis)

| Coal | Bituminous | Subbituminous |
|---|---|---|
| Oxygen content as: | 80.13 % C maf | |
| Hydroxylic (-OH) | 2.4 | 5.6 |
| Carboxylic (-COOH) | 0.7 | 4.4 |
| Carnonylic (-C=O) | 0.4 | 1.0 |
| Etheric (-O-) | 2.8 | 0.9 |
| Total | 6.3 | 11.9 |
| Oxygen by difference: | | |
| Ash basis | 5.9 | 16.2 |
| Mineral matter basis | - | 16.0 |

TABLE 2.6 COAL MINERALS

| Group | Species | Formula |
|---|---|---|
| Aluminosilicates | Kaolinite | $Al_2Si_2O_5(OH)_4$ |
| | Illite | $KAl_3Si_3O_{10}(OH)_2$ |
| | Chlorite | $(FeMgAl)_6(AlSi)_4O_{10}(OH)_8$ |
| Oxides | Quartz | $SiO_2$ |
| | Rutile | $TiO_2$ |
| | Haematite | $Fe_2O_3$ |
| Carbonates | Siderite | $FeCo_3$ |
| | Ankerite | $(CaMgFe)CO_3$ |
| | Calcite | $CaCO_3$ |
| | Dolomite | $CaMg(CO_3)_2$ |
| Sulphides and Sulphates | Pyrite | $FeS_2$ |
| | Gypsum | $CaSO_4.2H_2O$ |

TABLE 5.1 PVDC/PAN COPOLYMER CARBONISATION RESULTS

A - Variation of heating rate; B - Variation of treatment time; C - Variation of nitrogen flowrate.

| A | | B | | C | |
|---|---|---|---|---|---|
| Heating rate (°C/min) | Carbon yield (%) | Treatment time (min) | Carbon yield (%) | $N_2$ flowrate ($cm^3$/min) | Carbon yield (%) |
| 0.5 | 33 | 10 | 34 | 25 | 34 |
| 1.0 | 34 | 30 | 34 | 50 | 34 |
| 2.0 | 33 | 60 | 33 | 75 | 34 |
| 5.0 | 33 | 90 | 33 | 100 | 33 |
| 10.0 | 34 | 120 | 33 | 200 | 34 |
| 20.0 | 33 | 180 | 32 | 300 | 33 |

TABLE 7.1 CORRECTION TO PRESSURE READINGS DUE TO THERMAL TRANSPIRATION IN THE SPRING BALANCE AND MICROBALANCE

| Pressure (Torr) | Spring Balance % error in pressure | | Microbalance % error in pressure | |
|---|---|---|---|---|
| | Ar | $CO_2$ | Ar | $CO_2$ |
| 0.001 | 15.82 | 14.85 | 31.7 | 13.4 |
| 0.01 | 7.29 | 2.62 | 4.5 | 1.5 |
| 0.02 | 2.88 | 0.88 | 1.6 | 0.5 |
| 0.05 | 0.65 | 0.17 | 0.3 | - |

TABLE 9.1 RESULTS FROM DESIGN CALCULATIONS

| Saturator Temperature (°C) | P (mm Hg) | b ($cm^3$/min) | c ($cm^3$/min) |
|---|---|---|---|
| 25 | 23.8 | 42.1 | 6.6 |
| 40 | 55.3 | 34.8 | 12.7 |
| 50 | 92.5 | 25.9 | 17.6 |
| 60 | 150.0 | 22.9 | 22.5 |
| 70 | 233.7 | 17.6 | 27.0 |
| 80 | 355.1 | 13.1 | 30.7 |

TABLE 9.2 MASS SPECTROMETER CALIBRATION RESULTS USING A GAS MIXTURE

Total pressure = $5.7 \times 10^{-7}$ Torr

| Gas | % in mixture | Theoretical partial pressure (Torr) | Measured partial pressure (Torr) |
|---|---|---|---|
| Argon | 74 | $4.22 \times 10^{-7}$ | $4.25 \times 10^{-7}$ |
| Methane | 20 | $1.14 \times 10^{-7}$ | $1.15 \times 10^{-7}$ |
| Hydrogen | 5 | $2.85 \times 10^{-8}$ | $2.90 \times 10^{-8}$ |
| Carbon monoxide | 1 | $5.70 \times 10^{-9}$ | $5.80 \times 10^{-9}$ |

TABLE 9.3 RELATIVE SENSITIVITIES OF VARIOUS GASES

| Gas | $H_2$ | $CH_4$ | $H_2O$ | CO | $N_2$ | $O_2$ | Ar | $CO_2$ |
|---|---|---|---|---|---|---|---|---|
| Relative sensitivity | 0.70 | 1.08 | 1.17 | 1.09 | 1.00 | 0.62 | 1.16 | 0.90 |

TABLE 9.4 CRACKING PATTERN CALIBRATION SHOWING SECONDARY PEAKS FOR DIFFERENT GASES

| | Molecular weight | | MASS 12 | 13 | 14 | 16 | 20 | 22 | 28 | 29 | 32 | 33 | 34 | 36 | 38 | 40 | 44 | 45 | 46 |
|---|---|---|---|---|---|---|---|---|---|---|---|---|---|---|---|---|---|---|---|
| Carbon monoxide | 28 | A | 4.5 | | 0.6 | 0.9 | | | 100 | 1.1 | | | | | | | | | |
| | | B | 4.4 | | 0.5 | 0.9 | | | 100 | 1.0 | | | | | | | | | |
| Nitrogen | 28 | A | | | 7.2 | | | | 100 | 0.8 | | | | | | | | | |
| | | B | | | 7.2 | | | | 100 | 0.7 | | | | | | | | | |
| Oxygen | 32 | A | | | | 11.4 | | | | | 100 | 0.1 | 0.4 | | | | | | |
| | | B | | | | 11.4 | | | | | 100 | 0.2 | 0.4 | | | | | | |
| Argon | 40 | A | | | | | 10.7 | | | | | | | 0.3 | 0.1 | 100 | | | |
| | | B | | | | | 10.8 | | | | | | | 0.4 | 0.2 | 100 | | | |
| Carbon dioxide | 44 | A | 6.0 | 0.1 | | 8.5 | | 1.2 | 11.4 | 0.1 | | | | | | | 100 | 1.3 | 0.4 |
| | | B | 5.9 | 0.2 | | 8.5 | | 1.1 | 11.4 | 0.2 | | | | | | | 100 | 1.2 | 0.5 |

Row A designates literature values.

Row B designates experimental results.

TABLE 10.1 ULTIMATE AND PROXIMATE ANALYSES FOR PVDC CHAR AND MARKHAM MAIN CHAR (wt % dmmf)

| | Ultimate Analysis | | | Proximate Analysis | | |
|---|---|---|---|---|---|---|
| Sample | Carbon | Hydrogen | Nitrogen | Moisture | Ash | Volatile matter |
| PVDC | 93.5 | 1.9 | 3.5 | 4.1 | 0.6 | 3.3 |
| Markham Main | 96.4 | 2.1 | n.d. | 2.8 | 5.4 | 3.4 |

n.d. not determined

TABLE 10.2 MINERAL MATTER ANALYSES BY EDAX (wt % of detected elements)

| Char Sample | Na | Mg | Al | Si | K | Ca | Ti | Fe |
|---|---|---|---|---|---|---|---|---|
| Markham Main | - | - | 33.4 | 47.5 | 9.9 | 1.7 | 1.5 | 5.1 |
| PVDC | 30.1 | - | - | - | - | 8.5 | - | 27.5 |

TABLE 12.1 MERCURY POROSIMETRY AND HELIUM PYCNOMETRY RESULTS

| % Burn-off | Helium Density ($g/cm^3$) | Mercury Density ($g/cm^3$) | Void Volume ($cm^3/g$) | Porosity |
|---|---|---|---|---|
| Markham Main Char | | | | |
| 0 | 1.83 | 1.04 | 0.42 | 0.43 |
| 20 | 1.95 | 0.77 | 0.79 | 0.61 |
| 40 | 2.14 | 0.66 | 1.04 | 0.69 |
| 60 | 2.22 | 0.46 | 1.74 | 0.79 |
| 80 | 2.24 | 0.40 | 2.07 | 0.82 |
| PVDC Char | | | | |
| 0 | 1.94 | 0.51 | 1.45 | 0.74 |
| 20 | 2.38 | 0.47 | 1.71 | 0.80 |
| 40 | 2.75 | 0.44 | 1.92 | 0.84 |
| 60 | 2.93 | 0.37 | 2.39 | 0.88 |
| 80 | 3.15 | 0.28 | 3.28 | 0.91 |

TABLE 12.2 BET, DR AND IS PARAMETERS FOR Ar ADSORPTION AT 77 K ON PVDC CHAR

| % Burn-off | Total Surface Area | Non-microporous Surface Area | Proportion of Non-microporous Surface | BET Constant | | Micropore Volume | DR Constant |
|---|---|---|---|---|---|---|---|
| | $S/(m^2/g)$ | $S'/(m^2/g)$ | $S'/S$ | C | C' | $V_0/(ml/g)$ | D |
| 0 | 109 | - | - | 4030 | - | 0.04 | 0.017 |
| 6 | 165 | 35 | 0.21 | 2410 | 4 | 0.06 | 0.018 |
| 12 | 252 | 35 | 0.14 | 4350 | 5 | 0.09 | 0.019 |
| 15 | 266 | 37 | 0.14 | 3070 | 4 | 0.10 | 0.019 |
| 28 | 443 | 35 | 0.08 | 3050 | 4 | 0.16 | 0.020 |
| 40 | 567 | 45 | 0.08 | 2960 | 4 | 0.21 | 0.020 |
| 52 | 684 | 55 | 0.08 | 5230 | 5 | 0.25 | 0.022 |
| 60 | 766 | 77 | 0.10 | 6290 | 5 | 0.29 | 0.023 |
| 70 | 864 | 43 | 0.05 | 6090 | 7 | 0.33 | 0.024 |
| 80 | 868 | 43 | 0.05 | 6460 | 7 | 0.33 | 0.025 |
| 85 | 850 | 34 | 0.04 | 5630 | 7 | 0.32 | 0.023 |

TABLE 12.3 BET, DR AND IS PARAMETERS FOR Ar ADSORPTION AT 77 K ON MARKHAM MAIN CHAR

| % Burn-off | Total Surface Area | Non-microporous Surface Area | Proportion of non-microporous Surface | BET Constant | | Micropore Volume | DR Constant |
|---|---|---|---|---|---|---|---|
| | | $S'/(m^2/g)$ | $S'/S$ | C | C' | $V_0/(ml/g)$ | D |
| 0 | 45 | - | | 1500 | - | 0.02 | 0.026 |
| 6 | 86 | - | | 1410 | - | 0.03 | 0.026 |
| 12 | 127 | 20 | 0.16 | 1620 | 6 | 0.05 | 0.027 |
| 20 | 192 | 38 | 0.20 | 1750 | 4 | 0.07 | 0.029 |
| 22 | 209 | 44 | 0.21 | 1910 | 4 | 0.08 | 0.029 |
| 40 | 254 | 56 | 0.22 | 1400 | 2 | 0.10 | 0.031 |
| 52 | 315 | 85 | 0.27 | 1420 | 2 | 0.12 | 0.033 |
| 65 | 385 | 100 | 0.26 | 1020 | 3 | 0.14 | 0.034 |
| 80 | 503 | 65 | 0.13 | 1100 | 4 | 0.19 | 0.035 |
| 90 | 472 | 47 | 0.10 | 1270 | 4 | 0.18 | 0.034 |

TABLE 12.4 COMPARISON OF MICROPORE VOLUMES OBTAINED USING THE DR METHOD AND THE IS METHOD

| Markham Main Char % Burn-off | Micropore Volume $V_0$/(ml/g) | |
|---|---|---|
| | DR | IS |
| 0 | 0.02 | 0.02 |
| 6 | 0.03 | 0.03 |
| 12 | 0.05 | 0.04 |
| 20 | 0.07 | 0.07 |
| 22 | 0.08 | 0.08 |
| 40 | 0.10 | 0.09 |
| 52 | 0.12 | 0.11 |
| 65 | 0.14 | 0.14 |
| 80 | 0.19 | 0.18 |
| 90 | 0.18 | 0.18 |
| PVDC CHAR % Burn-off | | |
| 0 | 0.04 | 0.04 |
| 6 | 0.06 | 0.06 |
| 12 | 0.09 | 0.09 |
| 15 | 0.10 | 0.09 |
| 28 | 0.16 | 0.16 |
| 40 | 0.21 | 0.20 |
| 52 | 0.25 | 0.25 |
| 60 | 0.29 | 0.28 |
| 70 | 0.33 | 0.32 |
| 80 | 0.33 | 0.33 |
| 85 | 0.32 | 0.32 |

TABLE 12.5 BET AND DR PARAMETERS FOR $CO_2$ ADSORPTION AT 195 K ON PVDC CHAR

| % Burn-off | Surface Area $S/(m^2/g)$ | C | Micropore Volume $V_0/(ml/g)$ | D |
|---|---|---|---|---|
| 0 | 260 | 1410 | 0.09 | 0.032 |
| 12 | 338 | 1190 | 0.11 | 0.033 |
| 22 | 440 | 1200 | 0.15 | 0.035 |
| 40 | 572 | 1180 | 0.20 | 0.037 |
| 60 | 751 | 1230 | 0.27 | 0.037 |
| 70 | 944 | 1220 | 0.35 | 0.039 |
| 80 | 1002 | 1130 | 0.36 | 0.039 |

TABLE 12.6 BET AND DR PARAMETERS FOR $CO_2$ ADSORPTION AT 195 K ON MARKHAM MAIN CHAR

| % Burn-off | Surface Area $S/(m^2/g)$ | C | Micropore Volume $V_0/(ml/g)$ | D |
|---|---|---|---|---|
| 0 | 160 | 1030 | 0.05 | 0.034 |
| 12 | 193 | 1270 | 0.07 | 0.035 |
| 22 | 233 | 1020 | 0.08 | 0.037 |
| 40 | 322 | 1060 | 0.12 | 0,041 |
| 52 | 414 | 1050 | 0.14 | 0.043 |
| 65 | 506 | 1270 | 0.20 | 0.044 |
| 80 | 636 | 1440 | 0.26 | 0,045 |

TABLE 12.7 DR PARAMETERS FOR $CO_2$ ADSORPTION AT 273 K ON PVDC CHAR

| % Burn-off | Micropore Volume $V_0$/(ml/g) | D |
|---|---|---|
| 0 | 0.10 | 0.034 |
| 12 | 0.12 | 0.035 |
| 22 | 0.16 | 0.037 |
| 40 | 0.21 | 0.039 |
| 60 | 0.28 | 0.040 |
| 70 | 0.36 | 0.042 |
| 80 | 0.37 | 0.042 |

TABLE 12.8 DR PARAMETERS FOR $CO_2$ ADSORPTION AT 273 K ON MARKHAM MAIN CHAR

| % Burn-off | Micropore Volume $V_0$/(ml/g) | D |
|---|---|---|
| 0 | 0.06 | 0.030 |
| 12 | 0.08 | 0.031 |
| 22 | 0.09 | 0.032 |
| 40 | 0.13 | 0.034 |
| 52 | 0.15 | 0.035 |
| 65 | 0.21 | 0.037 |
| 80 | 0.25 | 0.038 |

TABLE 13.1 A COMPARISON OF ACTIVE SURFACE AREAS FOR TWO COAL CHARS, DETERMINED BY THE VOLUMETRIC TECHNIQUE AND THE DYNAMIC TPD TECHNIQUE (THIS WORK)

1. Data from reference 296.

| Lignite coal char Sample Number | ASA/($m^2$/g) | |
|---|---|---|
| | Volumetric[1] | Dynamic |
| S - 1h (1475K) | 25 | 26 |
| S - 1h (975K) | 108 | 109 |

1. Data from Reference 12.

TABLE 13.2 VARIATION OF ASA WITH OXYGEN CHEMISORPTION PRESSURE FOR UNACTIVATED MARKHAM MAIN CHAR

| Oxygen pressure /($10^3$ Pa.) | ASA/($m^2$/g) |
|---|---|
| 1 | 30.1 |
| 5 | 29.9 |
| 10 | 29.8 |
| 50 | 30.2 |
| 100 | 30.1 |

TABLE 13.3 VARIATION OF ASA WITH THE NUMBER OF CHEMISORPTION-DESORPTION CYCLES FOR UNACTIVATED MARKHAM MAIN CHAR

| Number of cycles | ASA/($m^2$/g) |
|---|---|
| 1 | 30.1 |
| 2 | 30.7 |
| 3 | 31.5 |
| 4 | 32.3 |
| 5 | 33.0 |
| 6 | 33.8 |
| 7 | 34.7 |
| 8 | 35.7 |

TABLE 13.4 $[CO]/[CO_2]$ RATIOS FOR DESORPTION AS A FUNCTION OF BURN-OFF

| Markham Main Char | | PVDC Char | |
|---|---|---|---|
| % Burn-off | $[CO]/[CO_2]$ | % Burn-off | $[CO]/[CO_2]$ |
| 0 | 1.4 | 0 | 2.4 |
| 15 | 2.9 | 6 | 2.5 |
| 28 | 3.1 | 22 | 2.5 |
| 40 | 3.2 | 40 | 2.4 |
| 52 | 3.1 | 60 | 2.4 |
| 60 | 3.1 | 70 | 2.5 |
| 70 | 3.1 | 80 | 2.5 |
| 80 | 3.1 | 85 | 2.5 |
| 90 | 3.2 | | |

TABLE 14.1 ARRHENIUS PARAMETERS DERIVED FROM THE FIXED-BED REACTOR (FBR) SYSTEM AND THE THERMOGRAVIMETRIC (TGA) SYSTEM

| Char Sample | Activation Energy $E_A$/(kJ/mol) | | Pre-exponential Factor, $A_0$ | |
|---|---|---|---|---|
| | FBR | TGA | FBR | TGA |
| Markham Main | 131 | 126 | $1.2 \times 10^7$ | $7.4 \times 10^6$ |
| PVDC | 232 | 234 | $3.9 \times 10^{11}$ | $5.0 \times 10^{11}$ |

TABLE 14.2 EFFECT OF PARTICLE SIZE ON REACTIVITY

| Particle Size Range (μm) | Gasification Rate $R/10^{-5}$ (gC/gsec) | |
|---|---|---|
| | Markham Main Char | PVDC Char |
| 35-75 | 2.95 | 5.70 |
| 75-100 | 3.05 | 5.82 |
| 100-200 | 3.18 | 5.95 |
| 200-300 | 3.30 | 6.03 |
| 300-400 | 3.29 | 6.08 |
| 400-500 | 3.33 | 6.05 |
| 500-600 | 3.33 | 6.10 |
| 600-700 | 3.26 | 6.05 |
| 700-800 | 3.16 | 5.95 |

TABLE 14.3 EFFECT OF $pH_2/pH_2O$ RATIO ON ARRHENIUS PARAMETERS (USING FBR METHOD)

| $pH_2/pH_2O$ | Activation Energy $E_A$/(kJ/mol) | | Pre-exponential Factor, $A_0$ | |
|---|---|---|---|---|
| | Markhan Main Char | PVDC Char | Markham Main Char | PVDC Char |
| | | | $(A_0/10^6)$ | $(A_0/10^{10})$ |
| 0 | 113 | 200 | 4.0 | 3.2 |
| 0.05 | 118 | 205 | 5.4 | 4.5 |
| 0.10 | 122 | 213 | 6.9 | 8.2 |
| 0.20 | 126 | 227 | 8.2 | 25.4 |
| 0.25 | 131 | 232 | 12.1 | 39.0 |
| 0.30 | 135 | 234 | 15.8 | 43.2 |
| 0.40 | 136 | 235 | 16.1 | 44.2 |
| 0.50 | 140 | 237 | 22.3 | 52.8 |
| 0.75 | 144 | 241 | 26.1 | 71.6 |
| 1.00 | 147 | 243 | 31.0 | 78.5 |

TABLE 14.4 VALUES OF $t_{0.5}$ AS A FUNCTION OF TEMPERATURE

| Temperature | $t_{0.5}$ (min) | |
|---|---|---|
| (°C) | PVDC Char | Markham Main Char |
| 900 | 496 | 480 |
| 920 | 300 | 380 |
| 940 | 215 | 300 |
| 960 | 140 | 255 |
| 980 | 102 | 200 |
| 1000 | 80 | 165 |
| 1020 | 60 | 150 |

TABLE 15.1 CORRELATION OF REACTIVITY AND SURFACE AREA DATA

| % Burn-off | $R_1$ | $R_2$ | $R_3$ |
|---|---|---|---|
| PVDC Char | | | |
| 0 | 0.72 | 0.56 | 0.23 |
| 6 | 0.70 | 0.39 | - |
| 12 | - | 0.27 | 0.20 |
| 22 | 0.57 | 0.21 | 0.18 |
| 40 | 0.52 | 0.18 | 0.17 |
| 60 | 0.59 | 0.20 | 0.19 |
| 70 | 0.63 | 0.21 | 0.18 |
| 80 | 0.64 | 0.21 | 0.18 |
| 85 | 0.66 | 0.21 | - |
| Markham Main Char | | | |
| 0 | 1.11 | 0.74 | 0.21 |
| 12 | - | 0.30 | 0.20 |
| 15 | 1.11 | - | - |
| 22 | - | 0.21 | 0.18 |
| 28 | 1.07 | - | - |
| 40 | 1.00 | 0.22 | 0.17 |
| 52 | 1.00 | 0.21 | 0.16 |
| 65 | - | 0.21 | 0.16 |
| 80 | 1.06 | 0.19 | 0.15 |
| 90 | 1.03 | 0.19 | - |

$R_1$ - Gasification rate $/10^{-6}$ ($g\ sec^{-1}\ m^{-2}$ ASA)

$R_2$ - Gasification rate $/10^{-6}$ [$g\ sec^{-1}\ m^{-2}$ TSA (Ar)]

$R_3$ - Gasification rate $/10^{-6}$ [$g\ sec^{-1}\ m^{-2}$ TSA ($CO_2$)]

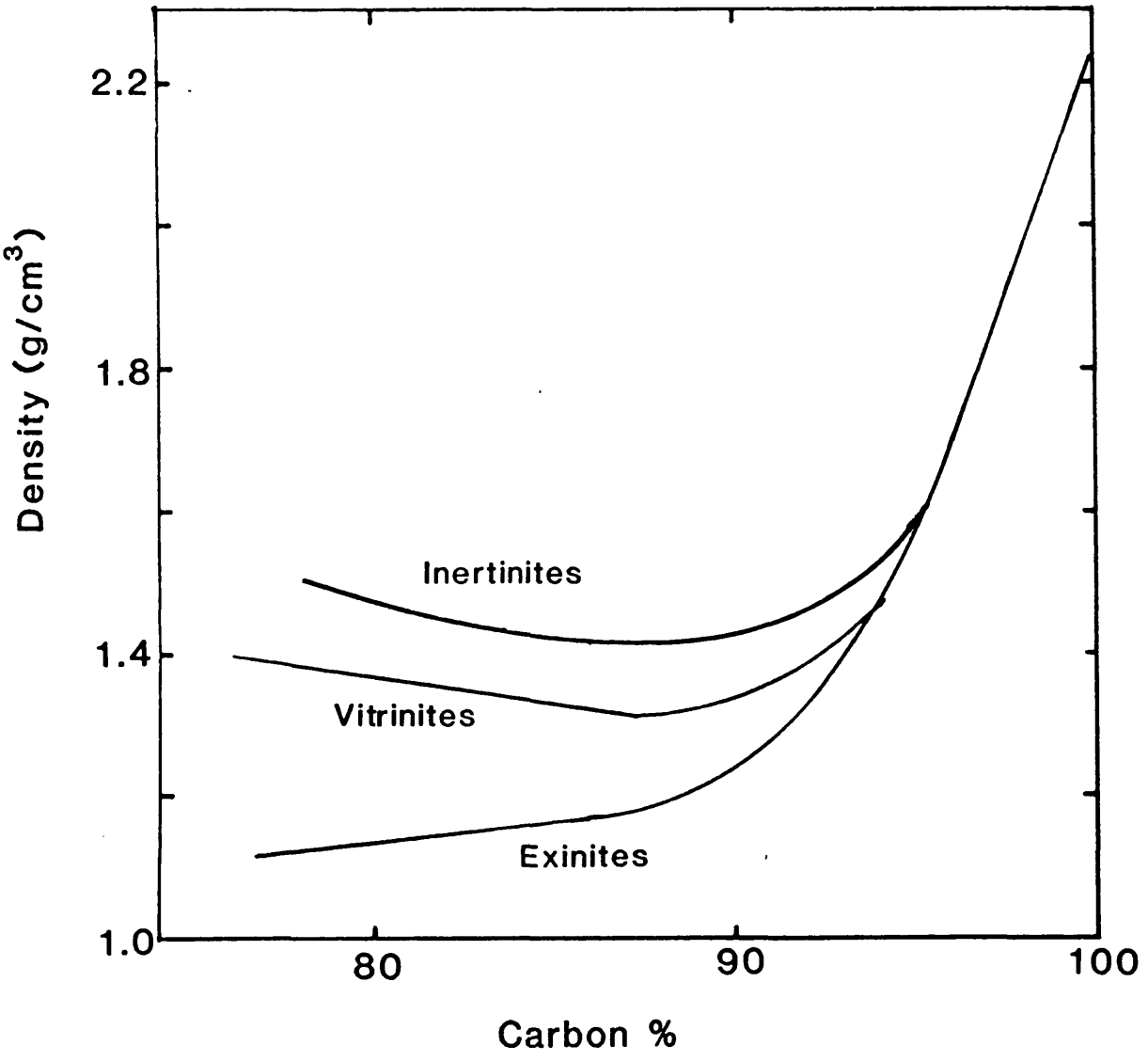


Figure 2.1 Densities of coal macerals.

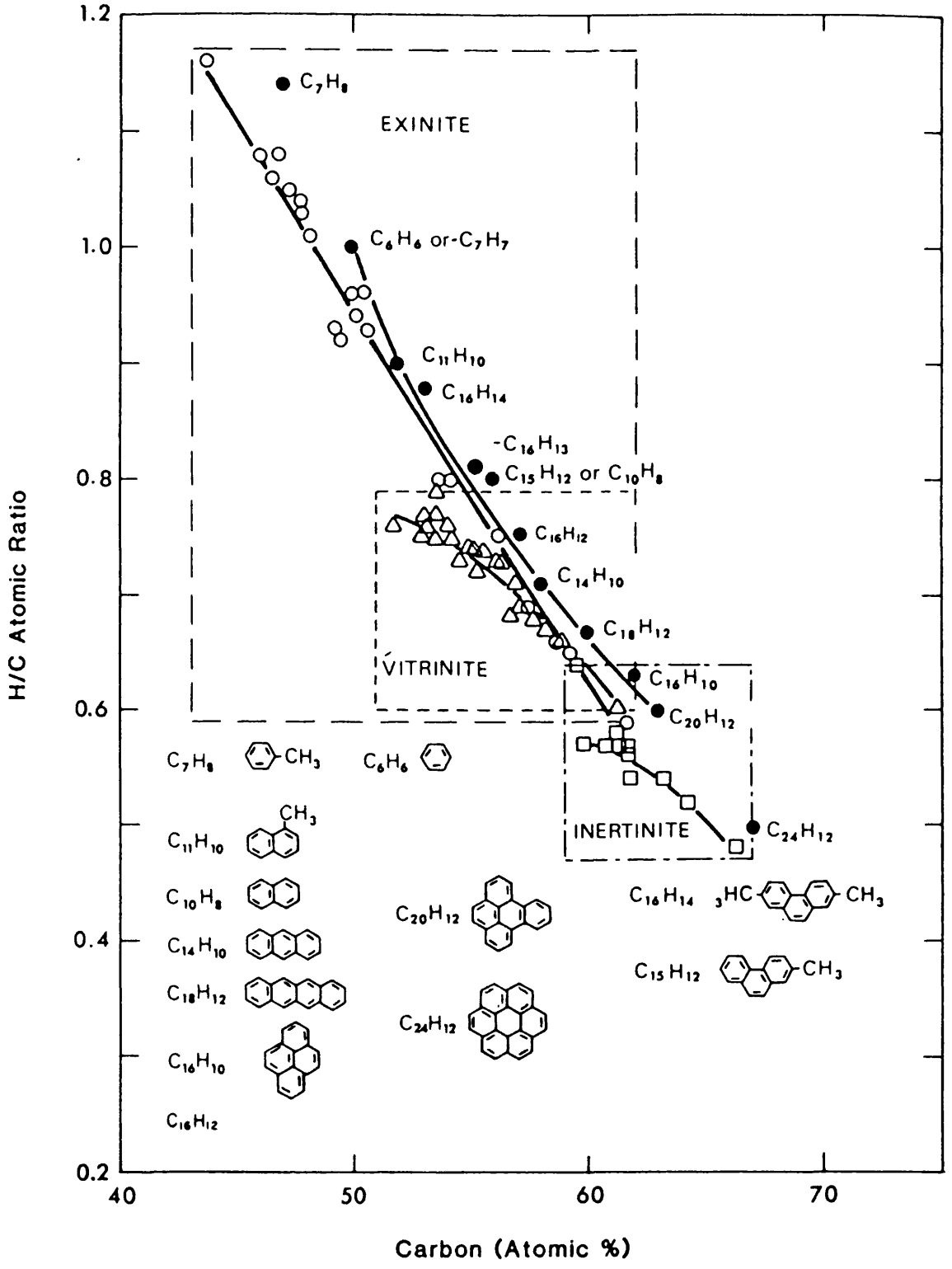


Figure 2.2 H/C atomic ratio *versus* percent atomic carbon of bituminous coal maceral groups.

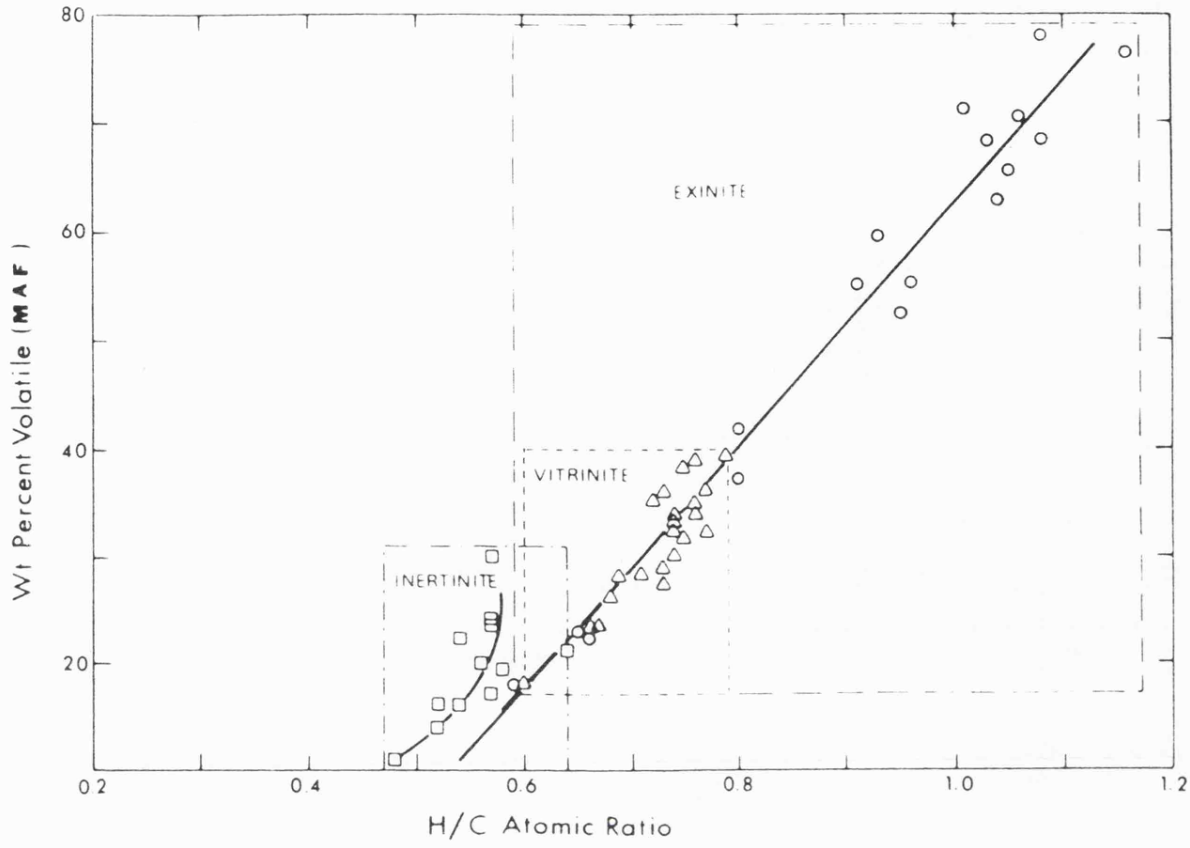


Figure 2.3 Volatile content of bituminous coal maceral groups.

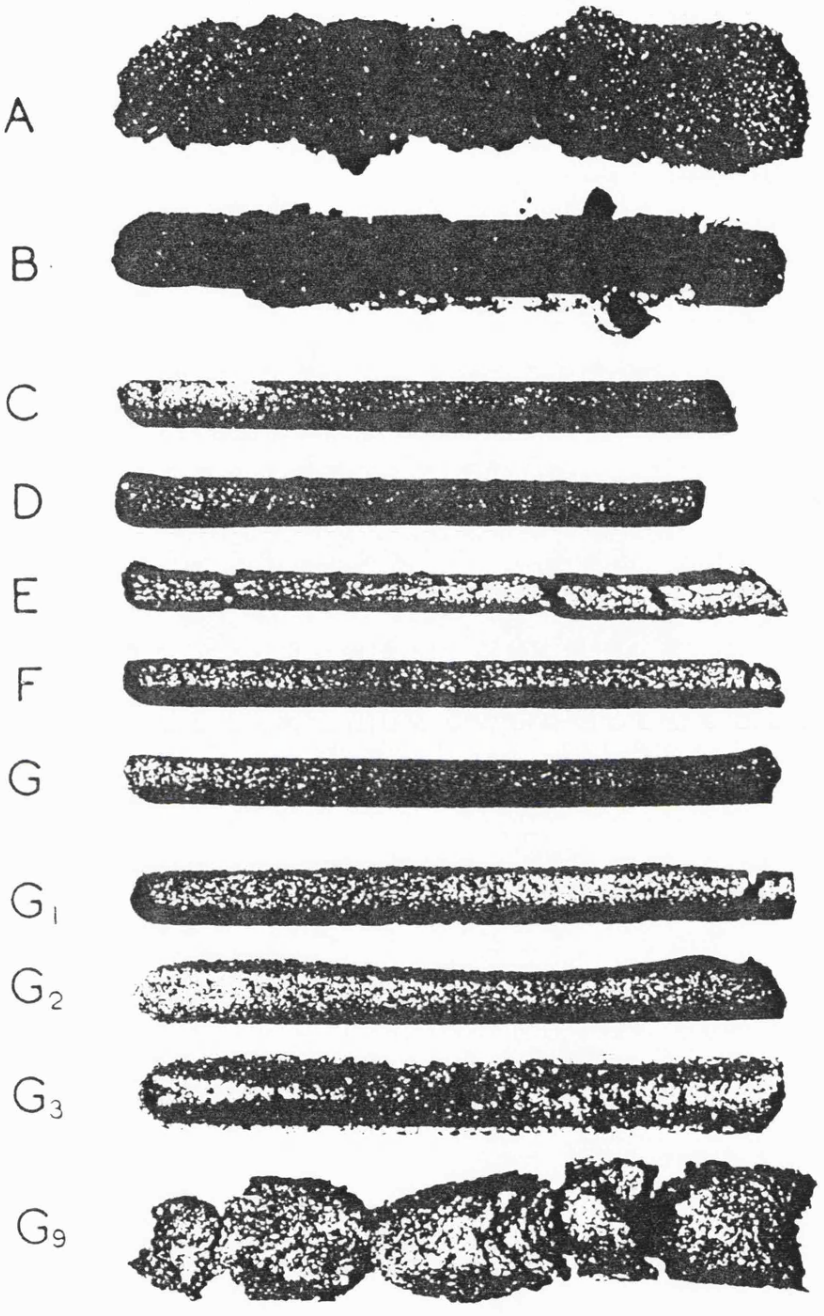


Figure 2.4 Gray-King coke types.

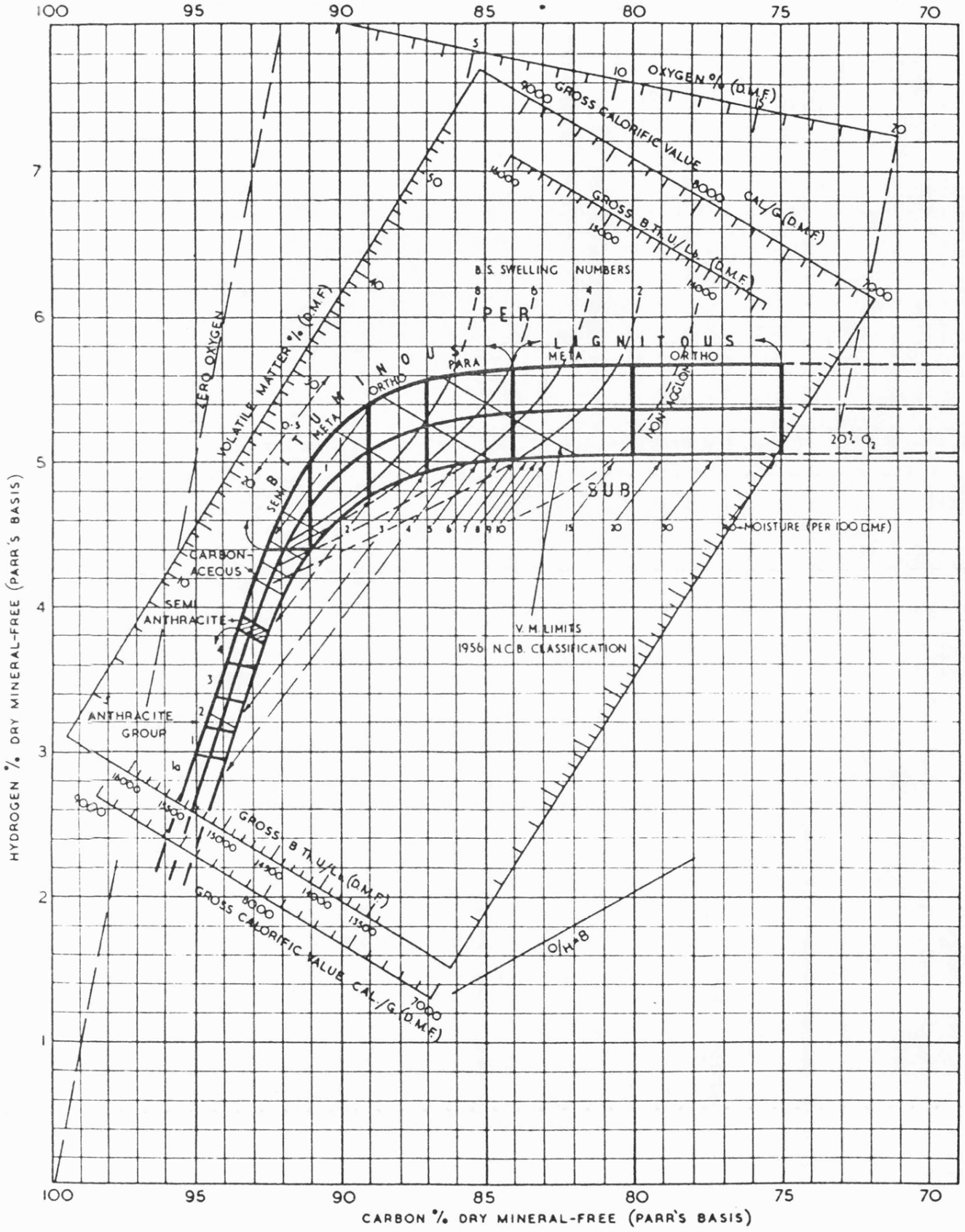


Figure 2.5 Seyler's coal chart.

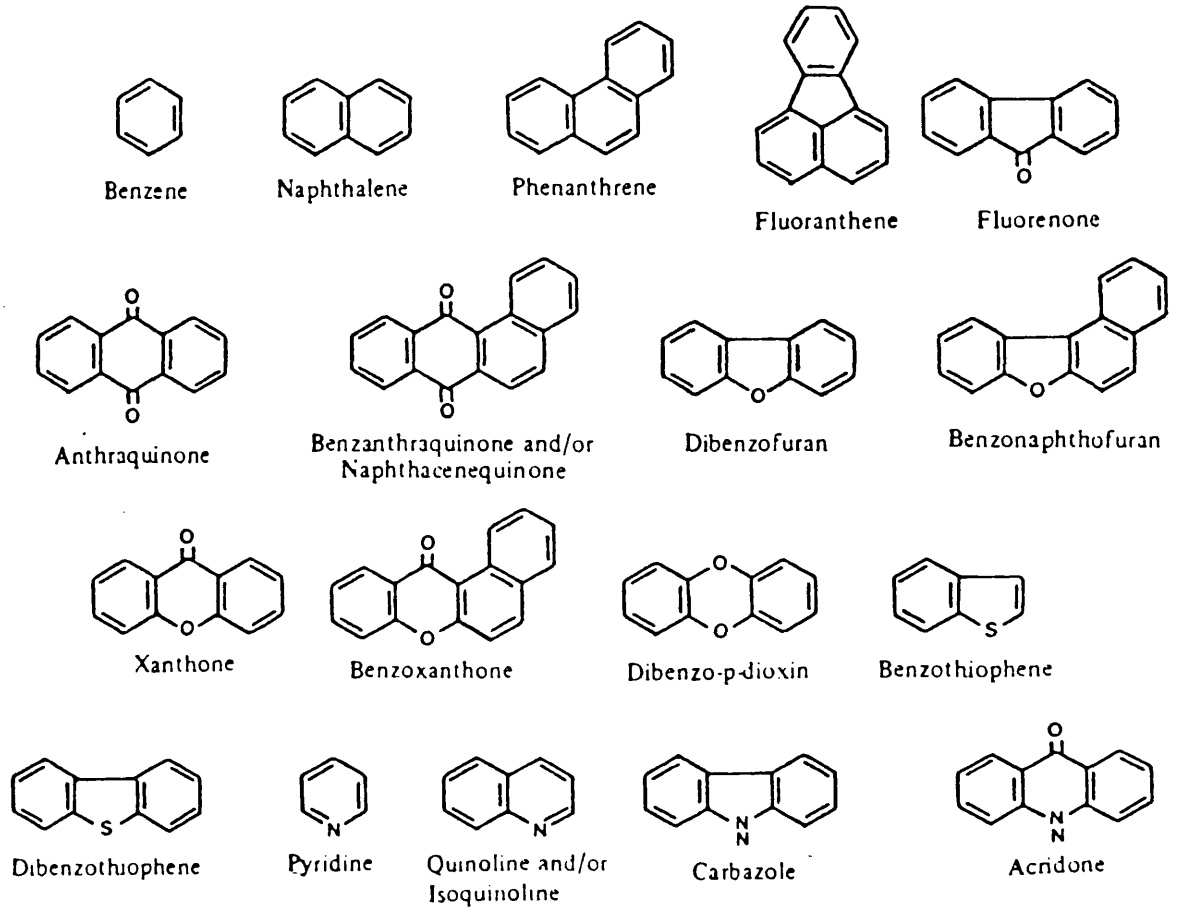


Figure 2.6 Aromatic units indigenous to coal.

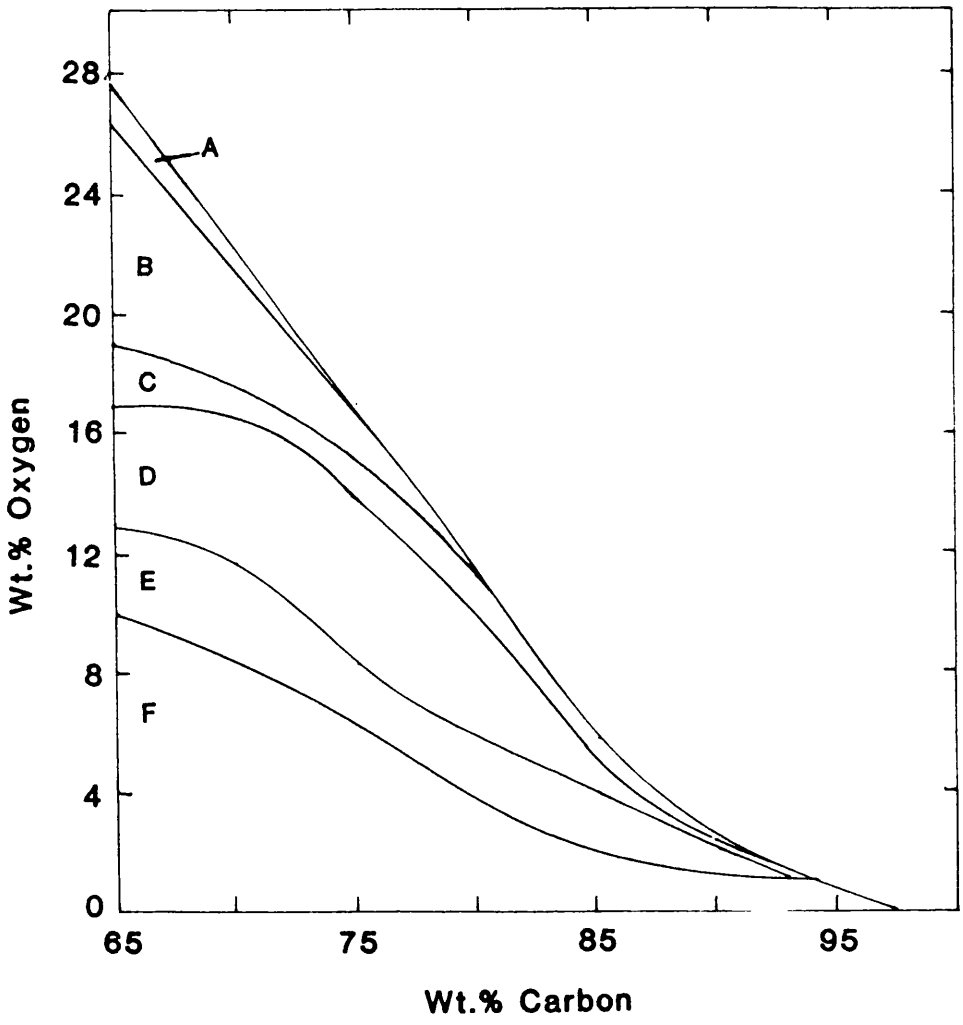


Figure 2.7 Oxygen functional groups in coal: (A) $OCH_3$; (B) COOH; (C) C=O; (D) OH acid; (E) OH alcohol; (F) C-O-C and other groups.

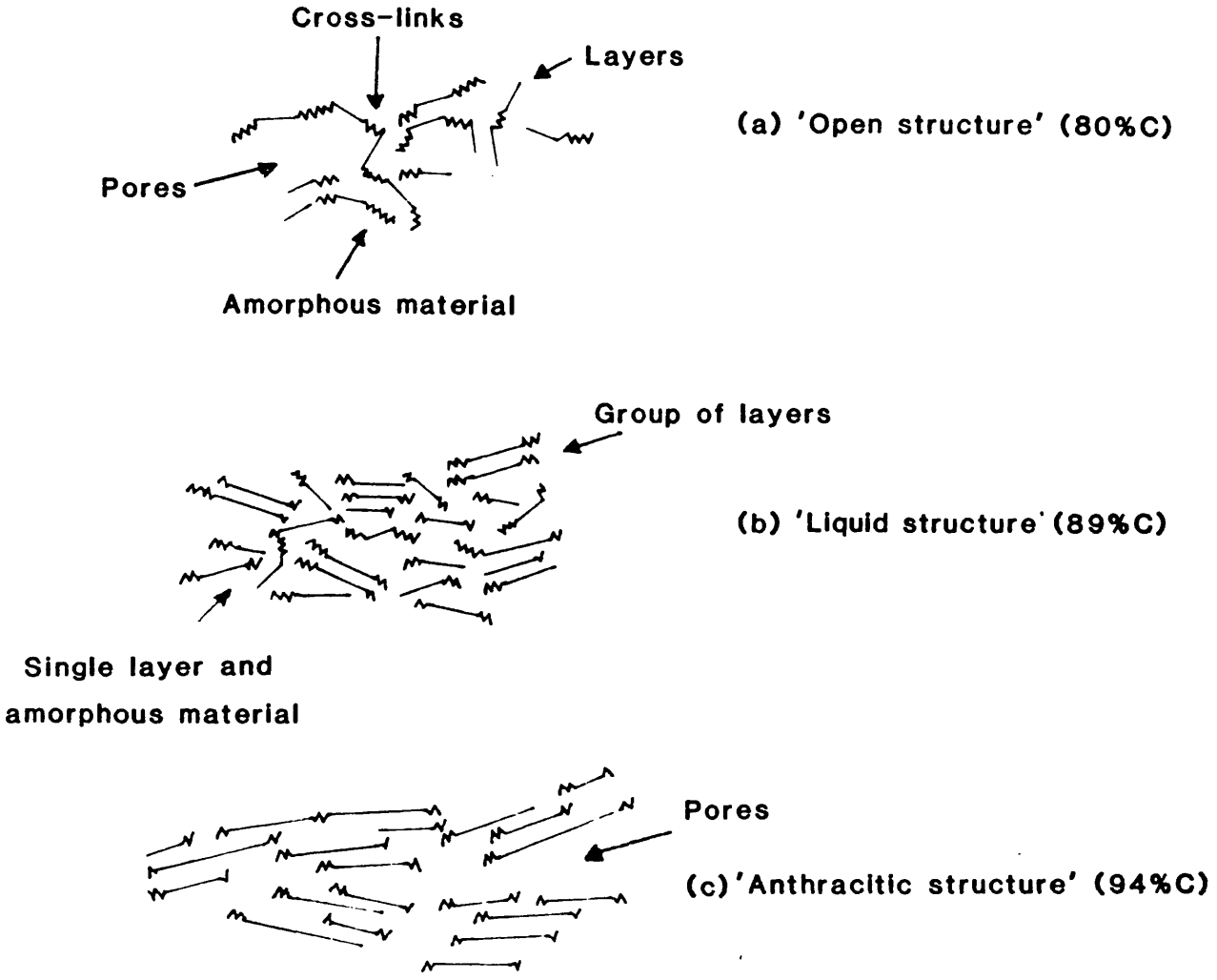


Figure 2.8 Structure types for (a) a low rank coal, (b) a coking coal and (c) an anthracite.

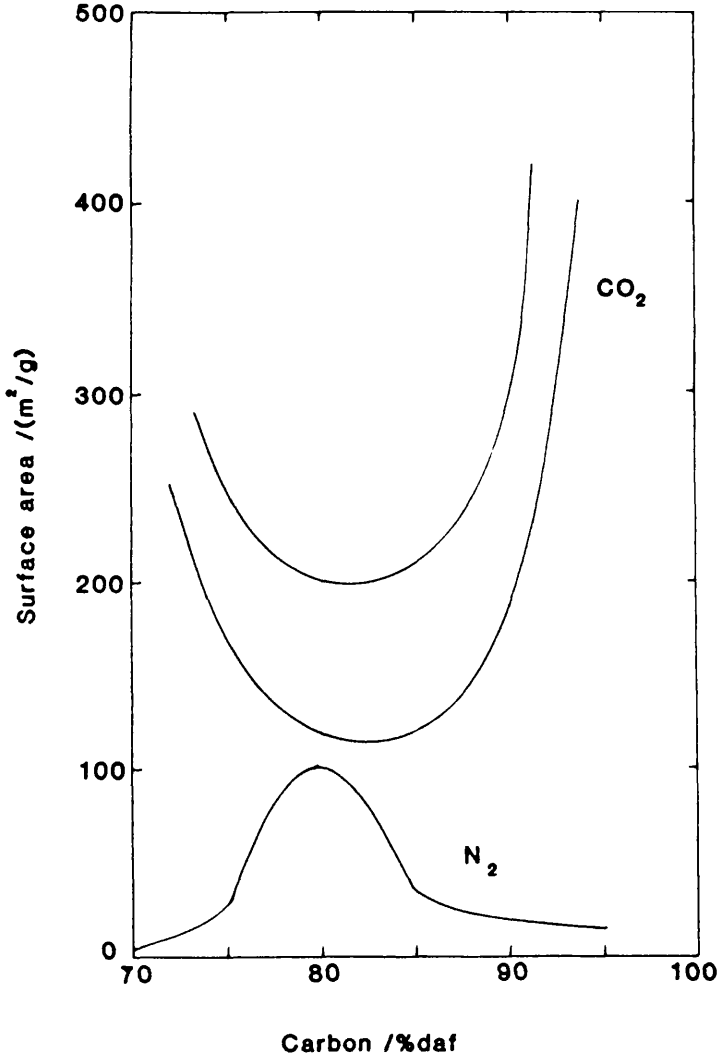


Figure 2.9 Pore area *versus* coal rank, determined by $CO_2$ and $N_2$ adsorption.

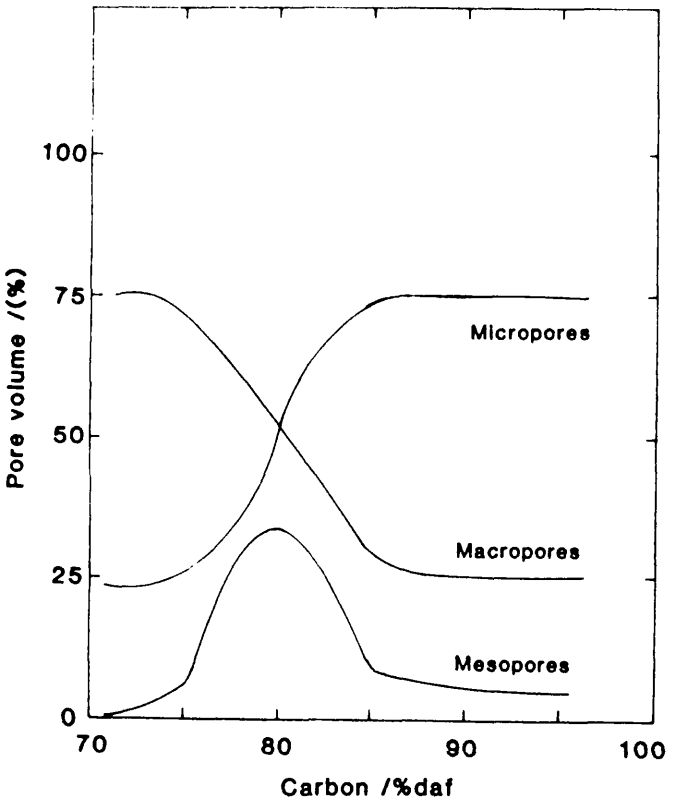


Figure 2.10 Pore volume *versus* coal rank for different size pores.

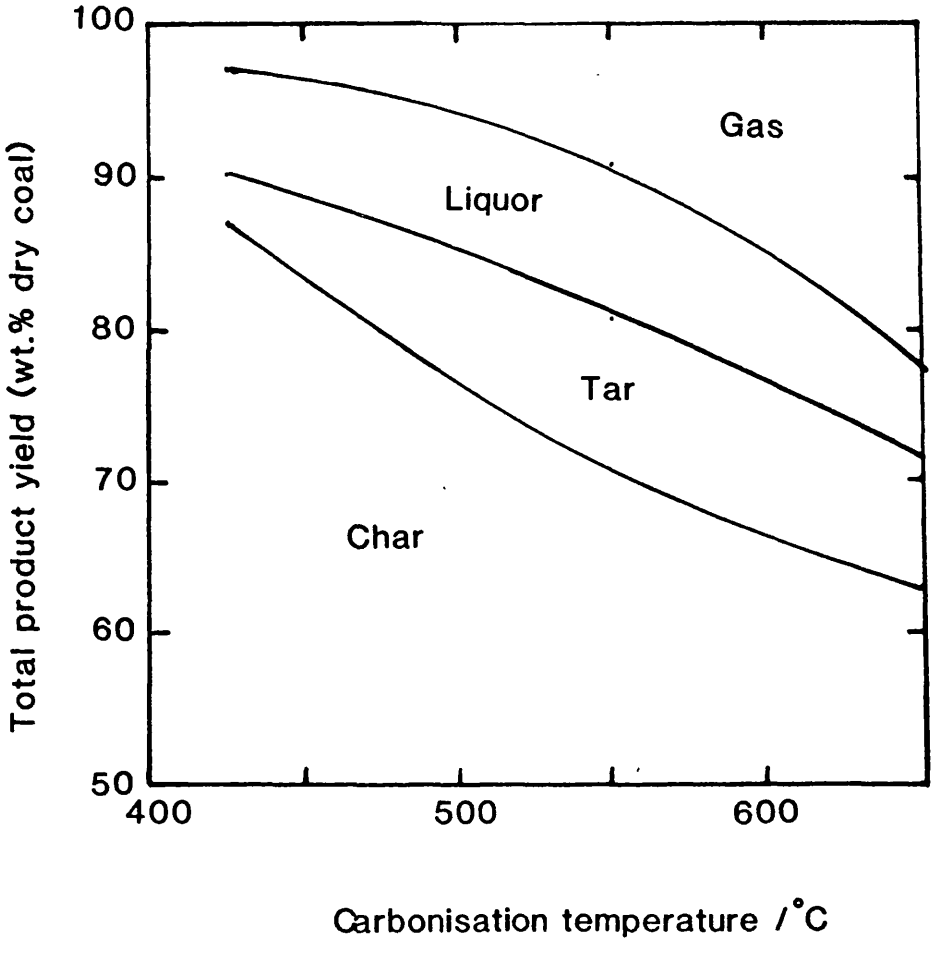


Figure 3.1 Typical distribution of carbonisation products as a function of carbonisation temperature.

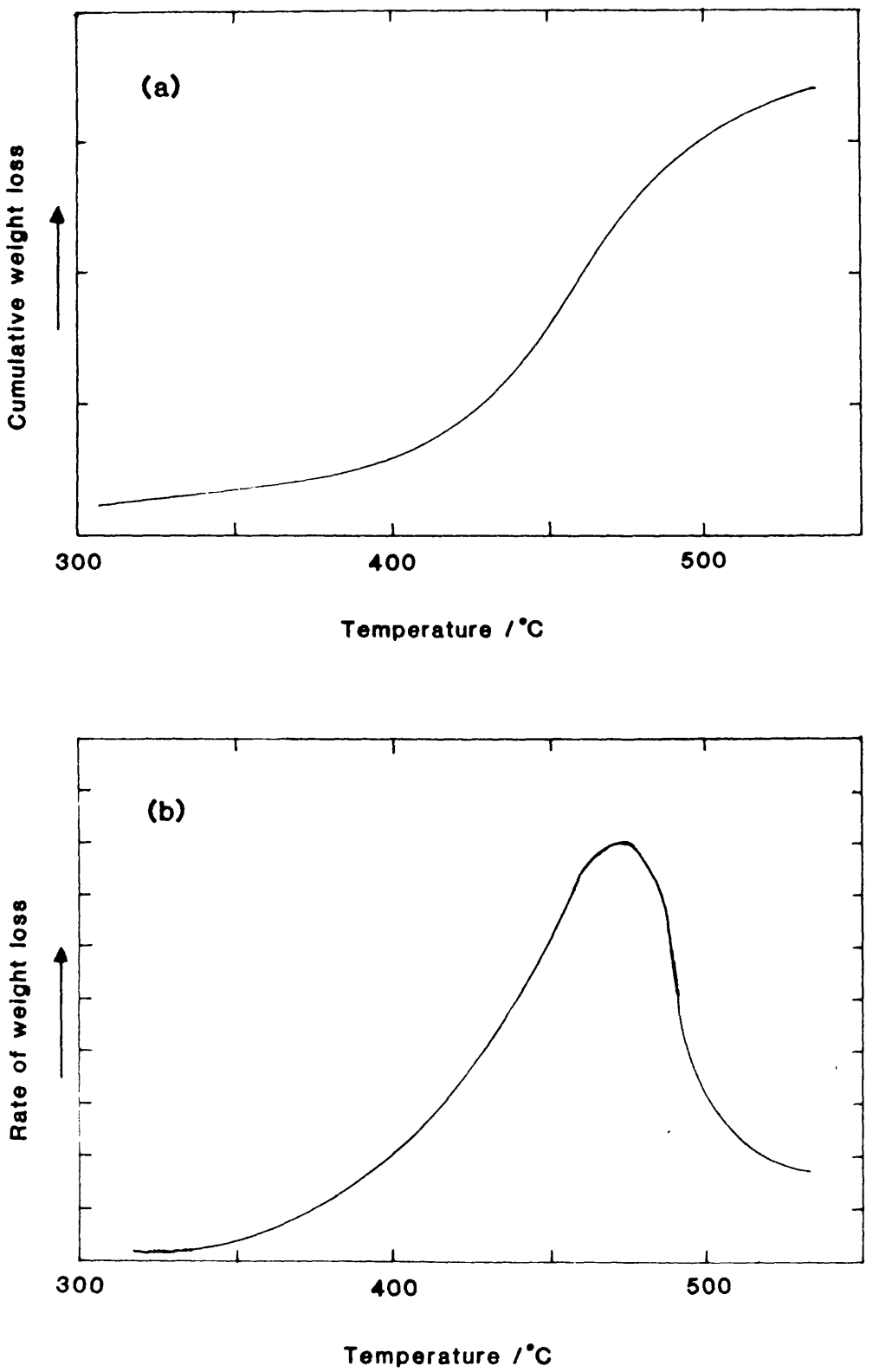


Figure 3.2 Typical variation of (a) cumulative weight loss and (b) weight loss rate with temperature.

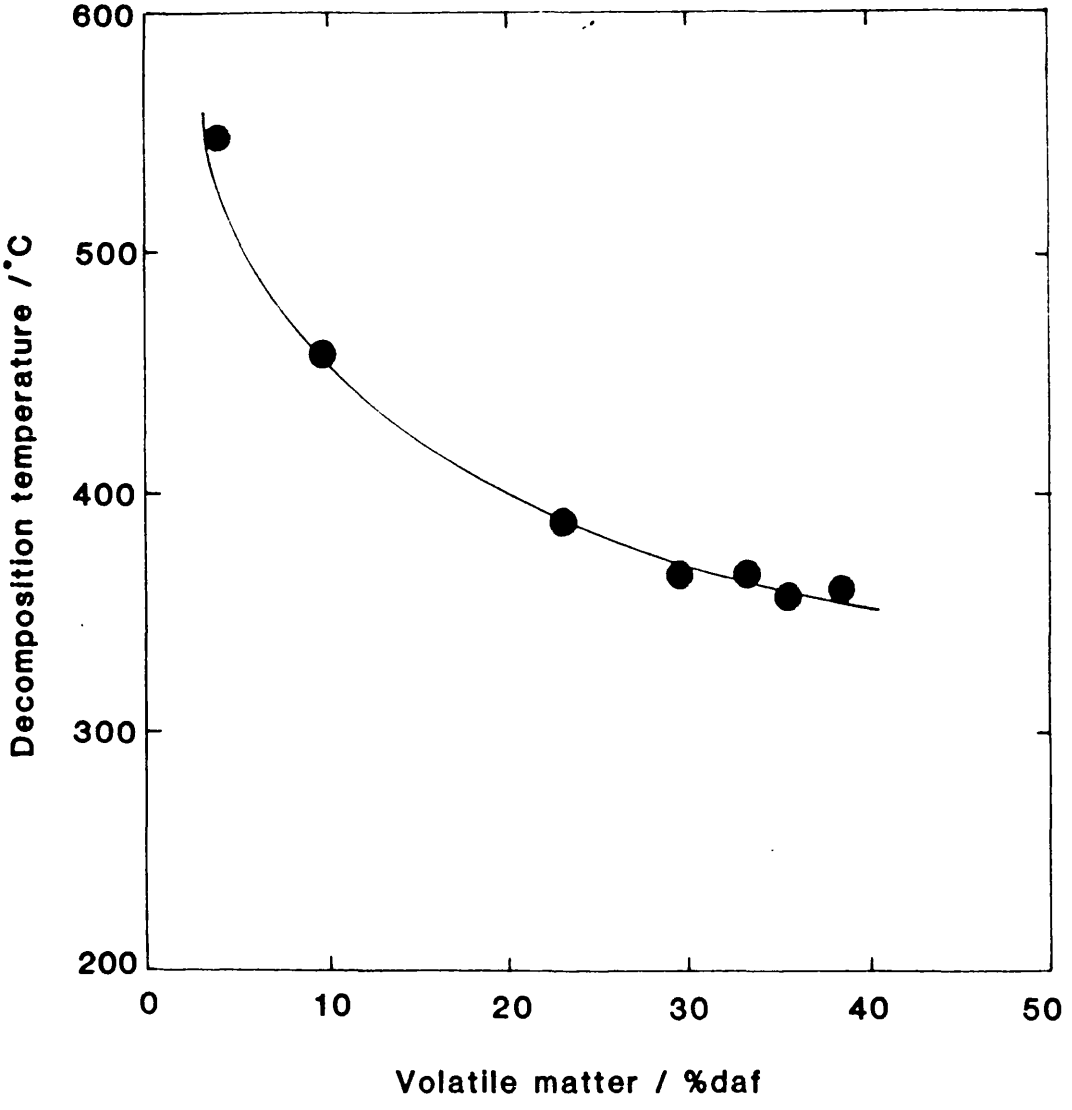


Figure 3.3 Variation of decomposition temperature $T_d$ with rank.

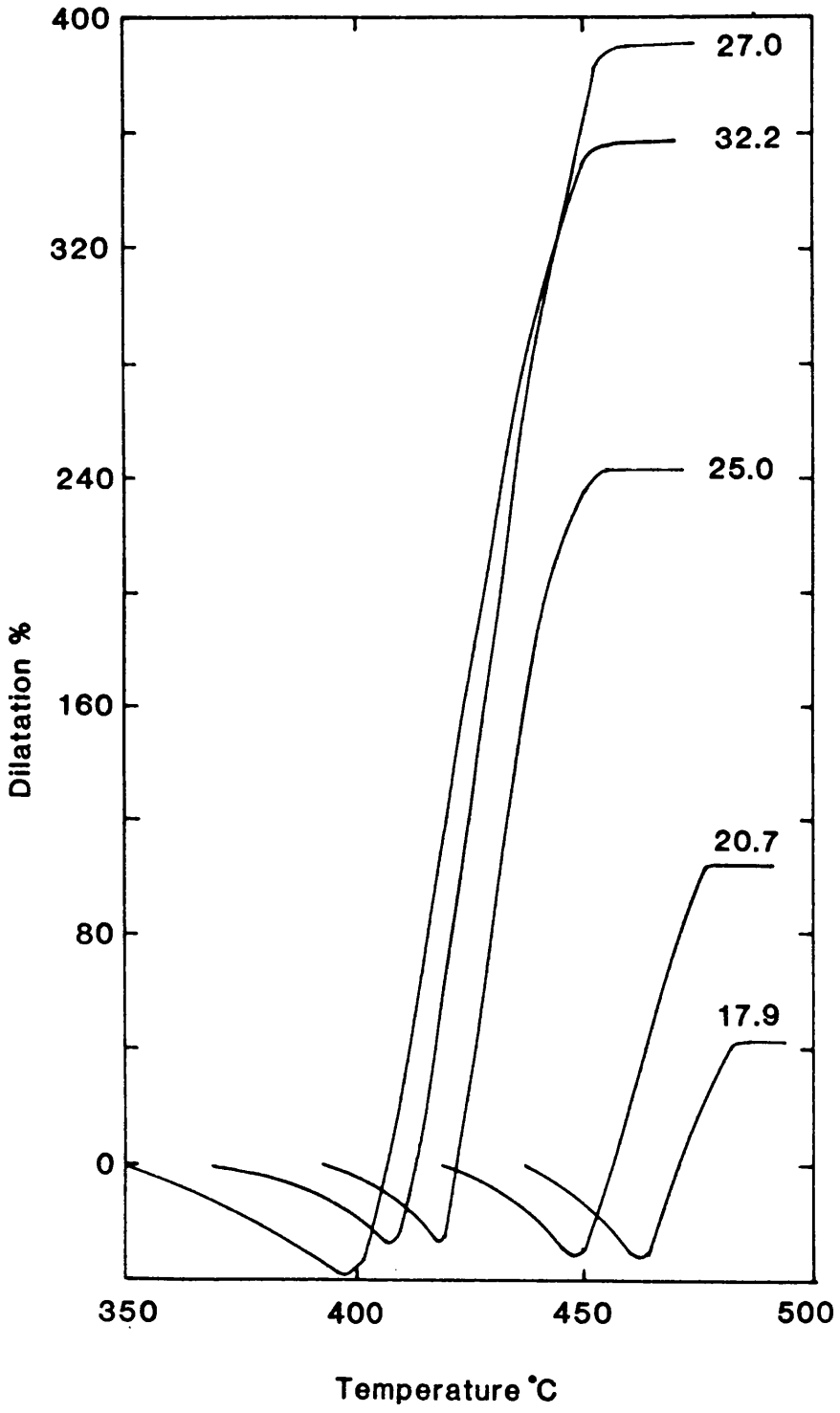


Figure 3.4 Contraction/expansion behaviour for coals of different rank (numbers indicate % volatile matter content).

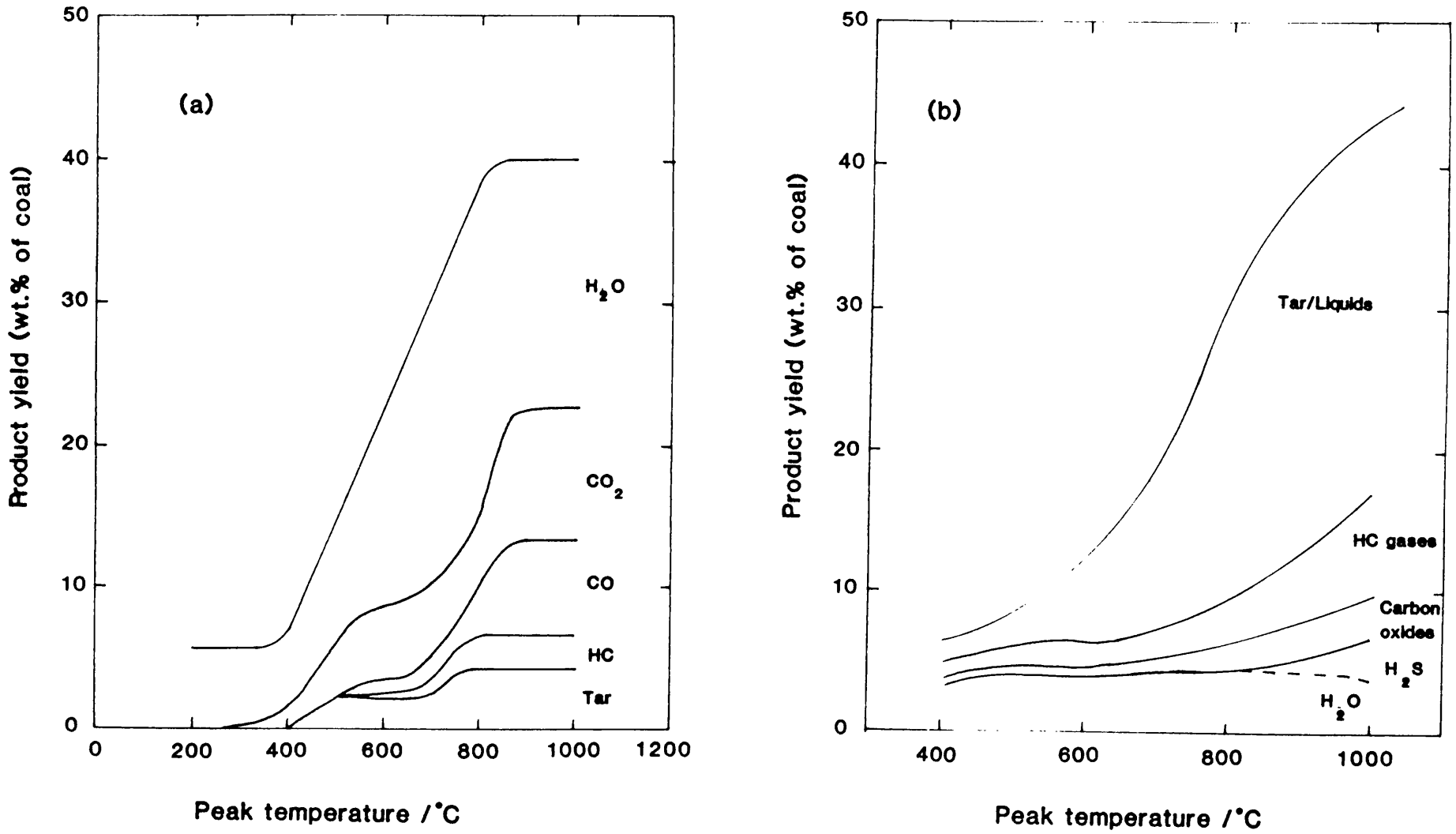


Figure 3.5 Pyrolysis product distributions from (a) lignite and (b) bituminous coal, heated to different peak temperatures.

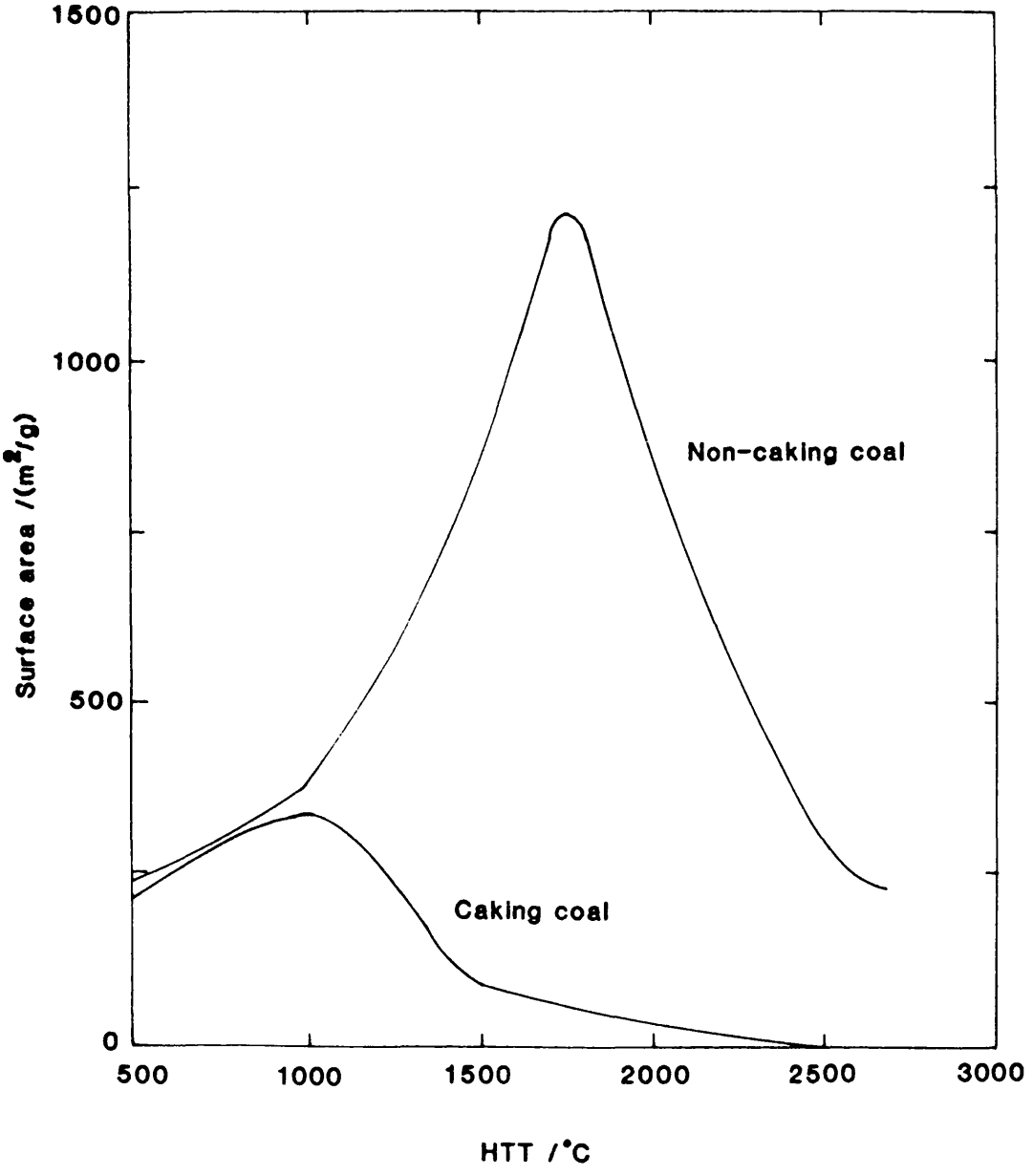


Figure 3.6 Effect of pyrolysis temperature on internal surface area for caking and non-caking coals.

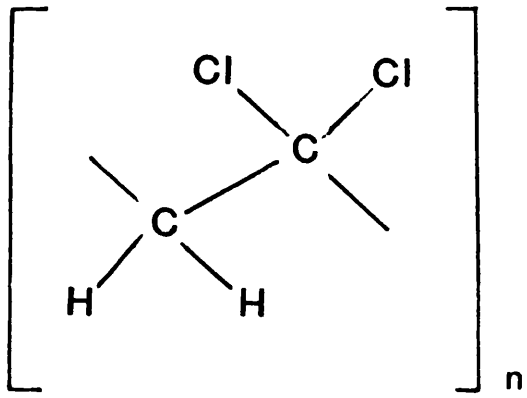


Polyvinylidene chloride

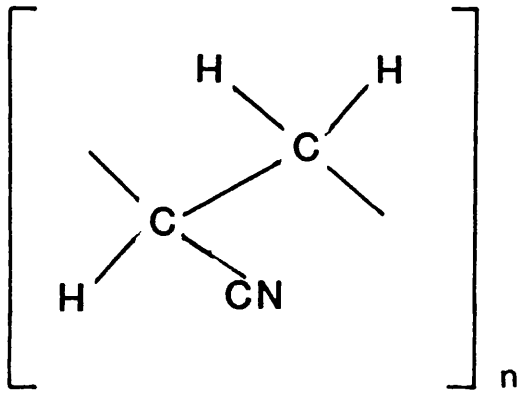


Polyacrylonitrile

Figure 3.7 Structure of polyvinylidene chloride and polyacrylonitrile.

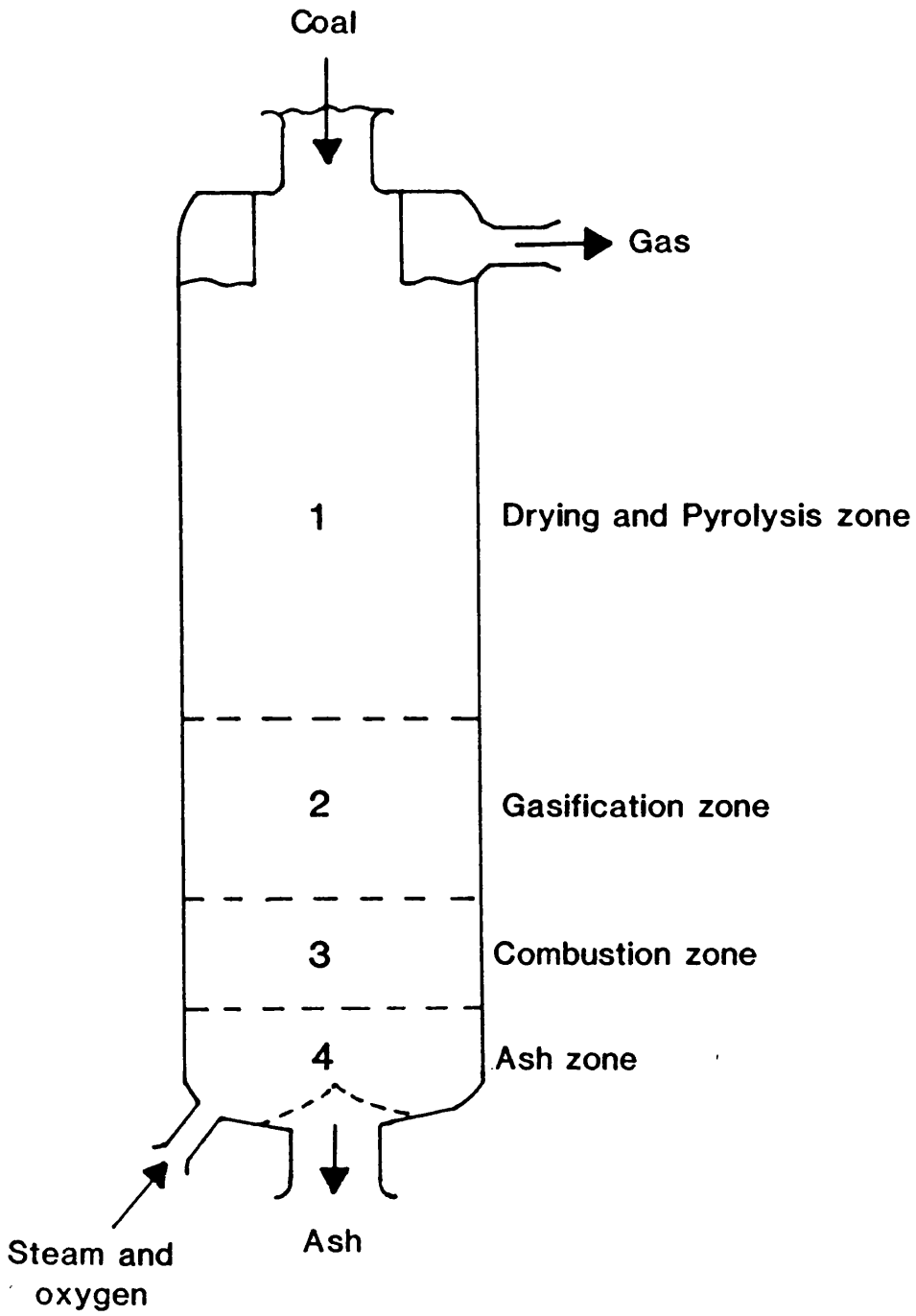


Figure 4.1 Reaction zones in a dry ash fixed-bed gasifier.

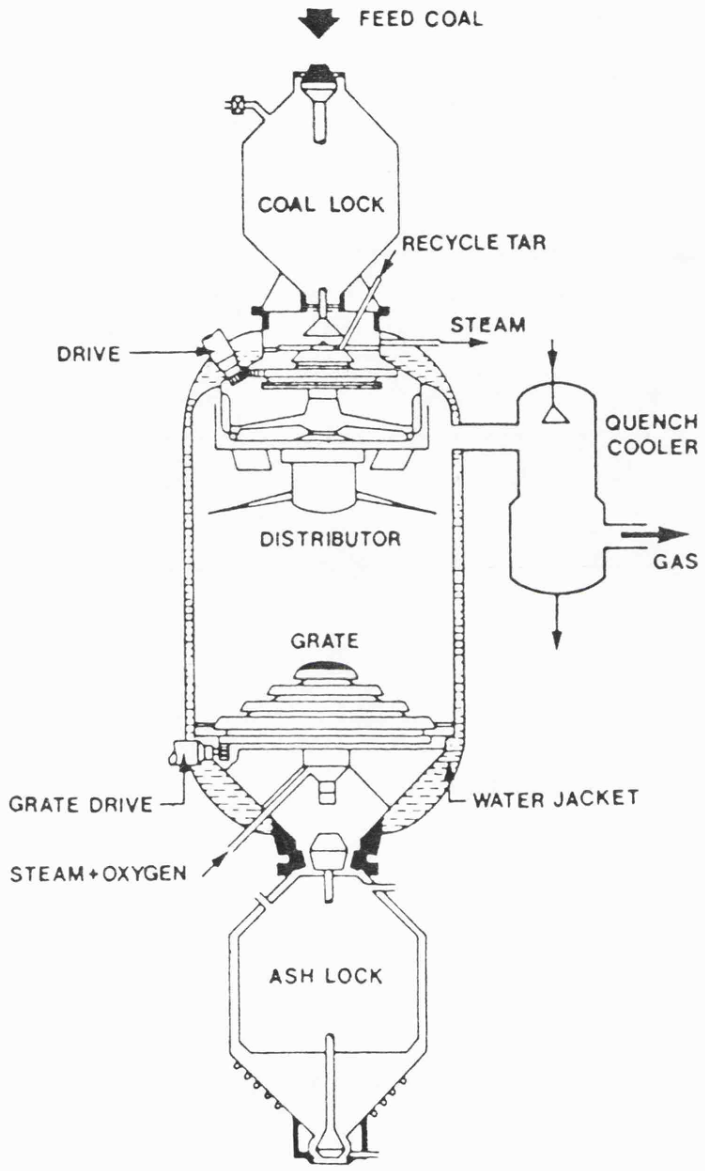


Figure 4.2 Schematic of a dry ash Lurgi pressure gasifier.

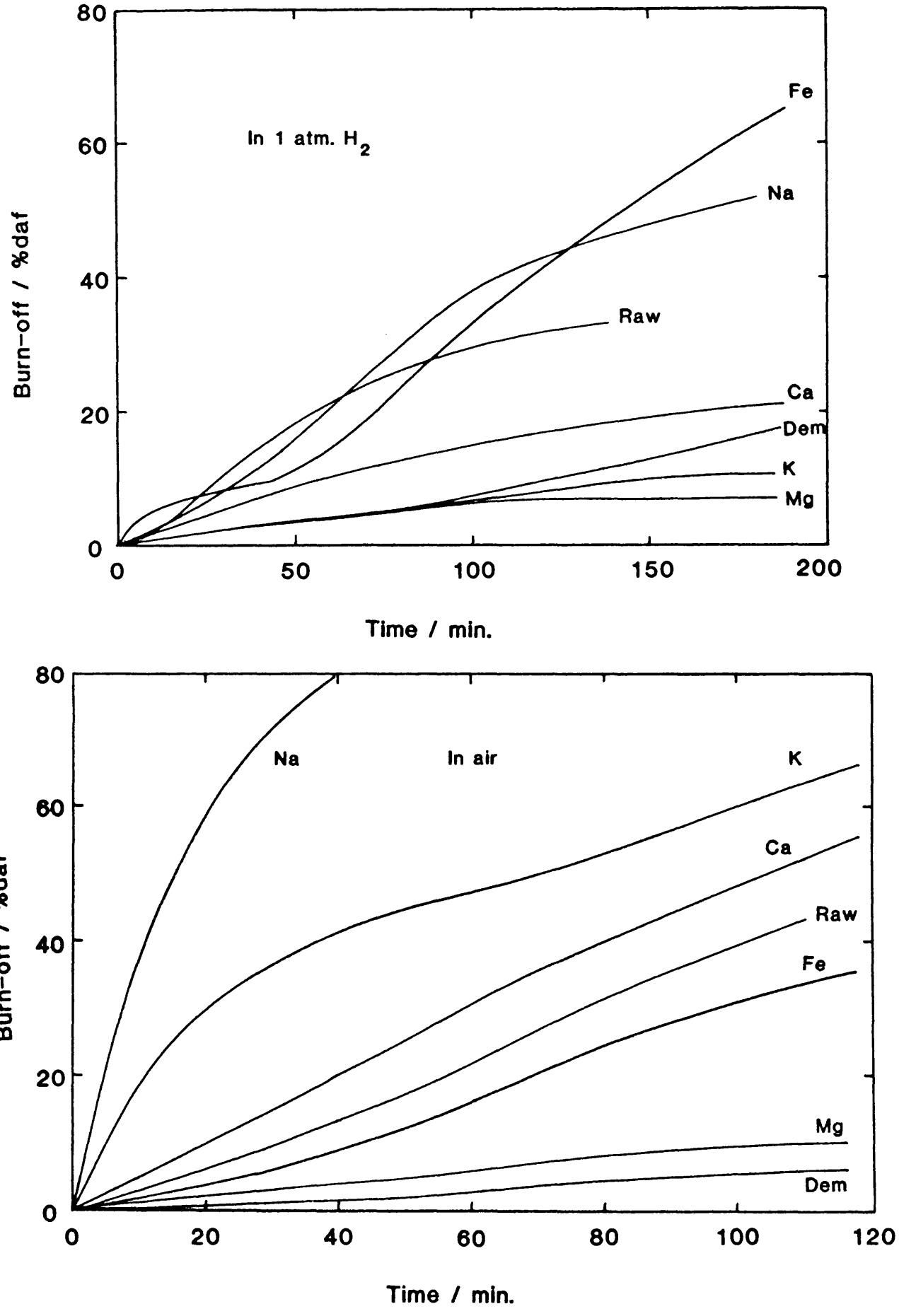


Figure 4.3 Catalytic effects of metal cations on lignite char reactivity at 790 °C in different atmospheres.

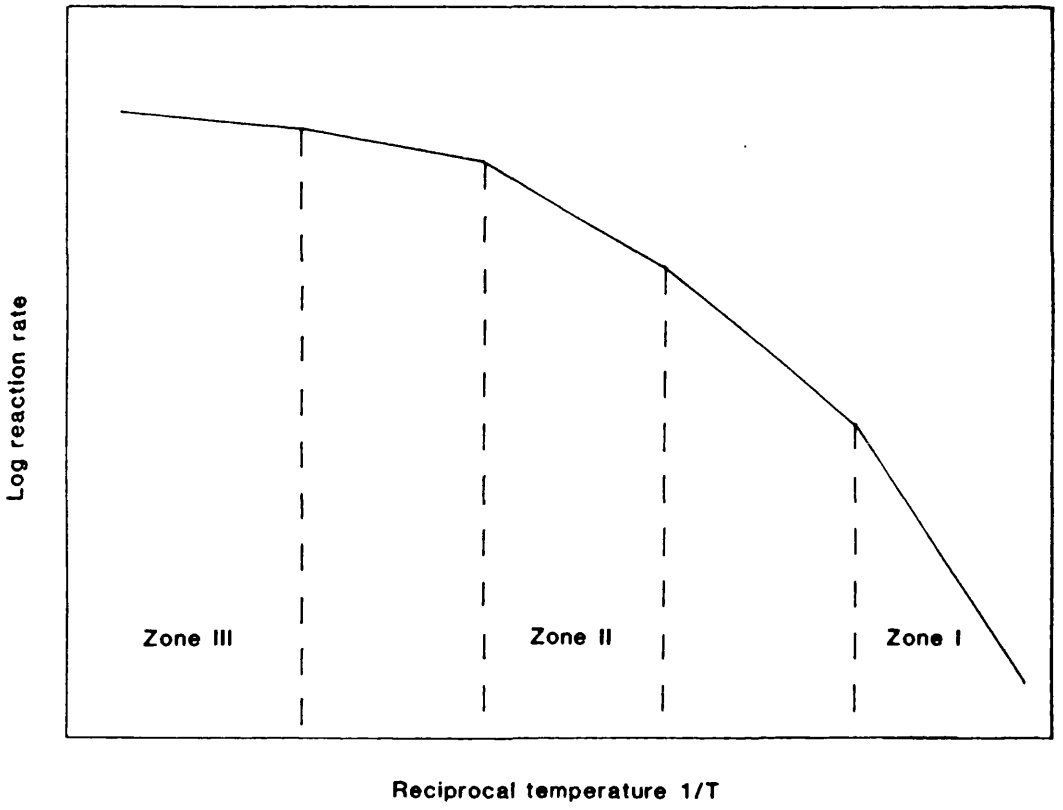


Figure 4.4 The three ideal zones representing the change of reaction rate of a porous char with temperature.

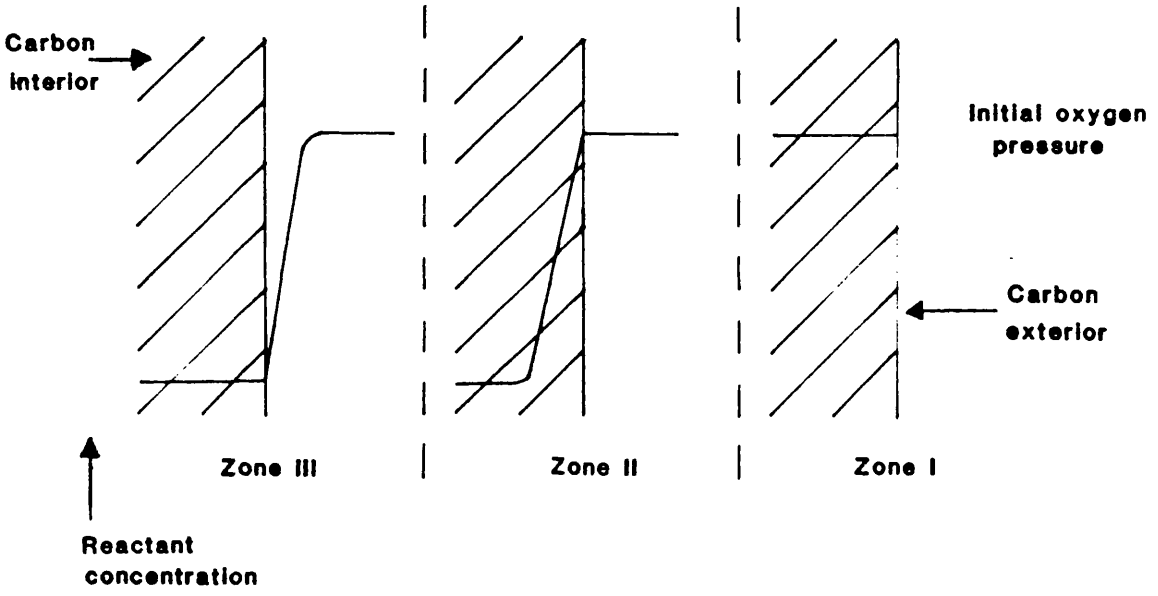


Figure 4.5 Diagram indicating how the concentration (pressure) of reactant may vary relative to the interior (zone I) and exterior (zone III) of the carbon specimen.

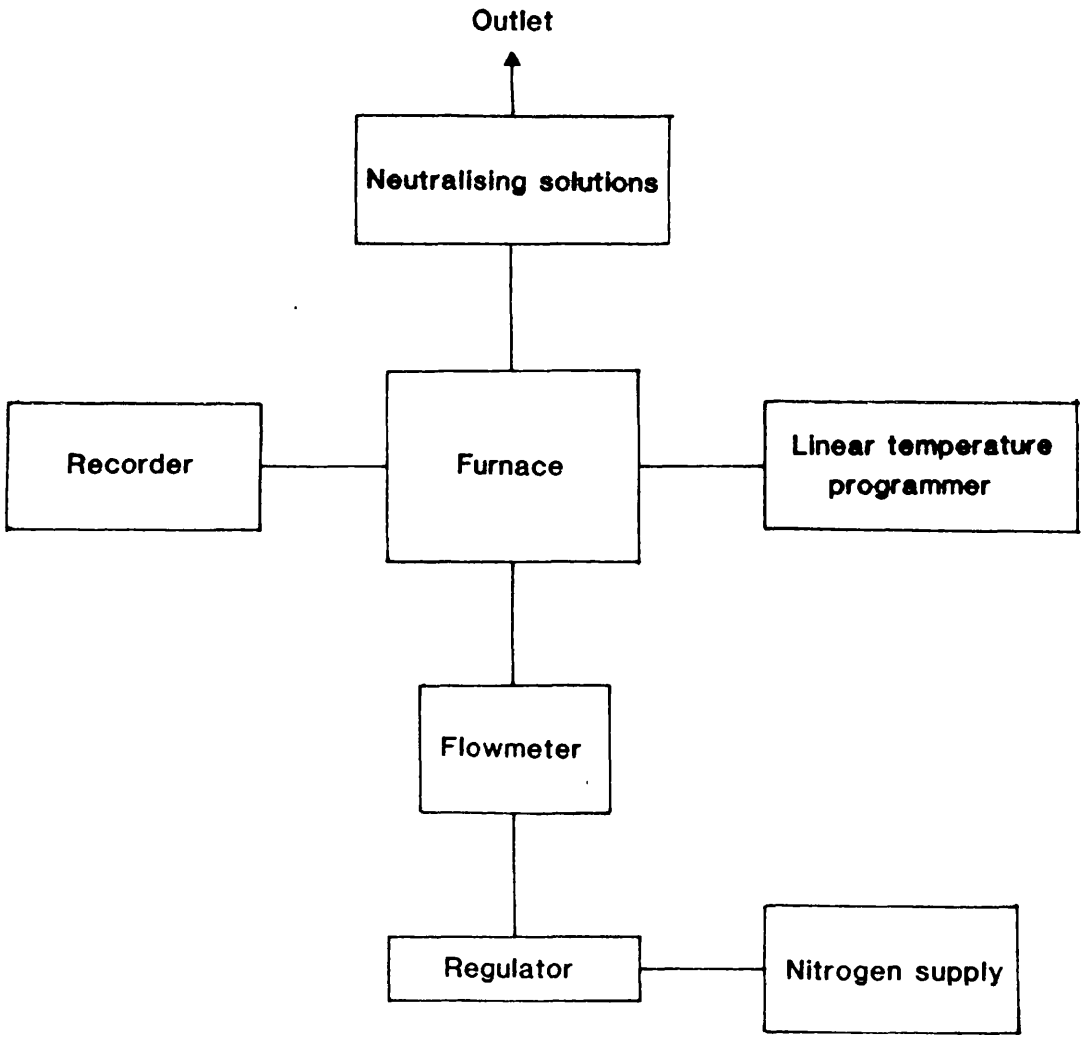


Figure 5.1 Block diagram of the PVDC/PAN heat treatment circuit.

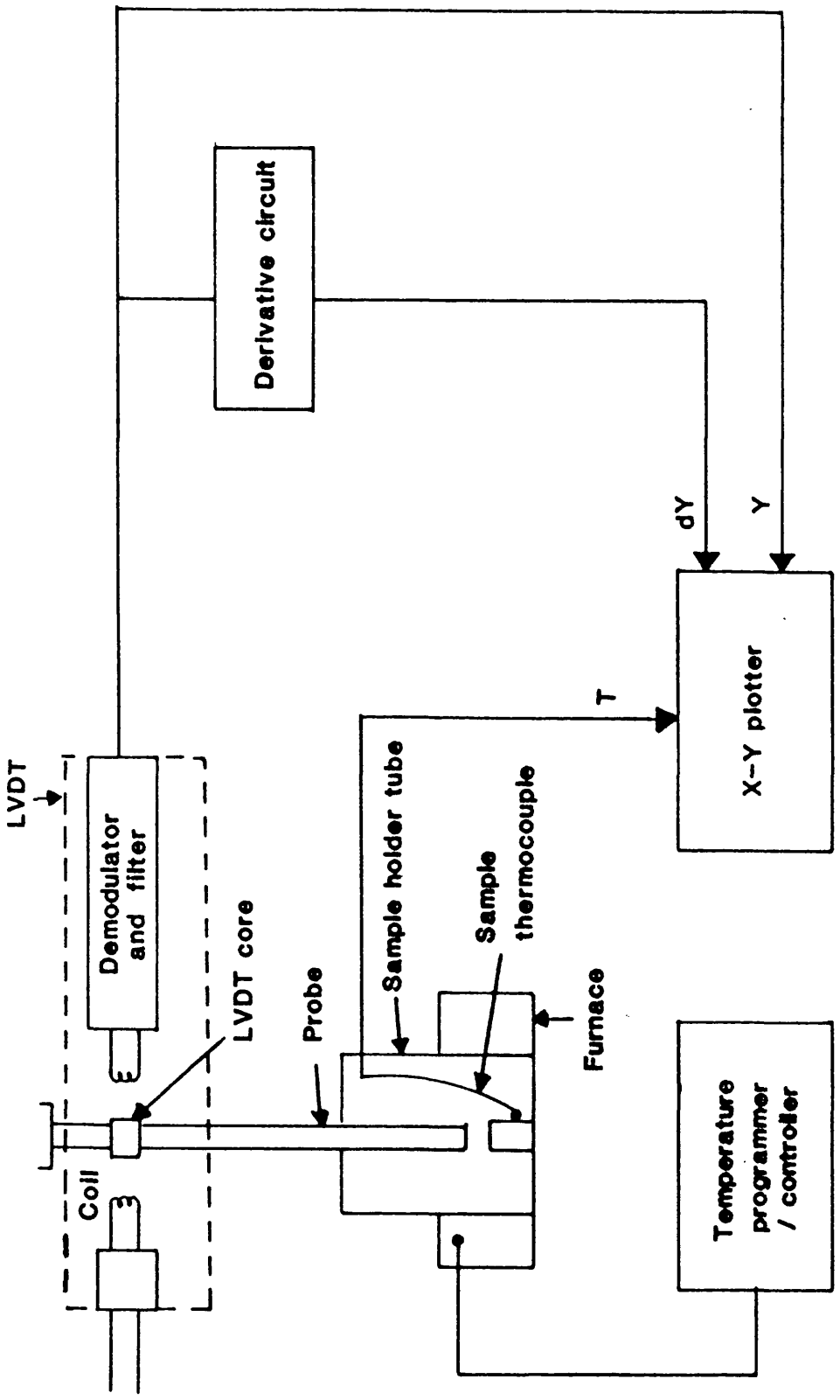


Figure 6.1 Block diagram of the dilatometry apparatus.

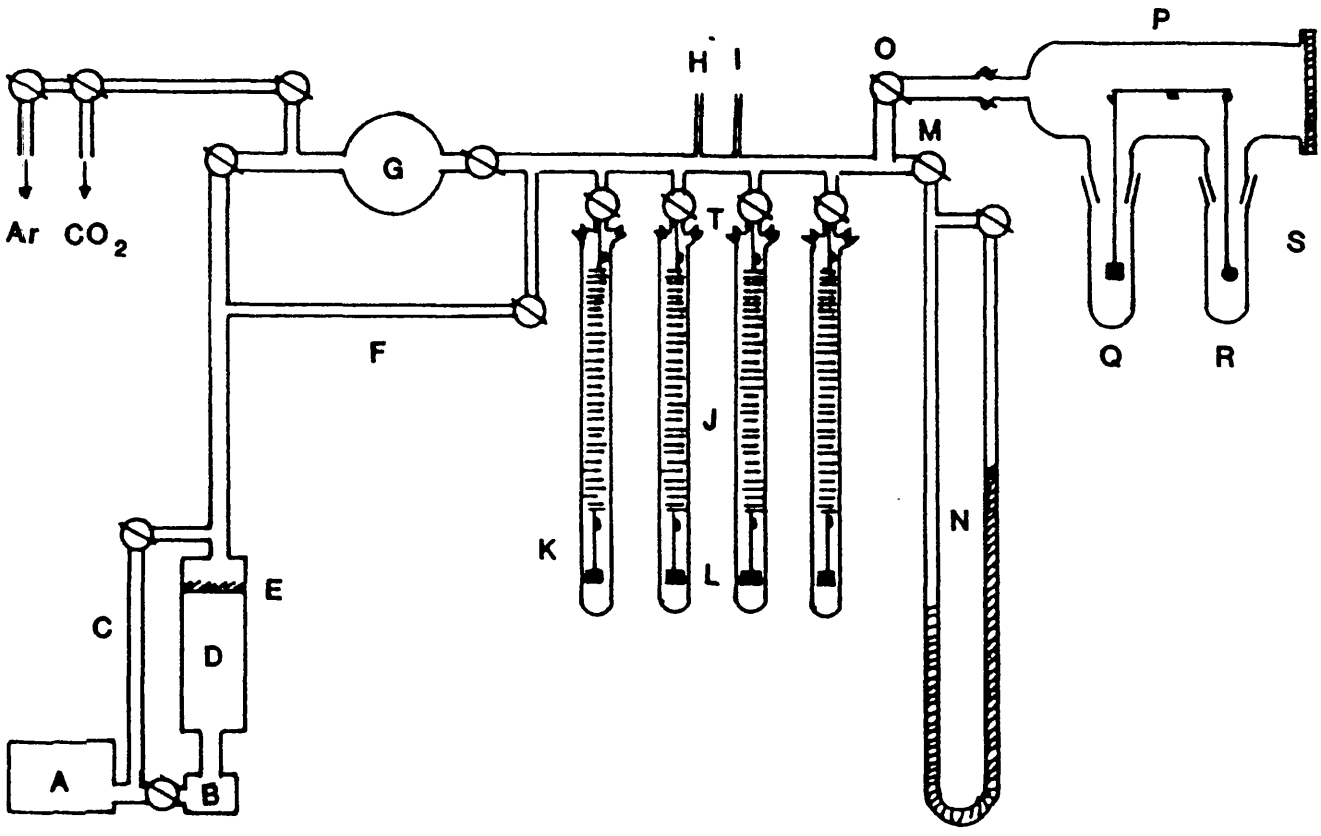


A Rotary pump
B Oil diffusion pump
C By-pass line
D Liquid nitrogen trap
E Baffle valve
F By-pass line
G One litre volume
H Pirani head
I Baratron head
J Hangdown tubes
K Sample support fibre
L Samples
M Manometer isolation tap
N Mercury manometer
O Microbalance isolation tap
P Microbalance case
Q Sample pan
R Counterweight pan
S Sample support fibre
T 'O'ring joints

Figure 7.1 The Adsorption Balance.

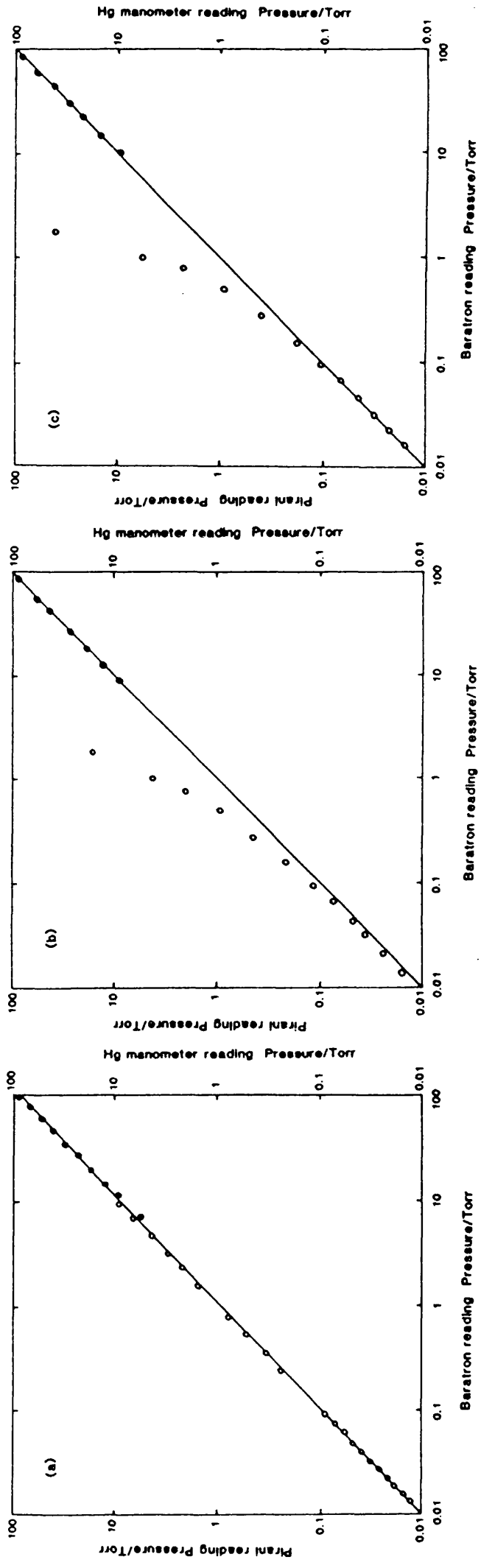


Figure 7.2 Calibration of the Pirani gauge and mercury manometer against the Baratron gauge for (a) air, (b) Ar and (c) $CO_2$.

—Baratron; O Pirani; ● mercury manometer

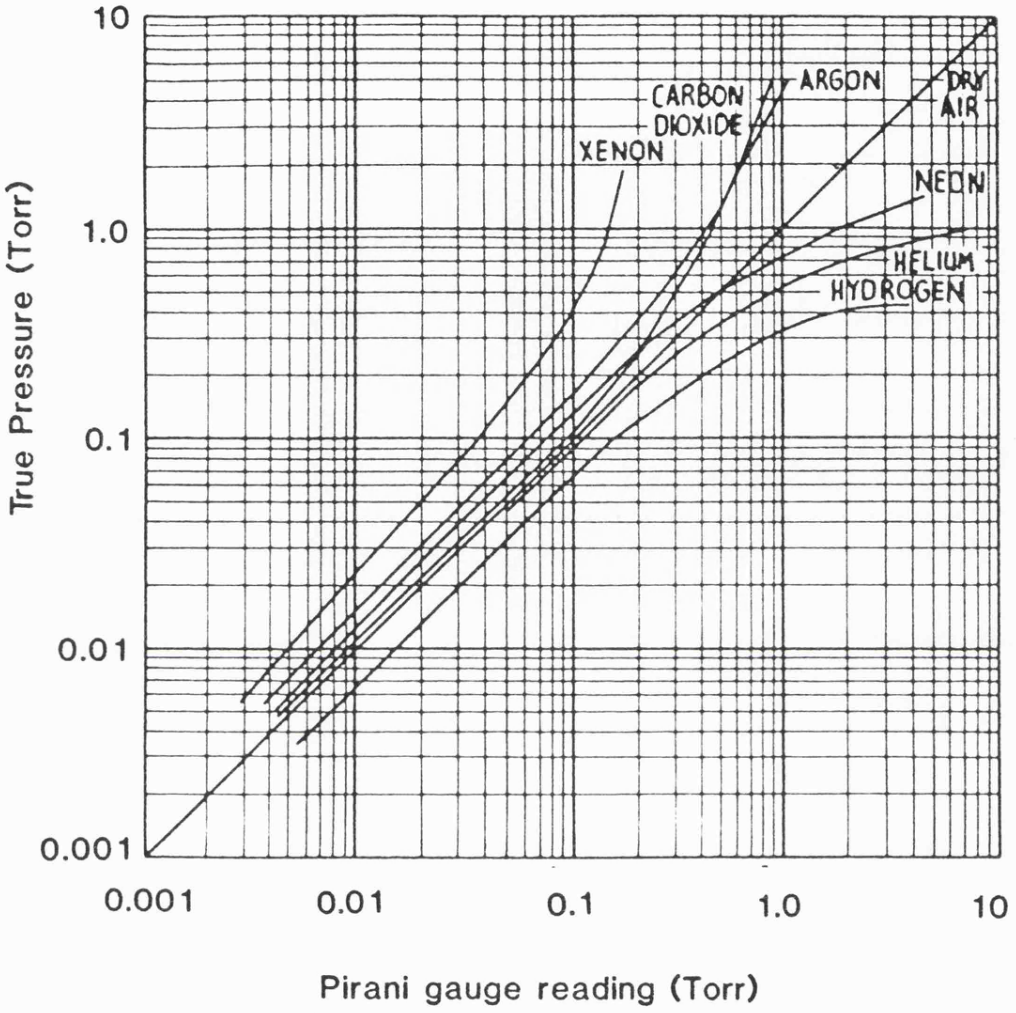


Figure 7.3 Correction curves for Pirani gauges.

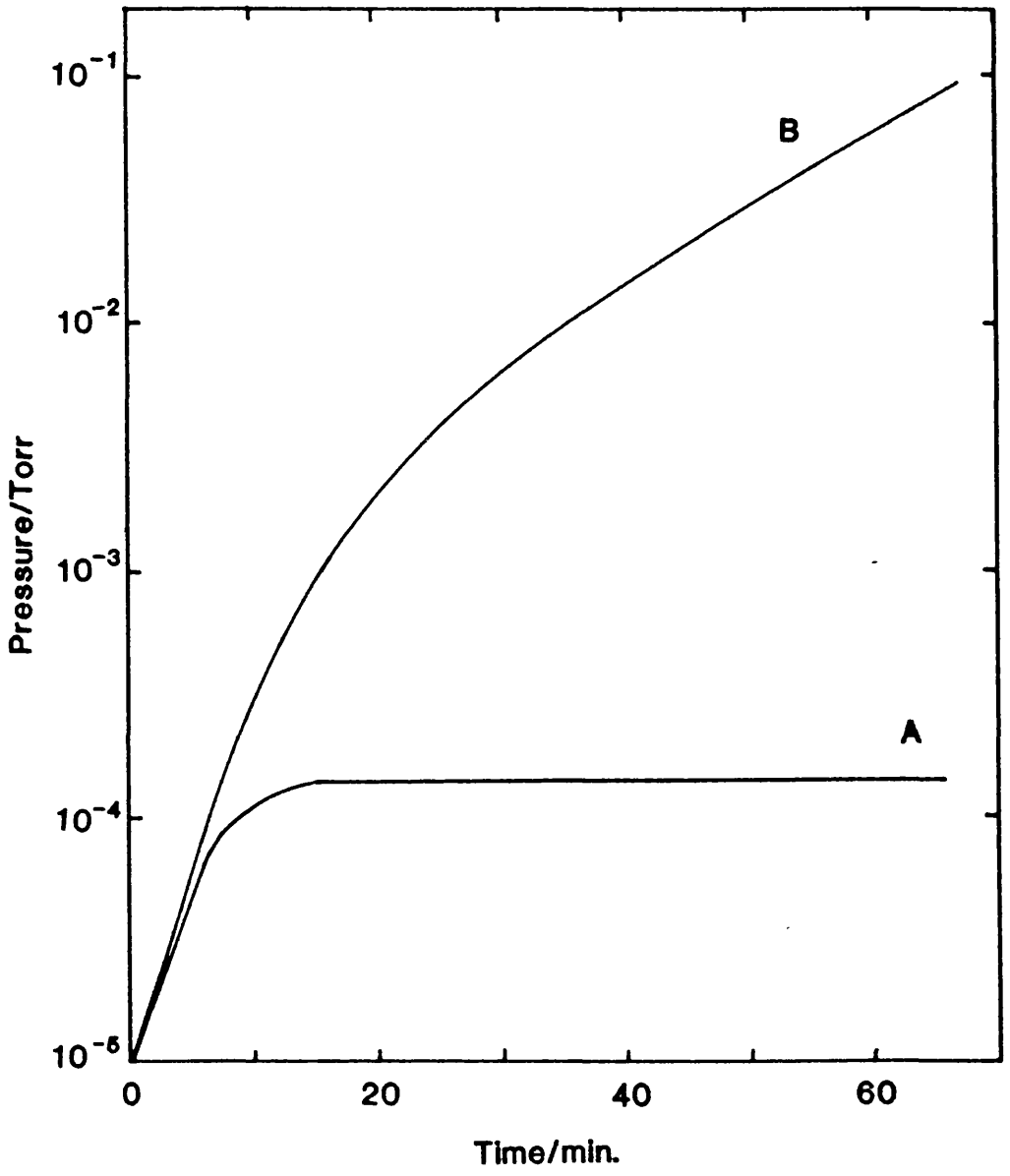


Figure 7.4 Adsorption balance leak rate plot. Curve A represents a virtual leak and curve B represents a real leak.

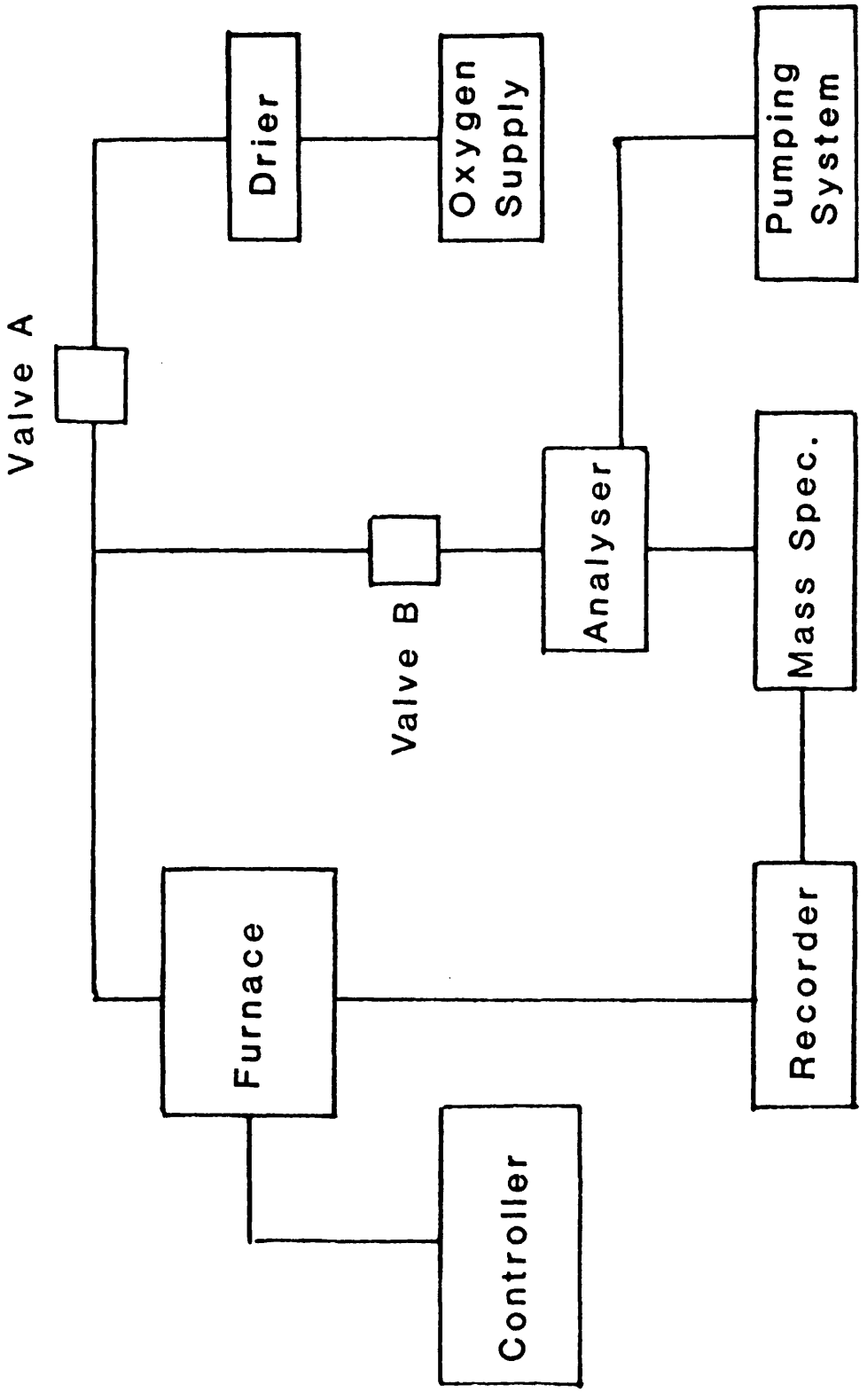


Figure 8.1 Block diagram of the TPD system.

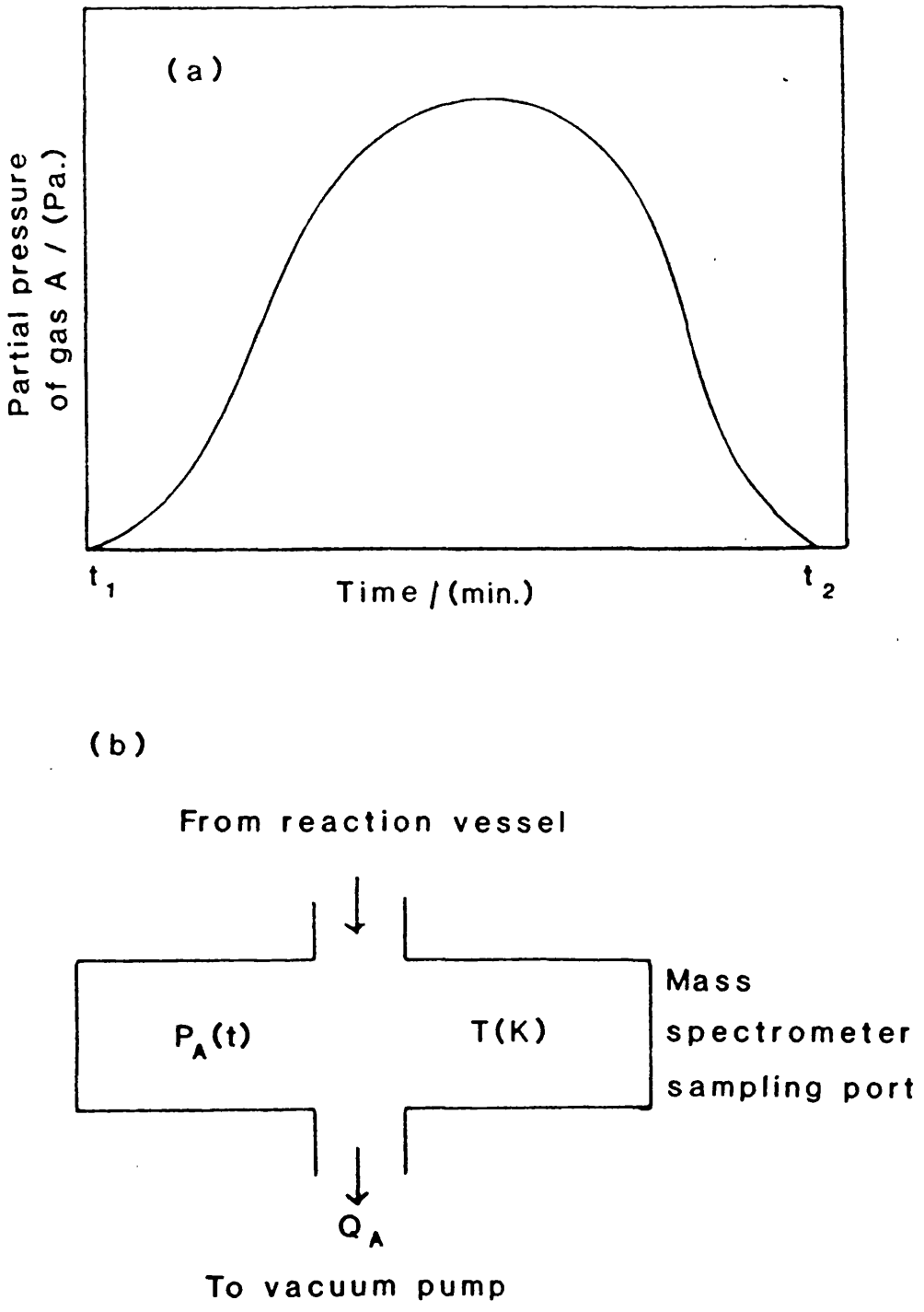


Figure 8.2 (a) Schematic desorption curve of partial pressure of gas A, $P_A(t)$ as a function of time, t
(b) Conditions at the mass spectrometer sampling port.

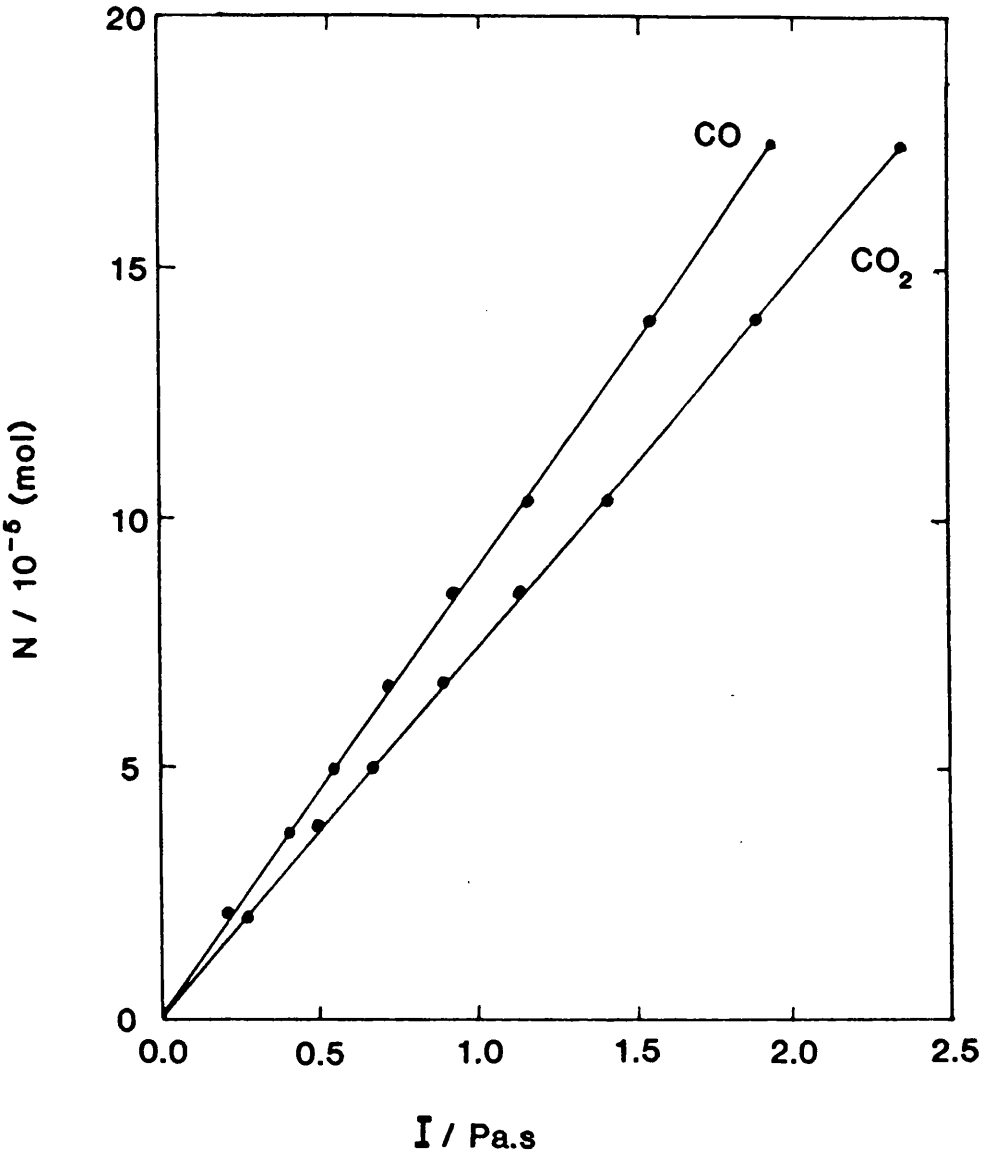


Figure 8.3 Calibration plot of the number of moles, N, of CO and $CO_2$ against the area, I/(Pa.s) under the P *versus* t curves for decomposition of calcium oxalate to CO and $CO_2$.

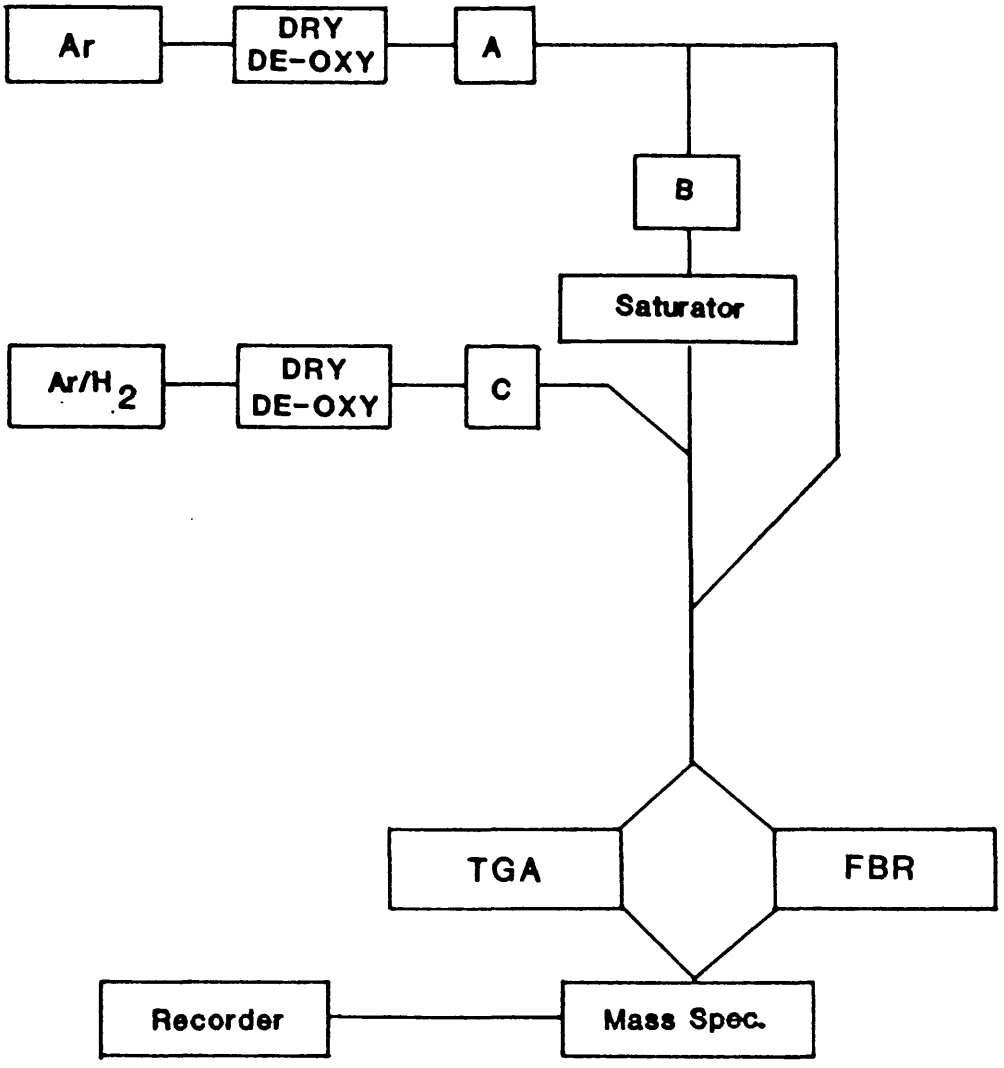


Figure 9.1 Block diagram of the steam gasification system (A, B and C represent flow meters/regulators).

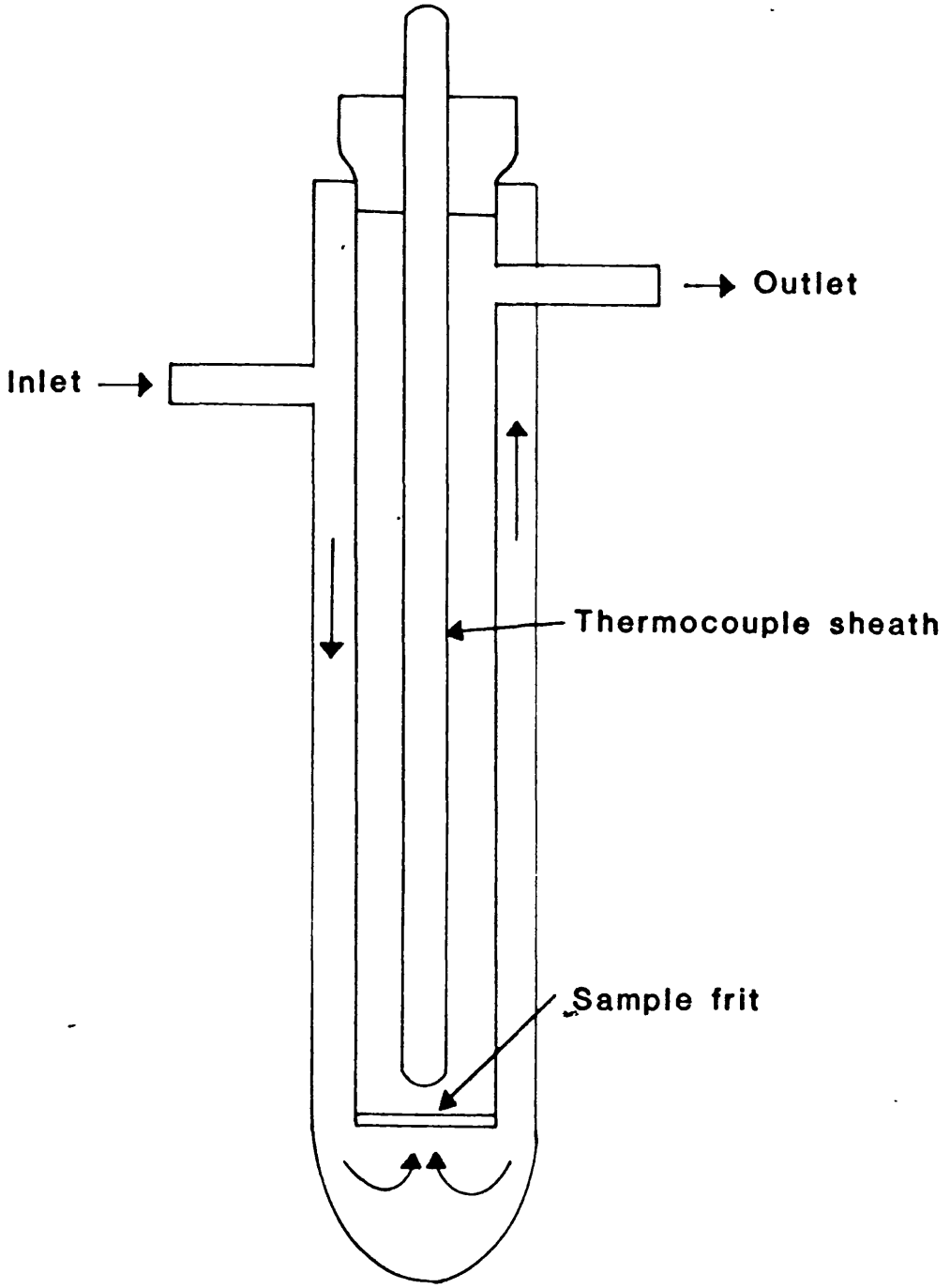


Figure 9.2 Quartz double-walled fixed-bed reactor.

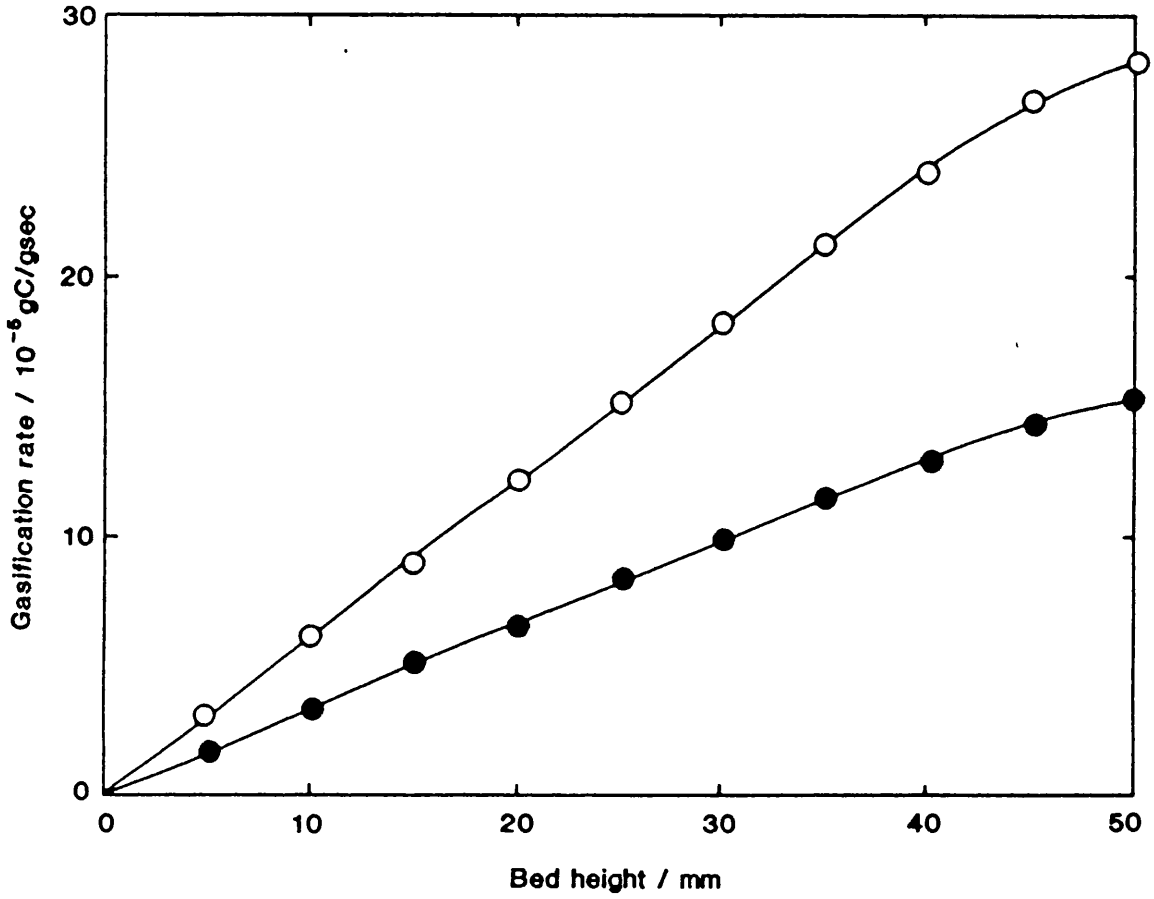


Figure 9.3 Effect of bed height in the fixed-bed reactor on gasification rate.

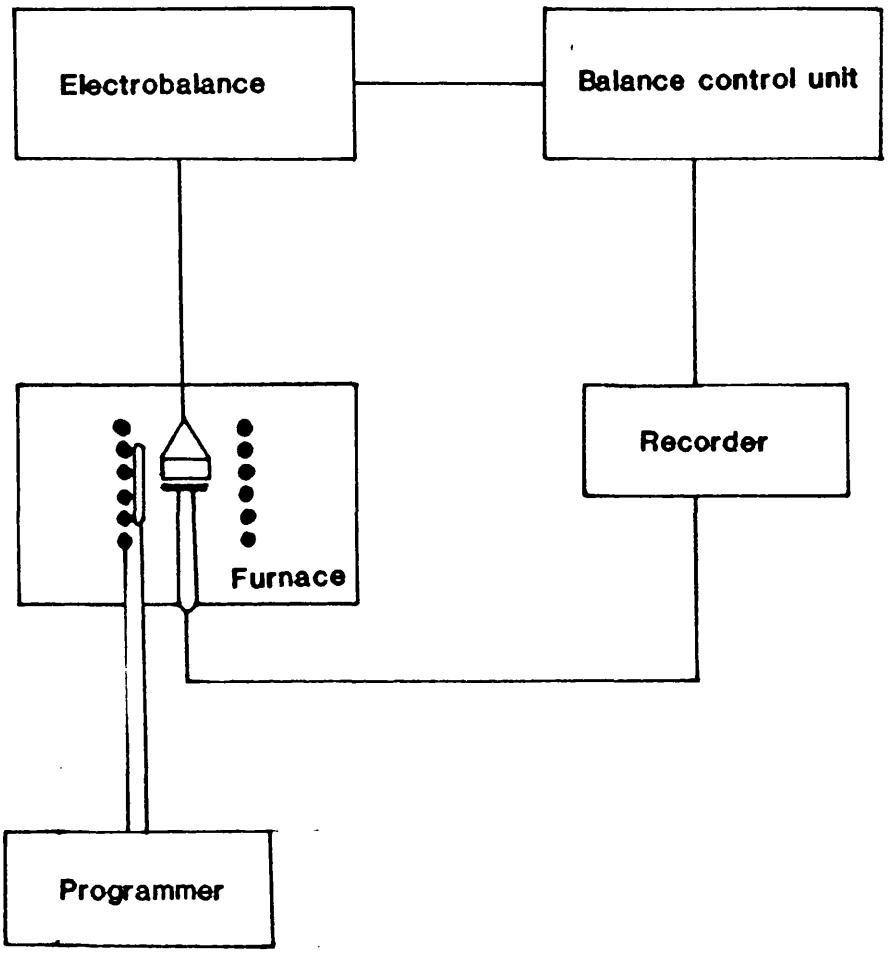


Figure 9.4 Block diagram of the Stanton Redcroft TG 750 thermobalance components.

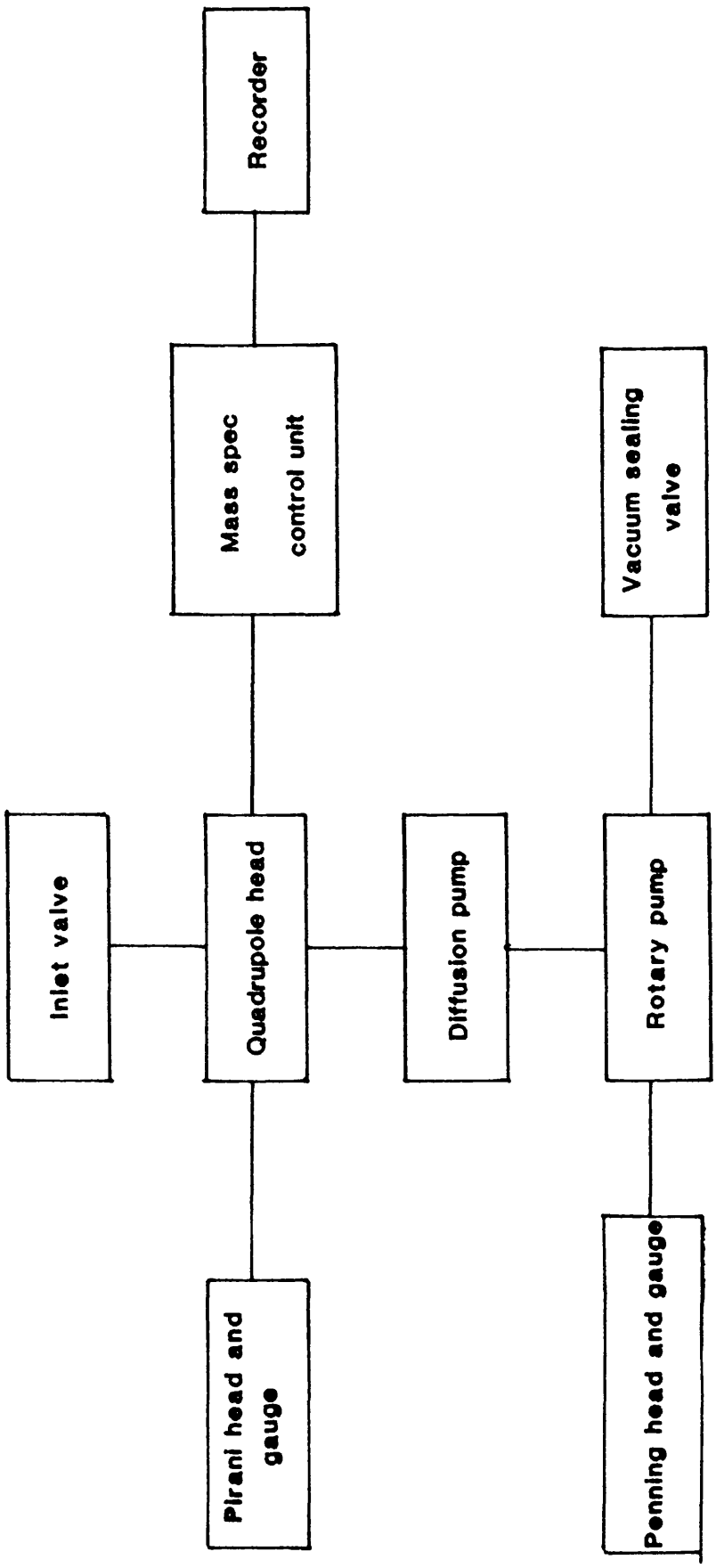


Figure 9.5 Block diagram of the mass spectrometer and its associated pumping system.

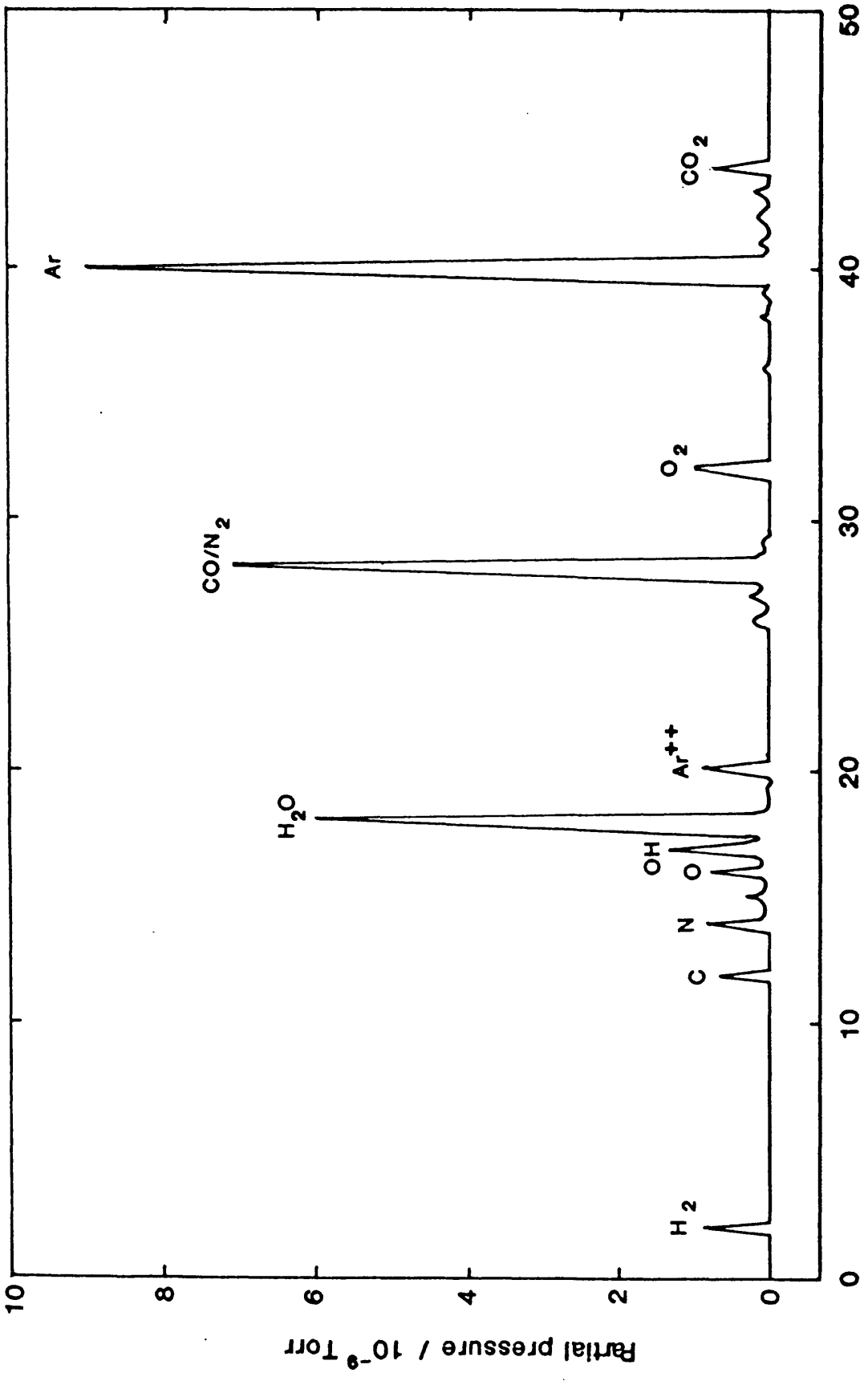


Figure 9.6 A typical spectrum, under gasification conditions, obtained from the mass spectrometer.

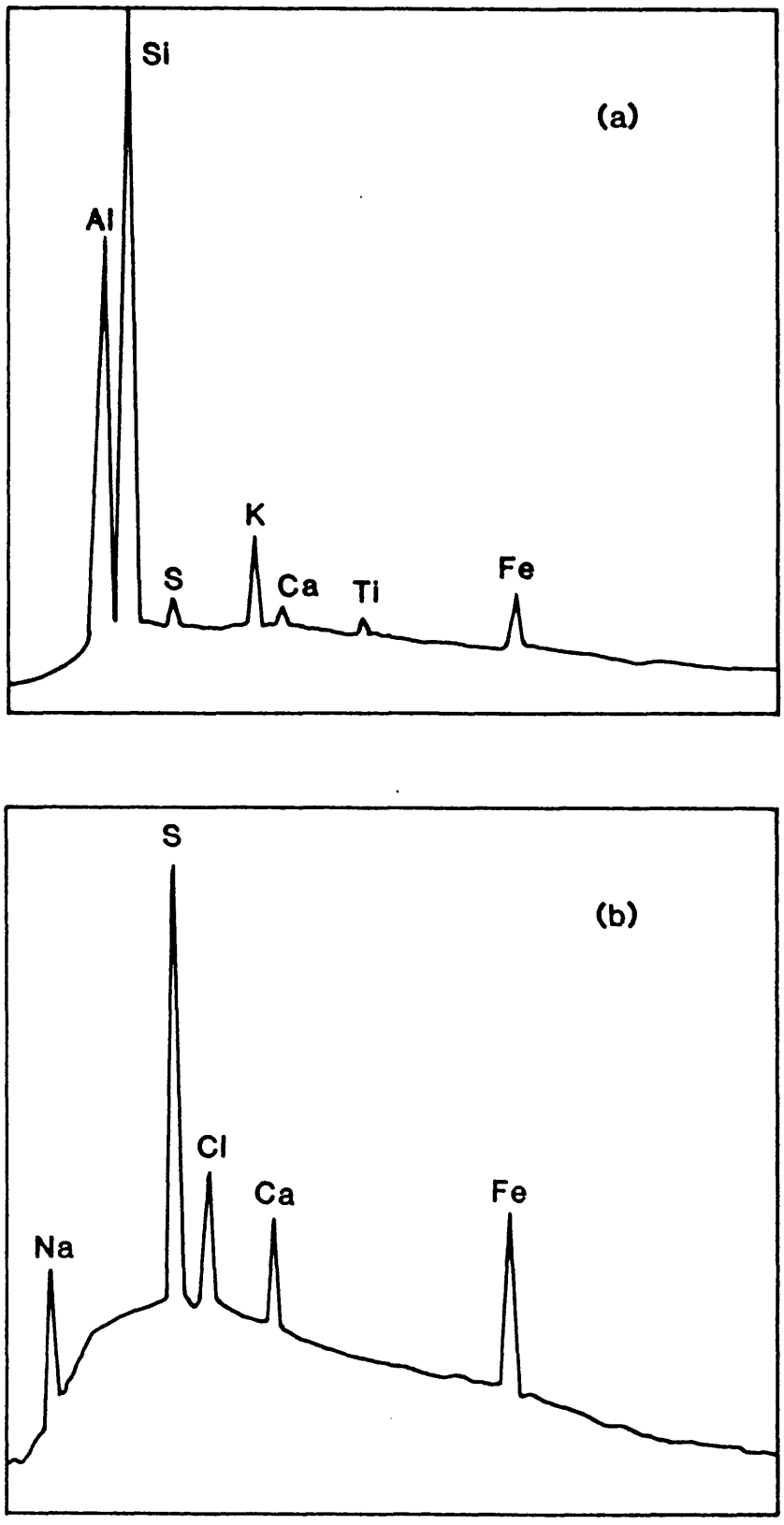


Figure 10.1 Typical examples of EDAX spectra for (a) Markham Main char and (b) PVDC char. *X*-ray intensities (ordinates) are on different arbitrary scales.

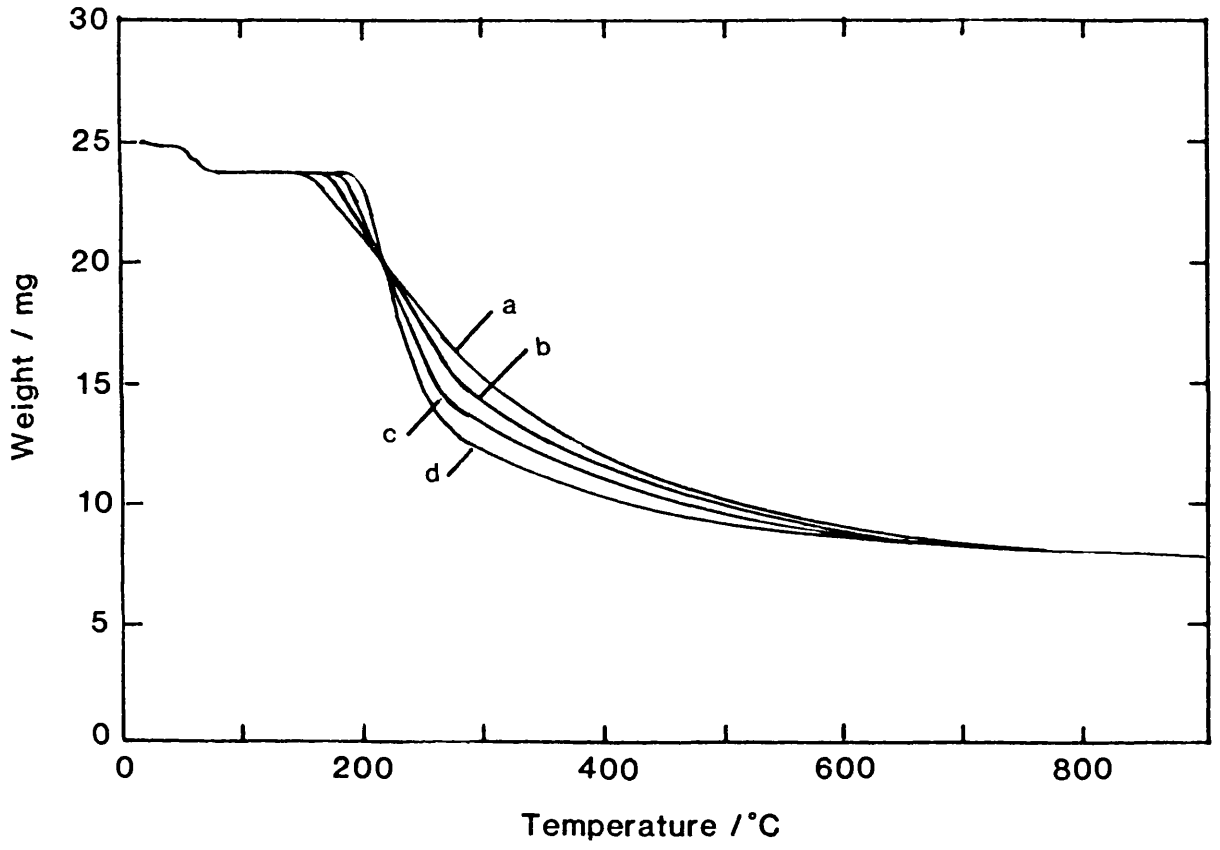


Figure 11.1 TGA curves for thermal degradation of the PVDC/PAN copolymer. Heating rates in °C/min are (a) 1; (b) 2; (c) 5; (d) 10.

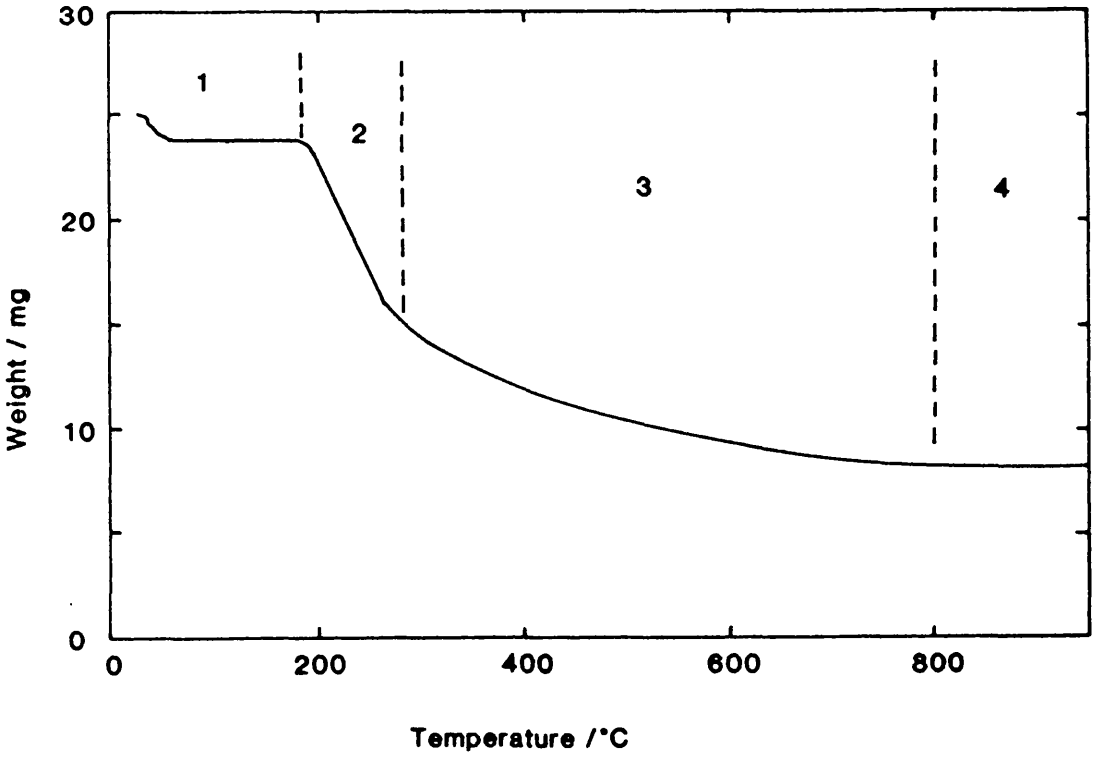


Figure 11.2 Characteristic weight loss curve for thermal degradation of the PVDC/PAN copolymer.

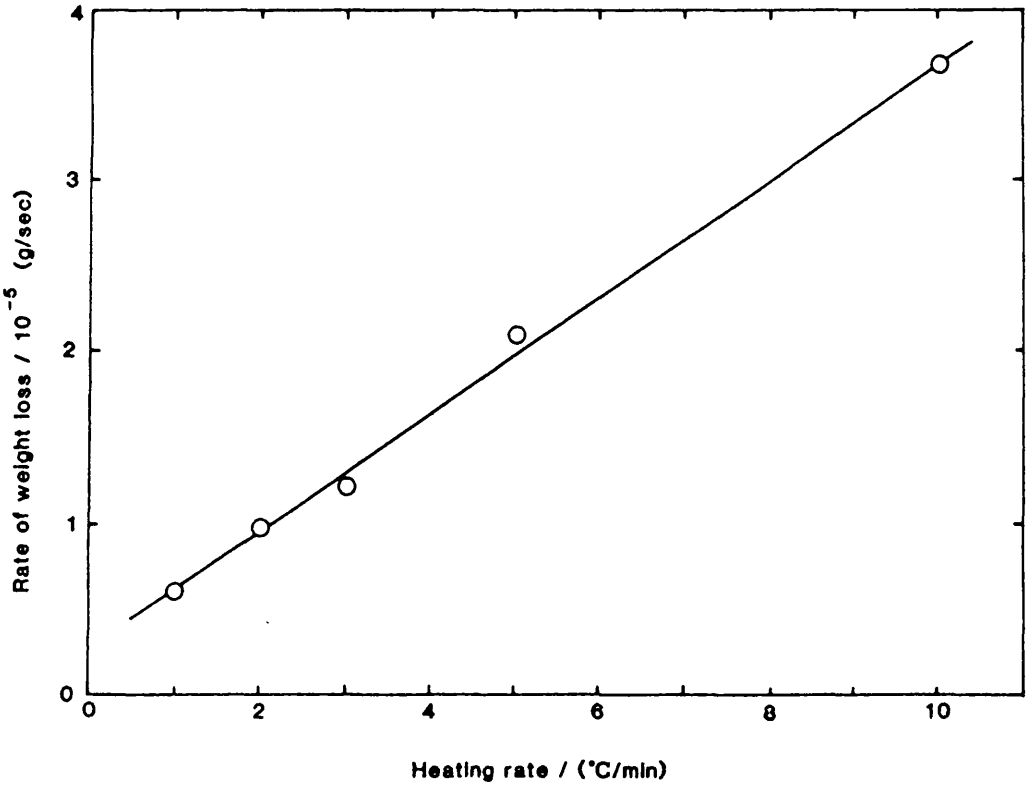


Figure 11.3 Rate of weight loss *versus* heating rate for degradation of the copolymer.

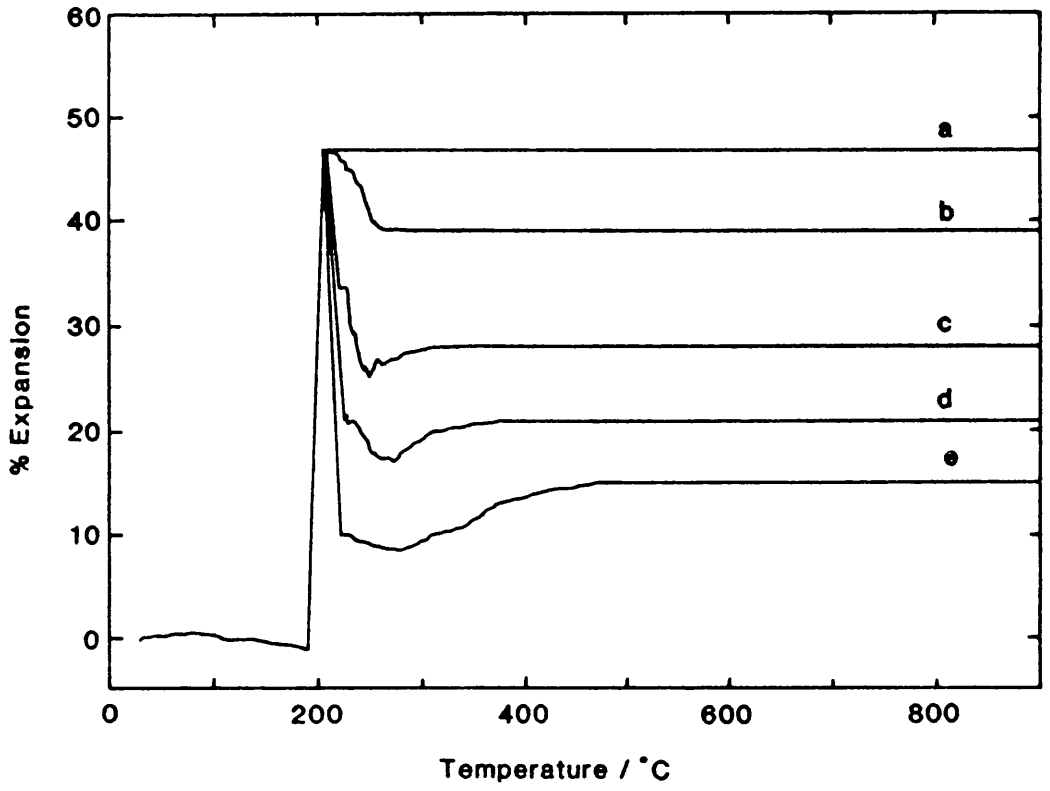


Figure 11.4 Expansion/contraction behaviour of the copolymer during heating. Heating rates in °C/min are (a) 10; (b) 5; (c) 2; (d) 1; (e) 0.5.

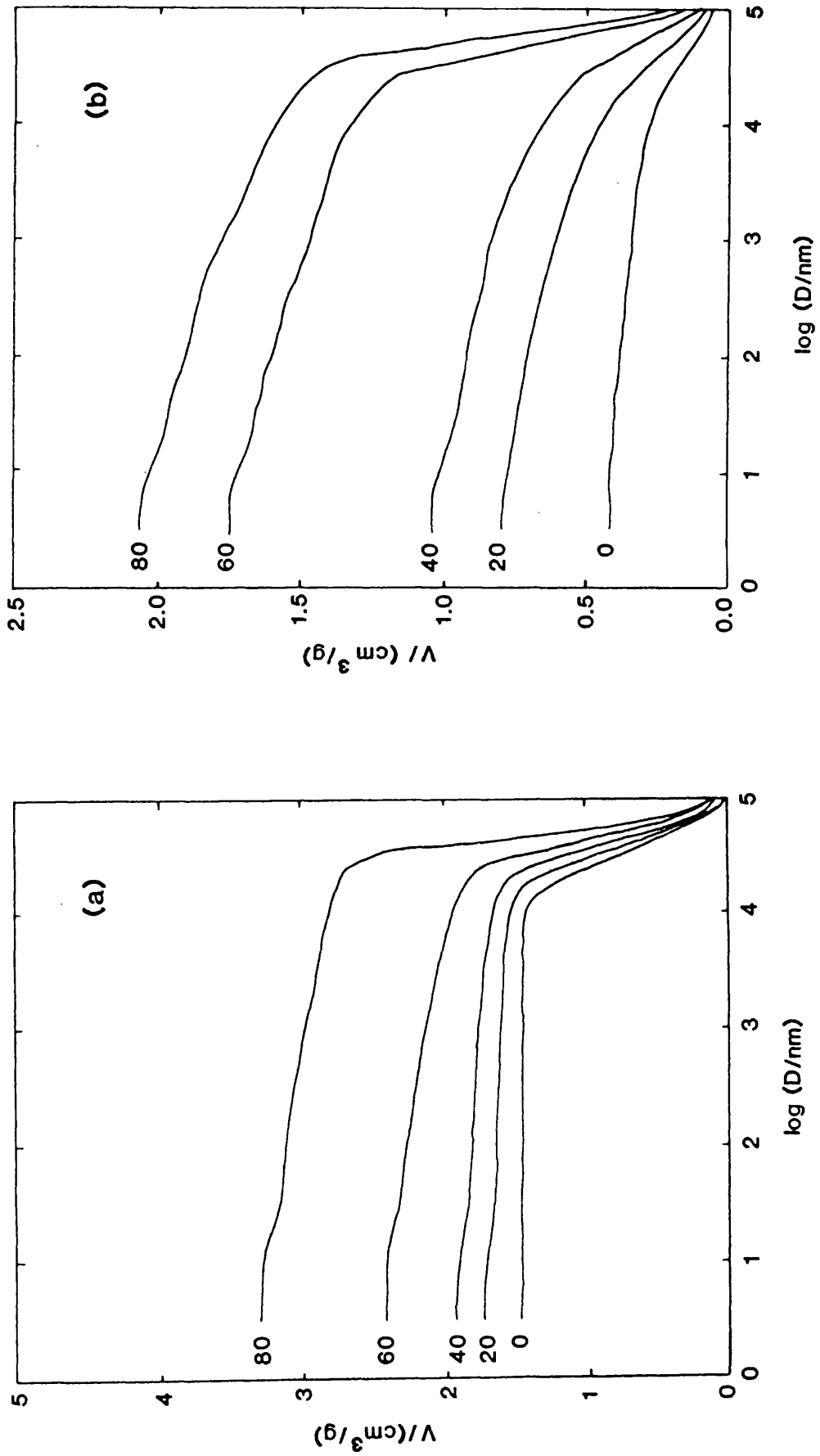


Figure 12.1 Mercury porosimetry curves - cumulative pore volumes for (a) PVDC char and (b) Markham Main char. Numbers represent % burn-off.

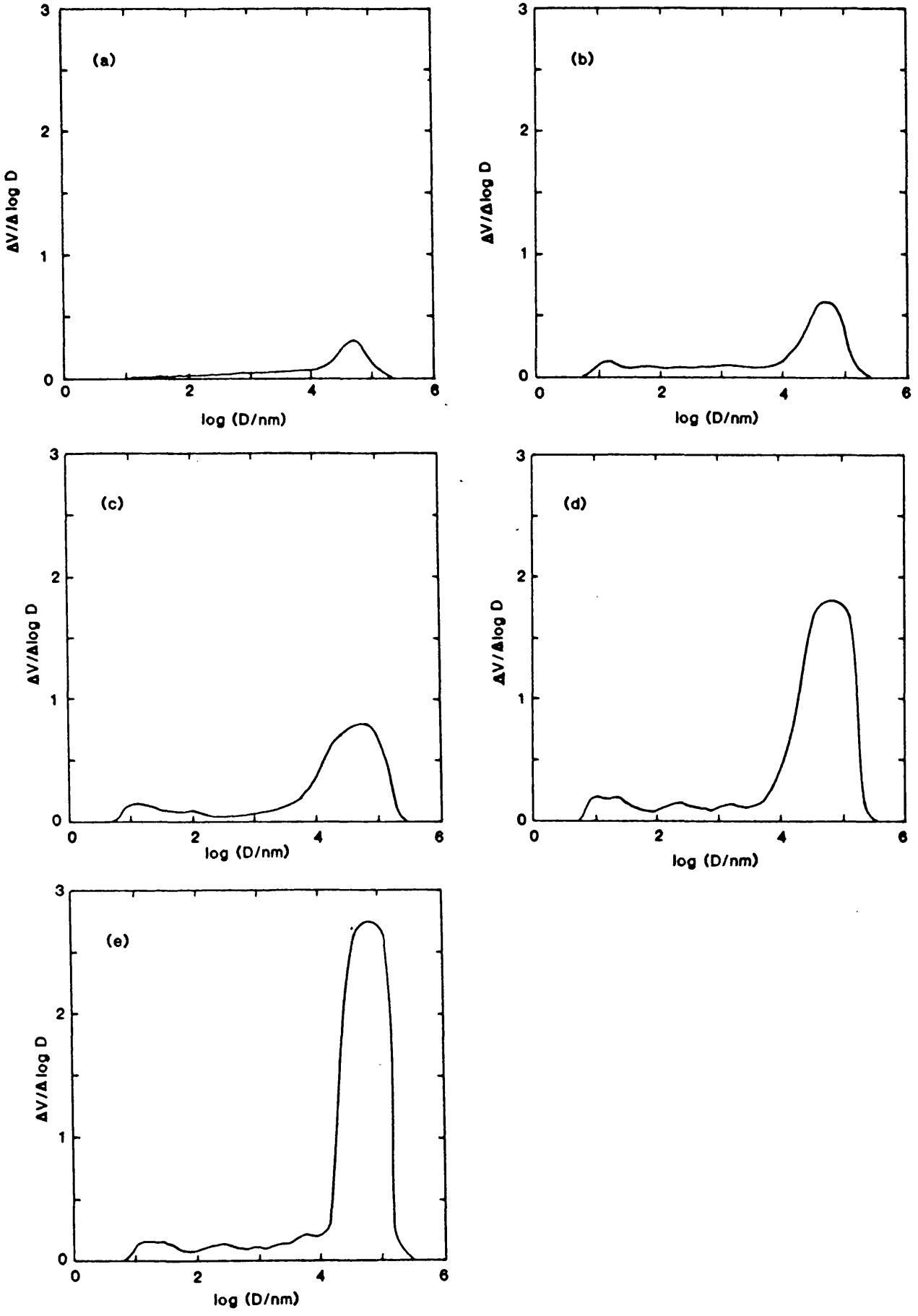


Figure 12.2 Mercury porosimetry curves - pore size distribution for Markham Main char at (a) 0; (b) 20; (c) 40; (d) 60; and (e) 80 % burn-off.

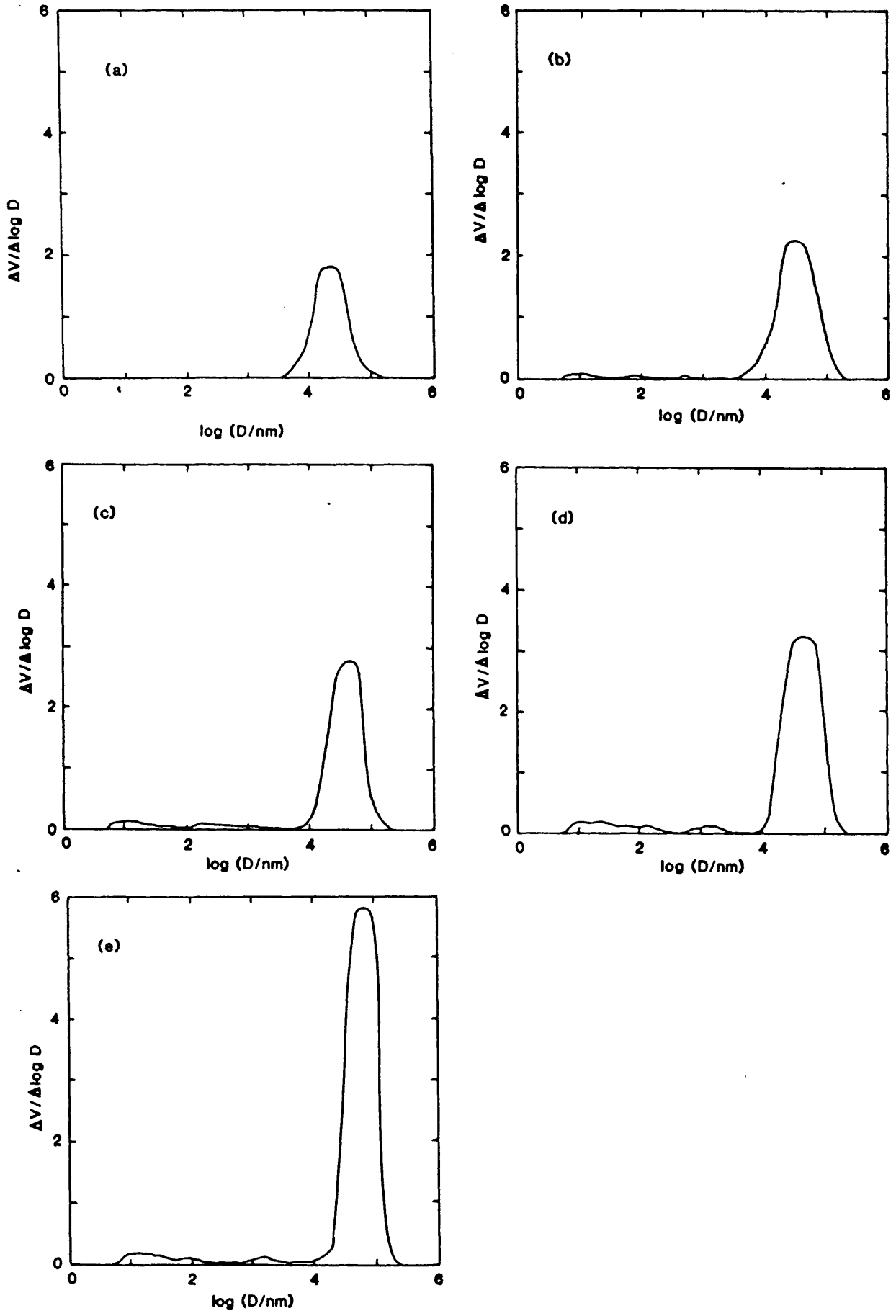


Figure 12.3 Mercury porosimetry curves - pore size distribution for PVDC char at (a) 0; (b) 20; (c) 40; (d) 60; and (e) 80 % burn-off.

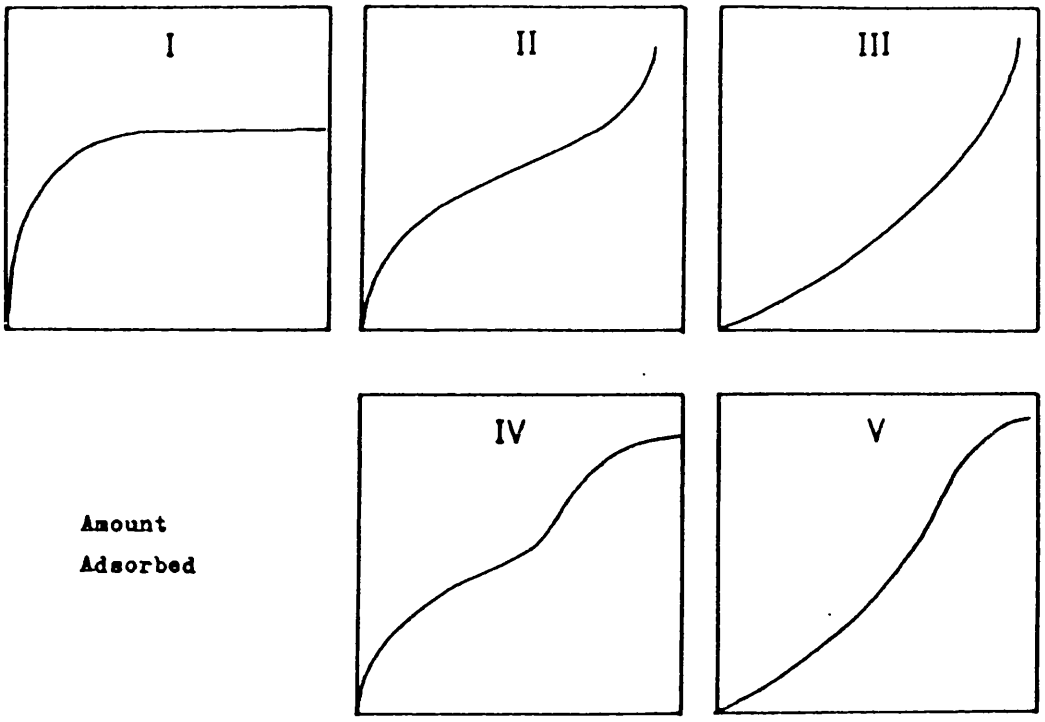


Figure 12.4 The Brunauer, Deming, Deming and Teller (BDDT) adsorption isotherm classification.

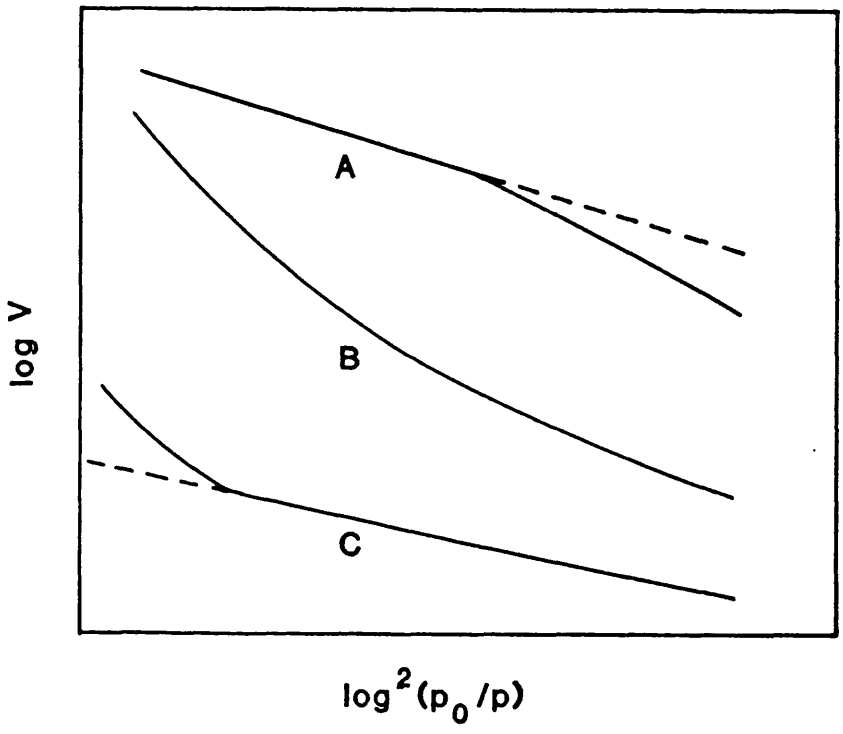


Figure 12.5 The Marsh and Rand classification of deviations from linear DR plots.

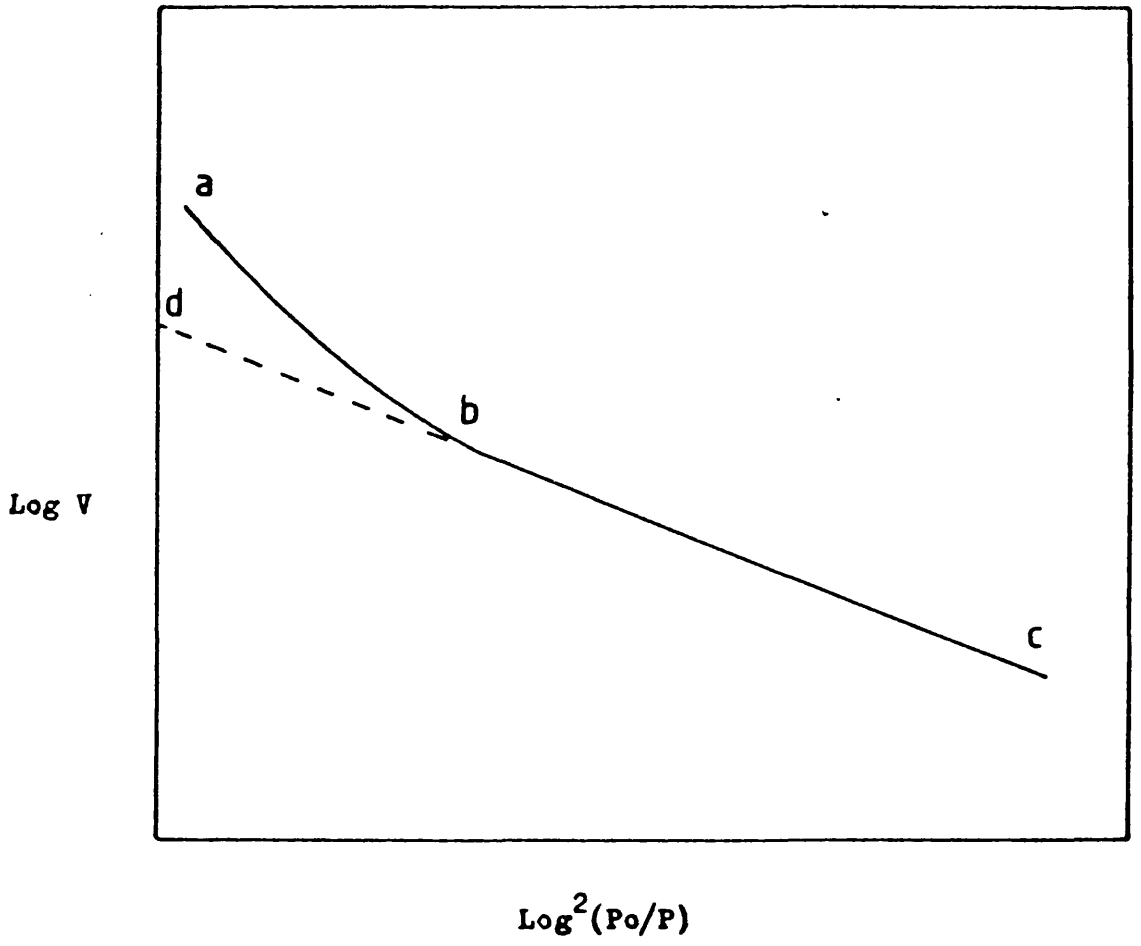


Figure 12.6 Schematic plot of type C deviation from the DR equation.

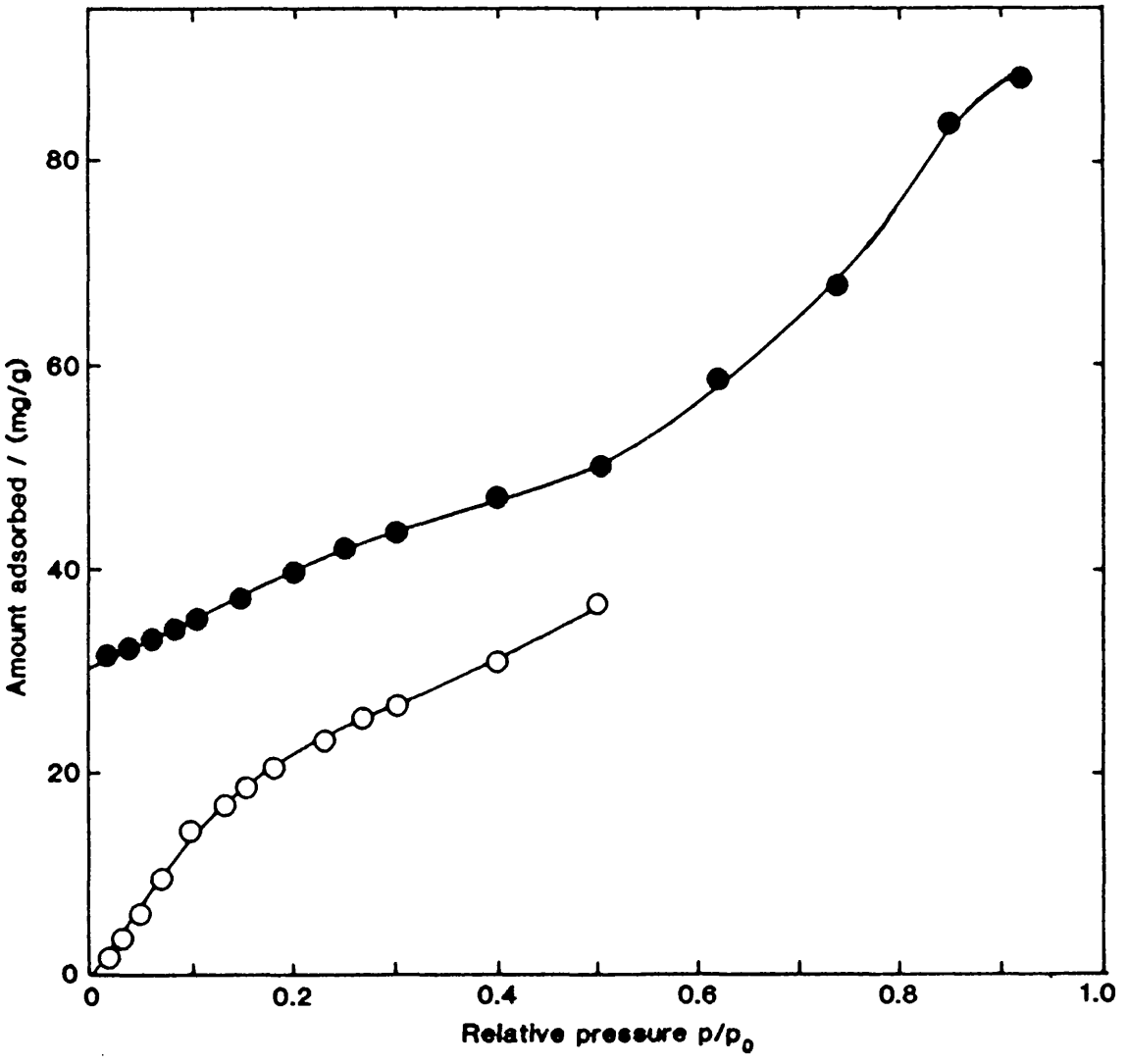


Figure 12.7 Adsorption isotherms of: Ar(●) at 77K and $CO_2$ (○) at 195 K on Vulcan 3-G.

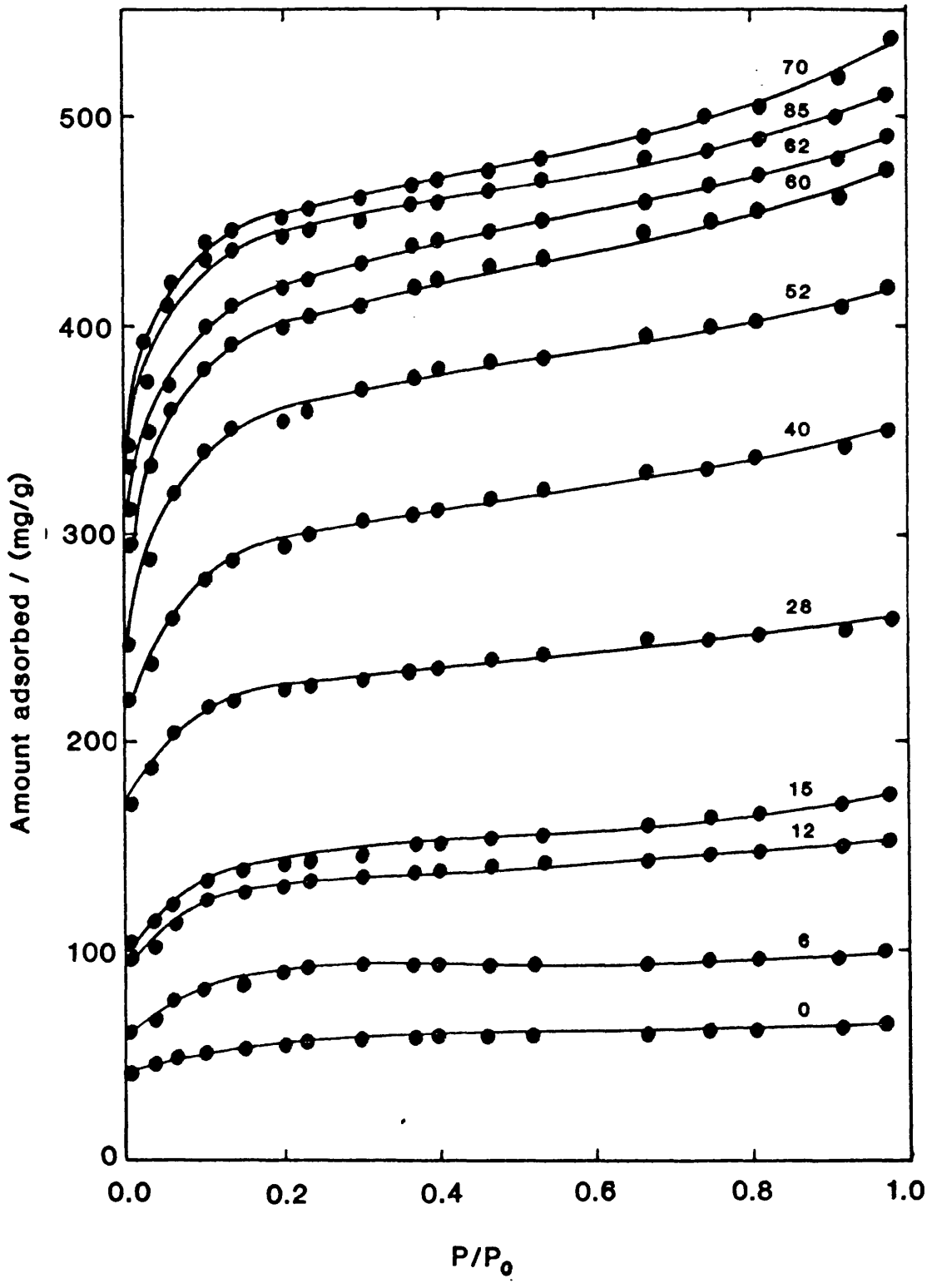


Figure 12.8 Adsorption isotherms of Ar at 77 K on PVDC char. Numbers represent burn-off.

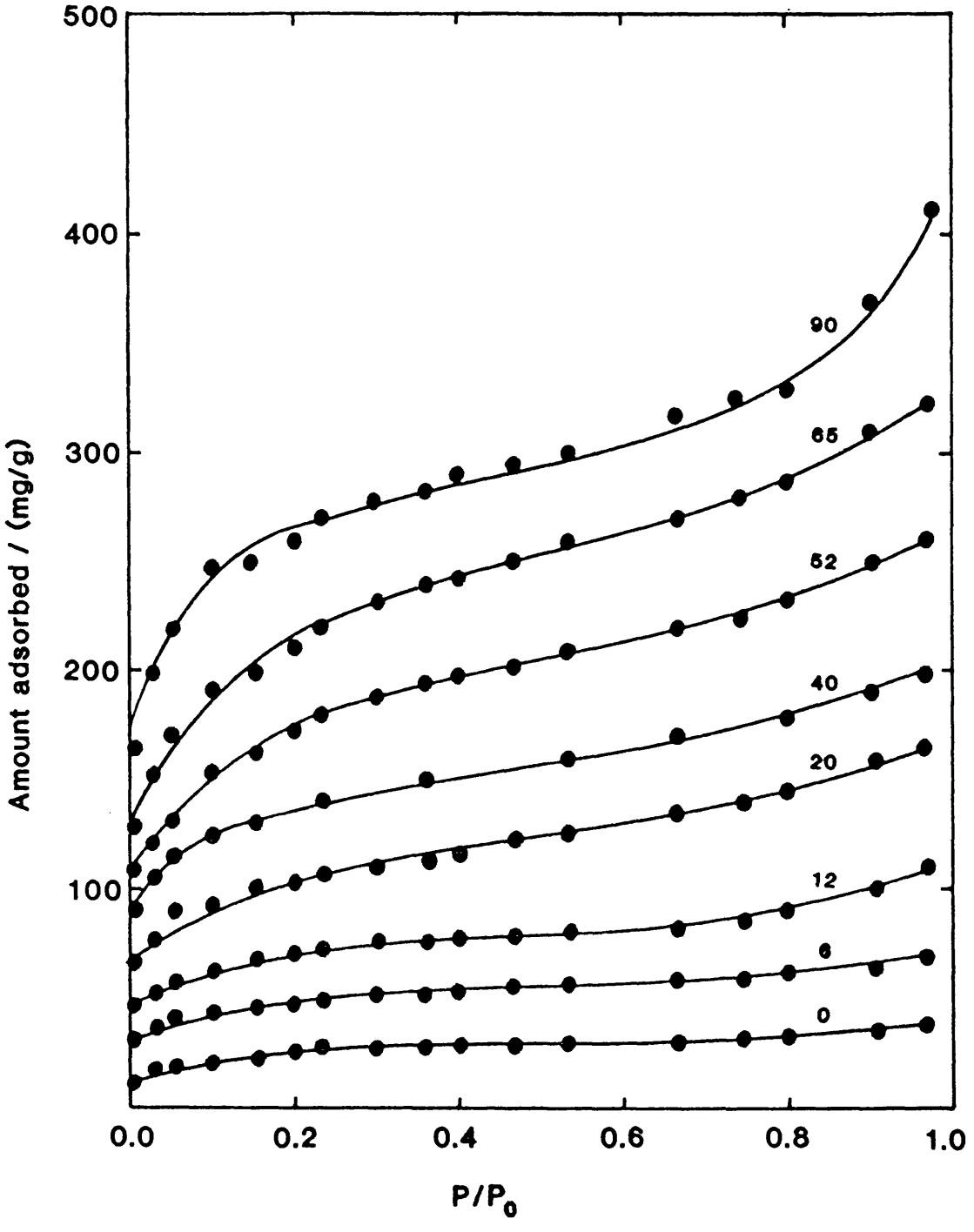


Figure 12.9 Adsorption isotherms of Ar at 77 K on Markham Main char. Numbers represent % burn-off.

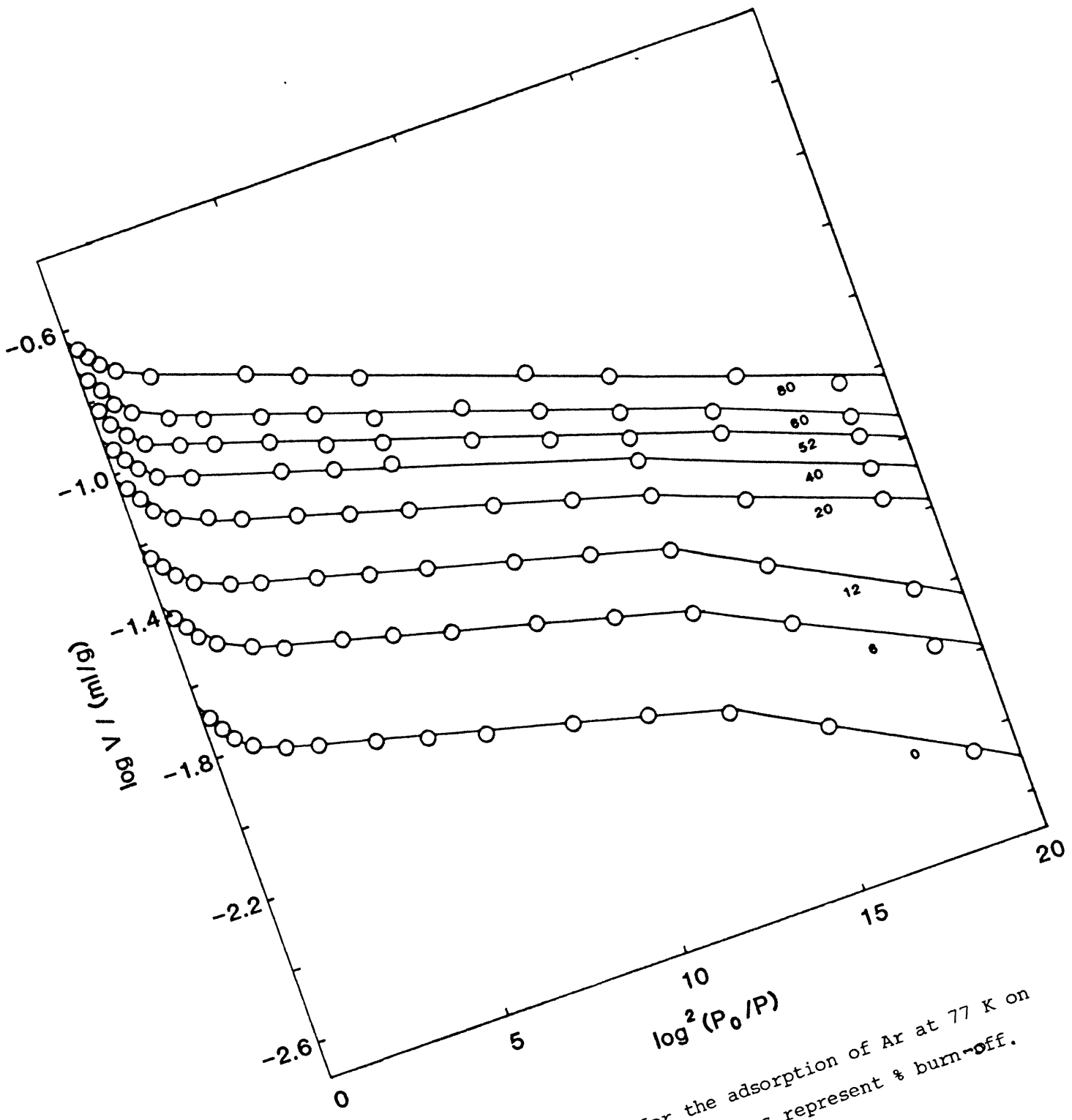


Figure 12.10 DR plots for the adsorption of Ar at 77 K on PVDC char. Numbers represent % burn-off.

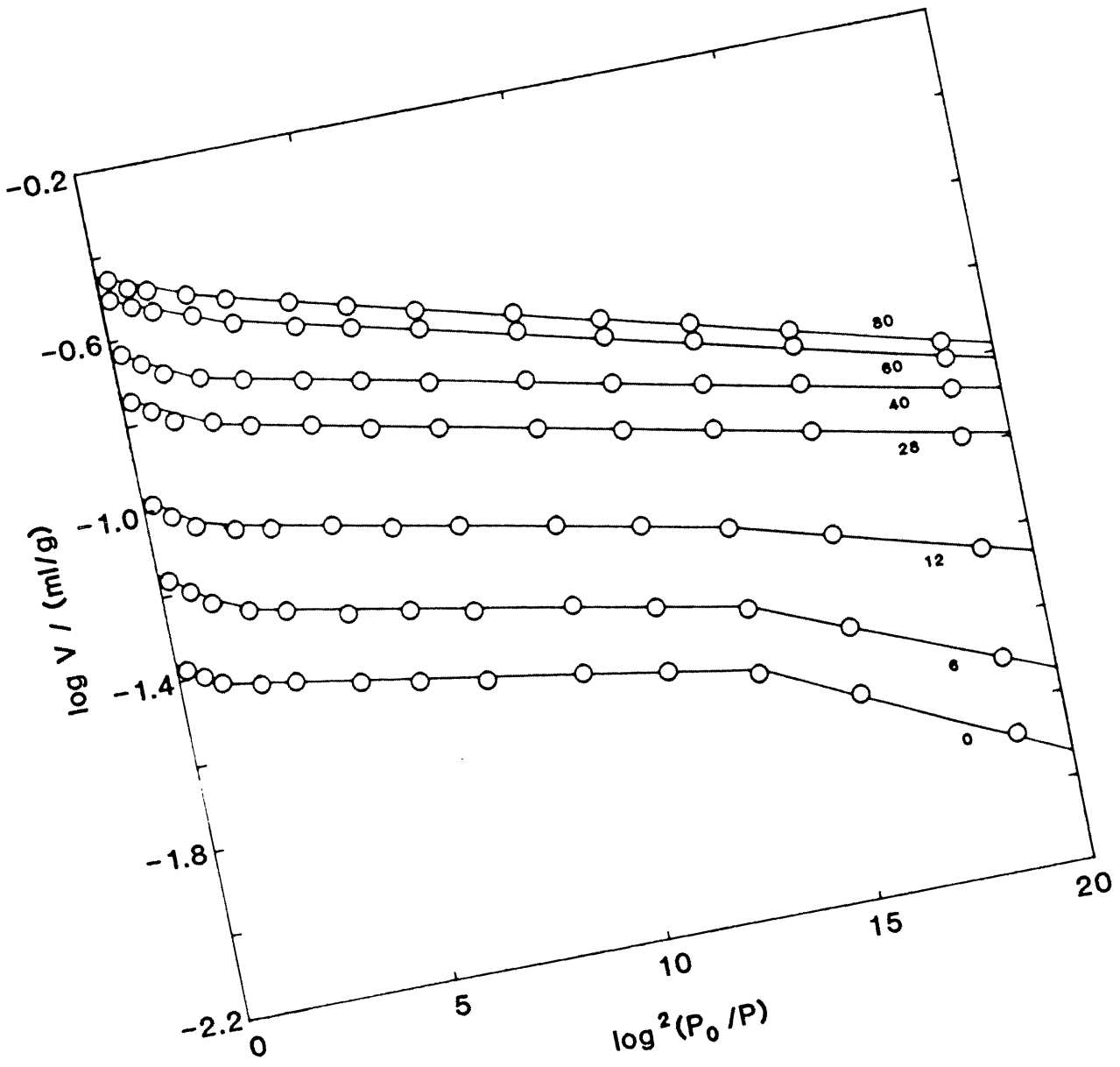


Figure 12.11 DR plots for the adsorption of Ar at 77 K on Markham Main char. Numbers represent % burn-off.

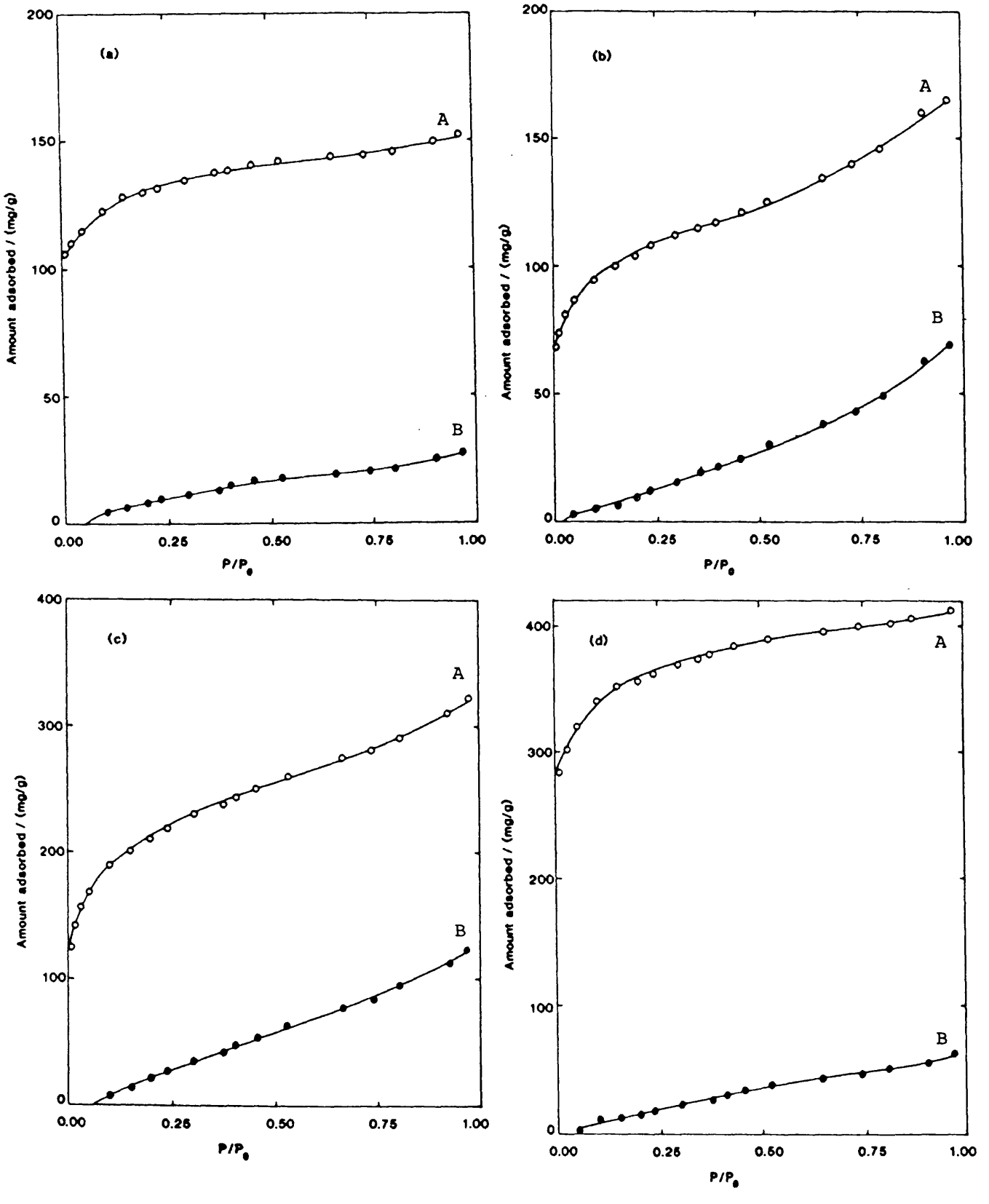


Figure 12.12 Adsorption isotherms of Ar at 77 K on (a) PVDC, 12% burn-off; (b) Markham Main, 20% burn-off; (c) Markham Main, 65% burn-off; (d) PVDC, 52% burn-off. These are typical examples and in each case A is the total isotherm and B is the residual isotherm obtained by applying the IS method.

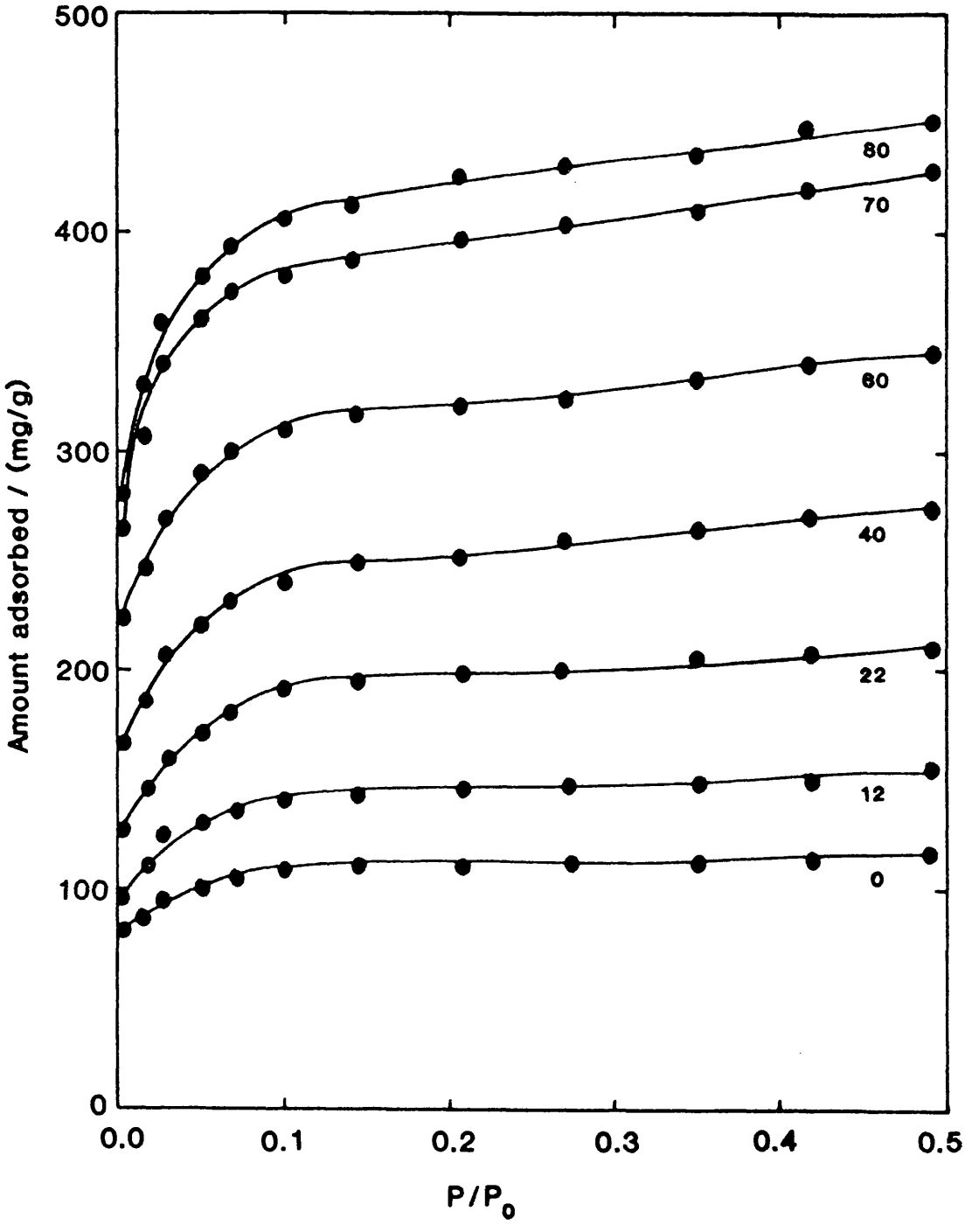


Figure 12.13 Adsorption isotherms of $CO_2$ at 195 K on PVDC char. Numbers represent % burn-off.

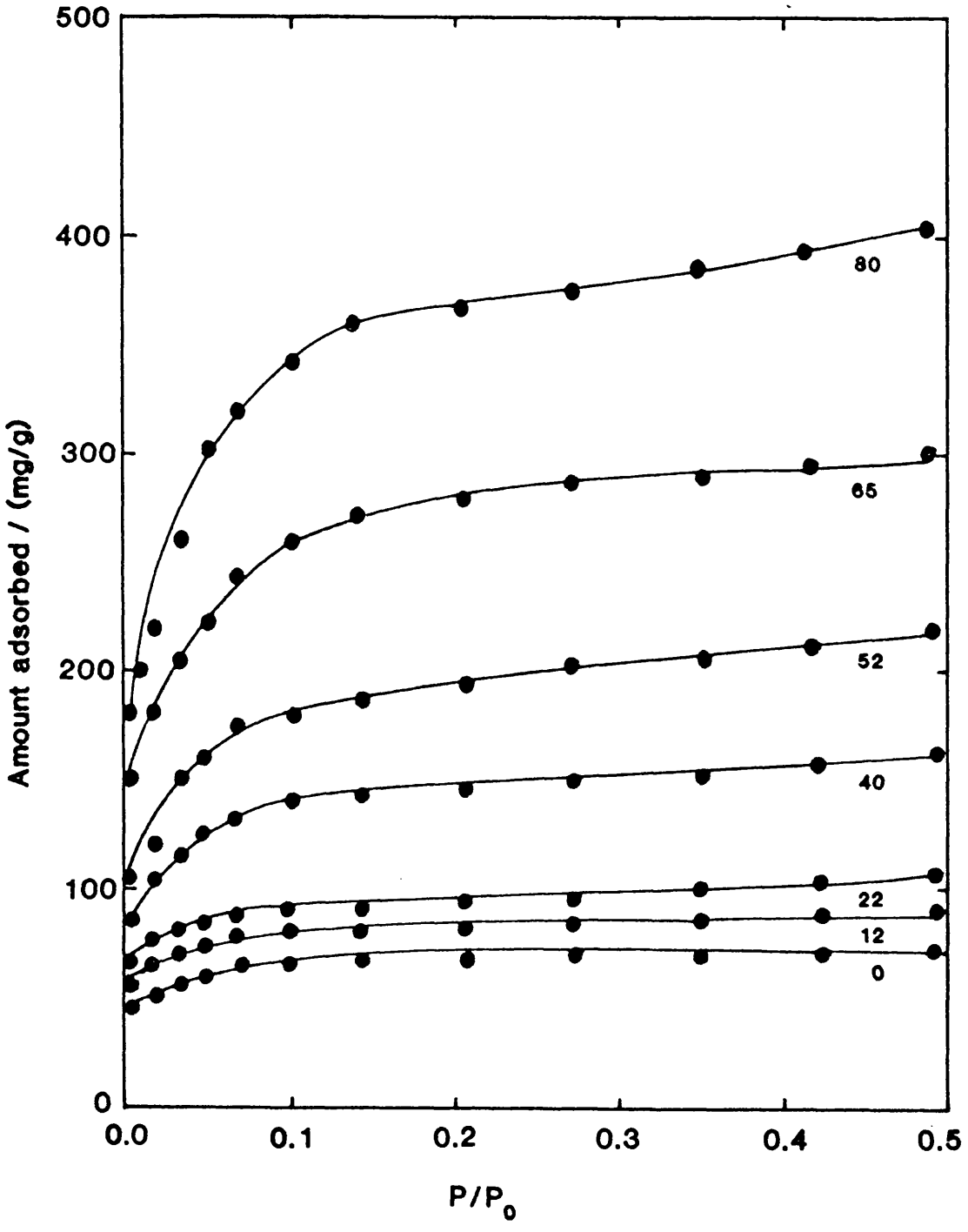


Figure 12.14 Adsorption isotherms of $CO_2$ at 195 K on Markham Main char. Numbers represent % burn-off.

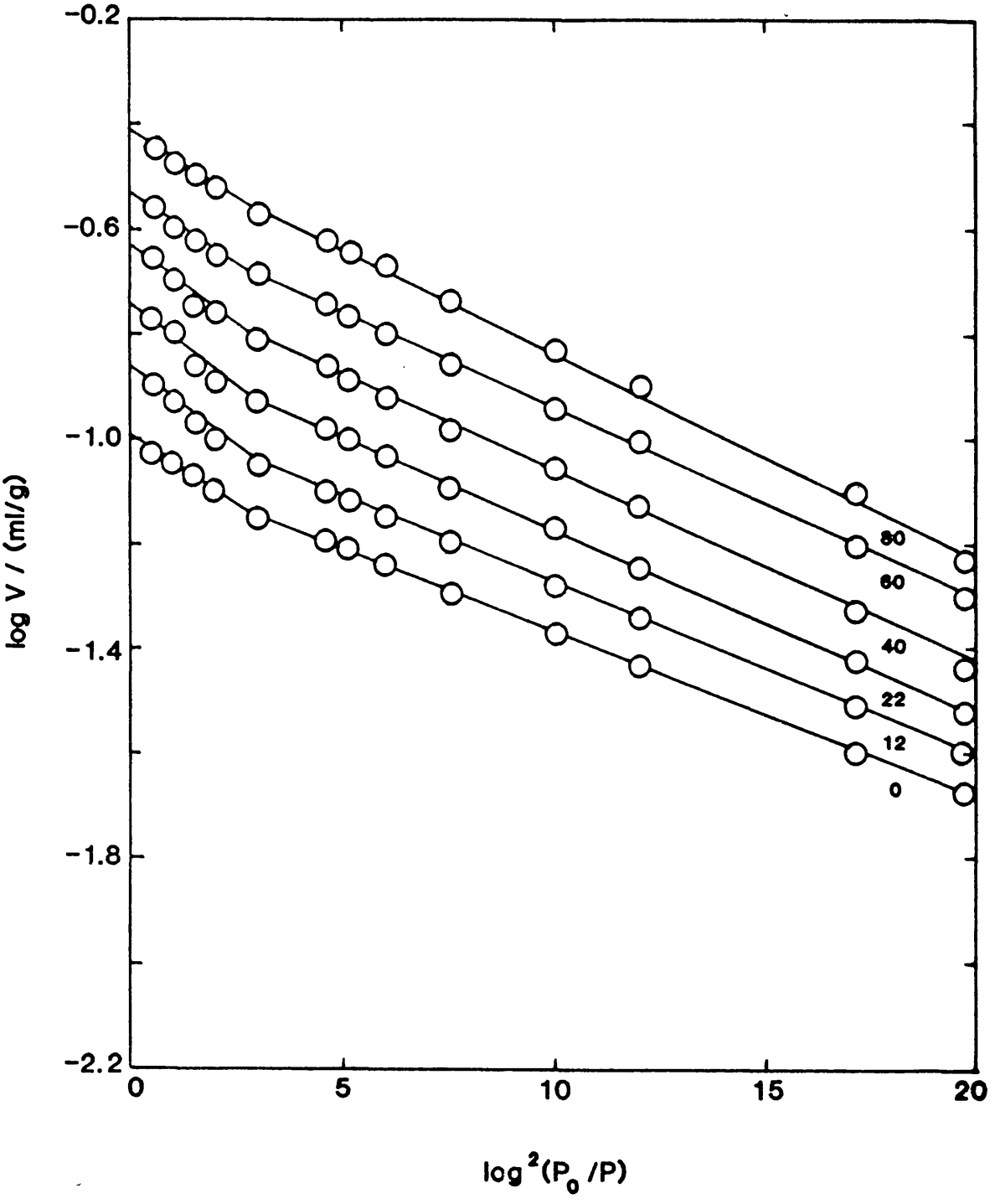


Figure 12.15 DR plots for the adsorption of $CO_2$ at 195 K on PVDC char. Numbers represent % burn-off.

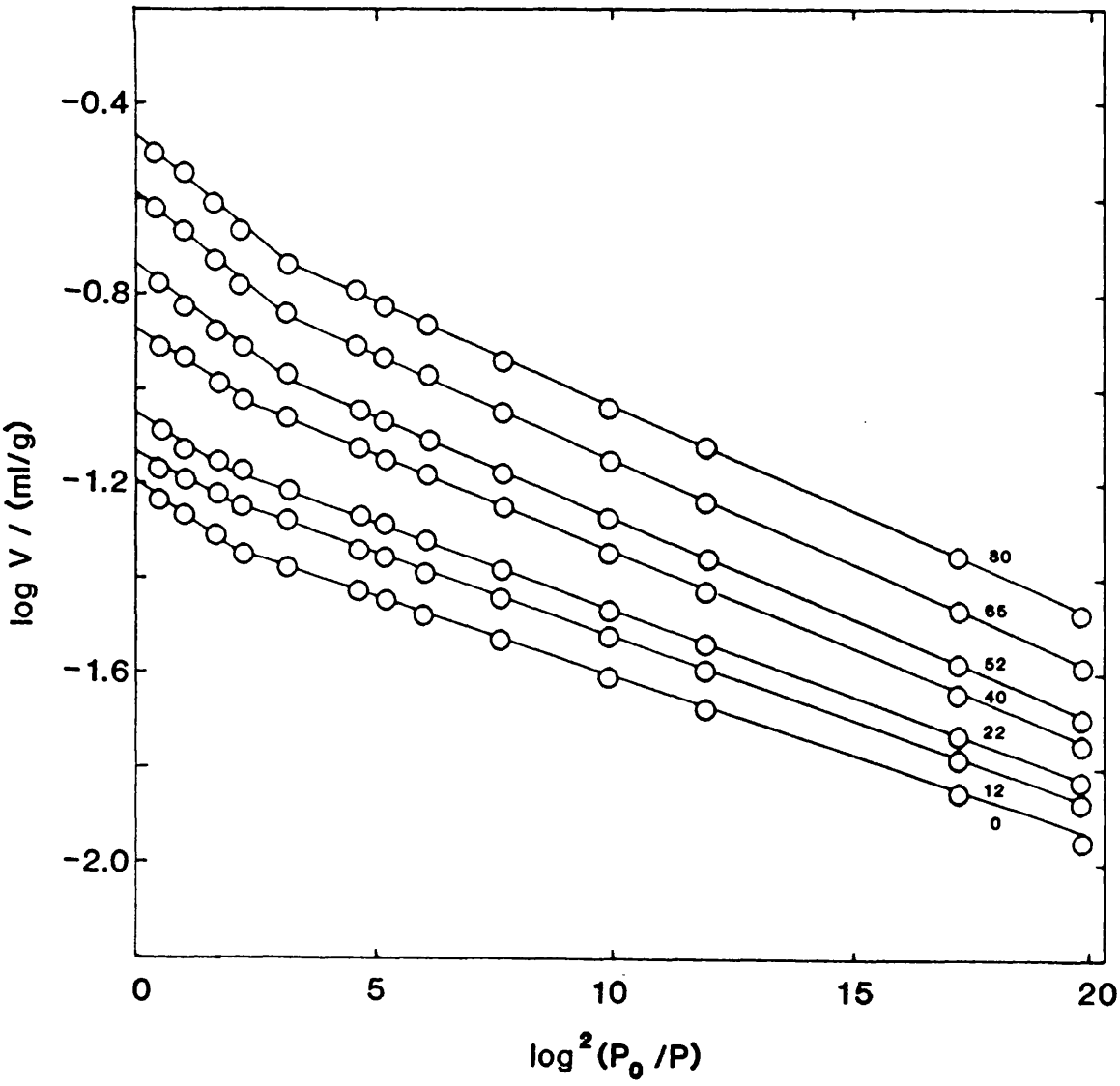


Figure 12.16 DR plots for the adsorption of $CO_2$ at 195 K on Markham Main char. Numbers represent % burn-off.

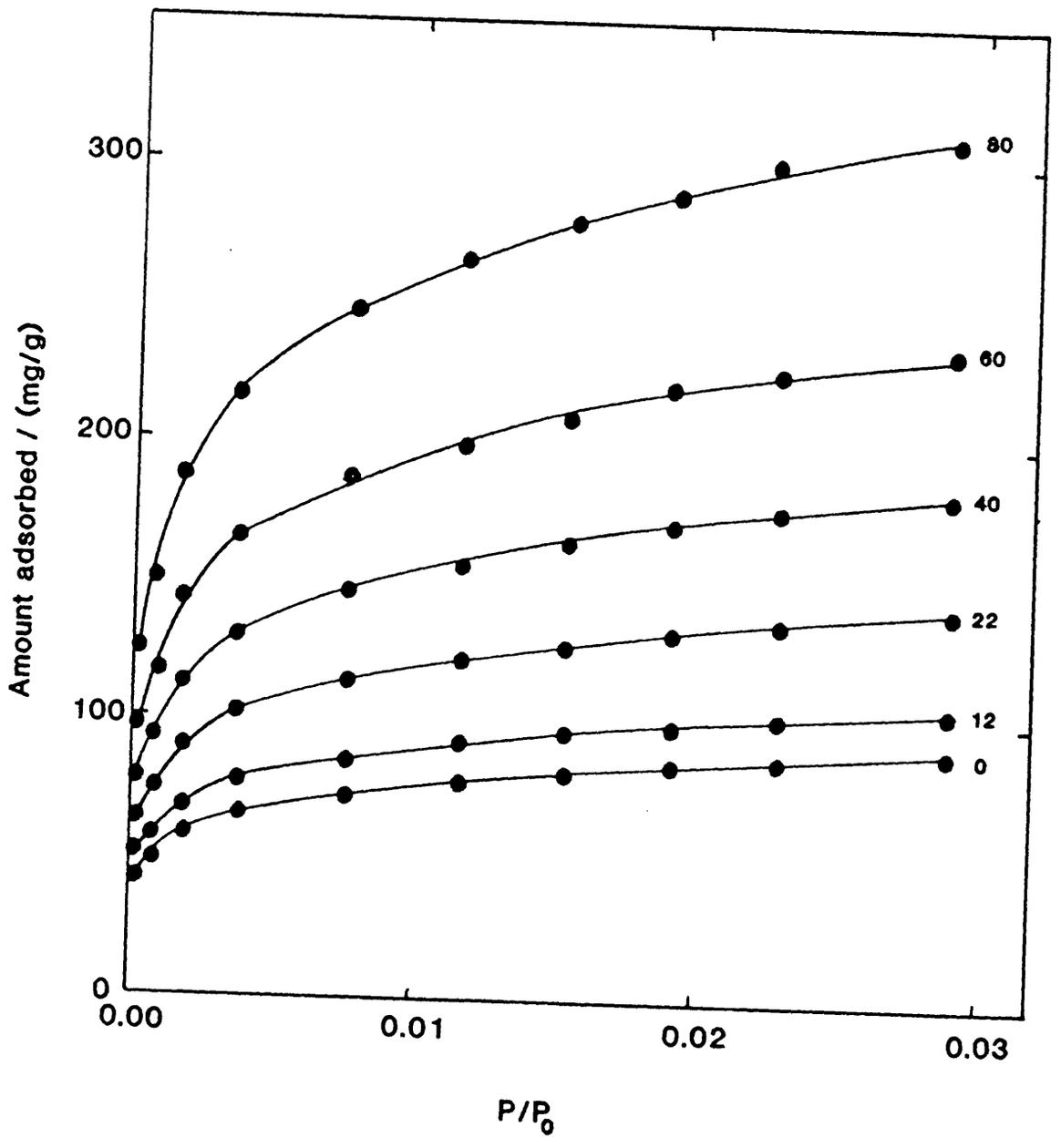


Figure 12.17 Adsorption isotherms of $CO_2$ at 273 K on PVDC char. Numbers represent % burn-off.

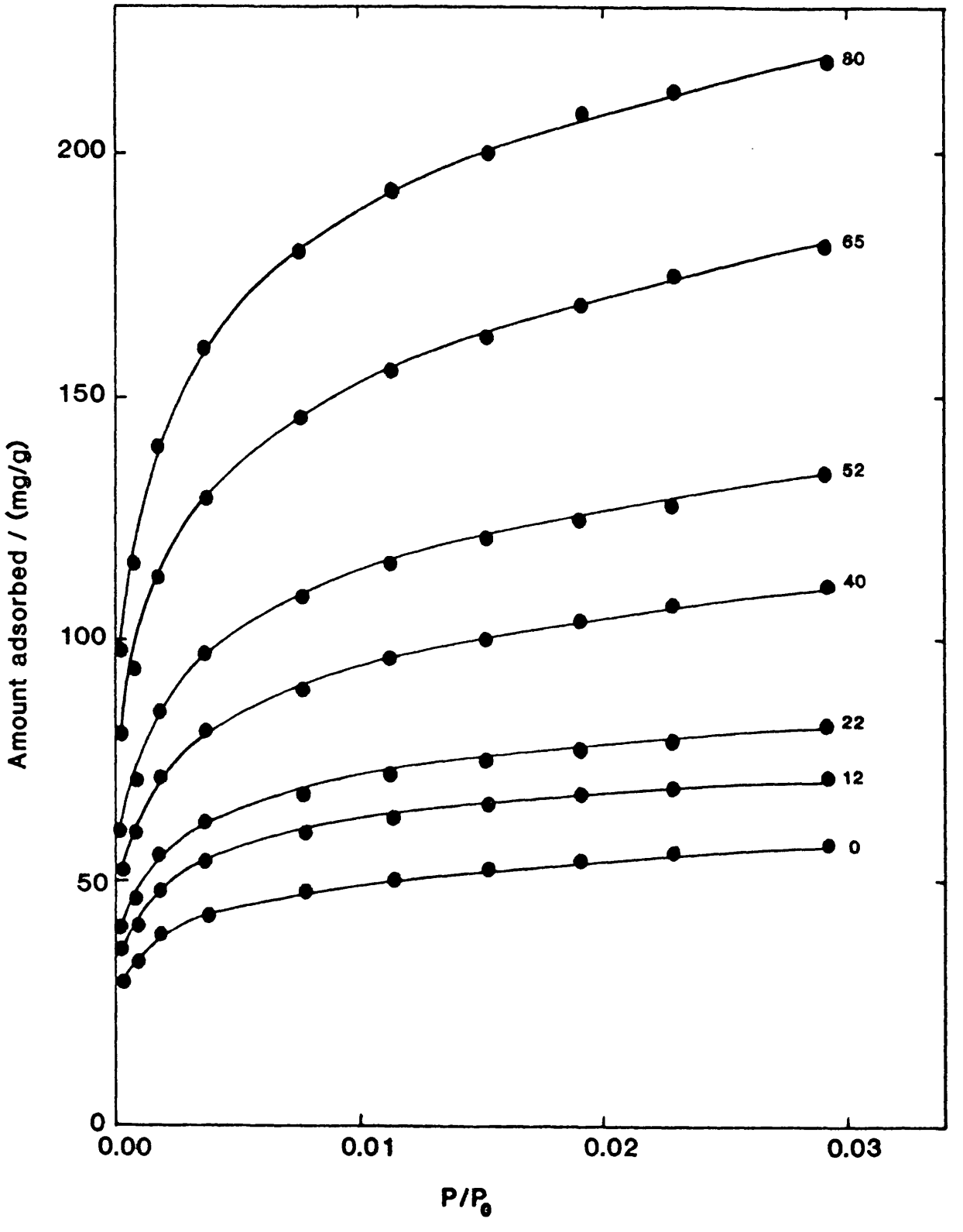


Figure 12.18 Adsorption isotherms of $CO_2$ at 273 K on Markham Main char. Numbers represent % burn-off.

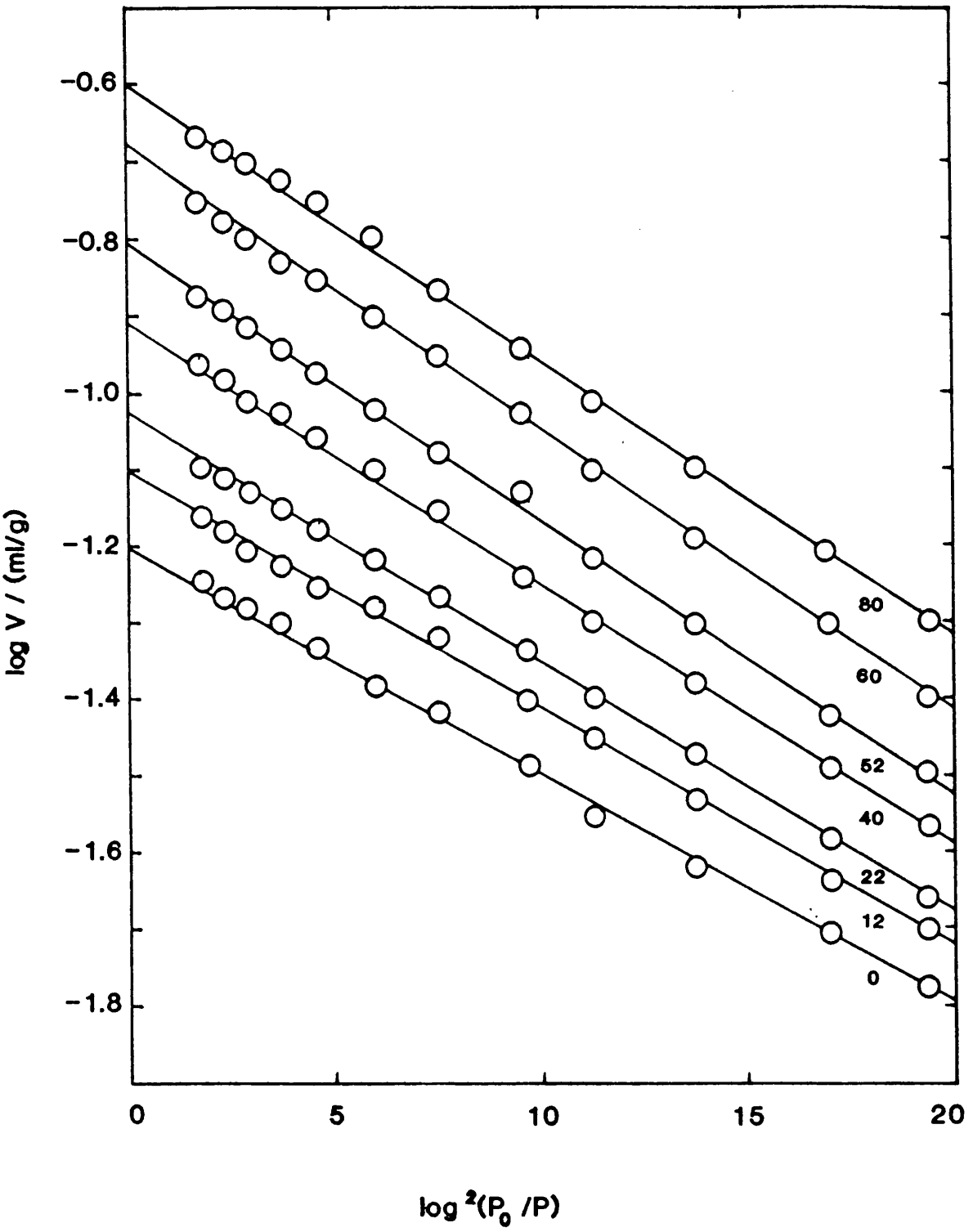


Figure 12.19 DR plots for the adsorption of $CO_2$ at 273 K on PVDC char. Numbers represent % burn-off.

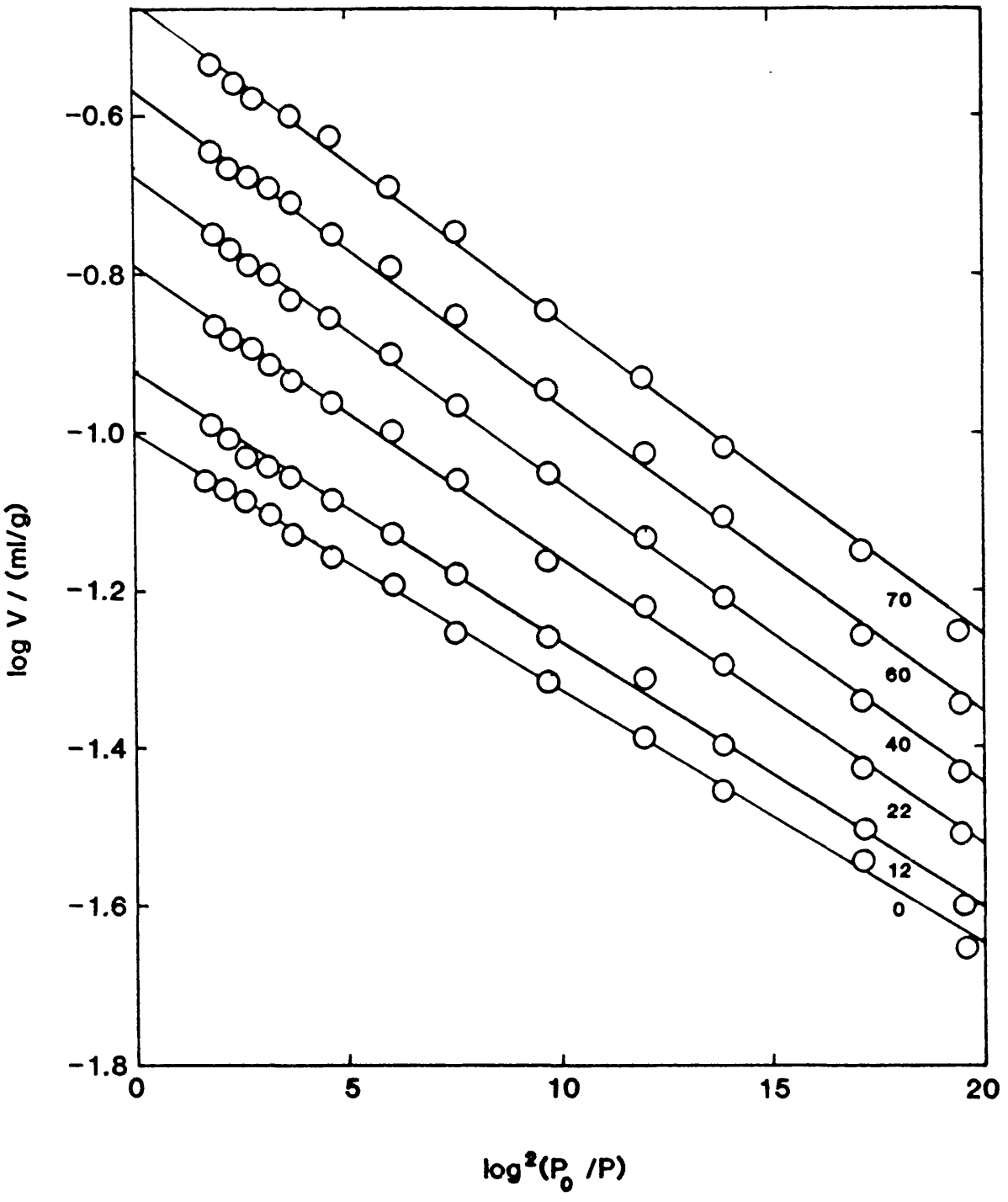


Figure 12.20 DR plots for the adsorption of $CO_2$ at 273 K on Markham Main char. Numbers represent % burn-off.

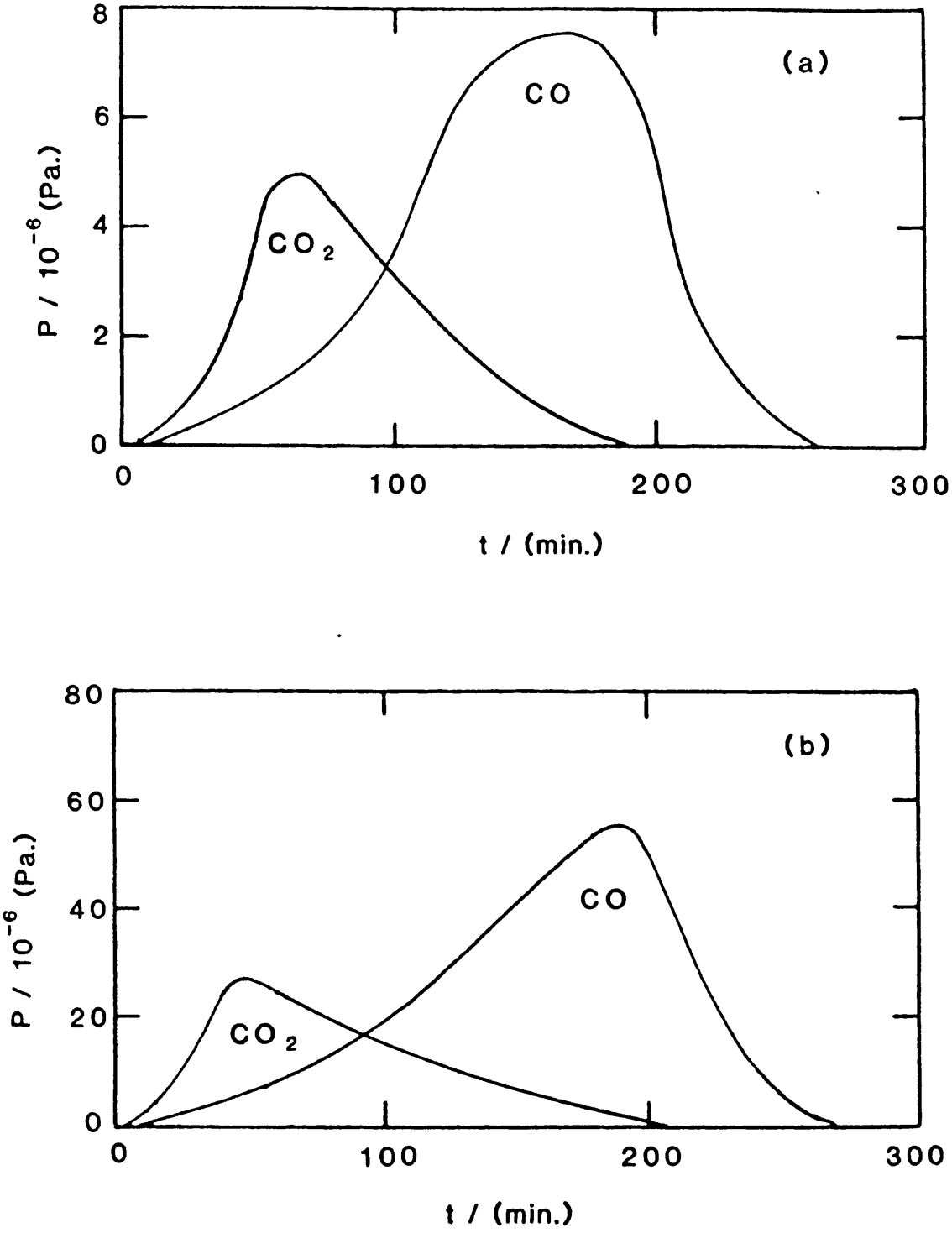


Figure 13.1 TPD curves for two lignite chars (a) S-1 h (1475 K), slow pyrolysis, residence time of 1 hour at 1475 K, and (b) S-1 h (975 K), slow pyrolysis, residence time of 1 hour at 975 K.

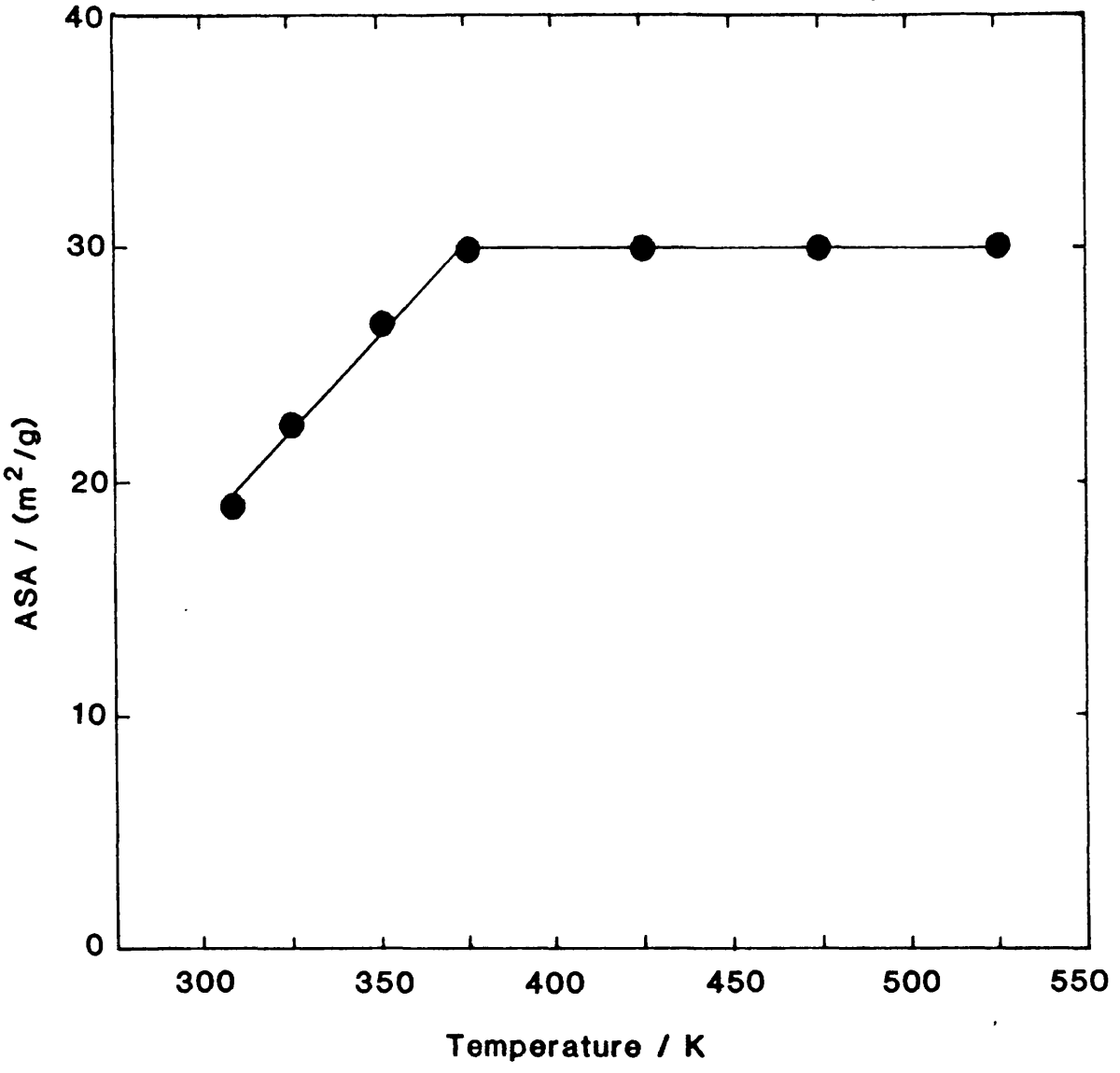


Figure 13.2 Effect of oxygen chemisorption temperature on the active surface area of unactivated Markham Main char.

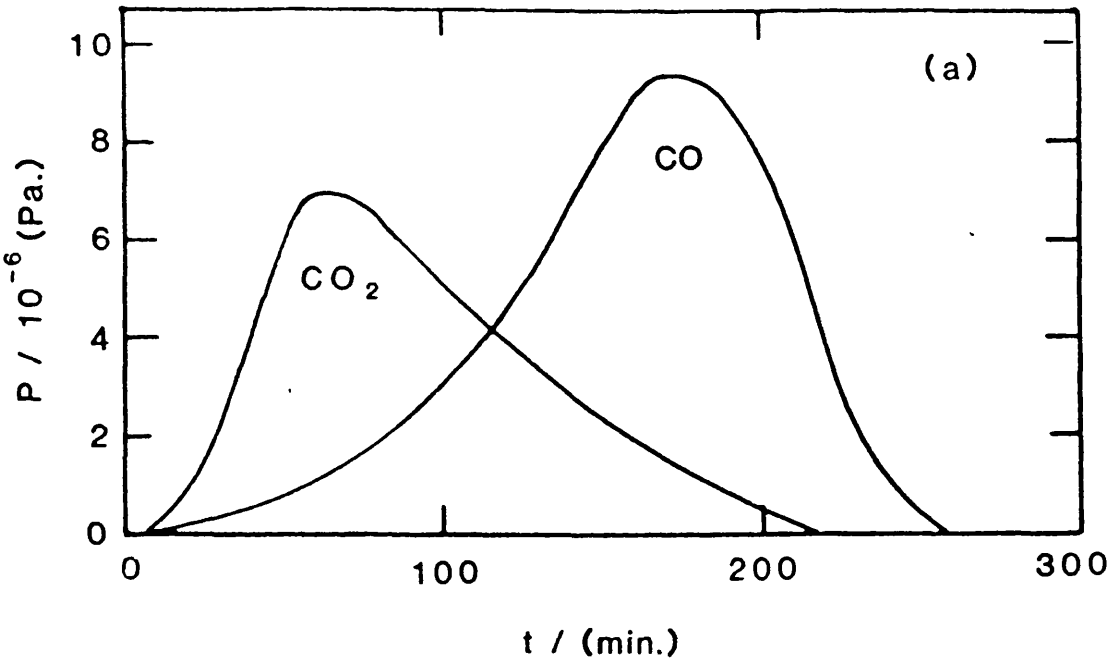


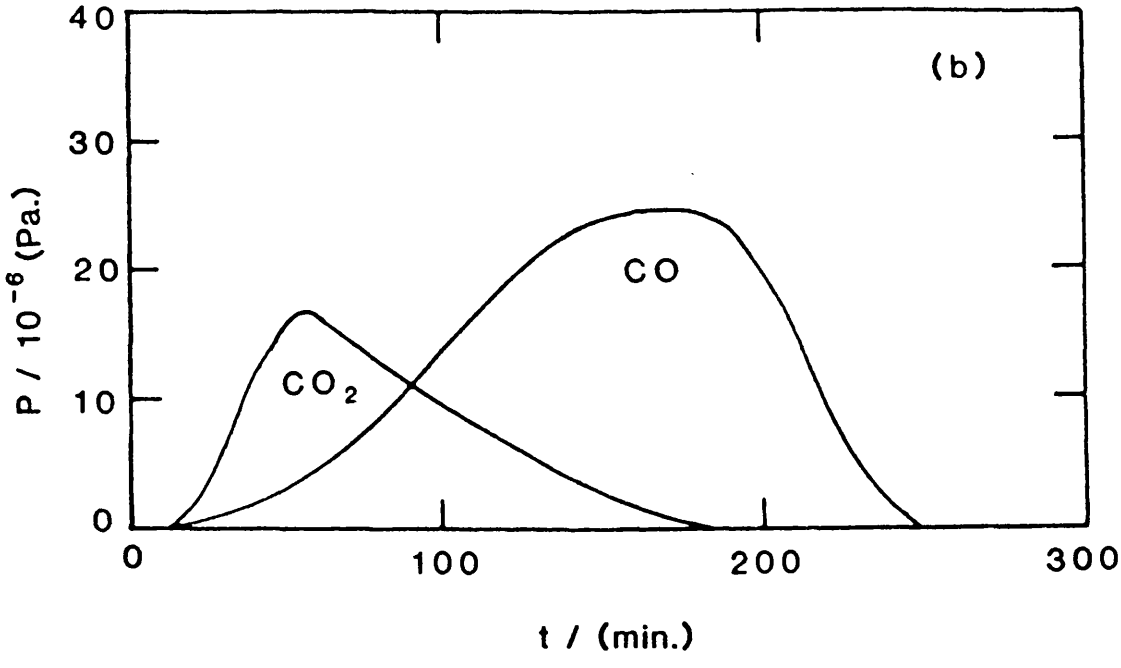


Figure 13.3 TPD curves for (a) Markham Main char and (b) PVDC char, in the unactivated state.

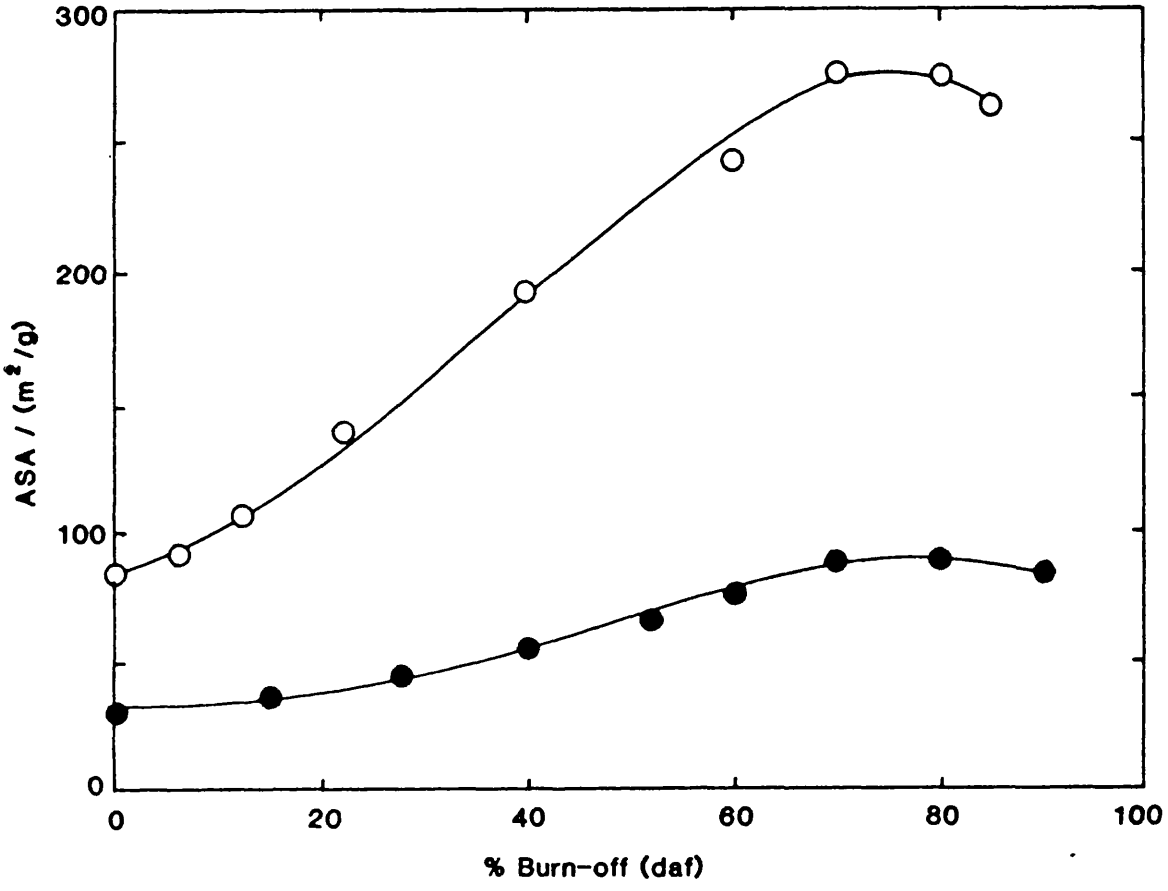


Figure 13.4 Active surface area as a function of burn-off for the PVDC char (O) and the Markham Main char (●).

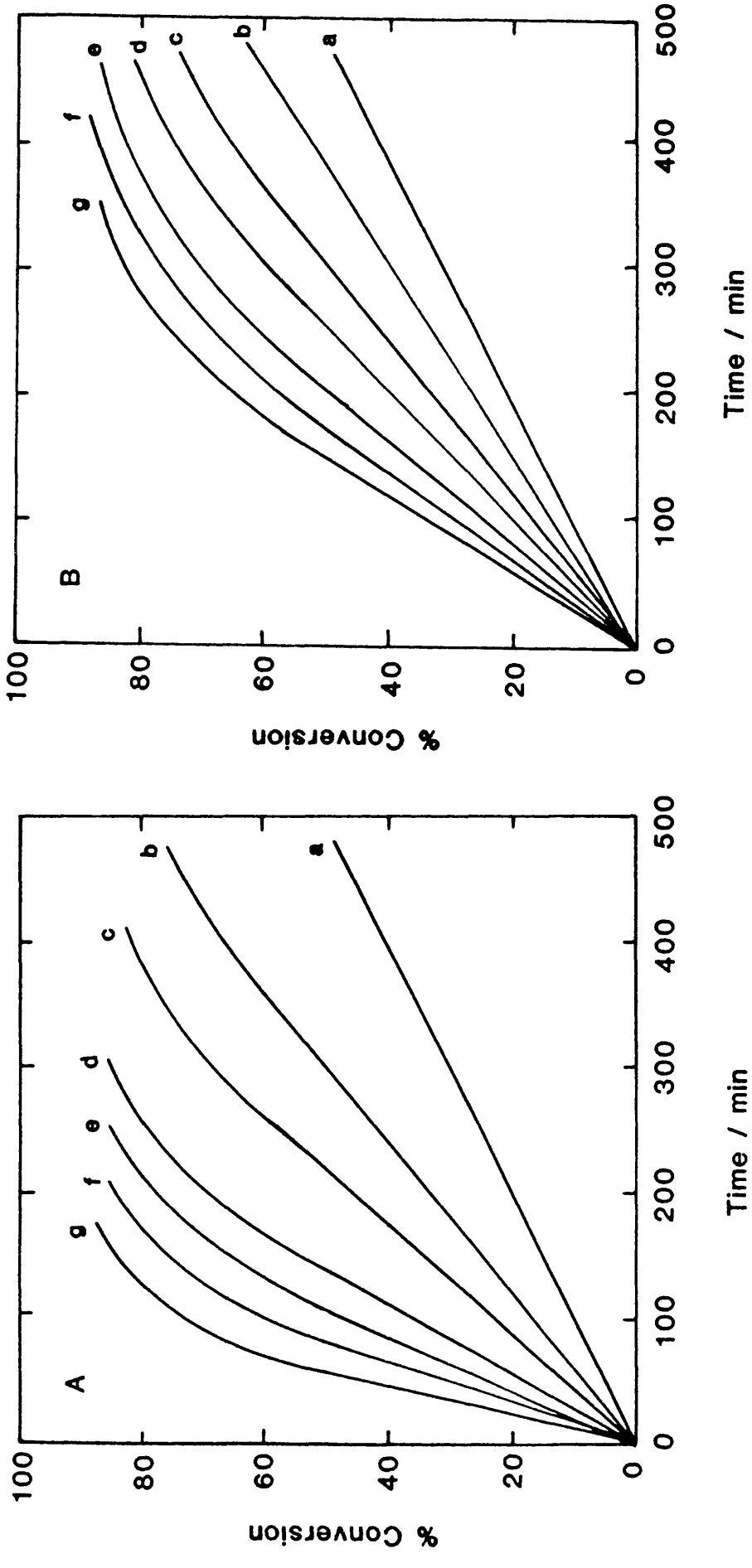


Figure 14.1 Conversion *versus* time plots for (A) PVDC char and (B) Markham Main char, obtained using the fixed-bed reactor. Gasification temperatures (°C) are: (a) 900; (b) 920; (c) 940; (d) 960; (e) 980; (f) 1000; and (g) 1020.

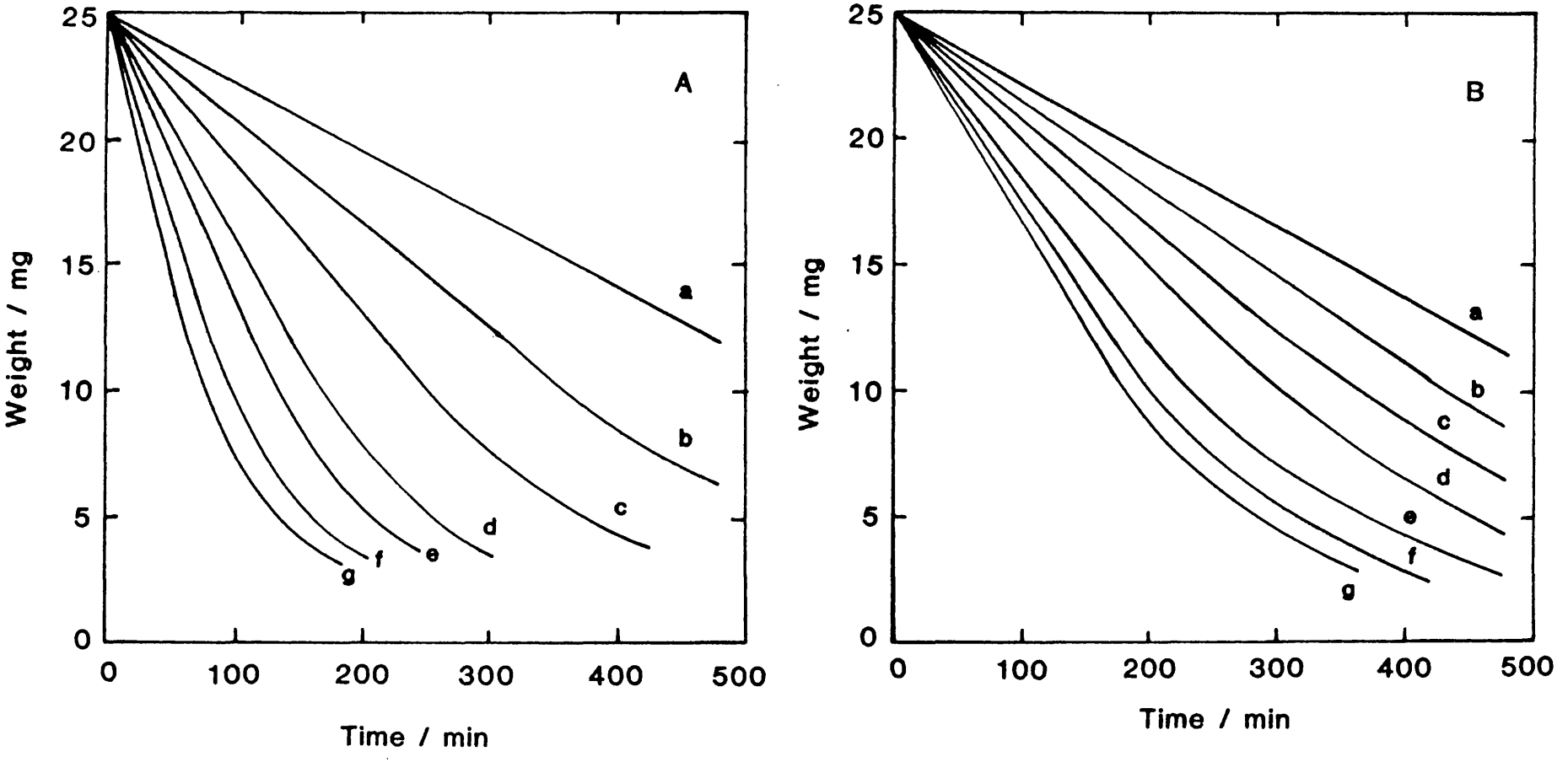


Figure 14.2 Weight loss *versus* time plots for (A) PVDC char and (B) Markham Main char, obtained using the TGA system. Gasification temperatures (°C) are: (a) 900; (b) 920; (c) 940; (d) 960; (e) 980; (f) 1000; and (g) 1020.

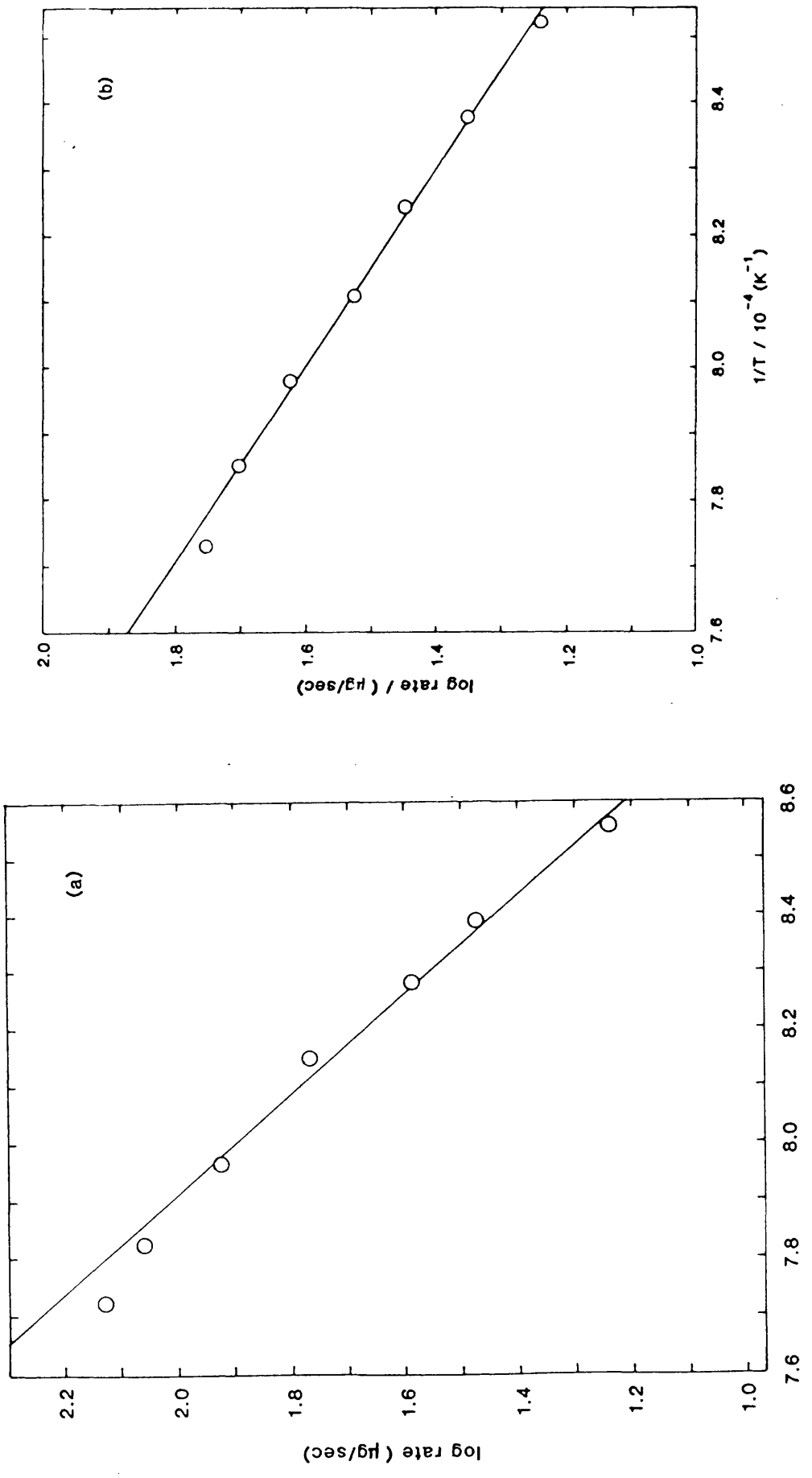


Figure 14.3 Arrhenius plots for (a) PVDC char and (b) Markham Main char, from the FBR system.

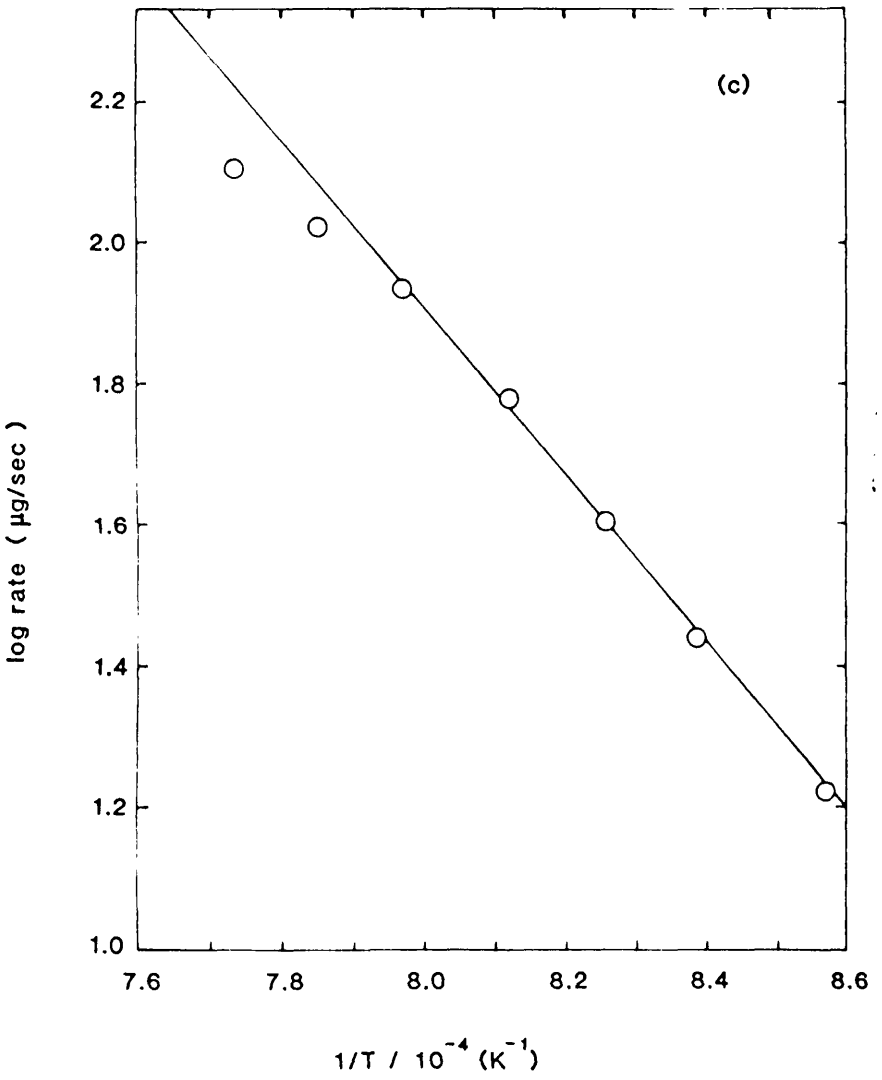


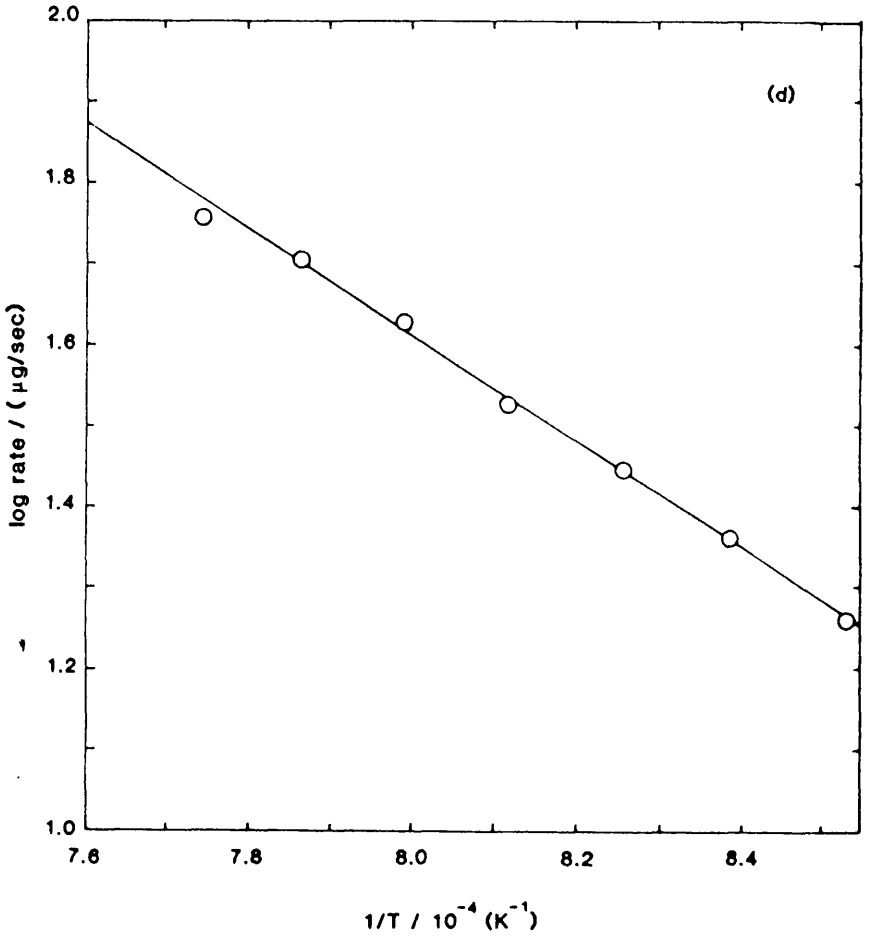


Figure 14.3 Arrhenius plots for (c) PVDC char and (d) Markham Main char, from the TGA system.

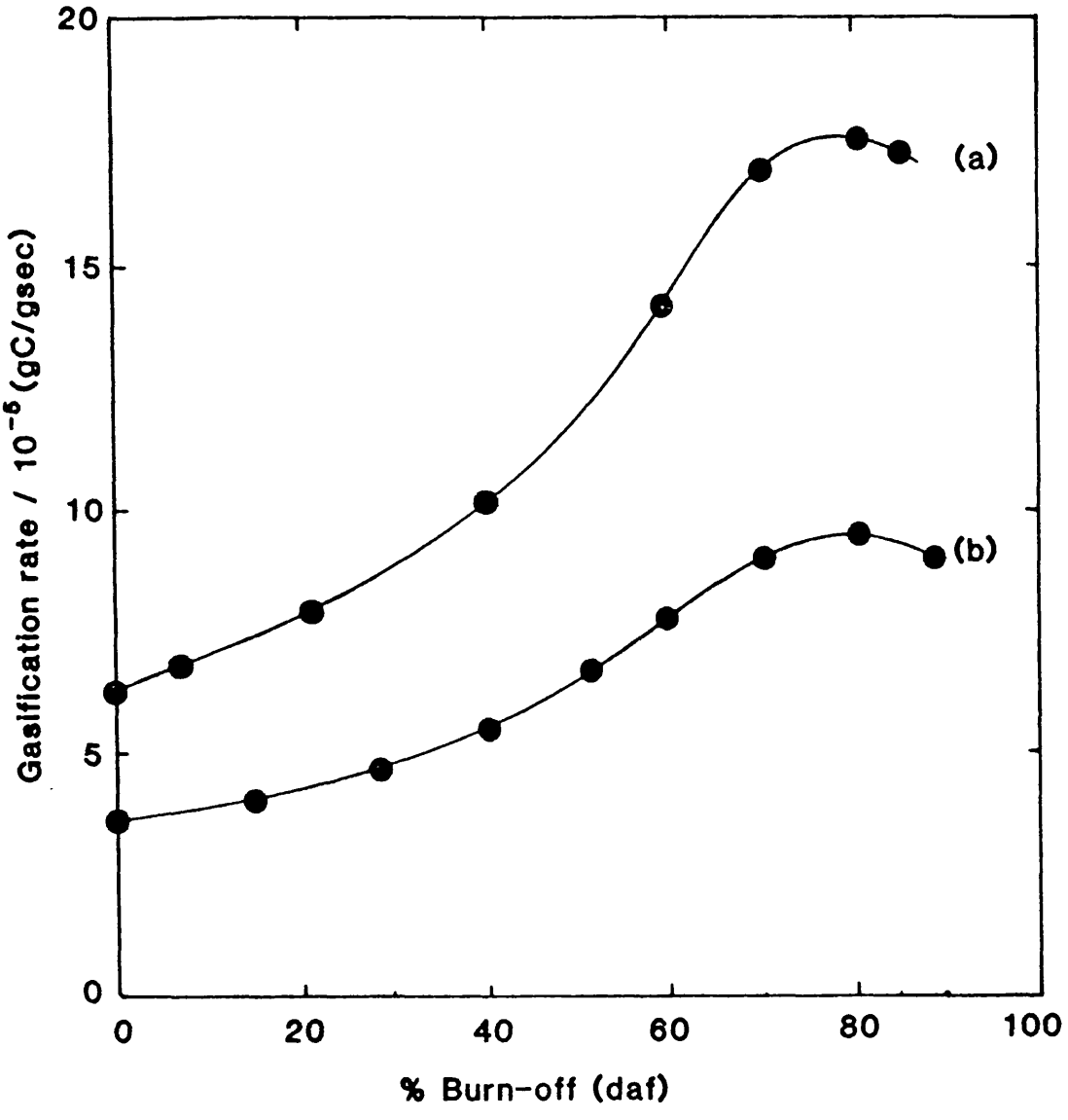


Figure 14.4 Gasification rate as a function of burn-off for (a) PVDC char and (b) Markham Main char.

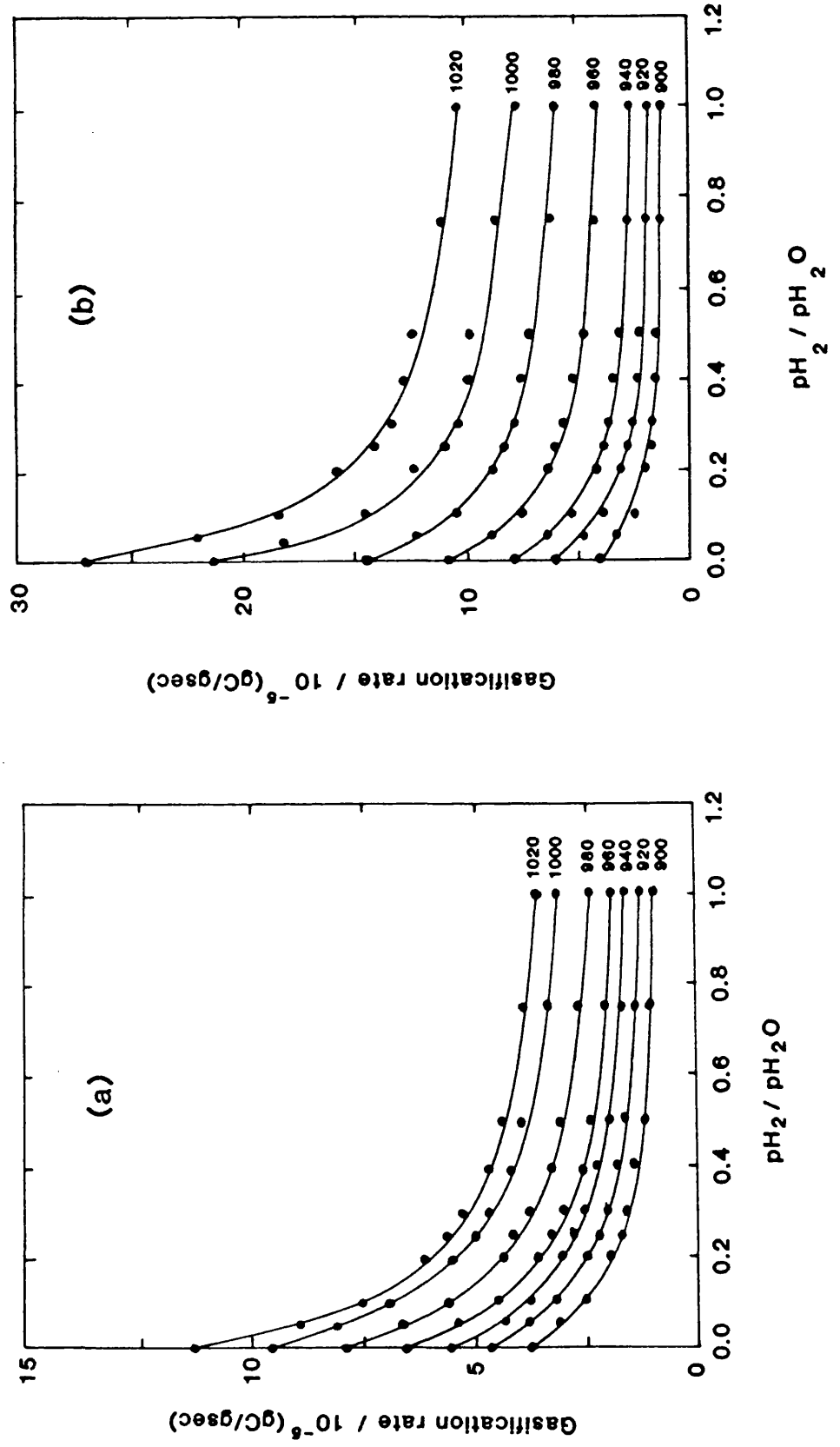


Figure 14.5 Variation of gasification rate with $pH_2/pH_2O$ ratio for (a) Markham Main char and (b) PVDC char. Gasification temperatures (°C) are shown.

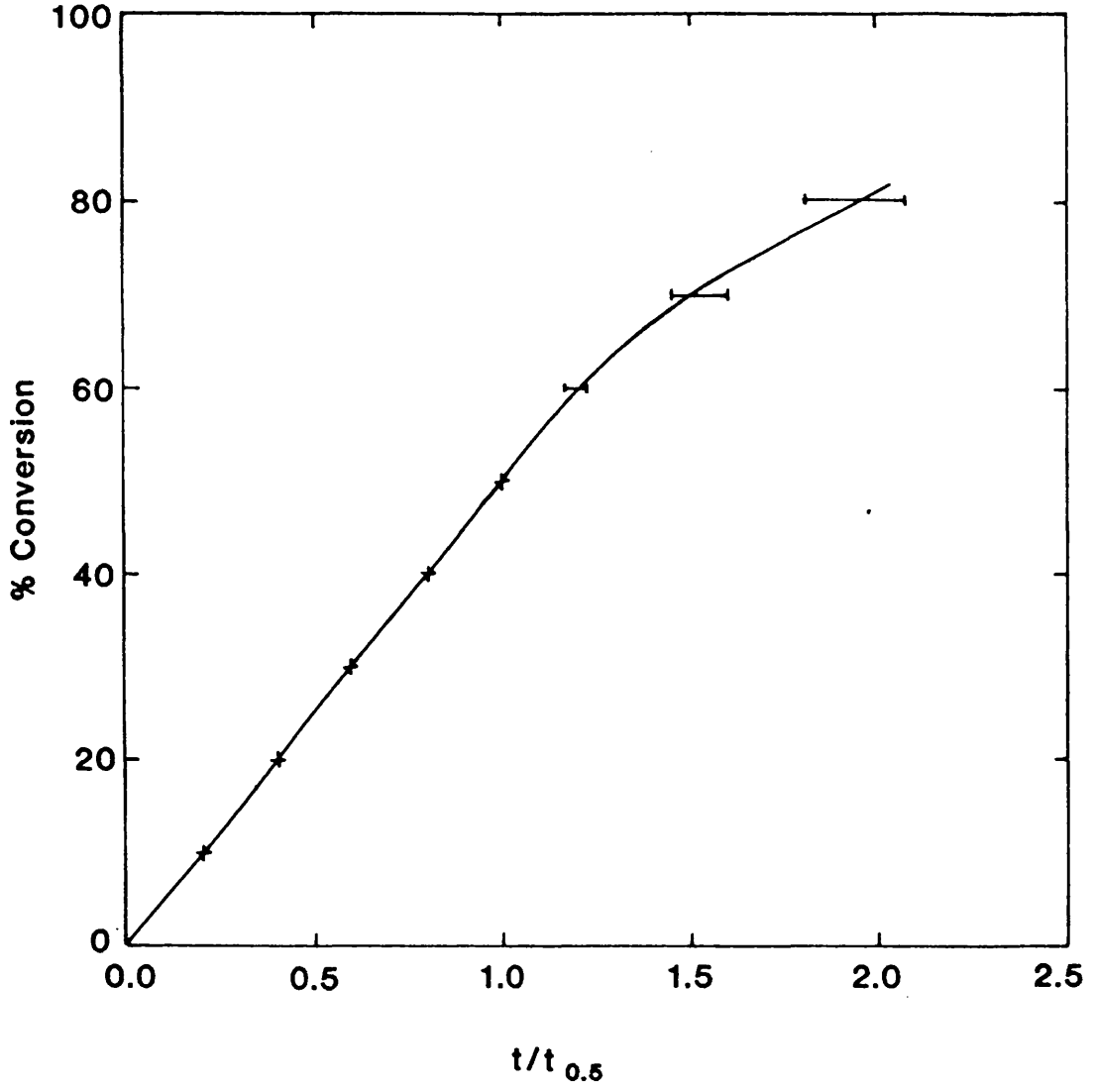


Figure 14.6 Normalisation of reactivity data using a dimensionless time scale.

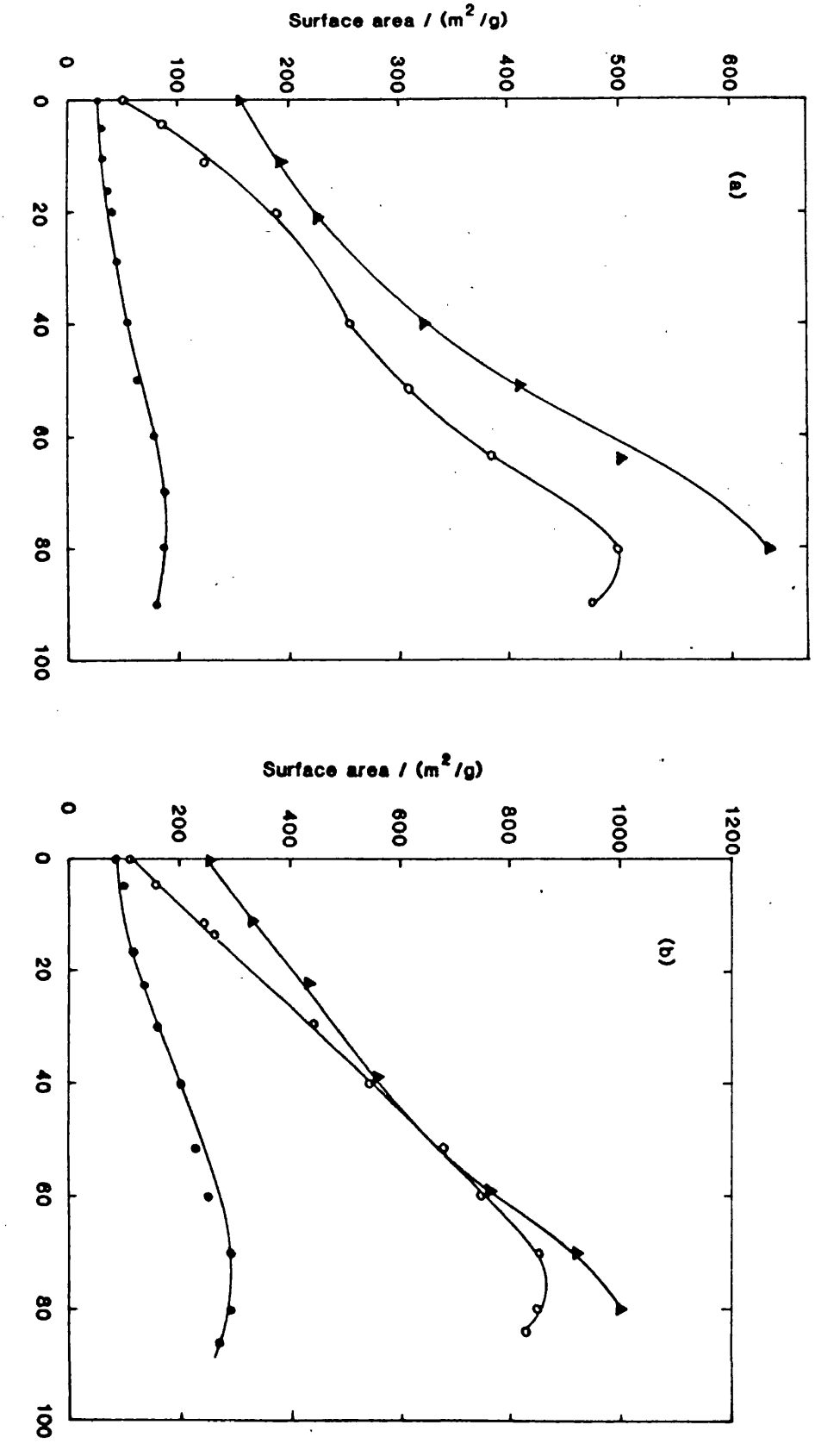


Figure 15.1 Variation of ASA (O), TSA measured by Ar adsorption at 77 K (O) and TSA measured by $CO_2$ adsorption at 195 K (▲) with burn-off for (a) Markham Main char, and (b) PVDC char.

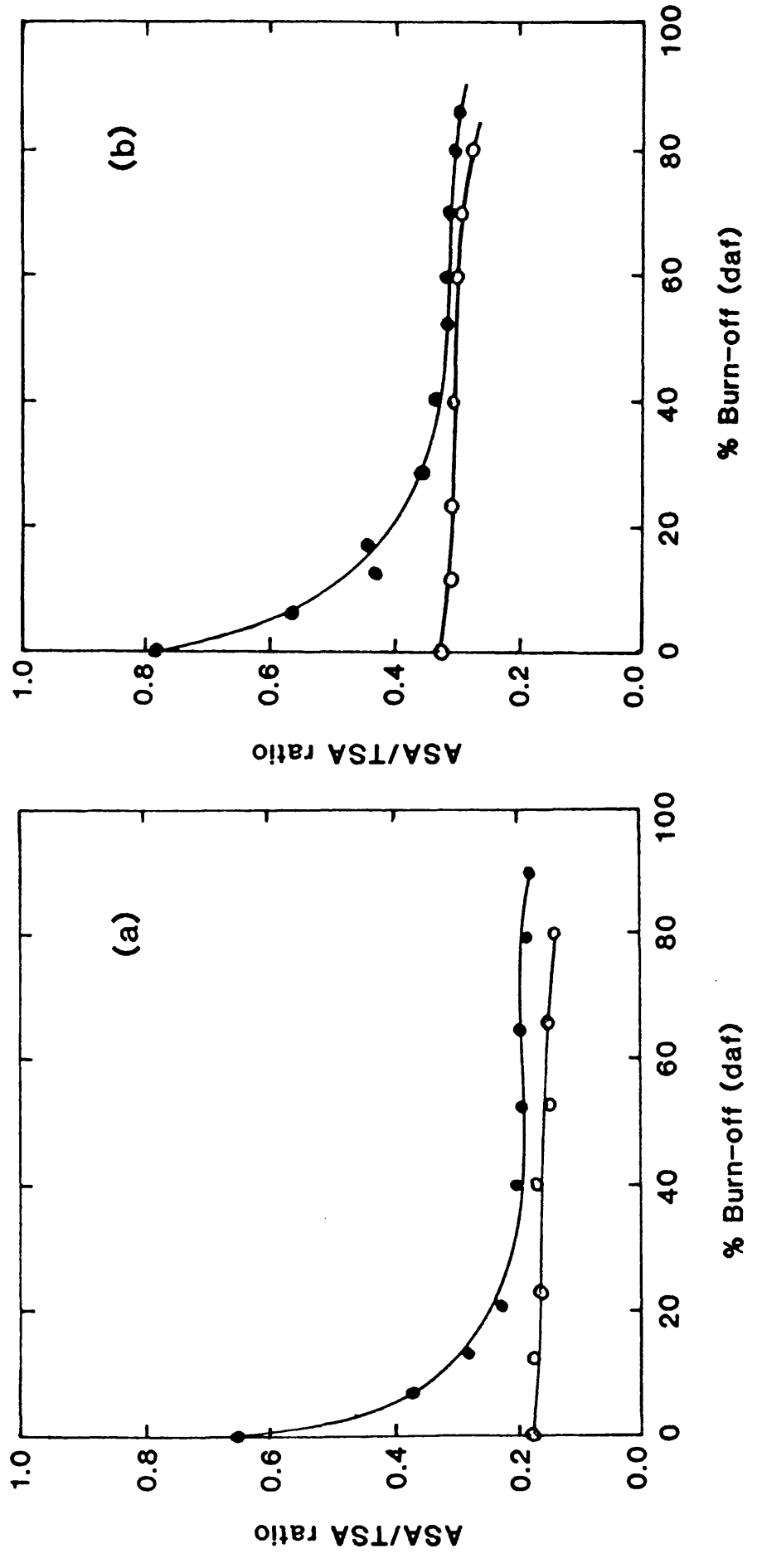


Figure 15.2 Variation of ASA/TSA ratio with burn-off for (a) Markham Main char and (b) PVDC char. (●) denotes TSA measured by Ar adsorption at 77 K and (O) denotes TSA measured by $CO_2$ adsorption at 195 K.